UNIVERSITÀ DEGLI STUDI DI PADOVA

UNIVERSITÀ DEGLI STUDI DI PADOVA

DIPARTIMENTO DI INGEGNERIA ELETTRICA

SCUOLA DI DOTTORATO DI RICERCA IN INGEGNERIA INDUSTRIALE
INDIRIZZO IN INGEGNERIA ELETTROTECNICA
CICLO XXIII

Design and Analysis of Interior Permanent Magnet Synchronous Machines for Electric Vehicles

Direttore della Scuola:
CH.MO PROF. PAOLO BARIANI .....

Coordinatore d'indirizzo:
CH.MO PROF. GIOVANNI MARTINELLI .....

Supervisore:
CH.MO PROF. NICOLA BIANCHI .....

Dottorando:
MASSIMO BARCARO .....

31 Gennaio 2011

A
Lidia
Maurizio
Enrico
e
Stefania

One has to grow hard
but without
ever losing tenderness

Ernesto "Che" Guevara

During times
of universal deceit,
telling the truth
becomes a revolutionary act

George Orwell

What is essential
is invisible to the eye

Antoine de Saint Exupéry

Acknowledgments

Firstly, I would like to express my deepest gratitude to Prof. Nicola Bianchi, for always being an enthusiastic supervisor throughout my doctoral period. I am truly grateful to him for being a master, not only about electrical machines. I am also indebted to Prof. Silverio Bolognani for his invaluable encouragement and the confidence he granted me.

I have been very fortunate to spend my doctoral period at the Electric Drive Laboratory. Even if with ups and downs, these years have been a bright and memorable period. I am very grateful to the members of past and actual EDlab staff for being genuine friends and supporting me. A special thank to "our" technician for his irreplaceable help during measurements.

My sincere appreciation to Dr. Freddy Magnussen for his constructive criticisms throughout my doctoral period. I very grateful to him for the five months period that I have spent in ABB Corporate Research. I would kindly like to thank all the researchers of the Electrical Machines and Motion Control group. This span of time has been so special only thanks to the "Italian ABB division" and my corridor friends of Norra Allégatan 24, Västerås.

My deep gratitude to all my close friends for being always present, even if job and distance are against us.

I am immensely grateful to my family for their support, encouragement and indestructible faith on my decisions. I would really thank them for believing me and being an irreplaceable tower of strength. A lovely thank to my uncle Bepi for having guarded my student reputation in front of every one up to the end of his days.

Lastly, but definitely not the least, I like to express my greatest love to Stefania, looking forward to share together the rest of our life.

Padova, 31 January 2011 Massimo Barcaro

This Thesis is written in LaTeX.
An electronic version is available at: *http://paduaresearch.cab.unipd.it*

Contents

Sommario

Contesto ed obiettivi della tesi

L'utilizzo dei magneti permanenti nel campo delle macchine elettriche rotanti attualmente rappresenta una scelta comune e vantaggiosa nella quasi totalità delle applicazioni: ad esempio il trasporto, i processi industriali, gli impianti di generazione, gli attuatori, gli elettrodomestici. Le potenze di queste macchine elettriche spaziano dalle frazioni di Watt ai milioni di Watt.

Tra le varie tipologie di macchine elettriche provviste di eccitazione mediante magnete permanente, le macchine sincrone a magnete permanente occupano un posto di rilievo nella ricerca, sia in ambito accademico che industriale. In particolare queste macchine sincrone permettono di combinare più vantaggi, come alto rendimento, elevato fattore di potenza, alta densità di coppia, notevole capacità di sovraccarico, robusta costruzione, limitata manutenzione, volumi compatti e quindi peso ridotto.

Negli ultimi anni questi vantaggi stanno diventando delle caratteristiche cruciali e preferibili, in particolare per le applicazioni non prettamente industriali come la trazione elettrica dei veicoli. Infatti, per queste nuove applicazioni, la compattezza dei volumi e le alte prestazioni in termini di coppia e rendimento sono le caratteristiche vincenti che li fanno preferire ai motori asincroni. Nell'ambito automobilistico le macchine elettriche a velocità variabile, come i motori sincroni a magnete permanente, sono attualmente sempre più utilizzati per migliorare le prestazioni complessive dei veicoli.

In aggiunta ai vantaggi già indicati, i motori a magnete permanente permettono una notevole flessibilità di progettazione. L'assenza di avvolgimento di eccitazione rotorico ha permesso di studiare varie di strutture. Conseguentemente, grazie a progettazioni dedicate, è possibile ottenere macchine che esibiscono una capacità di tollerare alcuni guasti o macchine in grado di operare lungo un campo di velocità estremamente esteso. Queste peculiaritàsono spesso richieste dalle applicazioni di mobilità, come il trasporto, che richiedono inoltre un alto livello di affidabilità.

Nonostante questi indubbi vantaggi sussistono delle problematiche legate all'utilizzo dei magneti permanenti. La tendenza odierna è, quindi, quella di studiare le configurazioni che permettono di limitare o minimizzare la quantità di magnete permanente, pur soddisfando le richieste di progetto.

Tra le soluzioni proposte, i motori sincroni a riluttanza assistita dai magneti permanenti o più semplicemente i motori a magnete interno rappresentano una valida scelta adatta alle richieste nel campo del trasporto. Grazie ad una struttura rotorica anisotropa, questi motori sono in grado di produrre coppia utile anche in assenza di magnete permanente. L'utilizzo dei magneti permanenti permette di migliorarne le prestazioni eliminando alcuni svantaggi. Questi motori sono oggetto di studio di un gran numero di gruppi universitari di ricerca.

Lo scopo di questa tesi di dottorato è analizzare in dettaglio alcuni aspetti di progettazione elettromeccanica delle macchine sincrone a magneti permanenti interni. Infatti la complessa struttura geometrica rotorica, che permette di ottenere i noti vantaggi, determina anche una serie di problematiche. In generale, queste macchine elettriche sono caratterizzate da elevate oscillazioni di coppia, distorsioni dei flussi magnetici e conseguenti perdite nel ferro, vibrazioni, ed altri effetti parassiti. Quindi, l'obiettivo della tesi è analizzare alcuni di questi aspetti mediante procedure analitiche, simulazioni agli elementi finiti e prove sperimentali al fine di valutare regole di progettazione che permettano di minimizzare gli svantaggi dei questa configurazione.

Nel ambito dell'analisi delle metodologie di progettazione del motore a magneti permanenti interni sono state affrontate le seguenti tematiche di studio:

- Investigare gli effetti della geometria rotorica sull'oscillazione di coppia ed individuare le soluzioni che permettono di minimizzare questo fenomeno.
- Investigare gli effetti della geometria rotorica sulle fluttuazioni dell'induzione nei denti statorici, e le conseguenti perdite nel ferro per effetto delle correnti parassite. In questo contesto, individuare le soluzioni che permettono di limitare le perdite alle alte velocità in condizioni di deflussaggio.
- Investigare il principio di produzione della coppia elettromagnetica, in particolare della componente non legata ai magneti permanenti, ed analizzare alcuni effetti parassiti legati all'utilizzo di avvolgimenti a passo frazionario.
- Investigare una particolare macchina, il motore a doppio avvolgimento trifase, che permette di ottenere un aumento della tolleranza ai guasti pur richiedendo componentistica standard.

Le tematiche di ricerca del dottorato sono state seguite sotto la guida del supervisore nel Laboratorio di Azionamenti Elettrici ed in concerto con il centro ricerca di ABB locato in Svezia (Västerås). In particolare, la borsa di studio è stata finanziata dal partner industriale svedese ABB Corporate Research, presso il quale ho trascorso un periodo di ricerca di 5 mesi.

Le pubblicazioni redatte durante il dottorato sono elencate nell'introduzione.

Contenuti della tesi

Di seguito sono descritti brevemente i contenuti dei singoli capitoli della tesi:

Il capitolo 1 introduce le motivazioni per una futura espansione del mercato dei veicoli elettrici ibridi. Sono descritte le principali architetture di gestione delle sorgenti di energia. Infine è presentata una selezione di veicoli elettrici ibridi, che utilizzano macchine sincrone a magnete permanente, al fine di fornire una panoramica sulla varietà di prestazioni richieste.

Il capitolo 2 illustra le peculiarità dei motori sincroni a magneti permanenti descrivendo le equazioni fondamentali e le strategie di controllo, ed evidenziando i comportamenti delle diverse geometrie rotoriche.

Il capitolo 3 presenta il modello analitico del motore sincrono a magneti permanent provvisto di rotore anisotropo. La geometria del polo rotorico è considerata provvista di multiple barriere di flusso. Nel modello sono implementati il calcolo della coppia elettromagnetica e dell'andamento dell'induzione al traferro.

Il capitolo 4 presenta i risultati dell'analisi dell'oscillazione di coppia ottenuti mediante il modello analitico del motore. Il modello, verificato dalle simulazioni agli elementi finiti, viene applicato in alcuni esempi di minimizzazione dell'oscillazione. I risultati sono congruenti con le soluzioni derivate applicando una procedura di progetto brevettata. Infine, sono presentate alcune soluzioni ottimizzate ottenute applicando il modello ad un algoritmo genetico.

Il capitolo 5 presenta i risultati ottenuti mediante il modello analitico del motore riguardanti le perdite per correnti parassite nel ferro nei denti di statore, in particolare in condizioni di deflussaggio. Il modello analitico, che permette di calcolare la distorsione dell'induzione sui denti, viene utilizzato per investigare l'effetto della geometria rotorica sull'andamento delle perdite al variare della velocità. I risultati del modello sono stati verificati sperimentalmente.

Il capitolo 6 introduce brevemente gli avvolgimenti a passo frazionario applicati alle macchine a magnete permanente interno. In questo ambito sono stati analizzati alcuni aspetti: (i) gli effetti dell'avvolgimento frazionario sulla anisotropia rotorica e la corrispondente coppia prodotta, (ii) la possibilità di applicare alcune semplificazioni durante l'analisi agli elementi finiti, (iii) l'effetto del mutuo accoppiamento tra gli assi magnetici di tali macchine.

Il capitolo 7 introduce alcune strategie per ottenere un azionamento tollerante ai guasti. Quindi viene investigata estesamente la soluzione di motore sincrono a magneti permanenti interni provvisto di doppio avvolgimento trifase, verificando sperimentalmente il comportamento a seguito di diverse tipologie di guasto. Questa tipologia di macchina permette di mantenere una limitata operatività anche a seguito di un guasto pur utilizzando componentistica standard. Varie prestazioni sono analizzate in caso di guasto, tra cui: coppia media, oscillazione di coppia, sbilanciamenti delle forze radiali, correnti di cortocircuito. Si propongo infine delle regole di progettazione per la scelta di una macchina che possa operare come macchina esafase, evidenziandone i relativi vantaggi.

Introduction

This chapter introduces the utilization of permanent magnets on electrical machines [1]. Then, the motivation of the thesis and the main contributions are described. Finally, a list of publications of the author is reported.

Background

Permanent magnet (PM) materials are known since ancient time. The ancients referred of a material coming from the region of Magnesia in Minor Asia (and because of this called Magnesia) exhibiting attraction or repulsion phenomena. In 1200's a steel that could be magnetized by contact with Magnesia was discovered and the construction of the first permanent magnet was described. In 1600's, Gilbert wrote the systematic and experimental treatise "De magnete magneticisque corporibus et de magno magnete tellure physiologia nova". In that publication Gilbert described his studies on the earth magnetism, the behaviour of Magnesia bodies, the improvement in magnetic actions by adding iron expansions and, in particular, he illustrated different technologies for manufacturing permanent magnets, that were used till the 19^{th} century.

The first permanent magnet material became available, in sufficient large quantities, was Carbon steel (C-steel) developed during the last part of the 19^{th} century. It was soon followed by Tungsten steel (W-steel) and Cobalt steel (Co-steel) , that exhibited better performance.

The next step forward was achieved in 1932 by the introduction of MK-steel by Mishima, which main advantages were the low price. This magnet can be regarded as precursors of the well-known Alnico-type magnets developed only a few years later, in 1936. The compositional freedom and the possibility to optimize the heat treatment led to the development of a large family of permanent magnet materials that found the first real industrial applications.

Therefore, the history of the PM electrical machines starts on an industrial basis with the availability of Alnico. Before such a date only laboratory or demonstrating prototypes were realized. The history can be reconstructed from technical and scientific publications, as well as pertinent registered patents. One of the first systematic contributions on PM principle and applications can be found around 1920 by S.Evershed. In 1941 the first applications in electrical machines were presented. During the 1949's

Alnico material dominates the interest of the industrial engineers. P.P. Cioffi (Bell Telephone Labs) wrote in 1948 about the critical problem of stabilizing PMs, describing the results in both cases of stabilization before and after assembling.

In the same decade a new class of permanent magnet material was developed. It was based on the composition formula MO 6Fe2O3, where M is a metal as Barium (Ba), Strontium (Sr) or Lead (Pb). These type of magnets was called "Ceramic" and are still used with the common name of "Ferrites". The first papers on ceramic ferrite magnets, and describing electrical apparatus made by them, published in the first years on the 1960. Small power motors gained the highest advantages of the new low cost, magnetically stable new material, increased also by the advent of the first solid state power components.

Magnets based on the rare earths (the Lanthanides) have been experienced since the 1960's. Initially, they were considered exotic materials by some even though significant deposits were found in many locations around the world. Now they are used in many common applications. Neodymium is a particularly good choice for a permanent magnet. It is the third most abundant Lanthanide, behind Cerium and Lanthanum but its demand is the highest between them, yielding the prices low today. Another important rare earth is the Samarium, that is less abundant than Neodymium. The continuous improvement in magnetic performance of rare earth PM together with the diffusion of more and more reliable and effective solid state power components and powerful digital components have determined the recent success of a large variety of PM motors.

In the low and medium power rating they exhibit at present the highest motor performance in terms of dynamic response, energy efficiency and torque density. As a consequence, in the last two decades, permanent magnet motors have found an increasing interest for their capabilities of meeting the requirement of a lot of applications.

Motivation of the thesis

The adoption of permanent magnet (PM) on rotating electrical machines represents now a fashionable design option in all fields as transportation, industrial processing, power plants, domestic appliances, actuators and so on. The corresponding power ratings of such machines ranges now from fractions of Watts to some million of Watts, as in a wind generator.

Actually, among the electrical machines, the PM synchronous machine is the more deeply studied from academia and industry. In particular, the PM synchronous machine combines several advantages as high efficiency, high power factor, high torque density, high overload capability, robustness, reduced maintenance, compactness and low weight.

These advantages are becoming crucial for those non–industrial application, as the electric vehicles. High performance and compactness are often the winning characteristics of such machines as respect to the induction machines. Referring to the automotive field, variable speed drives as PM synchronous machine are adopted to improve the overall performance of the vehicles.

The design flexibility due to the absence of rotor winding excitation and the variety of PM sizes and characteristics allow to achieve several features, e.g. fault–tolerance

and flux–weakening capability. Thanks to these features the PM machine is a suitable candidate for traction requirements.

However the recent trend is to select those configurations that allow to minimize the PM utilization. It is also due to the issues related to PM temperature derating, mechanical stress, and PM reliability.

The PM synchronous reluctance machine or interior PM machine is, among the others, a promising candidate to satisfy the traction requirements. Thanks to its anisotropy rotor structure is able to provide torque not only due to the PM flux. In addition the adoption of fractional–slot winding, as respect to the standard integral–slot winding, is imperative to achieve some of the appealing features. In this field, several topics are under study by the international community of researchers.

However, the aim of the doctoral work is to deepen some aspects concerning the design of these machines. It is worth noticing that the complexity of the rotor structure of these machine involves several drawbacks, such as torque oscillations, additional iron losses, vibrations, and so on. Therefore, some aspects have been analyzed by means of analytical procedures, finite element simulations and experiential measurements on prototypes. The variety of topic treated is directly due to the complexity of the design: a tradeoff between advantages and drawbacks is usually necessary rather than a perfect minimization of a single aspect. Therefore, an overview of the design options is required in order to design a suitable machine.

In the contest of the analysis of the interior permanent magnet machines, the objectives can be summarized as:

- To evaluate how the rotor geometry affects the torque ripple, and thus the solutions allowing to minimize it.
- To evaluate how the rotor geometry affects the eddy current iron losses in the stator teeth, and thus the solutions allowing to minimize it (in particular referring to the flux–weakening operating conditions).
- To deeply investigate the torque mechanism and complex magnetic phenomena, in particular adopting fractional–slot winding.
- To investigate a particular configuration of fault–tolerant machine, the dual three–phase machine provided of a suitable anisotropic rotor.

This doctoral study has been accomplished at the Electric Drives Laboratory within the Department of Electrical Engineering of the University of Padova in collaboration with the ABB research center in Västerås. The doctoral bursary was financed by ABB Corporate Research, Västerås (Sweden), where a 5–month period has been spent.

Main contributions of the thesis

To the knowledge of the author, the remarkable contribution of this thesis for future researchers in this field are:

- An analytical model of the anisotropic synchronous machine that can be simply adopted to evaluate optimal solutions allowing to satisfy selected objectives. It has been applied to the issues of torque ripple minimization and stator tooth eddy current minimization. The model has been verified experimentally comparing the measured and predicted stator tooth flux density.
- An extended analysis of the dual three–phase machine provided of an interior permanent magnet rotor, supported by experimental verification. A simple design rule to select the appropriate number of slots and poles in order to achieve a six–phase machine is proposed.

Outline of the thesis

Chapter 1 introduces the hybrid electric vehicles and their adoption as the common starting answer to the issues of the global transportation sector. A classification of the more common hybrid electric architecture is presented. Finally a selection of past and actual commercial vehicles are presented in order to give the idea of the different requirements and performance offered by the automotive market.

Chapter 2 illustrates the key features of the PM synchronous motors. Different geometrical topologies are presented. Finally, some control strategies are described, highlighting the relationship between the PM motor performance and its rotor geometry.

Chapter 3 presents the analytic model of the anisotropic synchronous machine. The computation of both the air gap flux–density and the electromagnetic torque is reported referring to geometries with one to four flux–barriers per pole.

Chapter 4 presents the application of the analytic model of the anisotropic machine to select the flux–barrier angles in order to minimize the torque ripple. The analytical model results are compared with suitable finite elements simulations. Examples of torque minimization with one and two flux–barrier rotor pole geometry are reported. The results of the model are in good agreement with those obtained applying an existing patent. Finally the results of a stochastic optimizer, that adopts the analytical model, are reported.

Chapter 5 presents the eddy current iron loss issue. The geometries minimizing the stator iron losses are evaluated by means of the analytical model of the anisotropic rotor machine. The dependence of such losses on the rotor geometry, or rather the flux–barrier angles will be highlighted. The analysis has been carried out considering a synchronous reluctance machine with one flux–barrier per pole rotor and a synchronous interior permanent magnet machine with two flux–barrier per pole rotor. The results of the analytical model are compared with both finite elements and experimental tests.

Chapter 6 presents a brief description of the fractional–slot winding machines. The star of slots theory is introduced since it is easily adopted to design these windings. Referring to the interior permanent magnet machine the relevance of the both PM and reluctance torque component is evaluated with both integral–slot and fractional–slot winding. Finally, two issues of the interior permanent magnet machines with fractional–slot winding are described: (i) the issue of the reduction of finite elements simulations, (ii) the issue of the cross saturation. The latter aspect will be highlighted during the design of a interior permanent magnet integrated starter–alternator.

Chapter 7 introduces the concept of fault tolerance in the electrical machine drive. The capability of a permanent magnet machine with a dual three–phase winding under faulty operating conditions is analyzed. Such a machine balances the requirements of fault tolerance and the adoption of standard components since it has two separate three–phase windings, each of them supplied by a separate standard converter. Several aspects are evaluated under faulty conditions, among the others: average torque, torque ripple, radial forces, short circuit current, mutual coupling, overload capability. The conditions to operate the machine as a six–phase machine are presented. Simple design rules are proposed to select those slot and pole combinations allowing a six–phase machine to be obtained.

List of pubblications

Several parts of the work reported in this thesis have been presented by the author during the course of his doctoral study in international conferences and journals. Hereafter the publications are listed. Conference papers are marked as $C*$, while the journal papers are marked as $J*$.

C1 A. Faggion, L. Sgarbossa, L. Alberti, M. Barcaro, M. Dai Pre, and S. Bolognani. "Effective control of an Integrated Starter-alternator with an IPM synchronous machine". In *Proceedings of the IEEE Power Electronics Specialists Conference, 2008. PESC 2008*, pages 3924-3929, Rhodes, June 15-19, 2008, DOI 10.1109/ PESC.2008.4592567

C2 M. Barcaro, N. Bianchi, and F. Magnussen. "PM Motors for Hybrid Electric Vehicles". In *Proceedings of the 43rd International Universities Power Engineering Conference IEEE UPEC 2008*, pages 1-5, Padova, Italy, September 1-5, 2008, DOI 10.1109/ UPEC.2008.4651682

Republished also on journal in 2009 as:

J1 M. Barcaro, N. Bianchi, and F. Magnussen. "PM Motors for Hybrid Electric Vehicles". The Open Fuels & Energy Science Journal, BENTHAM OPEN 2009, Issue 2, Pages 135-141, DOI 10.2174/ 1876973X01002010135

C3 M. Barcaro, N. Bianchi, and S. Bolognani. "Hybrid Electric Propulsion System Using Submersed SPM Machine". In *XVIII International Conference on Electrical Machines IEEE ICEM08*, pages 1-6, Vilamoura, Portugal, September 6-9, 2008, DOI 10.1109/ ICELMACH.2008.4800089

C4 M. Barcaro, L. Alberti, A. Faggion, L. Sgarbossa, M. Dai Pre; and N. Bianchi. "Experimental Tests on a 12-Slot 8-Pole Integrated Starter-Alternator". In *XVIII International Conference on Electrical Machines IEEE ICEM08*, pages 1-6, Vilamoura, Portugal, September 6-9, 2008, DOI 10.1109/ ICELMACH.2008.4799841

Accepted for republication on journal in 2010 and republished as:

J2 M. Barcaro, A. Faggion, L. Sgarbossa, N. Bianchi, S. Bolognani, "Performance Evaluation of an Integrated Starter Alternator using an Interior PM Machine". In *Proceedings of IET Electric Power Applications*, Vol.4, Issue 7, pages 539-546, August 2010. DOI 10.1049/ iet-epa.2009.0216

C5 M. Barcaro, L. Alberti, A. Faggion, L. Sgarbossa, M. Dai Pre; N. Bianchi, and S. Bolognani. "IPM Machine Drive Design and Tests for an Integrated Starter-alternator Application". In *IEEE Industry Applications Society Annual Meeting, 2008. IAS08*, pages 1-8, Edmonton, Alberta, Canada, October 5-9, 2008, DOI 10.1109/ 08IAS.2008.217

Republished also on journal in 2010 as:

J3 M. Barcaro, L. Alberti, A. Faggion, L. Sgarbossa, M. Dai Pre, N. Bianchi, and S. Bolognani. "IPM Machine Drive Design and Tests for an Integrated Starter-alternator Application". In *IEEE Transactions on Industry Applications*, vol. 46, no. 3, pp. 993-1001, May-June 2010, DOI 10.1109/ TIA.2010.2045323

C6 N. Bianchi and M. Barcaro, "Iron Losses Reduction in Synchronous Motors with Anisotropic Rotor". In *34th Annual Conference of the IEEE Industrial Electronics Society. IECON 2008*, pages 1-6, Orlando, Florida, USA, November 10-13, 2008, DOI 10.1109/ IECON.2008.4758135

Republished on journal in 2010 as:

J4 M. Barcaro and N. Bianchi, "Air-Gap Flux Density Distortion and Iron Losses in Anisotropic Synchronous Motors". In *IEEE Transactions on Magnetics*, vol. 46 , no. 1, pages: 121-126, Jan. 2010, DOI 10.1109/ TMAG.2009.2030675

C7 L. Alberti, N Bianchi, M. Barcaro, S. Bolognani, D. Bon, M. Castiello, A. Faggion, E. Fornasiero, and L. Sgarbossa. "Interior Permanent Magnet Integrated Starter Alternator". In *4th International Conference and Exhibition on Ecological Vehicles and Renewable Energies, EVER09*, pages 1-6, Monte Carlo, Monaco, March 26-29, 2009.

Accepted for republication on journal in 2009 and republished in 2011 as:

J5 L. Alberti, N Bianchi, M. Barcaro, S. Bolognani, D. Bon, M. Castiello, A. Faggion, E. Fornasiero, and L. Sgarbossa. "Interior Permanent Magnet Integrated Starter Alternator". In *The International Journal for Computation and Mathematics in Electronic Engineering COMPEL*, ISSN: 0332-1649

C8 M. Barcaro, N. Bianchi, and F. Magnussen. "Configurations of Fractional-slot IPM Motors with Dual Three-phase Winding". In *IEEE International Electrical Machine and Drive Conference, IEMDC2009*, pages 1148-1154, Miami, Florida, May 3-6 2009, DOI 10.1109/ IEMDC.2009.5075316

C9 M. Barcaro, N. Bianchi, and F. Magnussen. "Rotor Flux-barrier Geometry Design to Reduce Iron Losses in Synchronous IPM Motors Under FW Operations". In *IEEE International Electrical Machine and Drive Conference, IEMDC2009*, pages 1140-1147, Miami, Florida, May 3-6 2009, DOI 10.1109/ IEMDC.2009.5075315

Accepted for republication on journal in 2009 and republished in 2010 as:

J6 M. Barcaro, N. Bianchi, and F. Magnussen. "Rotor Flux-barrier Geometry Design to Reduce Iron Losses in Synchronous IPM Motors Under FW Operations". In *IEEE Transaction on Industry Applications*, Vol-46, Issue 5, pages 1950-1958, Sept.-Oct. 2010, DOI 10.1109/ TIA.2010.2060175

C10 M. Barcaro, N. Bianchi, and F. Magnussen. "Analysis and Tests of a Dual Three-Phase 12-slot 10-pole Permanent Magnet Motor". In *IEEE Energy Conversion Congress & Exposition, ECCE2009*, pages 3587-3594, San Jose, California, September 20-24 2009, DOI 10.1109/ ECCE.2009.5316094

Accepted for republication on journal in 2010 as:

J7 M. Barcaro, N. Bianchi, and F. Magnussen. "Analysis and Tests of a Dual Three-Phase 12-slot 10-pole Permanent Magnet Motor". In *IEEE Transaction on Industry Applications*, DOI 10.1109/ TIA.2010.2070784.

C11 P. Alotto, M. Barcaro, N. Bianchi, M. Guarnieri. "Optimization of IPM motors with Machaon rotor flux barriers". In *14th Biennial IEEE Conference on Electromagnetic Field Computation (CEFC2010)*, Chicago IL, 9-12 May 2010, DOI: 10.1109/ CEFC.2010.5481335

Accepted for republication on journal in 2010 as:

J8 P. Alotto, M. Barcaro, N. Bianchi, M. Guarnieri. "Optimization of Interior PM Motors with Machaon Rotor Flux Barriers". In *IEEE Transactions on Magnetics*, DOI 10.1109/ TMAG.2010.2073450

C12 M. Barcaro, N. Bianchi, E. Fornasiero, and F. Magnussen. "Experimental Comparison between two Fault-Tolerant Fractional-Slot Multiphase PM Motor Drives". In *IEEE International Symposium on Industrial Electronics, ISIE2010*, pages 2160-2165, Bari, Italy, July 4-7 2010, DOI 10.1109/ ISIE.2010.5637790

C13 M. Barcaro, N. Bianchi, and F. Magnussen. "Average and Oscillating Torque Determination in Fractional-Slot PM Motors". In *IX International Conference on Electrical Machines, ICEM2010*, Roma, Italy, September 6-8 2010, DOI 10.1109/ ICELMACH.2010.5607926

C14 M. Barcaro, N. Bianchi, and F. Magnussen. "Design Considerations to maximize Performance of an IPM Motor for a Wide Flux-Weakening Region". In *XIX International Conference on Electrical Machines, ICEM2010*, Roma, Italy, September 6-8 2010, DOI 10.1109/ ICELMACH.2010.5608077

C15 M. Barcaro, N. Bianchi, and F. Magnussen. "Six-phase Supply Feasibility using a PM Fractional-Slot Dual Winding Machine". In *IEEE Energy Conversion Congress & Exposition, ECCE2010*, Atlanta, Georgia, September 12-16 2010, DOI 10.1109/ ECCE.2010

Accepted for publication on journal in 2010:

J9 M. Barcaro, N. Bianchi, and F. Magnussen. "Faulty Operations of a PM Fractional-slot Machine with Dual Three-phase Winding". In *In IEEE Transaction on Industrial Electronics*, DOI 10.1109/ TIE.2010.2087300

Chapter 1

Hybrid electric vehicles

This chapter introduces the push to the hybrid electric vehicle adoption as the common starting answer to the issues of the global transportation sector. Then, a classification of the more common hybrid electric architecture is presented. Finally, a selection of past and actual commercial vehicles are presented in order to give the idea of the requirements and performance inequality offered by the automotive market.

1.1. A global bloom of electric vehicles

INCREASING awareness of air quality and interest in innovative vehicles stimulate the research activity to improve the propulsion systems by reducing the vehicle emissions.

There are two serious issues regarding energy and environment in a global dimension. The main challenges are (i) increased energy demand versus limited resources and rising prices, (ii) increased emissions, including green house gas emissions that are indicated as causes of the global warming.

Around three-quarters of the forecasted increase [2] in worldwide oil demand comes from the transport sector. This sector accounts for 57% of global primary oil consumption in 2030 with 52% now and 38% in 1980. From the forecasted scenarios [2] oil-based fuels will continue to dominate transport energy demand [2].

Despite of the several improvements adopted in average vehicle fuel efficiency, spurred in part by high oil prices, it is expected to continue to push up the total oil use for transport purposes. It can be noted that globally passenger-car ownership is assumed to grow at 3.6% through the projection period [2].

Therefore the trend is to achieve a sustainable transportation: from oil source to renewable sources. Greener vehicles are pushed up by national and international strategies in recent years, ie. the European Commission integrated energy and climate action plan and the US Energy Independence and Security Act [2].

Hybrid electric vehicles (HEVs) appear as the nearest forced first step in order to obtain a reduction in both emissions as well as fuel consumption. In fact, HEVs have attracted their fair share of attention from automakers worldwide and so on [3]. The

hybrid car sales in the United States market started in 1999 have been increased every year, as reported in Fig 1.1 [4].

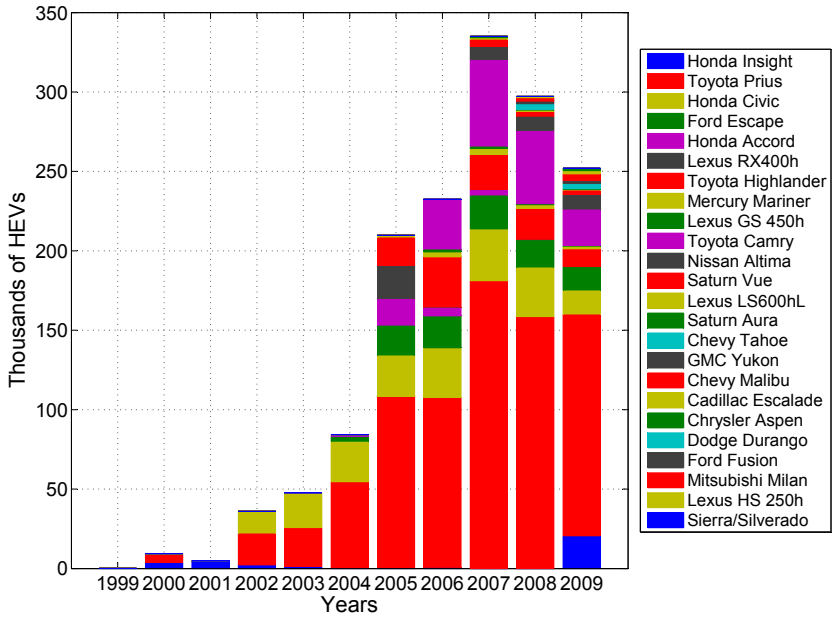

Figure 1.1: United States hybrid–electric vehicle sales [4].

An HEV is a vehicle which involves multiple sources of propulsions. In the common use, HEV means that the vehicle has a propulsion due to both an Internal Combustion Engine (ICE) and an electrical machine. Therefore, the onboard primary energy source can be gasoline, diesel, natural gas while the electrical energy can be stored in batteries, ultra capacitors, etc. A more electric vehicle is represented by the plug–in hybrid electric vehicle (PHEV), which is a vehicle that can be charged from the grid. Thanks to its storage system, it is commonly designed in order to consume only electrical energy for short distance travel. Oppositely a sole propulsion by electric motor yields an electric vehicle (EV), while obliviously a traditional vehicle propulsion is ICE or diesel engine.

The key advantages of HEVs can be summarized as [5]:

- Fuel economy optimization
    1. Optimize the operating point of ICE,
    2. Stop the ICE if not needed (ultra low speed and stops),
    3. Recover the kinetic energy at braking,
    4. Reduce the size (hp and volume) of ICE.
- Emissions reduction
    1. Minimize the emissions when ICE is optimized in operation,
    2. Stop the ICE when it's not needed
    3. Reduced size of ICE means less emissions

- Quiet Operation
  1. Ultra low noise at low speed since ICE is stopped,
  2. Quiet motor, the motor is stopped when vehicle comes to a stop, with engine already stopped.
- Maintenance reduction thanks to the optimized ICE operations
  1. fewer tune ups, longer life cycle of ICE,
  2. fewer spark-plug changes, oil changes,
  3. fewer fuel filters, antifreeze, radiator flushes or water pumps, etc.

But, there are obliviously concerns on the design and adoption of HEVs:

- High initial cost due to the increased number of components, such as battery, electric machines, motor controller, etc.
- Reliability concern due to the new components, especially power system, electronics, sensors,
- Warranty issues due to the new electric components to which standard repair shop are not familiar with,
- Safety linked with the high voltage system employed in HEV,
- Electromagnetic compatibility vulnerability.

Thus HEVs are able to achieve high performance by combining high-energy density combustible, with high efficiency of electric-drive systems. Moreover, the torque generated by the electric motor can be appropriately controlled so that the vehicle stability and safety are greatly improved. Recently, considerable improvements have been obtained in all studying area of HEVs due to the efficiency enhancement of both electrical machines and internal combustion motors.

Among the rotating electrical machines, the permanent magnet (PM) synchronous machines have found wide applications in various fields. Drive systems based on PM represent a competitive solution for actual automotive performance and naval applications [6]. Compared to other electrical machines, PM machines combine several advantages as high efficiency, high power factor, high torque density, high overload capability, robustness, reduced maintenance, compactness and low weight [7]. High energy PM exciting allows to reduce overall volume (i.e. weight) and stator losses. On the other hand, the absence of rotor copper losses allows a further increase of the efficiency. Also fault-tolerant capability [8], flux-weakening capability [9–11], low short-circuit current can be obtained with a proper design. Thanks to these features the PM machine is a suitable candidate for traction requirements [12, 13].

Although the PM excitation has some drawbacks, such as cost of the permanent magnets, risk of demagnetization at high temperature, and additional control effort; the technical advantages of the PM motor have yielded the extension of their area of application in the last years.

In addition, high relevance has the improvement of the energy storage system. Now the most promising battery technology to power these vehicles is the Lithium Ion (Li-ion) battery, though the Nickel Metal Hydride (NiMH) are the most utilized battery in commercial applications. Its high cost its is still a drawback and accounts for the continuing presence as NiMH batteries in the market.

The batteries are devices with high specific energy, while when a peak power is required a specific power density device could be very useful. The use of ultracapacitors has a high potential in the HEVs. Ultracapacitors have the advantage of being a more robust power device when compared to batteries, as example during regenerative braking that is considered to be a high-power event. On the other hand another storage system is represented by the flywheels. Each energy storage system has advantages or drawbacks according to the way in which the energy is stored: electrochemical for batteries, electrostatical for ultracapacitors and mechanical for flywheels.

1.2. Hybrid electric vehicles architecture

The major challenges for HEV design are managing multiple energy source, highly dependant of driving cycles, battery sizing and battery management. The architecture of a hybrid vehicle is usually defined as the connection between the components of the vehicle traction, and then the energy flow path [14]. Recently, with the introduction of some new features and improvements, the extended classification of HEVs is:

Series hybrid: the traction power is delivered by the electric motor, while the ICE, via a generator, produces electric power to drive the electric motor [5]. The excess power is then stored in the battery pack. The ICE is decoupled from the driven wheels and can be operated mostly in the maximum efficiency region. The major shortcomings of a series hybrid drive train configuration are the high power installed in each component and the request of a generator. The energy from the ICE has to be converter twice before to drive the wheels (Fig. 1.2). Thus the system is more expensive than the parallel one.

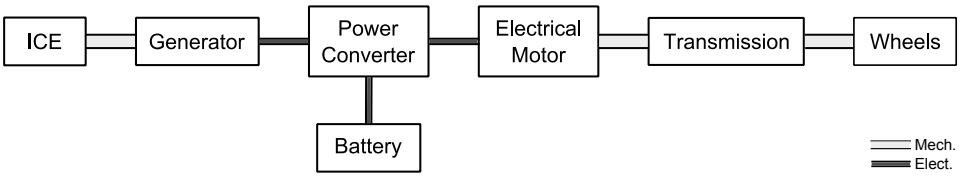

Figure 1.2: Series hybrid architecture.

Parallel hybrid: there is direct mechanical connection between the hybrid power unit and the wheels. In addition, this layout has an electric traction motor that drives the wheels, and can recuperate a share of the braking energy, in order to charge the batteries (regenerative braking) or help the ICE during the acceleration conditions.

Hence the ICE and the electrical motor are coupled by a mechanical device (Fig. 1.3). Then the electrical machine can be designed with a reduced capability, i.e. cost and volume. There are several configurations depending on the structure of the mechanical coupling between the ICE and the electrical motor. For instance, there can be

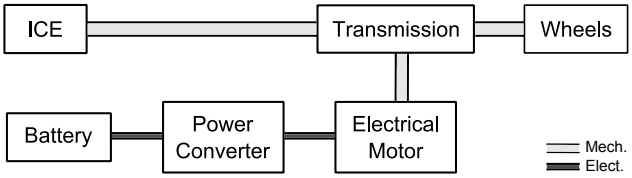

Figure 1.3: Parallel hybrid architecture.

a torque–coupling with single–shaft or two–shaft configuration, a speed–coupling with planetary gear unit, or a merge of both previous coupling system.

Series–parallel hybrid: the series layout and the parallel layout are merged together in order to have both advantages (Fig. 1.4). In particular the ICE is able to supply the electrical motor or charge the battery thanks to a generator.

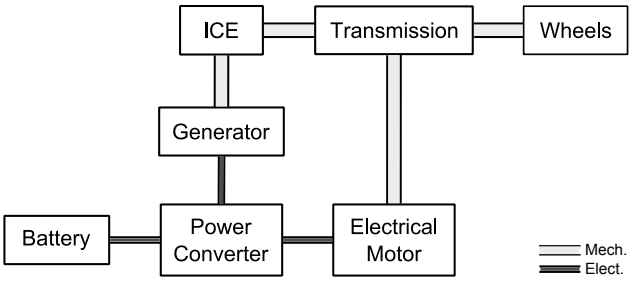

Figure 1.4: Series–parallel hybrid architecture.

Complex hybrid: there are two separate mechanical links obtaining a light transmission system and a flexible mounting. As an example, the front wheels are powered by an hybrid propulsion, while the rear wheels has a pure electric system. There is a wide flexibility on the power flux managing.

Moreover, the general hybrid electric vehicle can be also classified depending on the relevance of the power and function of the electric machines, as reported in Table 1.1 [4, 14].

Table 1.1: Hybrids classification

	Micro	Mild	Full
Power (kW)	2.5	10–20	30–100
Voltage level (V)	12	100–200	200–300
Energy saving (%)	5–10	20–30	30–50
Price increase (%)	3	20–30	30–40

It is worth noticing that the micro hybrid could allow to start-stop and a partly regeneration using a sole electrical machine that is often called integrated starter–alternator) while the mild hybrid and the full hybrid could deliver a high share or the whole power drive.

1.3. Commercial examples

As shown in Fig 1.1 the selling trend of HEVs of U.S. has shown a rapid increasing: 17 HEVs sold in 1999, 84.000 in 2004, 290.800 in 2009. The outlooks forecast that there will be several new hybrid and plug–in hybrid vehicles in the next years.

Table 1.2 reports the vehicles specifications of a selection of HEVs sold in the U.S. market [4] during 2008. The electric motor size reported in Table 1.2 refers only to the front wheels drive motor, also for those vehicles provided also of a rear wheel system. As indicated in the following models described, most of the available HEVs in the market of personal transportation adopt PM synchronous machines.

Table 1.2: HEVs specifications [4]

MODEL	ICE	EL. MOT.	BATTERY	
	(HP) at (rpm)	(kW)	dc (V)	Ah
Chevy Silverado 2004	295 at 5200	14	36	70
Ford Escape 2005	133 at 6000	70	330	5.5
Honda Accord 2005	240 at 6250	12	144	6.0
Honda Civic 2006	110 at 6000	14.6	158.4	5.5
Lexus RX400h 2006	268 at 5600	123	288	6.5
Mazda Tribune 2008	133 at 6000	70	330	-
Nissan Altima 2007	158 at 5200	105	244.8	6.5
Saturn Vue 2007	170 at 6600	14.5	36	18.4
Toyota Camry 2007	147 at 6000	105	244.8	6.5
Toyota Highlander 2006	268 at 5600	123	288	6.5
Toyota Prius 2004	76 at 5000	50	201.6	6.5

1.3.1. Toyota Prius

Toyota has started to study HEVs earlier than the first appear of Prius in the Japanese market in 1997. The Toyota Prius (2003) was the first full–hybrid vehicle in the word. It allows a complete electric traction, a regenerative brake and an automatic preferring use of the energy stored in the battery. There is a planetary differential gear/power split interface device that allows the mechanical coupling. The Prius adopts a series–parallel architecture (see Fig. 1.5) [15], and has two PM machines coupled to the ICE (1.5 L 76 HP).

Both machines can be motor and generator. The first (MG1) has to recharge the battery, to start the ICE and to supply power to the second PM machine (MG2) that has to do the regenerative brake and to drive the wheel. Both machines are water–cooled and the power are 28 kW and 50 kW respectively, with a maximum voltage equal to 500 V ac. Moreover, the PMs of the latter machine are buried in the rotor adopting a V–shape structure.

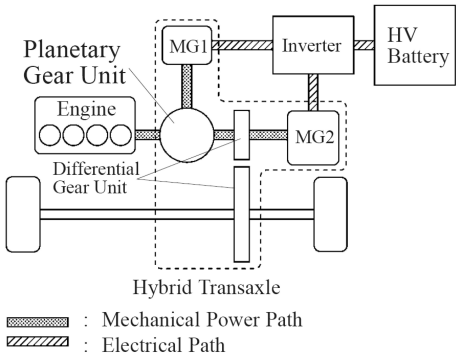

Figure 1.5: Series–parallel hybrid architecture of Toyota Prius [15].

As respect to the previous model of Prius (2003) the most important improvement is introduction of a boost converter. The previous Prius model had a 273.6 V dc bus voltage of both inverter and batteries: in the following system of Prius (2004) the boost converter adjusts the voltage between batteries (201.6 V dc) and the PM machines (500 V dc). This innovation has involved an improvement of the power to weight ratio. The NiMH battery consists of 168 cells with a power of 21 kW [15].

Now, Prius (2010) has been improved by Toyota adopting an advanced gasoline-electric powertrain. The new ICE (1.8 L 98 HP) is coupled with a 60–kW PM machine, supplied with a maximum voltage of 650 V ac. The NiMH battery remains designed at 201.6 V dc but the power output has been increased to 27 kW.

1.3.2. Toyota SUV models

The Toyota Highlander is a Sport–Utility vehicle (SUV) with 4–wheel drive. The hybrid system is slightly more complex than Prius, thanks to the bigger vehicle dimensions and the higher performance required (see Fig. 1.6 [16, 17]).

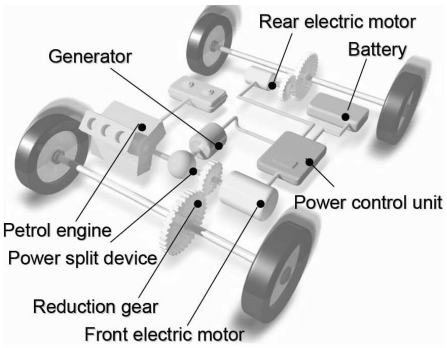

Figure 1.6: Toyota Highlander architecture layout [16].

The ICE is a 3.3 L 208 HP, while a 123 kW PM machine drives the front wheels and a 50 kW PM machine drives the rear wheels. The system is provided of the same 28 kW PM alternator. The NiMH battery has a 45 kW power and a nominal voltage equal to

288 V dc. The efficiency of the overall system is improved with a 650 V dc supplied by a boost converter. The volumetric power density of the control unit (including inverters and boost) is improved about 80% in comparison with Prius (2004) [16].

Also the Lexus RX400h has the same hybrid system of the Toyota Highlander. Instead, the Lexus GS450h has an improved hybrid system. The electrical machines have always PM rotor and a liquid–cooling system. The machine MG1 has nominal power of 134 kW (180 HP) at 13000 rpm. The machine MG2, the drive motor, has a continuous power equal to 147 kW and a maxium starting torque equal to 275 Nm up to 3840 rpm. It should be noted that the rated power to volume ratio of whole hybrid system is three times higher as respect to Prius (2004), and less than two times regarding the Highlander.

1.3.3. Honda Civic

The most recent Honda Civic Hybrid has considerably improved the performance, as respect to the old models, thanks to a high torque at low speed. When ICE and electric motor works together the Civic Hybrid is able to perform 85 kW at 6000 rpm with a maximum torque equal to 170 Nm at 2000 rpm (with a parallel hybrid architecture).

The ICE has a power of 70 kW at 6000 rpm with a torque equal to 123 Nm at 4500 rpm. The PM synchronous three–phase motor can supply 14.6 kW at 2000 rpm (103 Nm up to 1160 rpm). The storage system consists of 22 NiMH battery with a rated capacity of 5.5 Ah and a voltage of 158.4 V (that is the same of the electrical motor).

(a) (b)

Figure 1.7: Honda Civic Hybrid: (a) propulsion components (ICE, electric motor, gear box), (b) position of the battery.

1.3.4. Peugeot Citroën (PSA) group

The PSA group has developed two prototypes: Peugeout 307 Hybrid HDi and Citroën C4 hybrid HDi. The remarkable difference as respect the others manufactures is that the PSA group engineers have focused on the diesel ICE rather that the more usual gasoline one. The prototypes performance are about 29.41 km/litre and a carbon dioxide emissions of 90 g/km, considering a 1.6 L 66 kW diesel engine (with a automatic robotic 6–gear box) and a 16 kW electrical motor.

The hybrid system has a parallel architecture. The electrical machine has a nominal torque of 80 Nm but can overloaded up to 23 kW and 130 Nm. The electrical machine is a PM synchronous motor that can be supplied with an ac variable voltage from 210 V to 380 V. The 240–unit NiMH battery can exchange 23 kW with the inverter at 288 V dc.

1.3.5. General Motors models

The General Motor (GM) BioPower hybrid system couples an alternative fuel (i.e. E85 ethanol) with an electric propulsion. The GM layout is called two–mode hybrid system because the transmission splits up into two modes of operating, using a combination of two electric motors, a gasoline ICE and a set of gears. The input split mode is used for launching the vehicle from a stop, driving at low speeds, and for towing, when more power is needed. The compound split mode is used for cruising at highway (faster) speeds when less power is needed, Fig. 1.8. The hybrid system switches modes automatically. Both modes use a combination of electric motors and a gasoline engine.

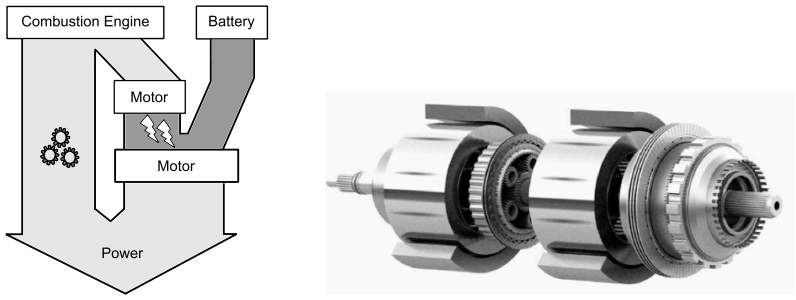

(a) (b)

Figure 1.8: General Motor two–mode system:
(a) layout and energy flow, (b) the two electrical motors with gears [18].

By way of example, Saab has designed the Saab 9–3 BioPower Hybrid concept [18]. It is provided of GM ICE 2.0 L Turbo calibrated for E100 ethanol, but however enabled for any blend of ethanol and gasoline. Fig. 1.8 shows the layout in principle (a) and a picture of the two electrical motors mounted with two clutches (b), that offer four fixed gears. Similar concept architecture characterizes the vehicle models of GM, as example Saturn Vue Hybrid, Chevrolet Tahoe Hybrid and GMC Yukon Hybrid.

In 2010 it will be commercially released the Chevy Volt, designed as a series–parallel plug–in hybrid vehicle. It is provided of a 130 kW electric drive machine and a 53 kW generator, combined with a 1.4L engine. The Lithium ion battery pack allows the home

plug–in charging and it is characterized by a 136 kW peak power and a 16 kWh energy content.

1.3.6. 2010's announces

In 2010 a new set of carmakers have begun making hybrids beginning to break the Toyota's hybrid hegemony.

For instance, the Hyundai's first gas-electric vehicle will be the Sonata Hybrid. It is provided of an efficient 30kW electric motor and a regenerative braking system. The electrical machine is coupled with a fuel–efficient 169 HP engine with a 6-speed automatic transmission. In addition the Sonata hybrid is provided of an integrated starter–alternator that enables the engine to turn off at stops and restart automatically under acceleration. The lithium polymer battery package has 5.3 Ah of capacity at 270 volts.

The announced new hybrid or plug–in hybrids in the near future [4] are:

2010 Chevrolet Volt, Dodge Ram, Honda CRZ, Honda Fit, Hyundai Sonata, Lincoln MKZ, Mercedes-Benz ML450, Porsche Cayenne Hybrid, Volkswagen Touareg.

2011 Audi Q5, BMW 5 Series, Hummer H3, Infiniti M35, Kia Optima.

2012 Volkswagen Jetta.

2013 Volkswagen Golf, Volkswagen Passat.

Chapter 2

Permanent magnet synchronous motor

This chapter illustrates the key features of the PM synchronous motors. Different geometrical topologies are presented. Finally, some control strategies are described, highlighting the relationship between the PM motor performance and its rotor geometry.

2.1. Introduction

THE permanent magnet (PM) motors are formed by a rotor containing PMs and a stator with a distributed multi–phase winding, typically a three–phase winding. They are supplied by current–controlled voltage source inverter. The phase coils of such a winding are fed by sinewave currents synchronous with the corresponding flux linkages due to the PM flux.

There are two key advantages in using the PMs to create the main magnetic flux of the machine. First, the space required by the PMs for the magnetization is small, so that the motor design exhibits several degrees of freedom. Second, since there are not losses for magnetization, the PM motors feature high torque density and high efficiency.

The increasing interest to PM motors is also due to the high energy density of the modern PMs, showing high residual flux density and high coercive force. In addition, the PM specific cost is decreasing, making the cost of the PM motor competitive with other motor types.

Now being prevailing the energy saving concerns, e.g. high efficiency electrical machines, the PM machines are more widely studied thanks to the availability of PM at low price. Consequently the PM machines are now designed for several applications, as example: railway, automotive [19–21], naval, industrial processing, robotics, wind and hydro energy, domestic appliances. As a consequence the power ratings of the PM synchronous motors is widening and today it ranges from fractions of Watts to some million of Watts.

2.2. The rotor configurations

A basic classification of the rotating electrical machines can be carried out focusing on the direction of the magnetic flux as respect to the axis of rotation. The main families are:

- Axial flux machines (Fig. 2.1(a)),
- Radial flux machines (Figs. 2.1(b) and 2.1(c)).

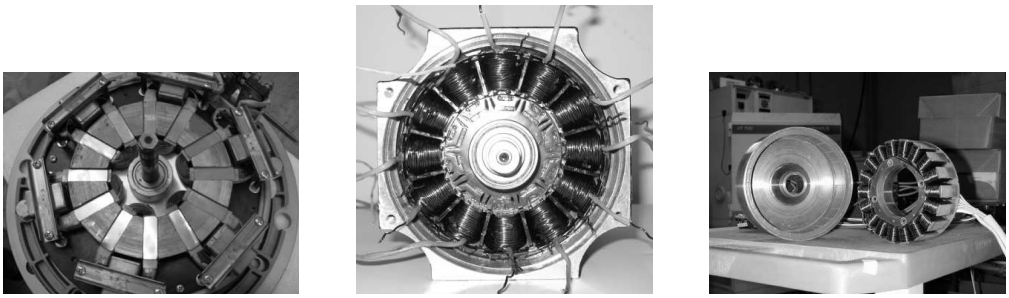

(a) (b) (c)

Figure 2.1: Machine topologies: (a) axial flux machine, (b) radial flux machine with internal rotor, (c) radial flux machine with external rotor.

In this study only radial flux machines are considered, since they are the more common and industrialized machine topologies. Among the radial flux machines, the rotor can be internal or external depending of the application (Figs. 2.1(b) and 2.1(c) respectively).

The stator of the radial PM synchronous motor is the same of the induction motor, and it is obtained using a stack of ferromagnetic laminations. Stator and rotor are separated by an air gap, allowing the rotor to rotate. The rotor can assume different topologies, according in which manner the PMs are placed in the rotor.

Therefore among the machines with radial magnetized PMs [22], the motors can be distinguished in two classes:

SPM - Surface–mounted PM motor: the PMs are mounted with alternating polarity on the surface of the rotor. Since the PM permeability is close to the air permeability, the rotor is isotropic.

IPM - Interior PM motor: the PMs are buried with alternating polarity inside the rotor iron. The rotor pole is provided also of flux barriers that allow to canalize the magnetic flux . The rotor becomes anisotropic exhibiting two torque components: the PM torque and the reluctance torque [23]. Several rotor geometries can be obtained playing with the position ad dimension of both the PMS and the flux–barriers. Higher the number of flux–barriers per pole and higher the rotor anisotropy that can be achieved [24].

For instance Fig. 2.2(a) shows the geometry of a 24–slot 4–pole SPM motor. The PMs are highlighted with gray color in the rotor. Similarly Figs. 2.2(b) and 2.2(c) show two examples of IPM geometries that are characterized by a different blend of PM and reluctance torque contributions.

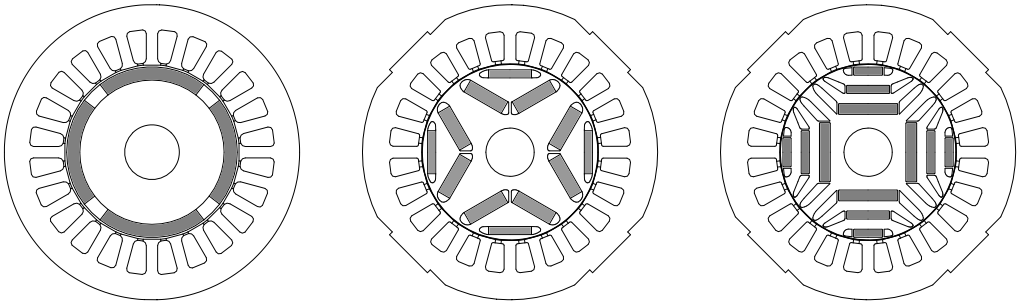

(a) SPM motor (b) IPM motor (c) IPM motor

Figure 2.2: PM synchronous motors with (a) SPM,(b) and (c) IPM rotors.

The present work focuses on the IPM motor with radial magnetization PMs and multiple flux–barriers since they exhibits some advantages:

1. PMs are more protected to demagnetization due to the stator current as respect of the SPMs, with a benefit for overload capability and safety.
2. Presence of two torque mechanisms, PM and magnetic anisotropy, allowing to achieve high torque density and wide flux–weakening operating range [25, 26]. In particular, the maximization of the reluctance torque allow to minimize the PM volume to achieve the required torque at high speed.
3. Limited short–circuit current thanks to the high inductance and the considerable reluctance torque component.

2.3. Fundamental equations

A sketch of the two–pole machine structure with an isotropic rotor is shown in Fig. 2.3. Considering a standard three–phase winding distributed along the stator slots, one coil for each phase (a, b and c) is shown. The mechanical angle ϑ_m is highlighted between the phase a axis and the rotor pole axis.

The positive rotor direction is fixed as the counter–clock side direction. Hereafter, for simplicity, the electrical and magnetic quantities of the synchronous machine are evaluated adopting the rotating reference frame. The Park transformation [27] allow to adopt an orthogonal d–q rotating reference frame, that is synchronous with the rotor movement as reported in Fig. 2.3.

Therefore the rotor position is represented by the d– and the q–axis that are locked with the rotor. The d–axis is chosen so as to be aligned with the PM flux axis, while the q–phase axis leads the d–phase axis of $\pi/2$ electrical radians. Each electrical and magnetic quantity governing the electromagnetic conversion will be referred to both axes using the corresponding components.

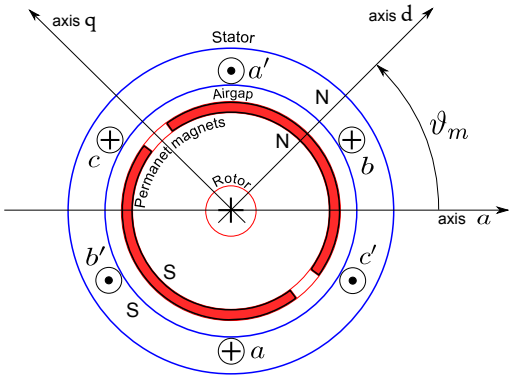

Figure 2.3: Schematic representation of a two–pole PM synchronous motor.

In the following the relationships governing the synchronous PM machines are presented with a particular attention to the control strategies, highlighting the relationship between the PM motor performance and its rotor geometry [28].

Finally, an isotropic machine is considered in order to introduce the main relationships that characterize a PM synchronous machine. Then, the anisotropy of the rotor will be taken into account. Indeed, all the IPM rotors exhibit magnetic pathes with different permeance, from which the possibility of developing a reluctance torque. Since the differential permeability of the PM is close to the air permeability, the d–axis magnetic permeance results to be lower than the q–axis permeance (in the adopted reference of Fig. 2.3).

2.3.1. Electric equations for an isotropic machine

The three phases of the winding are distributed along the stator with an electrical displacement equal to $2\pi/3$ radians. The general equations of the voltages for three phases, $v_a(t)$, $v_b(t)$, $v_c(t)$, are:

$$\begin{aligned} v_a(t) &= \mathrm{R}i_a(t) + \frac{\mathrm{d}\lambda_a(t)}{\mathrm{d}t} \\ v_b(t) &= \mathrm{R}i_b(t) + \frac{\mathrm{d}\lambda_b(t)}{\mathrm{d}t} \\ v_c(t) &= \mathrm{R}i_c(t) + \frac{\mathrm{d}\lambda_c(t)}{\mathrm{d}t} \end{aligned} \tag{2.1}$$

where i_a, i_b, i_c are the phase currents; and λ_a, λ_b, λ_c are the flux linkage of each stator phase. The stator phase resistance is R.

It is assumed for simplicity that, with no current in the stator the flux linkage due to the magnets is sinusoidal. The angle ϑ_{me} is the electrical angle between the PM axis and the axis of the phase A, resulting in the position of the rotor as respect to the stator. It is defined as:

$$\vartheta_{me} = \mathrm{p}\vartheta_m \tag{2.2}$$

where p is the number of pole pairs, and ϑ_m is the mechanical angle between the PM axis and the phase A axis, Fig. 2.3. Considering briefly only the phase A, the flux linked $\lambda_{a,m}$ due to the PMs can be expressed as:

$$\lambda_{a,m} = \Lambda_m \cos(\vartheta_{me}) \tag{2.3}$$

where Λ_m is the maximum value of the flux–linkage due to the PM.

Since the machine is provided of an anisotropic rotor and a symmetric winding, each phase is characterized by same value of self–inductance L_{ss} and mutual–inductance $\mathrm{L}_{\mathrm{M}ss}$. The latter is considered negative since the opposite sign of the flux linked.

$$\begin{aligned} \mathrm{L}_a &= \mathrm{L}_b = \mathrm{L}_c = \mathrm{L}_{ss} \\ \mathrm{L}_{\mathrm{M}ab} &= \mathrm{L}_{\mathrm{M}ac} = \mathrm{L}_{\mathrm{M}bc} = -|\mathrm{L}_{\mathrm{M}ss}| \end{aligned} \tag{2.4}$$

The flux–linkages, depending on the time instant t, are computed as the sum of the components due to the current in the three phases and the contribution due to the PM. For phase A:

$$\begin{aligned} \lambda_a(t) &= \mathrm{L}_a i_a(t) + \mathrm{L}_{\mathrm{M}ab} i_b(t) + \mathrm{L}_{\mathrm{M}ac} i_c(t) + \lambda_{a,m}(t) \\ &= \mathrm{L}_{ss} i_a(t) - |\mathrm{L}_{\mathrm{M}ss}|(i_b(t) + i_c(t)) + \lambda_{a,m}(t) \end{aligned} \tag{2.5}$$

Applying the Kirchhoff's law, the flux–linkages can be expressed for phase A as:

$$\lambda_a(t) = \mathrm{L} i_a(t) + \Lambda_m \cos(\vartheta_{me}) \tag{2.6}$$

where $\mathrm{L} = \mathrm{L}_{ss} + |\mathrm{L}_{\mathrm{M}ss}|$ is defined as the synchronous inductance. Thus the voltage equation for phase A reported in (2.1), applying the relationship in (2.6), becomes:

$$v_a(t) = \mathrm{R} i_a(t) + \mathrm{L}\frac{\mathrm{d}i_a(t)}{\mathrm{d}t} + e_a(t) \tag{2.7}$$

where $e_a(t)$ is the back electromotive forces (BEMF) due to the PM flux linked by the phase conductors:

$$e_a(t) = \frac{\mathrm{d}\lambda_{a,m}(t)}{\mathrm{d}t} = \omega_{me}\Lambda_m \cos(\vartheta_{me} + \frac{\pi}{2}) \tag{2.8}$$

where ω_{me} is the electrical speed. Thanks to the transformation to the d–q reference frame, the space vector of the PM flux $\boldsymbol{\lambda}_m$ results to have only real component being placed on the real axis of the rotating vectorial space. Therefore applying the transformation between the stationary reference frame to the rotating reference frame r (rotor), the voltage space vector becomes:

$$\boldsymbol{v}^r = \mathrm{R}\boldsymbol{i}^r + \mathrm{L}\frac{\mathrm{d}\boldsymbol{i}^r}{\mathrm{d}t} + j\omega_{me}\mathrm{L}\boldsymbol{i}^r + j\omega_{me}\Lambda_m \tag{2.9}$$

whose real component v_d and complex component v_q are:

$$\begin{aligned} v_d &= \mathrm{R} i_d + \frac{d\lambda_d}{dt} - \omega_{me}\lambda_q = \mathrm{R} i_d + \mathrm{L}\frac{\mathrm{d}i_d}{\mathrm{d}t} - \omega_{me}\mathrm{L} i_q \\ v_q &= \mathrm{R} i_q + \frac{d\lambda_q}{dt} + \omega_{me}\lambda_d = \mathrm{R} i_q + \mathrm{L}\frac{\mathrm{d}i_q}{\mathrm{d}t} + \omega_{me}\mathrm{L} i_d + \omega_{me}\Lambda_m \end{aligned} \tag{2.10}$$

The voltage equation reported in (2.10) allows to compute the electromechanical torque in the rotating reference frame r. Neglecting the resistive losses (Ri^2), it is possible to express the balance of the electromechanical energy conversion as:

$$\frac{3}{2}(v_d i_d + v_q i_q) = T\omega_m + \frac{dW_m}{dt} \tag{2.11}$$

where W_m is the magnetic energy. The state variables are the current components i_d and i_q, and the rotor position θ_m. The flux–linkage $\lambda(i)$ is assumed as a single–value relationship.

The ratio 3/2 in (2.11) allows to maintain the energy conservation during the transformation from the stationary reference frame to the d-q rotating reference frame.

Substituting $d\theta_m/\omega_m$ for dt yields after some manipulations:

$$T d\theta_m = \frac{3}{2} p \left(\lambda_d i_q - \lambda_q i_d\right) d\theta_m + \frac{3}{2} i_d d\lambda_d + \frac{3}{2} i_q d\lambda_q - dW_m \tag{2.12}$$

The magnetic energy and the flux–linkages can be expressed as a function of the selected independent state variables:

$$W_m = W_m(\theta_m, i_d, i_q) = \int_{0,0}^{\Lambda} i_d d\lambda_d + i_q d\lambda_q \tag{2.13}$$

$$dW_m = \frac{\partial W_m}{\partial \theta_m} d\theta_m + \frac{\partial W_m}{\partial i_d} di_d + \frac{\partial W_m}{\partial i_q} di_q \tag{2.14}$$

$$d\lambda_d = \frac{\partial \lambda_d}{\partial \theta_m} d\theta_m + \frac{\partial \lambda_d}{\partial i_d} di_d + \frac{\partial \lambda_d}{\partial i_q} di_q \tag{2.15}$$

$$d\lambda_q = \frac{\partial \lambda_q}{\partial \theta_m} d\theta_m + \frac{\partial \lambda_q}{\partial i_d} di_d + \frac{\partial \lambda_q}{\partial i_q} di_q \tag{2.16}$$

Therefore, substituting (2.14), (2.15) and (2.16) in (2.12), the energy balance becomes:

$$T d\theta_m = \frac{3}{2} p \left(\lambda_d i_q - \lambda_q i_d\right) d\theta_m + \underbrace{\left[\frac{3}{2} p \left(i_d \frac{\partial \lambda_d}{\partial \theta_m} + i_q \frac{\partial \lambda_q}{\partial \theta_m}\right) - \frac{\partial W_m}{\partial \theta_m}\right]}_{\frac{\partial W'_m}{\partial \theta_m}} d\theta_m + \underbrace{(\ldots) di_d}_{=0} + \underbrace{(\ldots) di_q}_{=0} \tag{2.17}$$

where $\partial W'_m/\partial \theta_m$ is the magnetic coenergy derivative as respect to the state variable θ_m. The last two terms of (2.17) within the parenthesis are always equal to zero [29]. It follows that the torque is independent of the change of current and flux–linkages during the arbitrary displacement $d\theta_m$.

Therefore, the electromagnetic torque is determined solely by the magnitudes of the currents and not by their rate of changes. Consequently, the electromagnetic torque results expressed as [29]:

$$T = \frac{3}{2} p \left(\lambda_d i_q - \lambda_q i_d\right) - \frac{\partial W'_m}{\partial \theta_m} \tag{2.18}$$

Considering steady state operations, the second term of (2.18) has not average value in a period. Therefore, it is common to omit it in the average torque computation. This simplification is generally applied to study the control strategies of the PM machine and in the preliminary machine design. However, the coenergy variation $\partial W'_m/\partial\theta_m$ has to be considered in the computation of the torque oscillation (torque ripple) as will be explained in chapter 6.

To the aim of maximizing the torque, the isotropic machine is supplied with only q–axis current. In this case the cross vector product between PM flux (Λ_d) and the supplied current is maximum, being the two space vector orthogonal. Therefore the torque formula is obtained from (2.18), and becomes equal to:

$$T = \frac{3}{2}\mathrm{p}\Lambda_m i_q \tag{2.19}$$

2.3.2. Electric equations for an anisotropic machine

The synchronous PM motors with anisotropic rotor are characterized by a rotor structure that yields a magnetic anisotropy, or rather a different magnetic behaviour along the magnetic axes. As introduced above, taking the advantage of rotor magnetic anisotropy the torque results due to both the PM flux and the reluctance principle.

Hypothesizing a sinusoidal distribution of the conductors and a proper magnet shape it is possible to consider sinusoidal the flux–linkages $\lambda_{a,m}$, $\lambda_{b,m}$, $\lambda_{c,m}$. Due to the magnetic anisotropy it is not possible to characterize the machine with only one value of self–inductance and mutual–inductance, differently than the isotropic motor, since their values varies as a function of the rotor position.

In the rotating reference frame each axis is characterized by a proper inductance, thus the equations becomes:

$$\begin{aligned} v_d &= \mathrm{R}i_d + \mathrm{L}_d\frac{\mathrm{d}i_d}{\mathrm{d}t} - \omega_{me}\mathrm{L}_q i_q \\ v_q &= \mathrm{R}i_q + \mathrm{L}_q\frac{\mathrm{d}i_q}{\mathrm{d}t} + \omega_{me}\mathrm{L}_d i_d + \omega_{me}\Lambda_m \end{aligned} \tag{2.20}$$

where the inductance of the two axes are defined as the direct synchronous inductance L_d and the quadrature synchronous inductance L_q.

The electromagnetic torque formulation is computed from (2.18) neglecting the coenergy variation, and results in:

$$T = \frac{3}{2}\mathrm{p}\Lambda_m i_q + \frac{3}{2}\mathrm{p}(\mathrm{L}_d - \mathrm{L}_q)i_d i_q \tag{2.21}$$

As expected the torque formulation shows an additional contribution as respect to the equation (2.19), that is the reluctance torque component.

2.4. Limits and operating regions

The available voltage and currents are subject to maximum limit values. The limit for each operating point is the more restrictive between the motor limits (i.e. thermal limit) and the supply system limits (i.e. maximum voltage).

In order to evaluate the limit of the operating region some assumption are taken into account: steady state operations, sinusoidal voltages and currents with constant amplitude and frequency, constant electrical speed ($\omega = \Omega$). Therefore in the synchronous reference frame the voltages and currents (V_d, V_q, I_d, I_q) have constant amplitude.

The nominal phase current I_{nom} of the machine satisfy the thermal limit in steady state. The thermal limit is due to the insulation properties. Obliviously the stator phase–to–phase voltage is fixed to the nominal value V_{nom}, that is the maximum value. However, it is possible to overload the motor supplying a current higher than the nominal one, still remaining lower than the demagnetizing current limit. This condition has to be limited for short period in order to not overcome the thermal limit.

It follows that, the limit of the operating region refer directly to the transformed components of the current, I_d and I_q, as

$$I_d^2 + I_q^2 \leq I_N^2 \tag{2.22}$$

where I_N is the amplitude of the spatial vector of the stator current (peak value of I_{nom}). Analogously, the voltage limit becomes:

$$V_d^2 + V_q^2 \leq V_N^2 \tag{2.23}$$

where V_N is the amplitude of the stator voltage spatial vector (peak value of V_{nom}).

2.4.1. Operating limits with isotropic rotor

In a synchronous PM motor with isotropic rotor the steady state behaviour is described with the relationships:

$$\begin{aligned} V_d &= RI_d - \Omega_{me} L I_q \\ V_q &= RI_q + \Omega_{me} L I_d + \Omega_{me} \Lambda_m \end{aligned} \tag{2.24}$$

Substituting (2.24) in (2.23) it is possible to express the voltage limit as a function of the current limit. The resistive voltage drop is neglected since it is commonly very low in comparison with the nominal voltage. It results in:

$$(\Omega_{me} L I_q)^2 + (\Omega_{me} L I_d + \Omega_{me} \Lambda_m)^2 \leq V_N^2 \tag{2.25}$$

Thus, equation (2.25) can be written as:

$$\left(I_d + \frac{\Lambda_m}{L} \right)^2 + I_q^2 \leq \frac{V_N^2}{(\Omega_{me} L)^2} \tag{2.26}$$

It follows that voltage and current limits yield both torque and speed limits. These operating limits can be easily reported in the d–q plane as in Fig. 2.4. The current limit

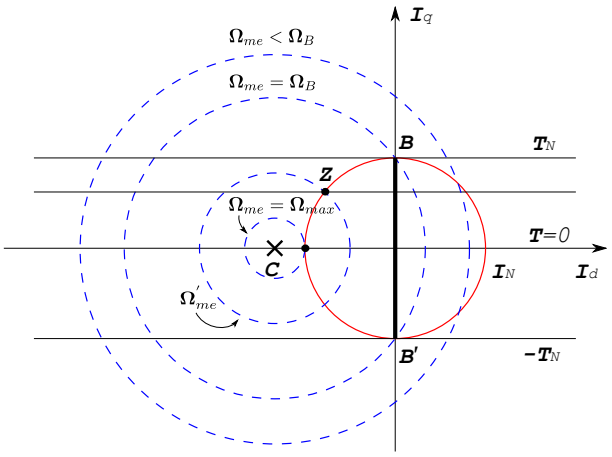

Figure 2.4: Operating limits of an isotropic PM machine.

of (2.22) is represented in the I_d–I_q plane as a circle with radius equal to I_N, shown with solid line in Fig. 2.4. The voltage limit of (2.26) is represented in Fig. 2.4 by a family of concentric circles using blue dashed lines. The ratio of each circle is inversely proportional to the rotor electrical speed, and then from the stator frequency. The circles center C is located at:

$$\begin{aligned} I_{Cd} &= -\frac{\Lambda_m}{L} \\ I_{Cq} &= 0 \end{aligned} \tag{2.27}$$

The two coordinates in the d–q plane correspond to the d–q components of the short–circuit current of the machine. Equations (2.27) are obtained from (2.24) posing zero the resistive voltage drops. Therefore, in case of $R << L$ the short circuit current components results independent of the speed.

Depending on the machine design, the short–circuit current can be higher or lower than the nominal one. Therefore the voltage limit circles's center can be placed outside or inside the current limit circle.

In addition, for the isotropic motor the constant torque curves are horizontal lines as reported in Fig. 2.4. The segment BB' contains all the tangent point between the constant torque lines and the current limits. Therefore each point along the BB' segment is characterized by the maximum ratio between the torque and the current, or rather satisfying the maximum torque per Ampere (MTPA) condition. It could be noted that, along the circle with radius I_N, the nominal torque is obtained as positive value at point B (motoring operation) and as a negative value at point B' (braking operation).

For each value of speed and current the motor has to satisfy a different combination of voltage and current limit in the d–q plane. At low speed the voltage circle radius is very high (ideally infinite at zero speed) while the current limit is more restrictive. The machine is operated in the point of segment BB' that provides the required torque. The MTPA condition is useful to limit the copper losses, and thus maximize the efficiency.

This strategy can be adopted until the segment BB' is inside the voltage limit, or rather up to the speed $\Omega_{me} = \Omega_B$. At this speed the points B and B' are on the voltage limit circle.

The speed Ω_B is defined as the base speed, since up to this value it is always possible to provide the nominal torque satisfying both the voltage and current limits. The value of the electrical base speed is:

$$\Omega_B = \frac{\mathrm{V}_N}{\sqrt{\Lambda_m^2 + (\mathrm{LI}_N)^2}} \tag{2.28}$$

In Fig. 2.5 it is highlighted the region of the available operating points that corresponds to the constant torque region, reported in Fig. 2.6.

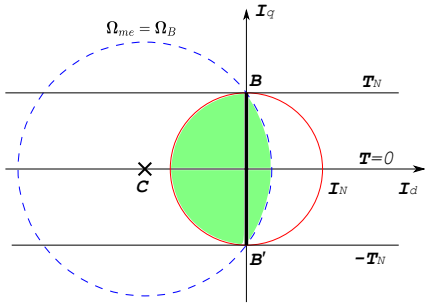

Figure 2.5: Operating limits of an isotropic PM machine at base speed.

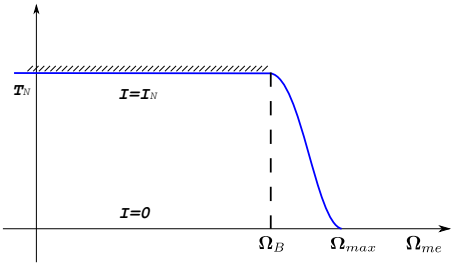

Figure 2.6: Operating regions of an isotropic PM machine.

At speed higher than the base one, the segment that highlights the available operating points is only a part of the segment BB'. For instance, with $\Omega'_{me} > \Omega_B$ the MTPA point becomes the point Z (Fig. 2.4). The maximum value of the achievable torque result lower than the nominal value: higher the speed and lower the current. It is possible to define a maximum speed Ω_{max} at which the torque becomes null since the voltage and current limit intersection correspond to only one point placed in the d axis, with current I_d. This operating region in the torque–to–speed plane is shown in Fig. 2.6. The maximum electrical speed is:

$$\Omega_{max,e} = \frac{\mathrm{V}_N}{\Lambda_m - \mathrm{LI}_N} \tag{2.29}$$

Commercial PM synchronous isotropic motors are commonly characterized by a value of PM flux Λ_m much higher than LI_N. Therefore the maximum speed becomes slightly higher than the base speed (about 10–20% higher).

As shown in (2.29), the inductance L has to be increased in order to achieve higher maximum speed. It is possible with a specific machine design (i.e. with fractional–slot winding) or adopting an external inductance. However, the increase of L involves a reduction of the base speed, (2.28).

Let us note that the maximum speed can reach the infinite value if the short–circuit current is equal to the nominal current. In this case the voltage limit circle's center C is placed on the current limit circle. If the short–circuit current is lower than the

nominal one, the center C is placed inside the current limit and the operating strategy changes according to Fig. 2.7.

In this case the strategy described above is adopted up to the electrical speed Ω_P, at which the voltage and current limit intersection is placed vertically to the center C in the d–q plane. The speed Ω_P is computed from (2.26) and satisfying the conditions $\mathrm{I}_q^2 = \mathrm{I}_N^2 - \mathrm{I}_d^2$ e $\mathrm{I}_d = -\Lambda_m/\mathrm{L}$, as

$$\Omega_P = \frac{\mathrm{V}_N^2}{(\mathrm{L}\mathrm{I}_N)^2 - \Lambda_m^2} \tag{2.30}$$

For electrical speed higher than Ω_P, the maximum available torque is achieved supplying the motor with current vectors along the segment PP'. Analogously as above for BB', the segment PP' allows to reach the maximum ratio between the torque and the available voltage, i.e. the maximum torque per Volts (MTPV) condition.

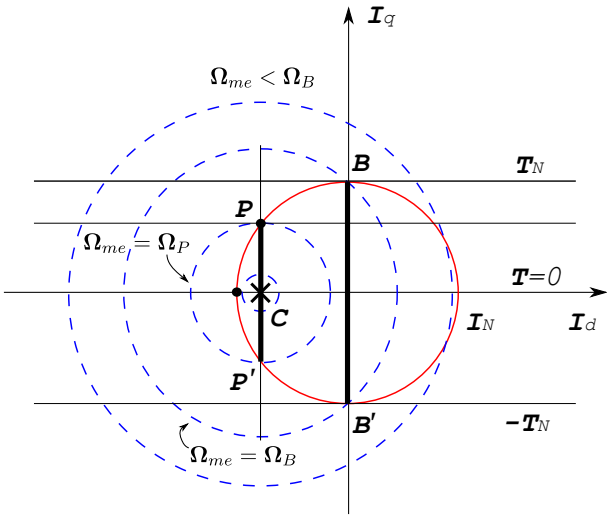

Figure 2.7: Operating limits of an isotropic PM machine at base speed with low short–circuit current.

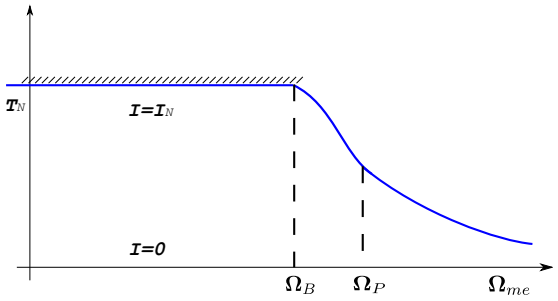

Figure 2.8: Operating regions of an isotropic PM machine with low short–circuit current.

Adopting this strategy there is not a speed limit: the center C, in the middle of the segment PP', is reached ideally only at infinite speed. Fig. 2.8 shows the behaviour of the torque versus speed in this region.

2.4.2. Operating limits with anisotropic rotor

At steady state, the voltage equations (2.23) are obtained from (2.20) assuming constant values of current and voltage.

$$\begin{aligned} \mathrm{V}_d &= \mathrm{RI}_d - \Omega_{me}\Lambda_q = \mathrm{RI}_d - \Omega_{me}\mathrm{L}_q\mathrm{I}_q \\ \mathrm{V}_q &= \mathrm{RI}_q + \Omega_{me}\Lambda_d = \mathrm{RI}_q + \Omega_{me}\mathrm{L}_d\mathrm{I}_d + \Omega_{me}\Lambda_m \end{aligned} \tag{2.31}$$

The voltage limit can be expressed as a function of the current replacing (2.31) in (2.23). The resistive voltage drop is neglected. It follows

$$(\Omega_{me}\mathrm{L}_q\mathrm{I}_q)^2 + (\Omega_{me}\mathrm{L}_d\mathrm{I}_d + \Omega_{me}\Lambda_m)^2 \leq \mathrm{V}_N^2 \tag{2.32}$$

Finally the (2.32) can be rewritten as:

$$\left(\mathrm{I}_d + \frac{\Lambda_m}{\mathrm{L}_d}\right)^2 + \left(\frac{\mathrm{L}_q}{\mathrm{L}_d}\mathrm{I}_q\right)^2 \leq \frac{\mathrm{V}_N^2}{(\Omega_{me}\mathrm{L}_d)^2} \tag{2.33}$$

Obviously the current limit (2.22) and the voltage limit (2.33) yield a limit on both torque and speed. As above, the current limit is a circle with radius equal to I_N in the d–q plane, highlighted with red solid line in Fig. 2.9. The voltage limit of (2.33) is represented by a family of concentric ellipses, which axes length depends of the speed Ω_{me}. As shown in (2.33), higher the speed and lower the ellipse's axes. The ellipse's center C is located in the d–q plane in:

$$\begin{aligned} \mathrm{I}_{Cd} &= \frac{\Lambda_m}{\mathrm{L}_d} \\ \mathrm{I}_{Cq} &= 0 \end{aligned} \tag{2.34}$$

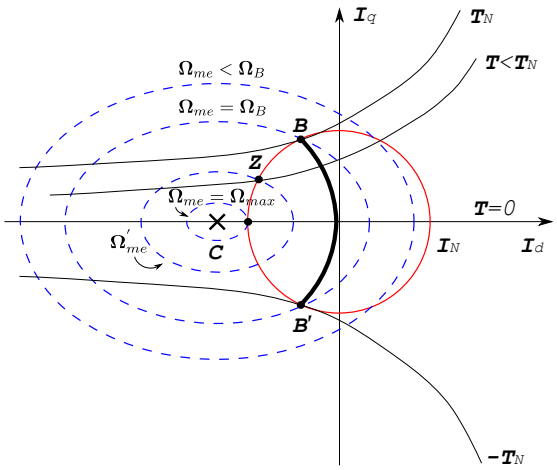

Figure 2.9: Operating limits of an isotropic PM machine.

I_{Cd} and I_{Cq} are the short–circuit current component. Assuming that the short–circuit current is higher than the nominal current, the ellipse's center C result placed outside the current limit, as in the case shown in Fig. 2.9.

The constant torque loci for an anisotropic synchronous machine corresponds to a family of hyperboles which asymptotes are the horizontal axis $\mathrm{I}_q = 0$ and the vertical line $\mathrm{I}_d = \Lambda_m/(\mathrm{L}_q - \mathrm{L}_d)$, as shown in Fig. 2.9.

The MTPA loci is shown in Fig. 2.9 as the curve BB'. This curve contains the tangent point between the constant torque hyperboles and the current circles at different current values. Let us note that each operating point of the motor has to satisfy the current limit and the specific voltage limit, that is related to the speed of the operating point. At low speed the voltage limit result to be extremely wide and then the current limit becomes more restrictive. In this case the motor is operated, depending on the current value, following the curve BB'. Therefore the MTPA condition is satisfied (e.g. minimum copper losses).

This strategy is applied until the curve BB' remains inside the voltage limit, or rather up to the electrical speed limit $\Omega_{me} = \Omega_B$, that is the base speed. At the base speed the voltage ellipse goes thought both point B and B'. Therefore, as described above for the isotropic motor, these operating conditions define the constant torque region shown in Fig. 2.6. In fact, up to the base speed it is always possible to achieve the nominal torque.

For electrical speed higher than the nominal value ($\Omega'_{me} > \Omega_B$) the area containing the available operating points, inside both voltage and current limit, does not contain all the curve BB'. The maximum torque is obtained at the intersection between the current circle and the voltage ellipse, as for instance the point Z of Fig. 2.9. The maximum torque results lower than the nominal torque: higher the speed and lower the torque up to become null at the speed Ω_{max}. At the maximum speed Ω_{max}, the intersection between voltage and current limits consists of only one point in the d–q plane, placed on the axis of I_d. The torque to speed characteristic, for speed higher than the nominal one, is the same of those reported in Fig. 2.6.

The value of the maximum speed, computed satisfying (2.33) and the conditions $\mathrm{I}_q = 0$, $\mathrm{I}_d = -\mathrm{I}_N$, is

$$\Omega_{max,e} = \frac{\mathrm{V}_N}{\Lambda_m - \mathrm{L}_d \mathrm{I}_N} \tag{2.35}$$

If the short–circuit current is lower than the nominal current the ellipse's center C is inside the current circle limit, as in Fig. 2.10. In this case the control strategy of the motor follows the same critera adopted in the section above up to the speed Ω_P. At this point the intersection between the voltage ellipse and the current circle is also the tangent between the constant torque hyperboles and the voltage ellipses.

At speed higher than Ω_p the maximum available torque is obtained operating the machine along the PP' loci. Analogously of the curve BB', the curve PP' allow to achieve the maximum torque per Volts (MTPV) condition. Also in this case there is no limit to the maximum speed: the ellipse's center C is reached with a speed that tends to infinite. Therefore, the operating region on the torque to speed plane result similar to those reported in Fig. 2.8 for the isotropic machine.

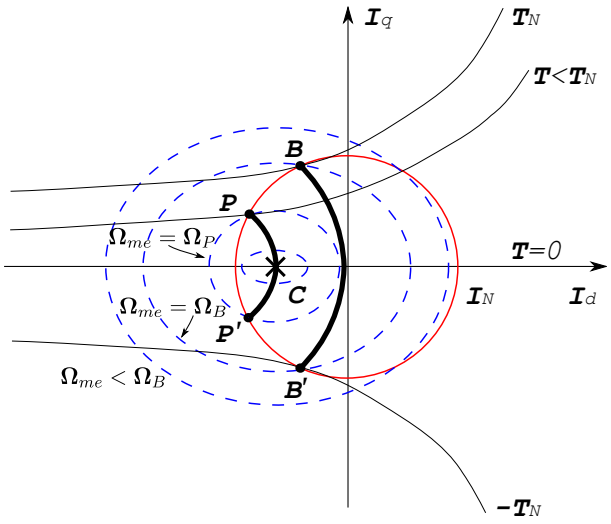

Figure 2.10: Operating limits of an anisotropic PM machine at base speed with low short–circuit current.

2.5. Limit operating regions

Summarizing the control strategies introduced above, depending on the value of the characteristic current I_C, three operating regions can be identified in torque to speed characteristic.

According to both voltage and current constraints, the current vector control that yields the maximum torque at any speed is obtained as follows.

Region I (Constant torque region): Below the base speed ω_B, the maximum torque is produced by the MTPA control. The current vector producing maximum torque corresponds to the point **B** in Fig. 2.11. In this region, $I = I_N$, $\Omega_{me}\Lambda < V_N$, while V reaches its limited value at the base speed Ω_B.

Region II (FW, constant volt-ampere region): Above the base speed, the current vector is controlled by the flux–weakening (FW) control, in which the voltage is kept fixed to $\omega\lambda = V_N$ by utilizing the demagnetizing d–axis armature reaction. This current vector corresponds to the intersecting point of the current limit circle and the voltage limit ellipse. The current vector angle α_i^e increases as the speed increases. The d–axis current increases toward negative direction and the q–axis current decreases. The current vector trajectory moves along the current limit circle (bold line in Fig. 2.11(a)). Assuming that $\Lambda_m > L_d I_N$, the FW operation continues up to a maximum speed ω_{max}. The minimum d–axis flux linkage is achieved when i_d reaches $-I_N$ and I_q becomes zero (point **F** in Fig. 2.11(a)), so that $\Lambda_{d,min} = \Lambda_m - L_d I_N$. The torque and power become zero, and the maximum speed results in $\Omega_{max,e} = V_N/\Lambda_{dmin}$.

Region III (FW, decreasing Volt–Ampere region): If $\Lambda_m < L_d I_N$, the center point of the voltage limit ellipse is located inside the current limit circle, as shown in Fig. 2.11(b). The current vector trajectory moves along the current limit circle up to the speed Ω_P, corresponding to the intersection point **P** between the current limit circle and the MTPV trajectory. Above Ω_P, the optimum current vector is achieved applying the MTPV control. Therefore, when the maximum voltage V_N is reached,

the flux linkage Λ is decreased along the MTPV trajectory with the increase of speed because $\lambda \approx V_N/\omega$. When the speed tends to infinity, the current vector tends to the center of the ellipses, defined by $I_d = -\Lambda_m/L_d$ and $i_q = 0$.

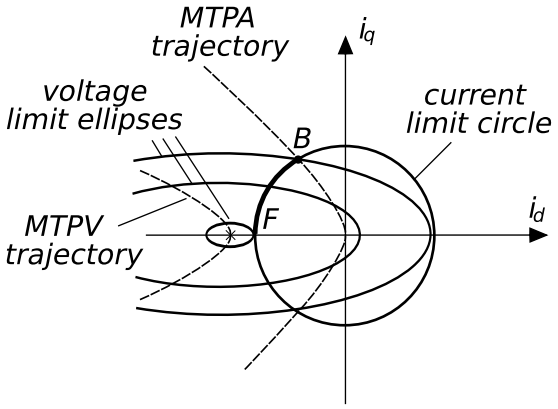

(a)

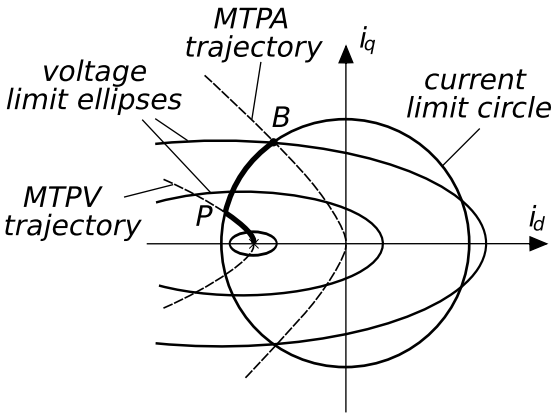

(b)

Figure 2.11: Selection of optimum current vector for producing maximum torque in consideration of voltage and current constraints.

Chapter 3

Anisotropic machine analytic model

The analytic model of the anisotropic synchronous machine is presented. The computation of both the air gap flux–density and the electromagnetic torque is reported referring to geometries with one to four flux–barriers per pole.

3.1. Model goals

THE synchronous reluctance machine (REL), sketched in Fig. 3.1, is characterized by a complex rotor structure in order to maximize the anisotropy, and as a consequence the torque. This complex structure yields a family of drawbacks,among the others high torque ripple [30, 31], high stator and rotor iron losses, vibrations. These drawbacks are due to the interaction between the spatial harmonics of the electric loading and the rotor anisotropy. Fig. 3.1 shows that each rotor pole is provided of multiple flux–barriers, while the mechanical structural strength is achieved by means of a proper thickness of the magnetic ribs.

Frequently, a permanent magnet (PM) is buried inside the rotor flux–barriers to the aim of saturating the magnetic ribs and increasing the power factor [32], which is generally low in the synchronous reluctance machine. If the PM volume is very limited and the major contribution to the torque due to the rotor saliency such of machine is usually defined as permanent magnet assisted REL (PMAREL). It results a specific case in the more general family of IPM machines.

The rotor geometry has a remarkable influence on the machine performances and in particular on the well know drawbacks. As a consequence in literature several analytical models have been presented. In particular Bianchi *et al* [33, 34] have presented an analytical model of the REL machine that take into account the rotor geometry. The analytical model allow to compute both the air gap radial flux–density and the electromagnetic motor torque.

This analytical model [33, 34] has been improved considering the effect of the PMs buried inside the flux–barriers and extending the number of flux–barrier up to four. The obtained analytical relationships are described hereafter, while in the following chapters the model is adopted to minimize specific drawbacks.

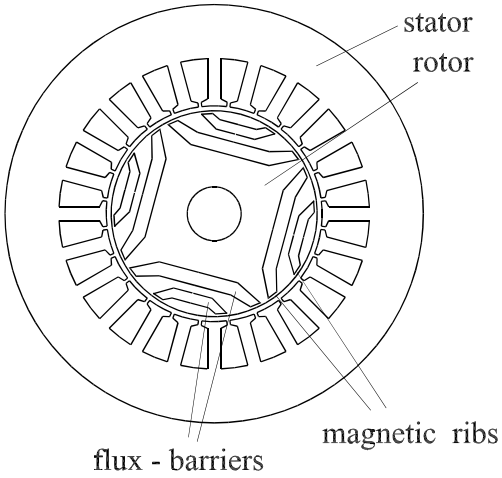

Figure 3.1: Sketch of a synchronous reluctance motor

Referring to the rotor geometries sketched in Fig. 3.2, the geometrical variables considered in the model are:

- the angle of the flux–barrier ends, e.g. the barrier angle (ϑ_b),
- the length and thickness of the flux–barriers,
- the volume of the PM buried inside each flux–barrier,
- the rotor volume (bore diameter and stack length),
- the stator slot number (e.g. the stator MMF harmonic content),
- the rotor position (θ_m).

Firstly, the equations describing the stator electrical and magnetic quantities are presented. Thus the computations of rotor quantities and the motor torque are presented referring separately to IPM rotors with one to four flux–barriers per pole.

3.2. Analytical model of the stator

3.2.1. References

Since the model has been firstly introduced [33, 34] considering only a REL machine, the reference d–q axes are differently placed in the rotor as respect to Chapter 2. It is shown in Fig. 3.2. This latter reference frame is the usual one adopted for the synchronous reluctance machines in literature [32, 35, 36]. In this thesis the reference axes reported in Fig. 3.2 are adopted only for the analytical model. The results of the following chapter refers to the axes defined in Fig. 2.3.

The d–axis is chosen aligned with the rotor path exhibiting the higher permeance, while the q–phase axis leads the d–phase axis of $\pi/2$ electrical radians.

As described in Chapter 2, the stator reference axis corresponds to the a–phase axis. It is placed along the x–axis of the reference system. The phase b axis leads the phase a axis of $2\pi/3$ electrical radians, while the c–phase axis leads the phase a axis of $4\pi/3$ electrical radians.

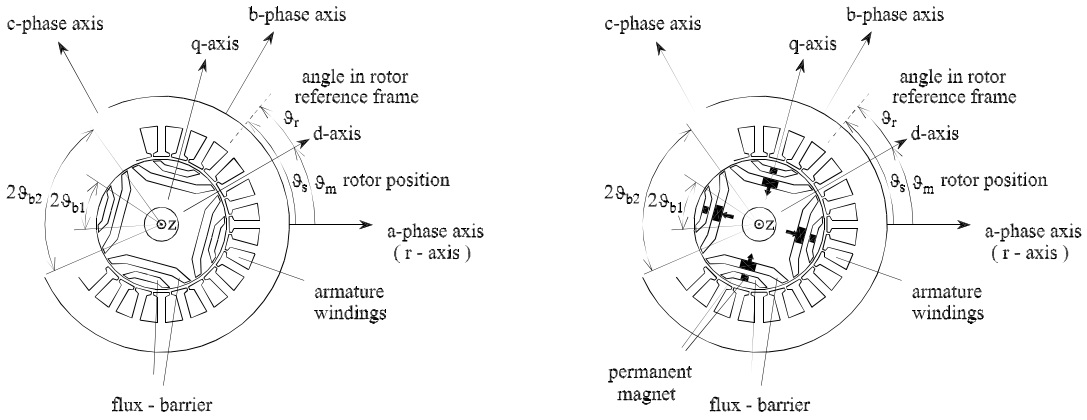

Figure 3.2: Reference used for the REL and PMAREL/IPM motors

3.2.2. Electrical loading

A slotless stator is considered, in which the conductors within the slots are replaced by a conductive sheet of infinitesimal thickness placed on the inner surface of the stator. Along this sheet a distribution of a density of conductors $n_d(\vartheta_s)$ is considered, equivalent to the actual distribution of the coils within the slots, as reported in Fig. 3.3.

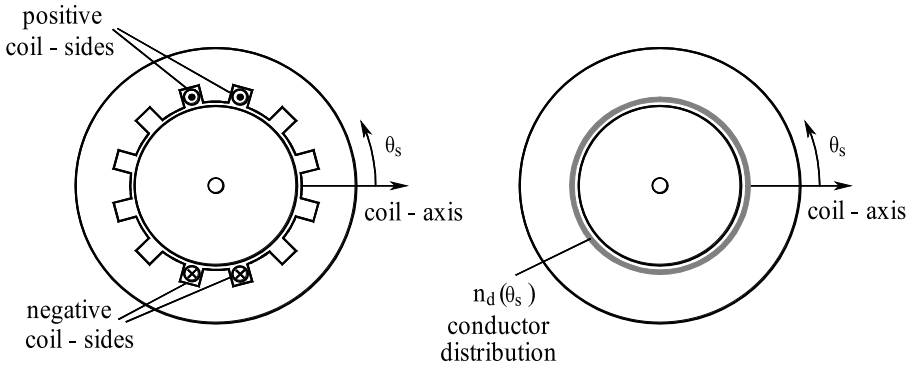

Figure 3.3: Conductor density distribution

Therefore, a linear current density distribution along the conductive sheet is considered when the current is carried by the actual coils. This linear current density distribution is called electrical loading K_s. In the stator reference frame, it is given by

$$\begin{aligned} K_s(\vartheta_s) &= \sum_{\nu} \hat{K}_\nu \sin(\nu p \vartheta_s - p\vartheta_m - \alpha_i^e) \\ &= \sum_{\nu} \hat{K}_\nu \sin(\nu p \vartheta_s - \omega_{me} t - \alpha_i^e) \end{aligned} \tag{3.1}$$

with

ν	the harmonic order,
$\hat{K}_\nu$	the peak value of electric loading harmonic of ν order, in (A/m),
p	the number of pole pairs,
ϑ_s	the coordinate angle (mechanical degrees), in the stator reference frame,
ϑ_m	the angular position of rotor (mechanical degrees),
α_i^e	the phase angle of the current (electrical degrees), shown in Fig. 3.4.

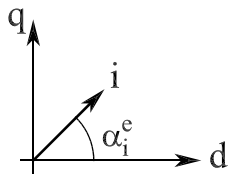

Figure 3.4: Electrical angle α_i^e of the stator current vector

Adopting a standard three–phase winding, with an integer number of slot per pole per phase, only harmonics of odd order exist, non multiple of three. Then ν can be expressed as $\nu = 6k + 1$ with k integer with sign, i.e. $k = 0, \pm1, \pm2, ...$, so that $\nu = +1, -5, +7, -11, +13, ...$

3.2.3. Stator magnetic potential

In the stator reference frame, the stator magnetic potential is given by:

$$U_s(\vartheta_s) = \int K_s(\vartheta_s)\frac{D}{2}d\vartheta_s \tag{3.2}$$

Since $K_s(\vartheta_s)$ is a periodic function, the integral ends can be omitted.

3.2.4. Quantities in the rotor reference frame

It is convenient to express the quantities defined above in the rotor reference frame, by means the the angular coordinate ϑ_r. According to Fig. 3.2, ϑ_r is linked to the stator angular coordinate ϑ_s by

$$\begin{aligned} p\vartheta_s &= p\vartheta_r + p\vartheta_m \\ &= p\vartheta_r + \omega_{me}t \end{aligned} \tag{3.3}$$

It is worth noticing that, during steady–state operations, the rotor position is linked to the rotor speed by the relationship $p\vartheta_m = \omega_{me}t$, where $\vartheta_m = 0$ at the time $t = 0$. In the following, the angle $\omega_{me}t$ will be used to individuate the rotor position. Substituting $p\vartheta_s$ into the equations (3.1) and (3.2), they result

$$K_s(\vartheta_r) = \sum_\nu \hat{K}_\nu \sin[\nu p\vartheta_r + (\nu - 1)\omega_{me}t - \alpha_i^e] \tag{3.4}$$

and

$$U_s(\vartheta_r) = \int K_s(\vartheta_r)\frac{D}{2}d\vartheta_r$$
$$= \sum_{\nu} -\frac{\hat{K}_\nu}{\nu}\frac{D}{2p}\cos[\nu p\vartheta_r + (\nu-1)\omega_{me}t - \alpha_i^e] \tag{3.5}$$

The geometrical motor components considerednin the model are sketched in Fig. 3.5(a). The distribution of the magnetic potential along the stator periphery is shown in Fig. 3.5(b). As a consequence of the stator magnetic potential, a magnetic flux flows in the rotor. Referring to a REL machine, the rotor "island", bordered by these flux–barriers, assumes a magnetic potential proportional to the flux–barrier reluctance and the flux (Fig. 3.6(a)). The distribution of such a rotor magnetic potential is shown in Fig. 3.6(a) as well. Finally, the air–gap flux density can be computed as the difference between the two magnetic potentials, as in Fig. 3.6(b).

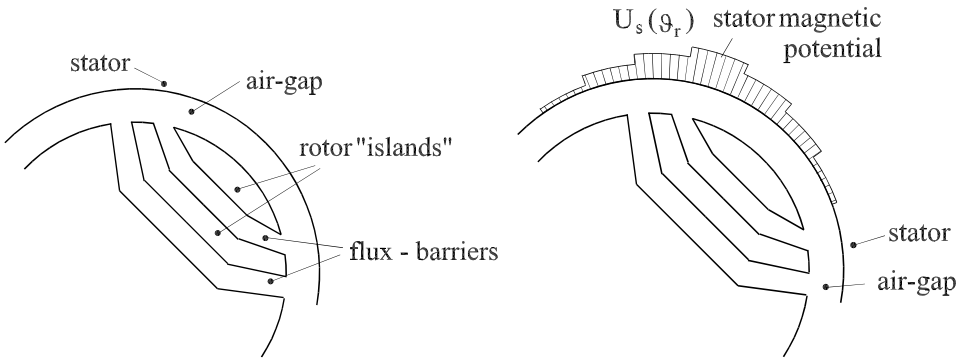

(a) Model (b) Stator magnetic potential

Figure 3.5: Magnetic potential along the stator periphery

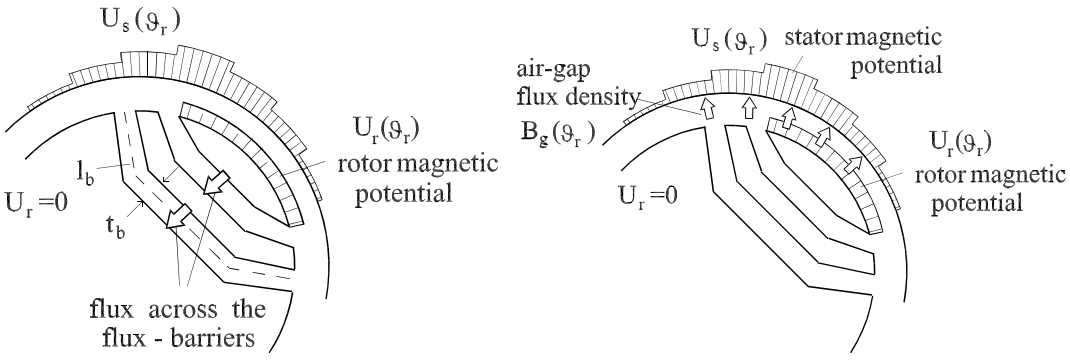

(a) Rotor magnetic potential (b) Air–gap flux density

Figure 3.6: Rotor magnetic reaction and air–gap flux density

The analytical model is based on the resolution of the magnetic circuit under the geometrical simplifications. Firstly, as introduced above the stator is replaced by a infinitesimal sheet. Then, the geometry of the flux—barrier is simplified considering equivalent reference value that describe their length and the thickness. Thanks to the

magnetic symmetries of the machine it is possible to identify equipotential magnetic axes. Therefore, in this case, it is possible to consider only half of the complete rotor pole magnetic circuit [37]. It is of course permissible to simplify the circuit in this way only if the two halves are balanced. An additional simplification is related to the iron and steel that are assumed to be infinitely permeable.

3.3. Rotor with one flux–barrier per pole

3.3.1. Rotor magnetic potentials

As shown in Fig. 3.3.1, the flux–barrier angle ϑ_b indicates the half–angle of the flux–barrier, expressed in mechanical degrees. In Fig. 3.3.1 the linearized rotor geometry with one flux–barrier per pole is sketched.

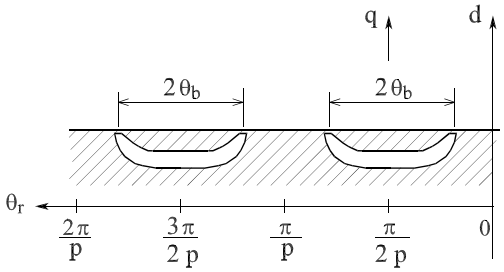

Figure 3.7: Geometrical references of the flux–barriers

Neglecting the magnetic voltage drop in the stator iron path, the air–gap flux density distribution (Fig. 3.6) is given by

$$B_g(\vartheta_r) = \mu_0 \frac{-U_s(\vartheta_r) + U_r(\vartheta_r)}{g} \tag{3.6}$$

The magnetic potential of the rotor $U_r(\vartheta_r)$ can be considered to be constant in the magnetic "island" bordered by the flux–barrier and the air gap (labeled as U_{r1}), and null elsewhere.

According to a rotor with one flux–barriers per pole, the magnetic lumped–parameter network shown in Fig. 3.8 is adopted. It is possible to recognize the reluctance of the air gap over the rotor island R_{g1}, the reluctance of the remainder air gap over the pole end R_{g2}, the flux–barrier reluctance R_{b1}, the PM remanent flux ϕ_{rem1}.

The magnetic reluctance of the flux–barrier is given by

$$R_{b1} = \frac{t_b}{\mu_0 L_{stk} l_b} \tag{3.7}$$

Where D is the bore diameter, g the air gap thickness, t_b and l_b the barrier thickness and length respectively. The flux due to the PM is defined as:

$$\phi_{rem1} = B_{rem1} h_m L_{stk} = \mu_0 \mu_r H_{c1} h_m L_{stk} \tag{3.8}$$

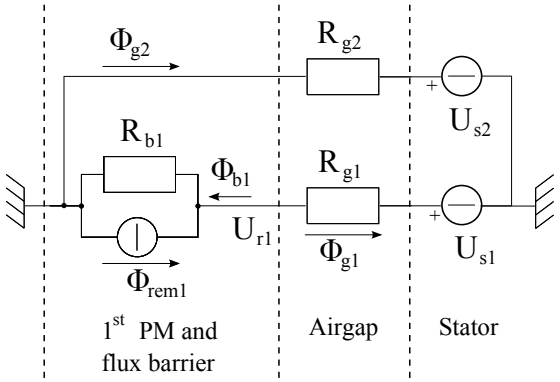

Figure 3.8: Magnetic network of IPM motor with one flux–barriers per pole.

where the quantities are:

ϕ_{rem1}	PM remanent flux,
h_m	PM length,
μ_r	PM relative permeability,
H_{c1}	PM coercitive force.

From the air–gap flux density distribution (3.6), the magnetic flux crossing the flux–barrier results in

$$\phi = \phi_{b1} + \phi_{rem1} = \int_{\frac{\pi}{2p}-\vartheta_b}^{\frac{\pi}{2p}+\vartheta_b} -B_g(\vartheta_r) L_{stk} \frac{D}{2} d\vartheta_r + \mu_0 \mu_r H_{c1} h_m L_{stk} \tag{3.9}$$

The rotor magnetic potential U_{r1}, computed as the flux crossing the flux-barrier times its reluctance, can be expressed as a function of $U_s(\vartheta_r)$:

$$\begin{aligned} U_{r1} &= [\phi_{b1} + \phi_{rem1}]\, R_b \\ &= \left[\int_{\frac{\pi}{2p}-\vartheta_b}^{\frac{\pi}{2p}+\vartheta_b} -B_g(\vartheta_r) L_{stk} \frac{D}{2} d\vartheta_r + \mu_0 \mu_r H_{c1} h_m L_{stk} \right] \frac{t_b}{\mu_0 L_{stk} l_b} \\ &= \mu_0 \frac{L_{stk} D}{2g} \left[\int_{\frac{\pi}{2p}-\vartheta_b}^{\frac{\pi}{2p}+\vartheta_b} U_s(\vartheta_r) d\vartheta_r - 2\vartheta_b U_r + \frac{2g}{D} \mu_r H_{c1} h_m \right] \frac{t_b}{\mu_0 L_{stk} l_b} \\ &= \frac{D}{2g} \frac{t_b}{l_b} \left[\int_{\frac{\pi}{2p}-\vartheta_b}^{\frac{\pi}{2p}+\vartheta_b} U_s(\vartheta_r) d\vartheta_r - 2\vartheta_b U_r + \frac{2g}{D} \mu_r H_{c1} h_m \right] \end{aligned} \tag{3.10}$$

then from

$$U_{r1} \left[1 + \frac{D}{2g} \frac{t_b}{l_b} 2\vartheta_b \right] = \frac{D}{2g} \frac{t_b}{l_b} \left[\int_{\frac{\pi}{2p}-\vartheta_b}^{\frac{\pi}{2p}+\vartheta_b} U_s(\vartheta_r) d\vartheta_r + \frac{2g}{D} \mu_r H_{c1} h_m \right] \tag{3.11}$$

it is possible to define the dimensionless coefficient a, that is a function of the rotor geometry only.

$$a = \frac{\frac{D}{2g} \frac{t_b}{l_b}}{1 + \frac{D}{2g} \frac{t_b}{l_b} 2\vartheta_b} \tag{3.12}$$

Then, the rotor magnetic potential is rewritten as

$$\begin{aligned} U_{r1} &= a\int_{\frac{\pi}{2p}-\vartheta_b}^{\frac{\pi}{2p}+\vartheta_b} U_s(\vartheta_r)d\vartheta_r + a\frac{2g}{D}\mu_r H_{c1}h_m \\ &= a\sum_\nu \int_{\frac{\pi}{2p}-\vartheta_b}^{\frac{\pi}{2p}+\vartheta_b} -\frac{\hat{K}_\nu}{\nu}\ \frac{D}{2p}\ \cos\left[\nu p\vartheta_r + (\nu-1)\omega_{me}t - \alpha_i^e\right] + a\frac{2g}{D}\mu_r H_{c1}h_m \\ &= a\sum_\nu -\frac{\hat{K}_\nu}{\nu}\ \frac{D}{2p}\ \frac{1}{\nu p}\ \sin\left[\nu p\vartheta_r + (\nu-1)\omega_{me}t - \alpha_i^e\right]\Big|_{\frac{\pi}{2p}-\vartheta_b}^{\frac{\pi}{2p}+\vartheta_b} + a\frac{2g}{D}\mu_r H_{c1}h_m \end{aligned} \tag{3.13}$$

It is possible to define an additional dimensionless coefficient b:

$$b = \frac{1}{1+\frac{D}{2g}\frac{t_{b1}}{l_{b1}}2\vartheta_{b1}} \tag{3.14}$$

and letting

$$\lambda_\nu = \frac{\nu\pi}{2} + (\nu-1)\omega_{me}t - \alpha_i^e \tag{3.15}$$

the rotor magnetic potential results in

$$U_{r1} = -aD\sum_\nu \frac{\hat{K}_\nu}{(\nu p)^2}\ \cos\lambda_\nu \sin(\nu p\vartheta_b) + k_{pm1} \tag{3.16}$$

where k_{pm1} is the contribution of the PM, defined as:

$$k_{pm1} = b\phi_{rem1}R_{b1} \tag{3.17}$$

3.3.2. Torque computation

The torque is obtained by integrating the Lorentz's force density $B_g(\vartheta_r)K_s(\vartheta_r)$ along the air–gap surface, and multiplying the result by the radius $D/2$. With the convention defined above it is

$$\begin{aligned} \tau_m &= -\frac{D}{2}\int_0^{2\pi} B_g(\vartheta_r)K_s(\vartheta_r)\frac{DL_{stk}}{2}d\vartheta_r \\ &= -\frac{D}{2}\int_0^{2\pi} \mu_0\frac{-U_s(\vartheta_r)+U_r}{g}K_s(\vartheta_r)\frac{DL_{stk}}{2}d\vartheta_r \\ &= \frac{\mu_0}{g}\frac{D^2L_{stk}}{4}\left[\underbrace{\int_0^{2\pi} U_s(\vartheta_r)K_s(\vartheta_r)d\vartheta_r}_{A} + \underbrace{\int_0^{2\pi} -U_r(\vartheta_r)K_s(\vartheta_r)d\vartheta_r}_{B}\right] \end{aligned} \tag{3.18}$$

The first integral of (3.18), i.e. the term A, is null since the Fourier series expansions of $U_s(\vartheta_r)$ and $K_s(\vartheta_r)$ are orthogonal functions. Thus the integral in a period of their product is null.

Then, only the second integral of (3.18), labelled B in (3.18), will be considered. The torque results in

$$\tau_m = \frac{\mu_0}{g}\frac{D^2 L_{stk}}{4}\int_0^{2\pi} -U_r(\vartheta_r)K_s(\vartheta_r)d\vartheta_r \tag{3.19}$$

Let us remember that

- $U_r(\vartheta_r)$ is a function piece–wise defined: it assumes a value different from zero only in the intervals $(\pi/2p-\vartheta_b, \pi/2p+\vartheta_b)$ and $(3\pi/2p-\vartheta_b, 3\pi/2p+\vartheta_b)$ and null elsewhere;
- $U_r(\vartheta_r)$ has opposite values under every other pole (this is true with the assumption of harmonics of odd order only);
- thanks to the motor symmetry, only two poles can be considered in the computation, and the quantities of the whole system are achieved by multiplying the result of the computation by the number of pole pairs p.

Then after several manipulations, the torque results in:

$$\tau_m = \frac{\mu_0}{g}\frac{D^2 L_{stk}}{4}U_{r1}(-2p)\int_{\frac{\pi}{2p}-\vartheta_b}^{\frac{\pi}{2p}+\vartheta_b} K_s(\vartheta_r)d\vartheta_r \tag{3.20}$$

Finally, substituting the relationships of the electrical loading (3.4) and the rotor magnetic potential (3.16), the motor torque becomes

$$\begin{aligned}\tau_m =& ak_\tau \sum_\nu \frac{\hat{K}_\nu}{(\nu p)^2}\, D\, \cos\lambda_\nu \sin(\nu p\vartheta_b)\sum_\xi \frac{\hat{K}_\xi}{\xi}\, \sin\lambda_\xi \sin(\xi p\vartheta_b)\\ &- k_\tau k_{pm1}\sum_\xi \frac{\hat{K}_\xi}{\xi}\, \sin\lambda_\xi \sin(\xi p\vartheta_b)\end{aligned} \tag{3.21}$$

where k_τ is defined as torque constant:

$$k_\tau = \mu_0 \frac{D^2 L_{stk}}{g} \tag{3.22}$$

In (3.21) the harmonic orders ν and ξ are used in order to avoid to confuse the components of the two series expansions. It should be noted that the first term of (3.21) corresponds to the torque component due to the anisotropy while the second terms refers to torque component due to the PM flux.

3.4. Rotor with two flux–barrier per pole

3.4.1. Rotor magnetic potentials

According to a rotor with two flux–barriers per pole, the magnetic lumped–parameter network shown in Fig. 3.9 is adopted. The subscript "1" will be used for the inner flux–barrier while the subscript "2" will be used for the outer flux–barrier. The components of the network are basically the same of the one shown in Fig. 3.8.

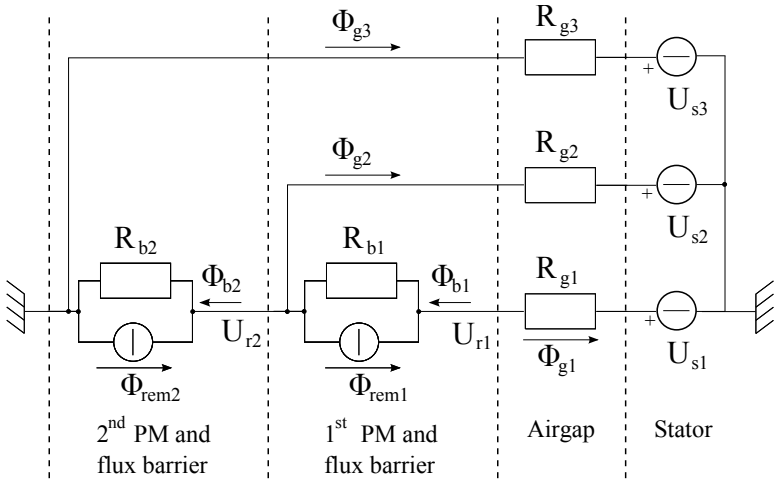

Figure 3.9: Magnetic network of IPM motor with two flux–barriers per pole.

In particular, the flux due to the PM, for both flux–barriers, is

$$\phi_{rem1} = B_{rem1} h_{m1} L_{stk} = \mu_0 \mu_{r1} H_{c1} h_{m1} L_{stk} \tag{3.23}$$

$$\phi_{rem2} = B_{rem2} h_{m2} L_{stk} = \mu_0 \mu_{r2} H_{c2} h_{m2} L_{stk} \tag{3.24}$$

where

ϕ_{rem1}, ϕ_{rem2}	PM remanent flux of inner (1) and outer flux-barrier (2),
h_{m1}, h_{m2}	PM length of inner (1) and outer flux-barrier (2),
μ_{r1}, μ_{r2}	PM relative permeability of inner (1) and outer flux-barrier (2),
H_{c1}, H_{c2}	PM coercitive force of inner (1) and outer flux-barrier (2),

The electric load and the stator magnetic potential are defined respectively from (3.4) and (3.2). The magnetic potential of the rotor "island" bordered by the inner flux–barrier is

$$\begin{aligned} U_{r1} &= (\phi_{b1} + \phi_{rem1})\, R_{b1} + U_{r2} \\ &= \int_{\frac{\pi}{2p} - \vartheta_{b1}}^{\frac{\pi}{2p} + \vartheta_{b1}} -B_g(\vartheta_r) \frac{L_{stk} D}{2} d\vartheta_r R_{b1} + \phi_{rem1} R_{b1} + U_{r2} \end{aligned} \tag{3.25}$$

$$
\begin{aligned}
&= \int_{\frac{\pi}{2p}-\vartheta_{b1}}^{\frac{\pi}{2p}+\vartheta_{b1}} \mu_0 \frac{U_s(\vartheta_r)-U_{r1}}{g}\frac{L_{stk}D}{2}d\vartheta_r R_{b1} + \phi_{rem1}R_{b1} + U_{r2} \\
&= \frac{D}{2g}\frac{t_{b1}}{l_{b1}}\left[\int_{\frac{\pi}{2p}-\vartheta_{b1}}^{\frac{\pi}{2p}+\vartheta_{b1}} U_s(\vartheta_r)d\vartheta_r - \underbrace{\int_{\frac{\pi}{2p}-\vartheta_{b1}}^{\frac{\pi}{2p}+\vartheta_{b1}} U_{r1}d\vartheta_r}_{2\vartheta_{b1}U_{r1}}\right] + \phi_{rem1}R_{b1} + U_{r2} \\
&= \frac{D}{2g}\frac{t_{b1}}{l_{b1}}\int_{\frac{\pi}{2p}-\vartheta_{b1}}^{\frac{\pi}{2p}+\vartheta_{b1}} U_s(\vartheta_r)d\vartheta_r - \frac{D}{g}\frac{t_{b1}}{l_{b1}}\vartheta_{b1}U_{r1} + \phi_{rem1}R_{b1} + U_{r2}
\end{aligned} \tag{3.26}
$$

from which U_{r1} is

$$
\begin{aligned}
U_{r1} &= a\int_{\frac{\pi}{2p}-\vartheta_{b1}}^{\frac{\pi}{2p}+\vartheta_{b1}} U_s(\vartheta_r)d\vartheta_r + b\phi_{rem1}R_{b1} + bU_{r2} \\
&= a\int_{\frac{\pi}{2p}-\vartheta_{b1}}^{\frac{\pi}{2p}+\vartheta_{b1}} U_s(\vartheta_r)d\vartheta_r + k_{pm1} + bU_{r2}
\end{aligned} \tag{3.27}
$$

Where k_{pm1} is defined as in (3.17). The two dimensionless coefficients a (3.12) and b (3.12) are a function of the motor geometry, as reported in the previous section.

The magnetic potential of the rotor "island" bordered by the outer flux–barrier is computed by means of the flux crossing through the flux–barrier itself, which is

$$
\begin{aligned}
U_{r2} &= \left[\phi_{b2} + \phi_{rem2}\right] R_{b2} \\
&= \left[\phi_{b1} + \int_{\frac{\pi}{2p}-\vartheta_{b2}}^{\frac{\pi}{2p}-\vartheta_{b1}} -B_g(\vartheta_r)\frac{L_{stk}D}{2}d\vartheta_r + \int_{\frac{\pi}{2p}+\vartheta_{b1}}^{\frac{\pi}{2p}+\vartheta_{b2}} -B_g(\vartheta_r)\frac{L_{stk}D}{2}d\vartheta_r\right] R_{b2} + \phi_{rem2}R_{b2} \\
&= \left[\frac{U_{r1}-U_{r2}}{R_{b1}} - \phi_{rem1} + \int_{\frac{\pi}{2p}-\vartheta_{b2}}^{\frac{\pi}{2p}-\vartheta_{b1}} \mu_0\frac{U_s(\vartheta_r)-U_{r2}}{g}\frac{L_{stk}D}{2}d\vartheta_r + \right. \\
&\qquad \left. + \int_{\frac{\pi}{2p}+\vartheta_{b1}}^{\frac{\pi}{2p}+\vartheta_{b2}} \mu_0\frac{U_s(\vartheta_r)-U_{r2}}{g}\frac{L_{stk}D}{2}d\vartheta_r \right] R_{b2} + \phi_{rem2}R_{b2} \\
&= \left[\frac{U_{r1}-U_{r2}}{t_{b1}}l_{b1} + \frac{D}{2g}\left(\int_{\frac{\pi}{2p}-\vartheta_{b2}}^{\frac{\pi}{2p}-\vartheta_{b1}} (U_s(\vartheta_r)-U_{r2})d\vartheta_r + \right.\right. \\
&\qquad \left.\left. + \int_{\frac{\pi}{2p}+\vartheta_{b1}}^{\frac{\pi}{2p}+\vartheta_{b2}} (U_s(\vartheta_r)-U_{r2})d\vartheta_r\right)\right]\frac{t_{b2}}{l_{b2}} + (\phi_{rem2}-\phi_{rem1})R_{b2}
\end{aligned} \tag{3.28}
$$

Substituting the expression of U_{r1} given in (3.27) and having assumed U_{r2} to be

constant in the rotor "island", it results in

$$\begin{aligned} U_{r2} =& U_{r2}\frac{t_{b2}}{l_{b2}}\left[(b-1)\frac{l_{b1}}{t_{b1}} - \frac{D}{2g}2(\vartheta_{b2}-\vartheta_{b1})\right] + \frac{t_{b2}}{l_{b2}}\left[a\frac{l_{b1}}{t_{b1}}\int_{\frac{\pi}{2p}-\vartheta_{b1}}^{\frac{\pi}{2p}+\vartheta_{b1}} U_s(\vartheta_r)d\vartheta_r + \right. \\ &\left. + \frac{D}{2g}\left(\int_{\frac{\pi}{2p}-\vartheta_{b2}}^{\frac{\pi}{2p}-\vartheta_{b1}} U_s(\vartheta_r)d\vartheta_r + \int_{\frac{\pi}{2p}+\vartheta_{b1}}^{\frac{\pi}{2p}+\vartheta_{b2}} U_s(\vartheta_r)d\vartheta_r\right)\right] \\ &+ k_{pm1}\frac{t_{b2}}{l_{b2}}\frac{l_{b1}}{t_{b1}} + (\phi_{rem2}-\phi_{rem1})R_{b2} \end{aligned} \tag{3.29}$$

Finally, collecting the common terms, U_{r2} can be expressed as

$$\begin{aligned} U_{r2} &= c\int_{\frac{\pi}{2p}-\vartheta_{b1}}^{\frac{\pi}{2p}+\vartheta_{b1}} U_s(\vartheta_r)d\vartheta_r + \\ &+ d\left(\int_{\frac{\pi}{2p}-\vartheta_{b2}}^{\frac{\pi}{2p}-\vartheta_{b1}} U_s(\vartheta_r)d\vartheta_r + \int_{\frac{\pi}{2p}+\vartheta_{b1}}^{\frac{\pi}{2p}+\vartheta_{b2}} U_s(\vartheta_r)d\vartheta_r\right) + \\ &+ \frac{k_{pm1}\frac{t_{b2}}{l_{b2}}\frac{l_{b1}}{t_{b1}} + (\phi_{rem2}-\phi_{rem1})R_{b2}}{1-(b-1)\frac{l_{b1}}{t_{b1}}\frac{t_{b2}}{l_{b2}} + \frac{D}{g}\frac{t_{b2}}{l_{b2}}(\vartheta_{b2}-\vartheta_{b1})} \\ &= c\int_{\frac{\pi}{2p}-\vartheta_{b1}}^{\frac{\pi}{2p}+\vartheta_{b1}} U_s(\vartheta_r)d\vartheta_r + \\ &+ d\left(\int_{\frac{\pi}{2p}-\vartheta_{b2}}^{\frac{\pi}{2p}-\vartheta_{b1}} U_s(\vartheta_r)d\vartheta_r + \int_{\frac{\pi}{2p}+\vartheta_{b1}}^{\frac{\pi}{2p}+\vartheta_{b2}} U_s(\vartheta_r)d\vartheta_r\right) + k_{pm2} \end{aligned} \tag{3.30}$$

where the PM contribution k_{pm2} is defined as

$$k_{pm2} = \frac{k_{pm1}\frac{t_{b2}}{l_{b2}}\frac{l_{b1}}{t_{b1}} + (\phi_{rem2}-\phi_{rem1})R_{b2}}{1-(b-1)\frac{l_{b1}}{t_{b1}}\frac{t_{b2}}{l_{b2}} + \frac{D}{g}\frac{t_{b2}}{l_{b2}}(\vartheta_{b2}-\vartheta_{b1})} \tag{3.31}$$

The dimensionless coefficients c and d are functions of geometrical quantities, and computed as

$$c = \frac{a\frac{l_{b1}}{t_{b1}}\frac{t_{b2}}{l_{b2}}}{1-(b-1)\frac{l_{b1}}{t_{b1}}\frac{t_{b2}}{l_{b2}} + \frac{D}{g}\frac{t_{b2}}{l_{b2}}(\vartheta_{b2}-\vartheta_{b1})} \tag{3.32}$$

$$d = \frac{\frac{D}{2g}\frac{t_{b2}}{l_{b2}}}{1-(b-1)\frac{l_{b1}}{t_{b1}}\frac{t_{b2}}{l_{b2}} + \frac{D}{g}\frac{t_{b2}}{l_{b2}}(\vartheta_{b2}-\vartheta_{b1})} \tag{3.33}$$

The integral of $U_s(\vartheta_r)$ in the rotor arc bordered by the air gap and and the inner flux–barrier result in

$$S_1 = \int_{\frac{\pi}{2p}-\vartheta_{b1}}^{\frac{\pi}{2p}+\vartheta_{b1}} U_s(\vartheta_r)d\vartheta_r = \sum_\nu -\frac{\hat{K}_\nu}{(\nu p)^2} D\big[\cos(\lambda_\nu)\sin(\nu p\vartheta_{b1})\big]$$

where λ_ν is given in (3.41). In the two arcs of rotor between the inner and the outer flux–barrier, it is

$$\begin{aligned} S_2 &= \int_{\frac{\pi}{2p}-\vartheta_{b2}}^{\frac{\pi}{2p}-\vartheta_{b1}} U_s(\vartheta_r)d\vartheta_r + \int_{\frac{\pi}{2p}+\vartheta_{b1}}^{\frac{\pi}{2p}+\vartheta_{b2}} U_s(\vartheta_r)d\vartheta_r = \\ &= \sum_\nu -\frac{\hat{K}_\nu}{(\nu p)^2} D\cos(\lambda_\nu)\big[\sin(\nu p\vartheta_{b2}) - \sin(\nu p\vartheta_{b1})\big] \end{aligned}$$

The rotor magnetic potential U_{r2} becomes

$$\begin{aligned} U_{r2} =& cS_1 + dS_2 + k_{pm2} = \\ =& \sum_\nu \frac{\hat{K}_\nu}{(\nu p)^2} D\Big[-c\cos(\lambda_\nu)\sin(\nu p\vartheta_{b1}) - d\cos(\lambda_\nu)[\sin(\nu p\vartheta_{b2}) - \sin(\nu p\vartheta_{b1})]\Big] + k_{pm2} \\ =& -\sum_\nu \frac{\hat{K}_\nu}{(\nu p)^2} D\cos(\lambda_\nu)\Big[(c-d)\sin(\nu p\vartheta_{b1}) + d\sin(\nu p\vartheta_{b2})\Big] + k_{pm2} \end{aligned} \tag{3.34}$$

while the magnetic potential U_{r1} is obtained from (3.27), and results in

$$\begin{aligned} U_{r1} =& a\int_{\frac{\pi}{2p}-\vartheta_{b1}}^{\frac{\pi}{2p}+\vartheta_{b1}} U_s(\vartheta_r)d\vartheta_r + k_{pm1} + bU_{r2} = \\ =& -a\sum_\nu \frac{\hat{K}_\nu}{(\nu p)^2} D\cos(\lambda_\nu)\sin(\nu p\vartheta_{b1}) + \\ &+ b\sum_\nu \frac{\hat{K}_\nu}{(\nu p)^2} D\cos(\lambda_\nu)\left[(c-d)\sin(\nu p\vartheta_{b1}) + d\sin(\nu p\vartheta_{b2})\right] + k_{pm1} + bk_{pm2} \\ =& -\sum_\nu \frac{\hat{K}_\nu}{(\nu p)^2} D\cos(\lambda_\nu)\Big[a\sin(\nu p\vartheta_{b1}) + b(c-d)\sin(\nu p\vartheta_{b1}) + bd\sin(\nu p\vartheta_{b2})\Big] + \\ &+ k_{pm1} + bk_{pm2} \end{aligned} \tag{3.35}$$

Equations (3.34) and (3.35) can be rewritten in a more compact form, observing that the terms within the square brackets depend on the motor geometry only. Thus, it yields

$$U_{r1} = -\sum_\nu \frac{\hat{K}_\nu}{(\nu p)^2} D\rho_1\cos\lambda_\nu + k_{pm1} + bk_{pm2} \tag{3.36}$$

$$U_{r2} = -\sum_\nu \frac{\hat{K}_\nu}{(\nu p)^2} D\rho_2\cos\lambda_\nu + k_{pm2} \tag{3.37}$$

where λ_ν is defined in 3.41, and the coefficients ρ_1 and ρ_2 are

$$\rho_1 = a\sin(\nu p\vartheta_{b1}) + b(c-d)\sin(\nu p\vartheta_{b1}) + bd\sin(\nu p\vartheta_{b2}) \tag{3.38}$$

$$\rho_2 = (c-d)\sin(\nu p\vartheta_{b1}) + d\sin(\nu p\vartheta_{b2}) \tag{3.39}$$

3.4.2. Torque computation

Applying the same considerations of the torque expression with one flux–barrier per pole, the motor torque is computed as

$$\tau_m = -\frac{D}{2}\int_0^{2\pi} B_g(\vartheta_r)K_s(\vartheta_r)\frac{D}{2}L_{stk}d\vartheta_r = \frac{\mu_0 D^2}{4g}\text{Ł}_{stk}\int_0^{2\pi} -U_r(\vartheta_r)K_s(\vartheta_r)d\vartheta_r$$

Thus

$$\begin{aligned}
\tau_m &= \frac{k_\tau}{4}(-2p)\left[\int_{\frac{\pi}{2p}-\vartheta_{b2}}^{\frac{\pi}{2p}-\vartheta_{b1}} U_{r2}K_s(\vartheta_r)d\vartheta_r + \int_{\frac{\pi}{2p}-\vartheta_{b1}}^{\frac{\pi}{2p}+\vartheta_{b1}} U_{r1}K_s(\vartheta_r)d\vartheta_r + \int_{\frac{\pi}{2p}+\vartheta_{b1}}^{\frac{\pi}{2p}+\vartheta_{b2}} U_{r2}K_s(\vartheta_r)d\vartheta_r\right] \\
&= -\frac{k_\tau p}{2}\left[\int_{\frac{\pi}{2p}-\vartheta_{b2}}^{\frac{\pi}{2p}-\vartheta_{b1}}\left(-\sum_\nu \frac{\hat{K}_\nu}{(\nu p)^2}D\rho_2\cos\lambda_\nu + k_{pm2}\right)\cdot\sum_\xi \hat{K}_\xi\sin\lambda_\xi d\vartheta_r + \cdots\right] \\
&= \frac{k_\tau p}{2}\left[\sum_\nu \frac{\hat{K}_\nu}{(\nu p)^2}D\rho_2\cos\lambda_\nu\cdot\sum_\xi \hat{K}_\xi\left(\rho_2\int_{\frac{\pi}{2p}-\vartheta_{b2}}^{\frac{\pi}{2p}-\vartheta_{b1}}\sin\lambda_\xi d\vartheta_r + \right.\right. \\
&\quad + \rho_1\int_{\frac{\pi}{2p}-\vartheta_{b1}}^{\frac{\pi}{2p}+\vartheta_{b1}}\sin\lambda_\xi d\vartheta_r + \rho_2\int_{\frac{\pi}{2p}+\vartheta_{b1}}^{\frac{\pi}{2p}+\vartheta_{b2}}\sin\lambda_\xi d\vartheta_r\Big) - \\
&\quad - \sum_\xi \hat{K}_\xi\left(k_{pm2}\int_{\frac{\pi}{2p}-\vartheta_{b2}}^{\frac{\pi}{2p}-\vartheta_{b1}}\sin\lambda_\xi d\vartheta_r + (k_{pm1}+bk_{pm2})\int_{\frac{\pi}{2p}-\vartheta_{b1}}^{\frac{\pi}{2p}+\vartheta_{b1}}\sin\lambda_\xi d\vartheta_r + \right. \\
&\quad \left.\left. + k_{pm2}\int_{\frac{\pi}{2p}+\vartheta_{b1}}^{\frac{\pi}{2p}+\vartheta_{b2}}\sin\lambda_\xi d\vartheta_r\right)\right]
\end{aligned} \tag{3.40}$$

where k_τ is (3.22) and λ_ξ is analogously to λ_ν defined as

$$\lambda_\xi = \frac{\xi\pi}{2} + (\xi-1)\omega_{me}t - \alpha_i^e \tag{3.41}$$

The integrals along the arcs of the air–gap, bordered by the inner and the outer flux–barriers, are given by

$$\begin{aligned}
\int_{\frac{\pi}{2p}-\vartheta_{b1}}^{\frac{\pi}{2p}+\vartheta_{b1}}\sin\lambda_\xi d\vartheta_r &= -\frac{1}{\xi p}\left[\cos(\lambda_\xi + \xi p\vartheta_{b1}) - \cos(\lambda_\xi - \xi p\vartheta_{b1})\right] \\
&= \frac{2}{\xi p}\sin\lambda_\xi\sin(\xi p\vartheta_{b1})
\end{aligned} \tag{3.42}$$

$$\int_{\frac{\pi}{2p}-\vartheta_{b2}}^{\frac{\pi}{2p}-\vartheta_{b1}}\sin\lambda_\xi d\vartheta_r + \int_{\frac{\pi}{2p}+\vartheta_{b1}}^{\frac{\pi}{2p}+\vartheta_{b2}}\sin\lambda_\xi d\vartheta_r = \frac{2}{\xi p}\sin\lambda_\xi\left[\sin(\xi p\vartheta_{b2}) - \sin(\xi p\vartheta_{b1})\right] \tag{3.43}$$

that substituted in (3.40) yield

$$\begin{aligned}
\tau_m =& k_\tau\sum_\nu \frac{\hat{K}_\nu}{(\nu p)^2}D\cos\lambda_\nu\left[(\rho_1-\rho_2)\sum_\xi\frac{\hat{K}_\xi}{\xi}\sin\lambda_\xi\sin(\xi p\vartheta_{b1}) + \rho_2\sum_\xi\frac{\hat{K}_\xi}{\xi}\sin\lambda_\xi sin(\xi p\vartheta_{b2})\right] - \\
&- k_\tau\left[(k_{pm1}+(b-1)k_{pm2})\sum_\xi\frac{\hat{K}_\xi}{\xi}\sin\lambda_\xi\sin(\xi p\vartheta_{b1}) + k_{pm2}\sum_\xi\frac{\hat{K}_\xi}{\xi}\sin\lambda_\xi sin(\xi p\vartheta_{b2})\right]
\end{aligned} \tag{3.44}$$

Also in this case the two torque components (the reluctance one and the PM one) are highlighted separately, in (3.44).

3.5. Rotor with three flux–barriers per pole

3.5.1. Rotor magnetic potentials

According to a rotor with three flux–barriers per pole, the magnetic lumped–parameter network shown in Fig. 3.10 is adopted. The subscript "1" will be used for the inner flux–barrier, subscript "2" will be used for the middle flux–barrier, and finally the subscript "3" will be used for the outer flux–barrier. The components of the network are basically the same of the one shown in Fig. 3.8.

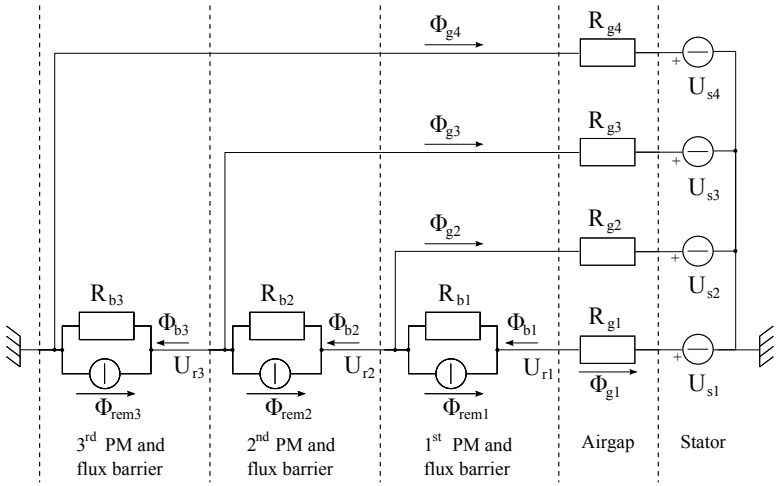

Figure 3.10: Magnetic network of IPM motor with three flux–barriers per pole.

As above, the flux due to the PM of each flux–barrier is defined as

$$\phi_{rem} = B_{rem} h_m L_{stk} = \mu_0 \mu_r H_c h_m L_{stk} \tag{3.45}$$

where ϕ_{rem}, h_m, μ_r, and H_c are respectively the remanent flux, the length, the relative permeability and the coercitive force of each flux–barrier (subscripts 1, 2, 3).

The electric load and the stator magnetic potential are defined respectively from (3.4) and (3.2). The magnetic potential of the rotor "island" bordered by the inner flux–barrier is

$$\begin{aligned} U_{r1} &= \left[\phi_{b1} + \phi_{rem1}\right] R_{b1} + U_{r2} \\ &= \int_{\frac{\pi}{2p}-\vartheta_{b1}}^{\frac{\pi}{2p}+\vartheta_{b1}} -B_g(\vartheta_r)\frac{L_{stk} D}{2} d\vartheta_r R_{b1} + \phi_{rem1} R_{b1} + U_{r2} \\ &= \frac{D}{2g}\frac{t_{b1}}{l_{b1}} \int_{\frac{\pi}{2p}-\vartheta_{b1}}^{\frac{\pi}{2p}+\vartheta_{b1}} U_s(\vartheta_r) d\vartheta_r - \frac{D}{g}\frac{t_{b1}}{l_{b1}} \vartheta_{b1} U_{r1} + \phi_{rem1} R_{b1} + U_{r2} \end{aligned} \tag{3.46}$$

from which U_{r1} is

$$\begin{aligned} U_{r1} &= a\int_{\frac{\pi}{2p}-\vartheta_{b1}}^{\frac{\pi}{2p}+\vartheta_{b1}} U_s(\vartheta_r)d\vartheta_r + b\phi_{rem1}R_{b1} + bU_{r2} \\ &= a\int_{\frac{\pi}{2p}-\vartheta_{b1}}^{\frac{\pi}{2p}+\vartheta_{b1}} U_s(\vartheta_r)d\vartheta_r + k_{pm1} + bU_{r2} \end{aligned} \tag{3.47}$$

where k_{pm1}, a and b have been already defined in section 3.3. The rotor magnetic potential U_{r2} is computed as

$$\begin{aligned} U_{r2} &= (\phi_{b2}+\phi_{rem2})R_{b2} + U_{r3} \\ &= \left(\phi_{b1} + \int_{\frac{\pi}{2p}-\vartheta_{b2}}^{\frac{\pi}{2p}-\vartheta_{b1}} -B_g(\vartheta_r)\frac{L_{stk}D}{2}d\vartheta_r + \right. \\ &\quad \left. + \int_{\frac{\pi}{2p}+\vartheta_{b1}}^{\frac{\pi}{2p}+\vartheta_{b2}} -B_g(\vartheta_r)\frac{L_{stk}D}{2}d\vartheta_r + \phi_{rem2}\right)\frac{t_{b2}}{\mu_0 L_{stk} l_{b2}} + U_{r3} \end{aligned} \tag{3.48}$$

with

$$\phi_{b1} = \frac{U_{r1}-U_{r2}}{R_{b1}} - \phi_{rem1} \tag{3.49}$$

$$B_g = \mu_0\frac{-U_s(\vartheta_r)+U_{r2}}{g} \tag{3.50}$$

Then

$$\begin{aligned} U_{r2} = \Bigg[& a\frac{l_{b1}}{t_{b1}}\int_{\frac{\pi}{2p}-\vartheta_{b1}}^{\frac{\pi}{2p}+\vartheta_{b1}} U_s(\vartheta_r)d\vartheta_r + (b-1)\frac{l_{b1}}{t_{b1}}U_{r2} + \\ & + \frac{D}{2g}\Big(\int_{\frac{\pi}{2p}-\vartheta_{b2}}^{\frac{\pi}{2p}-\vartheta_{b1}} U_s(\vartheta_r)d\vartheta_r + \int_{\frac{\pi}{2p}+\vartheta_{b1}}^{\frac{\pi}{2p}+\vartheta_{b2}} U_s(\vartheta_r)d\vartheta_r\Big) - \\ & - \frac{D}{2g}U_{r2}\Big((\vartheta_{b2}-\vartheta_{b1}) + (\vartheta_{b2}-\vartheta_{b1})\Big)\Bigg]\frac{t_{b2}}{l_{b2}} - \phi_{rem1}R_{b2} + \\ & + \phi_{rem2}R_{b2} + k_{pm1}\frac{l_{b1}}{t_{b1}}\frac{t_{b2}}{l_{b2}} + U_{r3} \end{aligned} \tag{3.51}$$

The geometric dimensionless coefficient c and d have been already defined in section 3.4, while the coefficient z is

$$z = \frac{1}{1-(b-1)\frac{l_{b1}}{t_{b1}}\frac{t_{b2}}{l_{b2}} + \frac{D}{g}\frac{t_{b2}}{l_{b2}}(\vartheta_{b2}-\vartheta_{b1})} \tag{3.52}$$

Then the magnetic potential results in

$$\begin{aligned} U_{r2} = c\int_{\frac{\pi}{2p}-\vartheta_{b1}}^{\frac{\pi}{2p}+\vartheta_{b1}} U_s(\vartheta_r)d\vartheta_r + d\Big(\int_{\frac{\pi}{2p}-\vartheta_{b2}}^{\frac{\pi}{2p}-\vartheta_{b1}} U_s(\vartheta_r)d\vartheta_r + \\ + \int_{\frac{\pi}{2p}+\vartheta_{b1}}^{\frac{\pi}{2p}+\vartheta_{b2}} U_s(\vartheta_r)d\vartheta_r\Big) + k_{pm2} + zU_{r3} \end{aligned} \tag{3.53}$$

where k_{pm2} is defined in (3.31). The magnetic potential of the rotor "island" bordered by the outer flux–barrier is computed by means of the flux crossing through the flux–barrier itself, which is:

$$\begin{aligned} U_{r3} &= (\phi_{b3} + \phi_{rem3})R_{b3} \\ &= \Big(\phi_{b2} + \int_{\frac{\pi}{2p}-\vartheta_{b3}}^{\frac{\pi}{2p}-\vartheta_{b2}} -B_g(\vartheta_r)\frac{L_{stk}D}{2}d\vartheta_r + \\ &+ \int_{\frac{\pi}{2p}+\vartheta_{b2}}^{\frac{\pi}{2p}+\vartheta_{b3}} -B_g(\vartheta_r)\frac{L_{stk}D}{2}d\vartheta_r + \phi_{rem3}\Big)\frac{t_{b3}}{\mu_0 L_{stk} l_{b3}} \end{aligned} \tag{3.54}$$

with

$$\phi_{b2} = \frac{U_{r2} - U_{r3}}{R_{b2}} - \phi_{rem2} \tag{3.55}$$

$$B_g = \mu_0 \frac{(-U_s(\vartheta_r) + U_{r3})}{g} \tag{3.56}$$

Thus

$$\begin{aligned} U_{r3} = \Bigg[& c\frac{l_{b2}}{t_{b2}} \int_{\frac{\pi}{2p}-\vartheta_{b1}}^{\frac{\pi}{2p}+\vartheta_{b1}} U_s(\vartheta_r)d\vartheta_r + d\frac{l_{b2}}{t_{b2}} \left(\int_{\frac{\pi}{2p}-\vartheta_{b2}}^{\frac{\pi}{2p}-\vartheta_{b1}} U_s(\vartheta_r)d\vartheta_r + \int_{\frac{\pi}{2p}+\vartheta_{b1}}^{\frac{\pi}{2p}+\vartheta_{b2}} U_s(\vartheta_r)d\vartheta_r \right) + \\ & + (z-1)\frac{l_{b2}}{t_{b2}}U_{r3} + \frac{D}{2g}\Big(\int_{\frac{\pi}{2p}-\vartheta_{b3}}^{\frac{\pi}{2p}-\vartheta_{b2}} U_s(\vartheta_r)d\vartheta_r + \int_{\frac{\pi}{2p}+\vartheta_{b2}}^{\frac{\pi}{2p}+\vartheta_{b3}} U_s(\vartheta_r)d\vartheta_r \Big) - \\ & - \frac{D}{2g}U_{r3}\Big((\vartheta_{b3} - \vartheta_{b2}) + (\vartheta_{b3} - \vartheta_{b2})\Big) \Bigg] \frac{t_{b3}}{l_{b3}} + \frac{k_{pm2}R_{b3}}{R_{b2}} - \phi_{rem2}R_{b3} + \phi_{rem3}R_{b3} \end{aligned} \tag{3.57}$$

U_{r3} depends only from the geometric coefficients m, n, q, and the $U_s(\vartheta_r)$ integral along the given arc of the air–gap. The dimensionless coefficients are:

$$den = \left(1 - (z-1)\frac{l_{b2}}{t_{b2}}\frac{t_{b3}}{l_{b3}} + \frac{D}{g}\frac{t_{b3}}{l_{b3}}(\vartheta_{b3} - \vartheta_{b2})\right) \tag{3.58}$$

$$m = c\frac{\frac{l_{b2}}{t_{b2}}\frac{t_{b3}}{l_{b3}}}{den} \tag{3.59}$$

$$n = d\frac{\frac{l_{b2}}{t_{b2}}\frac{t_{b3}}{l_{b3}}}{den} \tag{3.60}$$

$$q = \frac{\frac{D}{2g}\frac{t_{b3}}{l_{b3}}}{den} \tag{3.61}$$

Then

$$U_{r3} = m\int_{\frac{\pi}{2p}-\vartheta_{b1}}^{\frac{\pi}{2p}+\vartheta_{b1}} U_s(\vartheta_r)d\vartheta_r + n\left(\int_{\frac{\pi}{2p}-\vartheta_{b2}}^{\frac{\pi}{2p}-\vartheta_{b1}} U_s(\vartheta_r)d\vartheta_r + \int_{\frac{\pi}{2p}+\vartheta_{b1}}^{\frac{\pi}{2p}+\vartheta_{b2}} U_s(\vartheta_r)d\vartheta_r\right) + q\left(\int_{\frac{\pi}{2p}-\vartheta_{b3}}^{\frac{\pi}{2p}-\vartheta_{b2}} U_s(\vartheta_r)d\vartheta_r + \int_{\frac{\pi}{2p}+\vartheta_{b2}}^{\frac{\pi}{2p}+\vartheta_{b3}} U_s(\vartheta_r)d\vartheta_r\right) + k_{pm3} \tag{3.62}$$

where the PMs contribution k_{pm3} is

$$k_{pm3} = \frac{\dfrac{k_{pm2}R_{b3}}{R_{b2}} - \phi_{rem2}R_{b3} + \phi_{rem3}R_{b3}}{den} \tag{3.63}$$

The computation of the integral of $U_s(\vartheta_r)$ in the arc of the rotor bordered by the air–gap and the inner flux–barrier results in

$$S_1 = \int_{\frac{\pi}{2p}-\vartheta_{b1}}^{\frac{\pi}{2p}+\vartheta_{b1}} U_s(\vartheta_r)d\vartheta_r = \sum_\nu -\frac{\hat{K}_\nu}{(\nu p)^2} D\big[\cos(\lambda_\nu)\sin(\nu p\vartheta_{b1})\big]$$

In the two arcs of rotor between the inner and the middle flux–barrier, it is

$$\begin{aligned} S_2 &= \int_{\frac{\pi}{2p}-\vartheta_{b2}}^{\frac{\pi}{2p}-\vartheta_{b1}} U_s(\vartheta_r)d\vartheta_r + \int_{\frac{\pi}{2p}+\vartheta_{b1}}^{\frac{\pi}{2p}+\vartheta_{b2}} U_s(\vartheta_r)d\vartheta_r \\ &= \sum_\nu -\frac{\hat{K}_\nu}{(\nu p)^2} D\cos(\lambda_\nu)\big[\sin(\nu p\vartheta_{b2}) - \sin(\nu p\vartheta_{b1})\big] \end{aligned}$$

In the two arcs of rotor between the middle and the outer flux–barrier, it is

$$\begin{aligned} S_3 &= \int_{\frac{\pi}{2p}-\vartheta_{b3}}^{\frac{\pi}{2p}-\vartheta_{b2}} U_s(\vartheta_r)d\vartheta_r + \int_{\frac{\pi}{2p}+\vartheta_{b2}}^{\frac{\pi}{2p}+\vartheta_{b3}} U_s(\vartheta_r)d\vartheta_r \\ &= \sum_\nu -\frac{\hat{K}_\nu}{(\nu p)^2} D\cos(\lambda_\nu)\big[\sin(\nu p\vartheta_{b3}) - \sin(\nu p\vartheta_{b2})\big] \end{aligned}$$

Therefore, the rotor magnetic potential U_{r3} results in

$$\begin{aligned} U_{r3} =& mS_1 + nS_2 + qS_3 + k_{pm3} = \\ =& \sum_\nu \frac{\hat{K}_\nu}{(\nu p)^2} D\Big[- m\cos(\lambda_\nu)\sin(\nu p\vartheta_{b1}) - n\cos(\lambda_\nu)[\sin(\nu p\vartheta_{b2}) - \sin(\nu p\vartheta_{b1})] - \\ & - q\cos(\lambda_\nu)[\sin(\nu p\vartheta_{b3}) - \sin(\nu p\vartheta_{b2})]\Big] + k_{pm3} \\ =& -\sum_\nu \frac{\hat{K}_\nu}{(\nu p)^2} D\cos(\lambda_\nu)\Big[(m-n)\sin(\nu p\vartheta_{b1}) + (n-q)\sin(\nu p\vartheta_{b2}) + q\sin(\nu p\vartheta_{b3})\Big] \\ & + k_{pm3} \end{aligned} \tag{3.64}$$

Consequently the magnetic potential U_{r2} is

$$\begin{aligned} U_{r2} =& cS_1 + dS_2 + k_{pm2} + zU_{r3} = \\ =& -\sum_\nu \frac{\hat{K}_\nu}{(\nu p)^2} D\cos(\lambda_\nu)\Big[(c - d + z(m-n))\sin(\nu p\vartheta_{b1}) + \\ & + (d + z(n-q))\sin(\nu p\vartheta_{b2}) + qz\sin(\nu p\vartheta_{b3})\Big] + k_{pm2} + zk_{pm3} \end{aligned} \tag{3.65}$$

and the magnetic potential U_{r1} is

$$\begin{aligned} U_{r1} =& aS_1 + bU_{r2} + k_{pm1} = \\ =& -\sum_{\nu} \frac{\hat{K}_\nu}{(\nu p)^2} D\cos(\lambda_\nu)\Big[(a + b(c - d + z(m - n)))\sin(\nu p\vartheta_{b1}) + \\ &+ (b(d + z(n - q)))\sin(\nu p\vartheta_{b2}) + bzq\sin(\nu p\vartheta_{b2})\Big] + k_{pm1} + bk_{pm2} + bzk_{pm3} \end{aligned} \tag{3.66}$$

Equations (3.64), (3.65) and (3.66) can be rewritten in a more compact form, observing that the terms within the square brackets are function of the motor geometry only, yielding

$$U_{r1} = -\sum_{\nu} \frac{\hat{K}_\nu}{(\nu p)^2} D\rho_1 \cos\lambda_\nu + k_{pm1} + bk_{pm2} + bzk_{pm3} \tag{3.67}$$

$$U_{r2} = -\sum_{\nu} \frac{\hat{K}_\nu}{(\nu p)^2} D\rho_2 \cos\lambda_\nu + k_{pm2} + zk_{pm3} \tag{3.68}$$

$$U_{r3} = -\sum_{\nu} \frac{\hat{K}_\nu}{(\nu p)^2} D\rho_3 \cos\lambda_\nu + k_{pm3} \tag{3.69}$$

where

$$\begin{aligned} \rho_1 &= (a + b(c - d + z(m - n)))\sin(\nu p\vartheta_{b1}) + (b(d + z(n - q)))\sin(\nu p\vartheta_{b2}) \\ &\quad + bzq\sin(\nu p\vartheta_{b2}) \end{aligned} \tag{3.70}$$

$$\begin{aligned} \rho_2 &= (c - d + z(m - n))\sin(\nu p\vartheta_{b1}) + (d + z(n - q))\sin(\nu p\vartheta_{b2}) \\ &\quad + qz\sin(\nu p\vartheta_{b3}) \end{aligned} \tag{3.71}$$

$$\rho_3 = (m - n)\sin(\nu p\vartheta_{b1}) + (n - q)\sin(\nu p\vartheta_{b2}) + q\sin(\nu p\vartheta_{b3}) \tag{3.72}$$

In addition it is possible to rewrite the coefficients k_{pm1}, k_{pm2}, and k_{pm3} in a more smart form:

$$k_{pm1} = b(\mu_{r1}h_{m1}H_{c1}) \cdot \frac{t_{b1}}{l_{b1}} \tag{3.73}$$

$$k_{pm2} = z\Big[(b - 1)\mu_{r1}h_{m1}H_{c1} + \mu_{r2}h_{m2}H_{c2}\Big] \cdot \frac{t_{b2}}{l_{b2}} \tag{3.74}$$

$$k_{pm3} = \frac{z(b - 1)\mu_{r1}h_{m1}H_{c1} + (z - 1)\mu_{r2}h_{m2}H_{c2} + \mu_{r3}h_{m3}H_{c3}}{den} \cdot \frac{t_{b3}}{l_{b3}} \tag{3.75}$$

3.5.2. Torque computation

Applying the same considerations of the torque expression with one flux–barrier per pole, the motor torque is computed as

$$\tau_m = -\frac{D}{2}\int_0^{2\pi} B_g(\vartheta_r)K_s(\vartheta_r)\frac{D}{2}L_{stk}d\vartheta_r = \frac{\mu_0 D^2}{4g}\mathrm{L}_{stk}\int_0^{2\pi} -U_r(\vartheta_r)K_s(\vartheta_r)d\vartheta_r$$

Thus, in a simplified form, the torque is

$$\begin{aligned}
\tau_m = -\frac{pk_\tau}{2}\Bigg[&\int_{\frac{\pi}{2p}-\vartheta_{b3}}^{\frac{\pi}{2p}-\vartheta_{b2}} U_{r3}(\vartheta_r)K_s(\vartheta_r)d\vartheta_r + \int_{\frac{\pi}{2p}-\vartheta_{b2}}^{\frac{\pi}{2p}-\vartheta_{b1}} U_{r2}(\vartheta_r)K_s(\vartheta_r)d\vartheta_r + \\
&+ \int_{\frac{\pi}{2p}-\vartheta_{b1}}^{\frac{\pi}{2p}+\vartheta_{b1}} U_{r1}(\vartheta_r)K_s(\vartheta_r)d\vartheta_r + \int_{\frac{\pi}{2p}+\vartheta_{b1}}^{\frac{\pi}{2p}+\vartheta_{b2}} U_{r2}(\vartheta_r)K_s(\vartheta_r)d\vartheta_r + \\
&+ \int_{\frac{\pi}{2p}+\vartheta_{b2}}^{\frac{\pi}{2p}+\vartheta_{b3}} U_{r3}(\vartheta_r)K_s(\vartheta_r)d\vartheta_r\Bigg] \\
= \frac{k_\tau p}{2}\Bigg[&\sum_\nu \frac{\hat{K}_\nu}{(\nu p)^2}D\rho_2\cos\lambda_\nu \cdot \sum_\xi \hat{K}_\xi\left(\rho_3\int_{\frac{\pi}{2p}-\vartheta_{b3}}^{\frac{\pi}{2p}-\vartheta_{b2}}\sin\lambda_\xi d\vartheta_r + \ldots\right) - \\
&- \hat{K}_\xi\left(k_{pm3}\int_{\frac{\pi}{2p}-\vartheta_{b3}}^{\frac{\pi}{2p}-\vartheta_{b2}}\sin\lambda_\xi d\vartheta_r + \cdots\right)\Bigg]
\end{aligned} \tag{3.76}$$

where k_τ is defined in (3.22). The integrals along the arcs of the air–gap, bordered by the inner, middle and the outer flux–barriers, are given by

$$\begin{aligned}
\int_{\frac{\pi}{2p}-\vartheta_{b1}}^{\frac{\pi}{2p}+\vartheta_{b1}} \sin(\xi p\vartheta_r + (\xi-1)\omega_{me}t - \alpha_i^e) &= -\frac{1}{\xi p}\left[\cos(\lambda_\xi + \xi p\vartheta_{b1}) - \cos(\lambda_\xi - \xi p\vartheta_{b1})\right] \\
&= \frac{2}{\xi p}\sin\lambda_\xi\sin(\xi p\vartheta_{b1})
\end{aligned} \tag{3.77}$$

$$\int_{\frac{\pi}{2p}-\vartheta_{b2}}^{\frac{\pi}{2p}-\vartheta_{b1}} \sin(\cdots) + \int_{\frac{\pi}{2p}+\vartheta_{b1}}^{\frac{\pi}{2p}+\vartheta_{b2}} \sin(\cdots) = \frac{2}{\xi p}\sin\lambda_\xi\left[\sin(\xi p\vartheta_{b2}) - \sin(\xi p\vartheta_{b1})\right] \tag{3.78}$$

$$\int_{\frac{\pi}{2p}-\vartheta_{b3}}^{\frac{\pi}{2p}-\vartheta_{b2}} \sin(\cdots) + \int_{\frac{\pi}{2p}+\vartheta_{b2}}^{\frac{\pi}{2p}+\vartheta_{b3}} \sin(\cdots) = \frac{2}{\xi p}\sin\lambda_\xi\left[\sin(\xi p\vartheta_{b3}) - \sin(\xi p\vartheta_{b2})\right] \tag{3.79}$$

that substituted in (3.76) yield the final formulation of the torque

$$\begin{aligned}\tau_m =& k_\tau \sum_\nu \frac{\hat{K}_\nu}{(\nu p)^2} \cos\lambda_\nu \sum_\xi \frac{\hat{K}_\xi}{\xi} \sin\lambda_\xi \Big[(\rho_1 - \rho_2)\sin(\xi p \vartheta_{b1}) + \\ &+ (\rho_2 - \rho_3)\sin(\xi p \vartheta_{b2}) + \rho_3 \sin(\xi p \vartheta_{b3}) \Big] - \\ &- k_\tau \sum_\xi \frac{\hat{K}_\xi}{\xi} \sin\lambda_\xi \Big[(k_{pm1} + (b-1)k_{pm2} + z(b-1)k_{pm3})\sin(\xi p \vartheta_{b1}) + \\ &+ (k_{pm2} + (z-1)k_{pm3})\sin(\xi p \vartheta_{b2}) + + k_{pm3}\sin(\xi p \vartheta_{b3}) \Big] \end{aligned} \quad (3.80)$$

3.6. Rotor with four flux–barriers per pole

3.6.1. Rotor magnetic potentials

According to a rotor with four flux–barriers per pole, the magnetic lumped–parameter network shown in Fig. 3.11 is adopted. The subscript "1" will be used for the inner flux–barrier, subscript "2" will be used for the first middle flux–barrier, subscript "3" will be used for the second middle flux–barrier, and finally the subscript "4" will be used for the outer flux–barrier. The components of the network are basically the same of the one shown in Fig. 3.8.

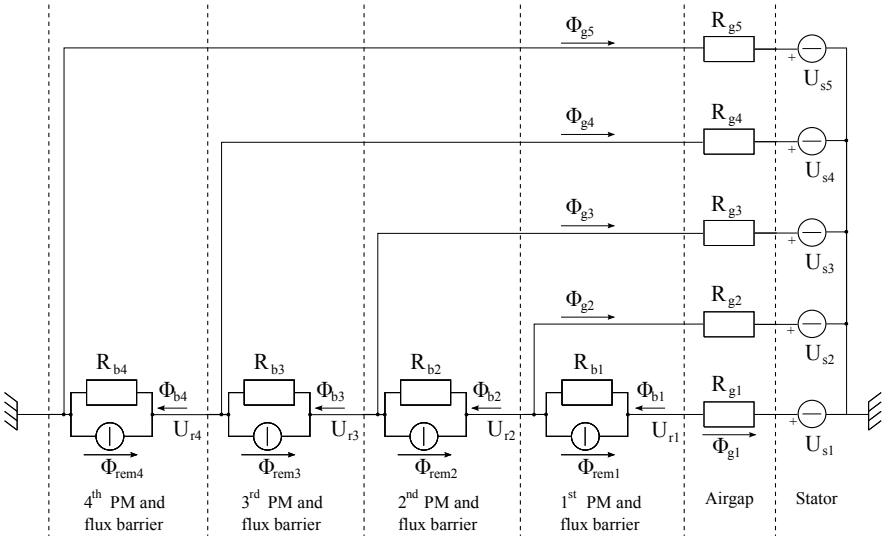

Figure 3.11: Magnetic network of IPM motor with four flux–barriers per pole.

As above, the flux due to the PM of each flux–barrier is defined as

$$\phi_{rem} = B_{rem} h_m L_{stk} = \mu_0 \mu_r H_c h_m L_{stk} \quad (3.81)$$

where ϕ_{rem}, h_m, μ_r, and H_c are respectively the remanent flux, the length, the relative permeability and the coercitive force of each flux–barrier (subscripts 1, 2, 3 and 4).

The electric load and the stator magnetic potential are defined respectively from (3.4) and (3.2). The magnetic potential of the rotor "island" bordered by the inner flux–barrier is

$$U_{r1} = a \int_{\frac{\pi}{2p}-\vartheta_{b1}}^{\frac{\pi}{2p}+\vartheta_{b1}} U_s(\vartheta_r)d\vartheta_r + k_{pm1} + bU_{r2} \tag{3.82}$$

where k_{pm1}, a and b have been already defined in section 3.3. The magnetic potential of the rotor "island" bordered by the second and third flux–barrier is

$$\begin{aligned} U_{r2} = c \int_{\frac{\pi}{2p}-\vartheta_{b1}}^{\frac{\pi}{2p}+\vartheta_{b1}} U_s(\vartheta_r)d\vartheta_r + d\Big(\int_{\frac{\pi}{2p}-\vartheta_{b2}}^{\frac{\pi}{2p}-\vartheta_{b1}} U_s(\vartheta_r)d\vartheta_r + \\ + \int_{\frac{\pi}{2p}+\vartheta_{b1}}^{\frac{\pi}{2p}+\vartheta_{b2}} U_s(\vartheta_r)d\vartheta_r \Big) + k_{pm2} + zU_{r3} \end{aligned} \tag{3.83}$$

where k_{pm2} is defined in (3.31). The magnetic potential of the rotor "island" bordered by the third and the fourth flux–barrier is:

$$U_{r3} = (\phi_{b3} + \phi_{rem3})R_{b3} + U_{r4} \tag{3.84}$$

Letting y equal to

$$y = \frac{1}{1 - (z-1)\frac{l_{b2}}{t_{b2}}\frac{t_{b3}}{l_{b3}} + \frac{D}{g}\frac{t_{b3}}{l_{b3}}(\vartheta_{b3} - \vartheta_{b2})} \tag{3.85}$$

the magnetic potential U_{r3} becomes

$$\begin{aligned} U_{r3} =& m \int_{\frac{\pi}{2p}-\vartheta_{b1}}^{\frac{\pi}{2p}+\vartheta_{b1}} U_s(\vartheta_r)d\vartheta_r + n \left(\int_{\frac{\pi}{2p}-\vartheta_{b2}}^{\frac{\pi}{2p}-\vartheta_{b1}} U_s(\vartheta_r)d\vartheta_r + \int_{\frac{\pi}{2p}+\vartheta_{b1}}^{\frac{\pi}{2p}+\vartheta_{b2}} U_s(\vartheta_r)d\vartheta_r \right) \\ &+ q \left(\int_{\frac{\pi}{2p}-\vartheta_{b3}}^{\frac{\pi}{2p}-\vartheta_{b2}} U_s(\vartheta_r)d\vartheta_r + \int_{\frac{\pi}{2p}+\vartheta_{b2}}^{\frac{\pi}{2p}+\vartheta_{b3}} U_s(\vartheta_r)d\vartheta_r \right) + k_{pm3} + yU_{r4} \end{aligned} \tag{3.86}$$

The magnetic potential of the rotor "island" bordered by the outer (fourth) flux–barrier is computed by means of the flux crossing through the flux–barrier itself, which is:

$$\begin{aligned} U_{r4} &= (\phi_{b3} + \phi_{rem4})R_{b4} \\ &= \Big(\phi_{b3} + \int_{\frac{\pi}{2p}-\vartheta_{b4}}^{\frac{\pi}{2p}-\vartheta_{b3}} -B_g(\vartheta_r)\frac{L_{stk}D}{2}d\vartheta_r + \\ &+ \int_{\frac{\pi}{2p}+\vartheta_{b3}}^{\frac{\pi}{2p}+\vartheta_{b4}} -B_g(\vartheta_r)\frac{L_{stk}D}{2}d\vartheta_r + \phi_{rem4} \Big) \frac{t_{b4}}{\mu_0 L_{stk} l_{b4}} \end{aligned} \tag{3.87}$$

with

$$\phi_{b3} = \frac{U_{r3} - U_{r4}}{R_{b3}} - \phi_{rem3} \tag{3.88}$$

$$B_g = \mu_0 \frac{(-U_s(\vartheta_r) + U_{r4})}{g} \tag{3.89}$$

Thus

$$U_{r3} = \Bigg[m\frac{l_{b3}}{t_{b3}} \int_{\frac{\pi}{2p}-\vartheta_{b1}}^{\frac{\pi}{2p}+\vartheta_{b1}} U_s(\vartheta_r)d\vartheta_r + n\frac{l_{b3}}{t_{b3}} \left(\int_{\frac{\pi}{2p}-\vartheta_{b2}}^{\frac{\pi}{2p}-\vartheta_{b1}} U_s(\vartheta_r)d\vartheta_r + \int_{\frac{\pi}{2p}+\vartheta_{b1}}^{\frac{\pi}{2p}+\vartheta_{b2}} U_s(\vartheta_r)d\vartheta_r \right) +$$
$$+ q\frac{l_{b3}}{t_{b3}} \left(\int_{\frac{\pi}{2p}-\vartheta_{b3}}^{\frac{\pi}{2p}-\vartheta_{b2}} U_s(\vartheta_r)d\vartheta_r + \int_{\frac{\pi}{2p}+\vartheta_{b2}}^{\frac{\pi}{2p}+\vartheta_{b3}} U_s(\vartheta_r)d\vartheta_r \right) + (y-1)\frac{l_{b3}}{t_{b3}}U_{r4} +$$
$$+ \frac{D}{2g}\Big(\int_{\frac{\pi}{2p}-\vartheta_{b4}}^{\frac{\pi}{2p}-\vartheta_{b3}} U_s(\vartheta_r)d\vartheta_r + \int_{\frac{\pi}{2p}+\vartheta_{b3}}^{\frac{\pi}{2p}+\vartheta_{b4}} U_s(\vartheta_r)d\vartheta_r \Big) -$$
$$- \frac{D}{2g}U_{r4}\Big((\vartheta_{b4}-\vartheta_{b3}) + (\vartheta_{b4}-\vartheta_{b3}) \Big) \Bigg] \frac{t_{b4}}{l_{b4}} + \frac{k_{pm3}R_{b4}}{R_{b3}} - \phi_{rem3}R_{b4} + \phi_{rem4}R_{b4} \tag{3.90}$$

U_{r4} depends only from the geometric coefficients r, s, t, u, and the $U_s(\vartheta_r)$ integral along the given arc of the air–gap. The dimensionless coefficients are:

$$den4 = \left(1 - (y-1)\frac{l_{b3}}{t_{b3}}\frac{t_{b4}}{l_{b4}} + \frac{D}{g}\frac{t_{b4}}{l_{b4}}(\vartheta_{b4}-\vartheta_{b3}) \right) \tag{3.91}$$

$$r = m\frac{\frac{l_{b3}}{t_{b3}}\frac{t_{b4}}{l_{b4}}}{den4} \tag{3.92}$$

$$s = n\frac{\frac{l_{b3}}{t_{b3}}\frac{t_{b4}}{l_{b4}}}{den4} \tag{3.93}$$

$$t = q\frac{\frac{l_{b3}}{t_{b3}}\frac{t_{b4}}{l_{b4}}}{den4} \tag{3.94}$$

$$u = \frac{\frac{D}{2g}\frac{t_{b4}}{l_{b4}}}{den4} \tag{3.95}$$

Then

$$U_{r4} = r\int_{\frac{\pi}{2p}-\vartheta_{b1}}^{\frac{\pi}{2p}+\vartheta_{b1}} U_s(\vartheta_r)d\vartheta_r + s\left(\int_{\frac{\pi}{2p}-\vartheta_{b2}}^{\frac{\pi}{2p}-\vartheta_{b1}} U_s(\vartheta_r)d\vartheta_r + \int_{\frac{\pi}{2p}+\vartheta_{b1}}^{\frac{\pi}{2p}+\vartheta_{b2}} U_s(\vartheta_r)d\vartheta_r \right) +$$
$$+ t\left(\int_{\frac{\pi}{2p}-\vartheta_{b3}}^{\frac{\pi}{2p}-\vartheta_{b2}} U_s(\vartheta_r)d\vartheta_r + \int_{\frac{\pi}{2p}+\vartheta_{b2}}^{\frac{\pi}{2p}+\vartheta_{b3}} U_s(\vartheta_r)d\vartheta_r \right) +$$
$$+ u\left(\int_{\frac{\pi}{2p}-\vartheta_{b4}}^{\frac{\pi}{2p}-\vartheta_{b3}} U_s(\vartheta_r)d\vartheta_r + \int_{\frac{\pi}{2p}+\vartheta_{b3}}^{\frac{\pi}{2p}+\vartheta_{b4}} U_s(\vartheta_r)d\vartheta_r \right) + k_{pm4} \tag{3.96}$$

where the PMs contribution k_{pm4} is

$$k_{pm4} = \frac{\dfrac{k_{pm3}R_{b4}}{R_{b3}} - \phi_{rem3}R_{b4} + \phi_{rem4}R_{b4}}{den4} \tag{3.97}$$

The computation of the integral of $U_s(\vartheta_r)$ in the arc of the rotor bordered named S_1, S_2 and S_3 are the same of the previous sections. It remains the integral on the two arcs of rotor between the third and the fourth flux–barrier, that is

$$\begin{aligned} S_4 &= \int_{\frac{\pi}{2p}-\vartheta_{b4}}^{\frac{\pi}{2p}-\vartheta_{b3}} U_s(\vartheta_r)d\vartheta_r + \int_{\frac{\pi}{2p}+\vartheta_{b3}}^{\frac{\pi}{2p}+\vartheta_{b4}} U_s(\vartheta_r)d\vartheta_r \\ &= \sum_{\nu} -\frac{\hat{K}_\nu}{(\nu p)^2} D\cos(\lambda_\nu)\big[\sin(\nu p\vartheta_{b4}) - \sin(\nu p\vartheta_{b3})\big] \end{aligned}$$

Therefore, the rotor magnetic potential U_{r4} after some manipulations results in the compact form

$$\begin{aligned} U_{r4} =& rS_1 + sS_2 + tS_3 + uS_4 + k_{pm4} = \\ =& -\sum_{\nu} \frac{\hat{K}_\nu}{(\nu p)^2} D\rho_4 \cos\lambda_\nu + k_{pm4} \end{aligned} \tag{3.98}$$

Consequently the magnetic potential U_{r3} is

$$\begin{aligned} U_{r3} =& mS_1 + nS_2 + qS_3 + k_{pm3} + yU_{r4} = \\ =& -\sum_{\nu} \frac{\hat{K}_\nu}{(\nu p)^2} D\rho_3 \cos\lambda_\nu + k_{pm3} + yk_{pm4} \end{aligned} \tag{3.99}$$

while the magnetic potential U_{r2} is

$$\begin{aligned} U_{r2} =& cS_1 + dS_2 + k_{pm2} + zU_{r3} = \\ =& -\sum_{\nu} \frac{\hat{K}_\nu}{(\nu p)^2} D\rho_2 \cos\lambda_\nu + k_{pm2} + zk_{pm3} + zyk_{pm4} \end{aligned} \tag{3.100}$$

and the magnetic potential U_{r1} is

$$\begin{aligned} U_{r1} =& aS_1 + k_{pm1} + bU_{r2} = \\ =& -\sum_{\nu} \frac{\hat{K}_\nu}{(\nu p)^2} D\rho_1 \cos\lambda_\nu + k_{pm1} + bk_{pm2} + bzk_{pm3} + bzyk_{pm4} \end{aligned} \tag{3.101}$$

The coefficients ρ_1, ρ_2, ρ_3, and ρ_4 are

$$\begin{aligned}
\rho_1 &= \Big[a + b\Big(c - d + z\big(m - n + y(r-s)\big)\Big)\Big]\sin(\nu p\vartheta_{b1}) + \\
&\quad + b\Big[d + z\big(n - q + y(s-y)\big)\Big]\sin(\nu p\vartheta_{b2}) + \\
&\quad + bz\big(q + y(t-u)\big)\sin(\nu p\vartheta_{b3}) + bzyu\sin(\nu p\vartheta_{b4}) \qquad (3.102)\\
\rho_2 &= \Big[c - d + z\big(m - n + y(r-s)\big)\Big]\sin(\nu p\vartheta_{b1}) + \\
&\quad + \Big[d + z\big(n - q + y(s-t)\big)\Big]\sin(\nu p\vartheta_{b2}) + \\
&\quad + z\big(q + y(t-u)\big)\sin(\nu p\vartheta_{b3}) + zyu\sin(\nu p\vartheta_{b4}) \qquad (3.103)\\
\rho_3 &= \big(m - n + y(r-s)\big)\sin(\nu p\vartheta_{b1}) + \big(n - q + y(s-t)\big)\sin(\nu p\vartheta_{b2}) + \\
&\quad + \big(q + y(t-u)\big)\sin(\nu p\vartheta_{b3}) + yu\sin(\nu p\vartheta_{b4}) \qquad (3.104)\\
\rho_4 &= (r-s)\sin(\nu p\vartheta_{b1}) + (s-t)\sin(\nu p\vartheta_{b2}) + \\
&\quad + (t-u)\sin(\nu p\vartheta_{b3}) + u\sin(\nu p\vartheta_{b4}) \qquad (3.105)
\end{aligned}$$

Finally it is possible to rewrite the coefficients k_{pm1}, k_{pm2}, k_{pm3} in a more elegant form showing the effect of each PM buried inside the different flux–barrier:

$$\begin{aligned}
k_{pm1} &= b(\mu_{r1}h_{m1}H_{c1}) \cdot \frac{t_{b1}}{l_{b1}} \qquad (3.106)\\
k_{pm2} &= z\Big[(b-1)\mu_{r1}h_{m1}H_{c1} + \mu_{r2}h_{m2}H_{c2}\Big] \cdot \frac{t_{b2}}{l_{b2}} \qquad (3.107)\\
k_{pm3} &= y\Big[z(b-1)\mu_{r1}h_{m1}H_{c1} + (z-1)\mu_{r2}h_{m2}H_{c2} + \mu_{r3}h_{m3}H_{c3}\Big] \cdot \frac{t_{b3}}{l_{b3}} \qquad (3.108)\\
k_{pm4} &= \frac{yz(b-1)\mu_{r1}h_{m1}H_{c1} + y(z-1)\mu_{r2}h_{m2}H_{c2} + (y-1)\mu_{r3}h_{m3}H_{c3} + \mu_{r4}h_{m4}H_{c4}}{den4} \cdot \frac{t_{b4}}{l_{b4}} \qquad (3.109)
\end{aligned}$$

3.6.2. Torque computation

Applying the same considerations of the torque expression with one flux–barrier per pole, the motor torque is computed as

$$\tau_m = -\frac{D}{2}\int_0^{2\pi} B_g(\vartheta_r)K_s(\vartheta_r)\frac{D}{2}L_{stk}d\vartheta_r = \frac{\mu_0 D^2}{4g}\text{L}_{stk}\int_0^{2\pi} -U_r(\vartheta_r)K_s(\vartheta_r)d\vartheta_r$$

Thus applying all the simplifications above the torque expression is computed after

several manipulations results in

$$\begin{aligned}\tau_m =& k_\tau \sum_\nu \frac{\hat{K}_\nu}{(\nu p)^2} \cos\lambda_\nu \sum_\xi \frac{\hat{K}_\xi}{\xi} \sin\lambda_\xi \Big[(\rho_1-\rho_2)\sin(\xi p\vartheta_{b1})+ \\ &+(\rho_2-\rho_3)\sin(\xi p\vartheta_{b2})+(\rho_3-\rho_4)\sin(\xi p\vartheta_{b3})+\rho_3\sin(\xi p\vartheta_{b4})\Big]- \\ &- k_\tau \sum_\xi \frac{\hat{K}_\xi}{\xi}\sin\lambda_\xi \\ &\Big[\big(k_{pm1}+(b-1)k_{pm2}+z(b-1)k_{pm3}+yz(b-1)k_{pm4}\big)\sin(\xi p\vartheta_{b1})+ \\ &+\big(k_{pm2}+(z-1)k_{pm3}+y(z-1)k_{pm4}\big)\sin\lambda_\xi\sin(\xi p\vartheta_{b2})+ \\ &+\big(k_{pm3}+(y-1)k_{pm4}\big)\sin(\xi p\vartheta_{b3})+k_{pm4}\sin(\xi p\vartheta_{b4})\Big] \end{aligned} \tag{3.110}$$

Chapter 4

Torque ripple reduction

This chapter presents the application of the analytic model of the anisotropic machine to select the flux–barrier angles in order to minimize the torque ripple. The analytical model results are compared with suitable finite elements simulations. Examples of torque minimization with one and two flux–barrier rotor pole geometry are reported. The results of the model are in good agreement with those obtained applying an existing patent. Finally the results of a stochastic optimizer that adopts the analytical model, are reported.

4.1. FE model for comparison

FOR the sake of a correct comparison, the results of the analytical model has to be compared with a simplified finite element model sketched in Fig. 4.1. The simplifications are:

- the stator slot is schematized by means of a conductive sheet with a number of points equal to the slot number,
- the current of each current point is changed according to the rotor position ϑ_m,
- the iron lamination has a linear behaviour,
- the mechanical ribs of the rotor flux–barrier, due to mechanical constrains, are replaced with air.

This simplified structure simulates the geometrical and physical conditions considered in the model. Fig. 4.2 reports some examples of comparison between analytical results and simplified FE simulations with 2, 3 and 4 flux–barrier per pole rotor geometries. It is possible to recognize a very good agreement between the analytical model and the FE simplified model.

The computations carried out by means of the analytical model does not allow to predict exactly the average torque and the torque ripple of the machine but it is very useful to evaluate the geometries yielding the minimum torque ripple. In fact, it

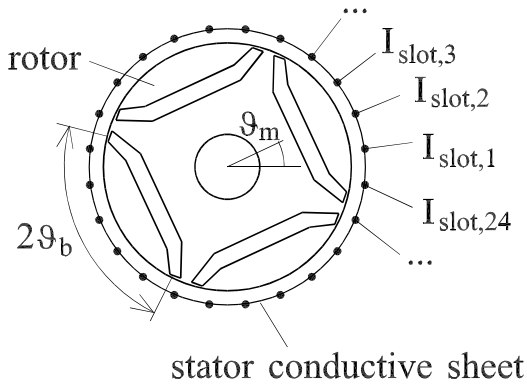

Figure 4.1: Stator conductive sheet with 24 current points

has been verified with FEA that the analytic minimums corresponds to torque ripple minima of the model with the actual geometry and materials (saturated iron lamination) [33, 34].

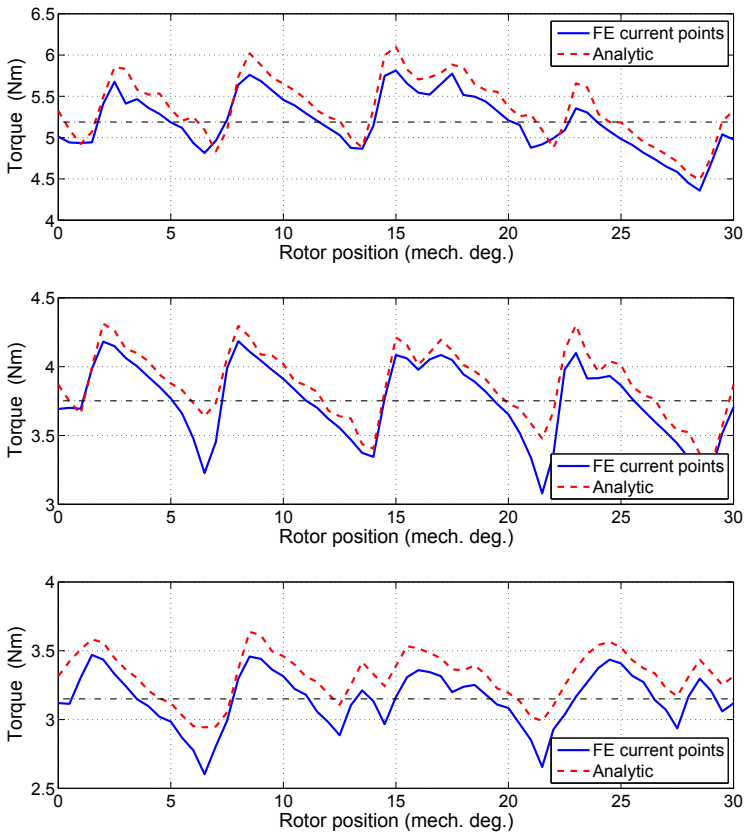

Figure 4.2: Torque vs. rotor position: (a) two, (b) three, (c) four flux–barrier per pole IPM rotor geometry.

4.2. Analytical analysis

4.2.1. Rotor with one flux–barrier per pole

The key design hint for torque minimization is based on the following remark. Considering the torque harmonic of different order separately, it is found that the torque ripple varies according to the position of the flux–barrier ends, i.e. according to ϑ_b^e.

From the analytical model it is possible to verify that the torque ripple components vary with the time due to the dependence of λ_ν on the time. Each single harmonic of the torque ripple behaviour exhibits some minima (theoretically equal to zero).

Referring to a 24–slot 4–pole synchronous reluctance machine with a rotor provided of one flux–barrier per pole, the amplitude of the peak–to–peak torque ripple due to the interaction among the electrical loading harmonics of different order is shown in Fig. 4.3. It could be noted that the effect of the harmonics of order 5 and 7 is limited. Conversely, the higher torque ripple is due to the electrical loading harmonics of order 11 and 13 (the slot harmonics). Their pulsation is 12 order. The amplitude of the torque ripple terms varies with ϑ_b, reaching some maxima and minima.

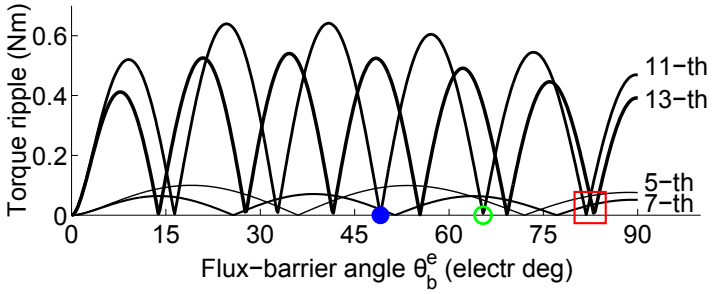

Figure 4.3: Torque ripple caused by different electrical loading harmonics

Since the simulated machine has a 2.5 Nm rated torque, it is evident that the choice of the flux–barrier angle is a thorough design step. From Fig. 4.3, a good design choice is a flux–barrier angle $\vartheta_b^e \simeq 82$ electrical degrees highlighted with the square □. This solution allows to achieve a low value of torque ripple.

Considering the different minima exhibited by the torque ripple components, it is possible to select for the harmonics yielding the higher torque ripple two minima that are almost in phase opposition. It should be noted that between two minima the phase of the torque ripple is almost the same, while between the two following minima the torque ripple is almost in phase opposition.

Applying this method it is possible to design a rotor characterized by different flux–barriers for different pole pairs. The resulting rotor configuration has been defined as the "**Machaon**" configuration [33]. Summarizing, the first flux–barrier angle is designed so as to have one harmonic with positive phase, while the second module is designed with flux–barrier angle so as to have the same harmonic with negative phase. The resulting motor produces a torque where the selected torque harmonics are almost compensated by the two geometries.

Table 4.1: Main data of the 48–slot 4–pole motor

D_e	=	460 mm	Stator external diameter
D	=	300 mm	Stator inner diameter
L_{stk}	=	400 mm	Stack length
g	=	1 mm	Air gap thickness
Vol_{PM1}	=	50 dm^3	PM volume in the inner barrier
Vol_{PM2}	=	75 dm^3	PM volume in the outer barrier

Referring to example of Fig. 4.3, in order to cancel the effect of the rotor magnetic potential harmonic of 11–th order the first flux–barrier has a barrier angle equal to ϑ_b^e=65.4 degrees (highlighted as •) while the second has a barrier angle equal to ϑ_b^e=49.1 degrees (highlighted as ◯).

Hence, the rotor magnetic potential harmonic of 13–th order produces a torque harmonic out of phase of 180 degrees for the two flux–barrier angles. Unfortunately the amplitude of the 13–th order harmonic in for the two flux–barrier angles is different. However, the combination of the two flux–barriers gives a torque with an almost null ripple of 12–th order. A residual torque ripple of 12–th order remains due to the different amplitudes of the single torque ripples, caused by the electrical loading harmonic of 13–th order.

4.2.2. Rotor with two flux–barriers per pole

Similarly, the torque ripple harmonics of a rotor with two flux–barriers per pole can be investigate with the analytic model. The results are reported by means of the constant–value curves in the plane (ϑ_{b1}/,ϑ_{b2}), that is generally referred as torque map.

A 48–slot 4–pole machine configuration is considered in this analysis. The machine requirements are suited for a traction motor drive in a commutator train for the Italian rail network. From the maximum available volume including the frame ($L_{fr} = 800\ m$, $D_{fr} = 550\ m$), the active dimensions of the machine considering medium voltage end winding are fixed as reported in Table 4.1. In order to achieve the high torque required NdFeB PMs are considered. From the analytical analysis several torque maps are obtained:

- Fig. 4.4 shows the average torque amplitude,
- Fig. 4.5 shows the torque ripple amplitude in per cent values,
- Fig. 4.6 shows the 6^{th} order torque harmonic,
- Fig. 4.7 shows the 12^{th} order torque harmonic,
- Fig. 4.8 shows the 24^{th} order torque harmonic,
- Fig. 4.9 shows the 36^{th} order torque harmonic,
- Fig. 4.10 shows the 48^{th} order torque harmonic,

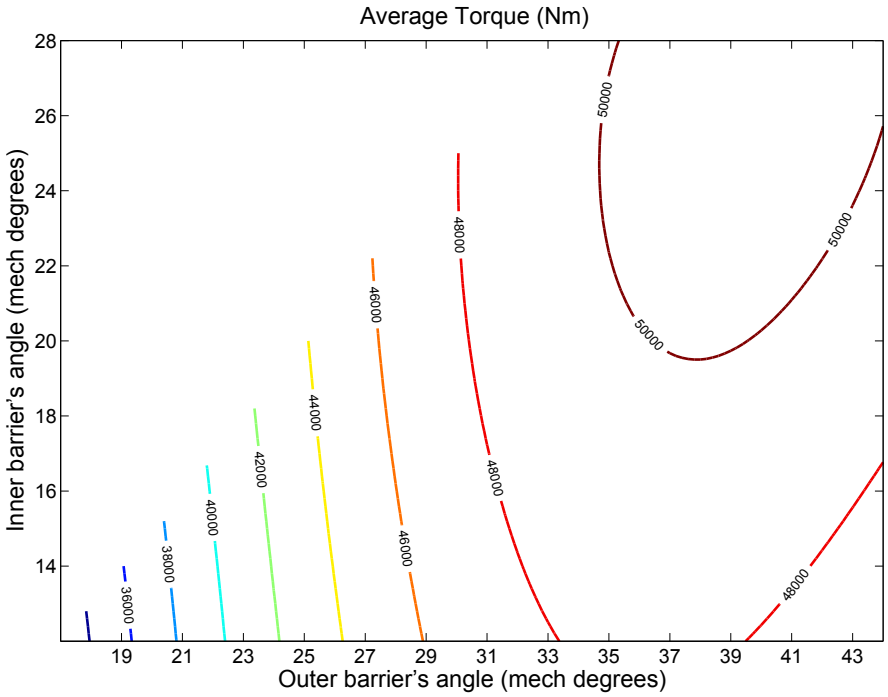

Figure 4.4: Map of the average torque

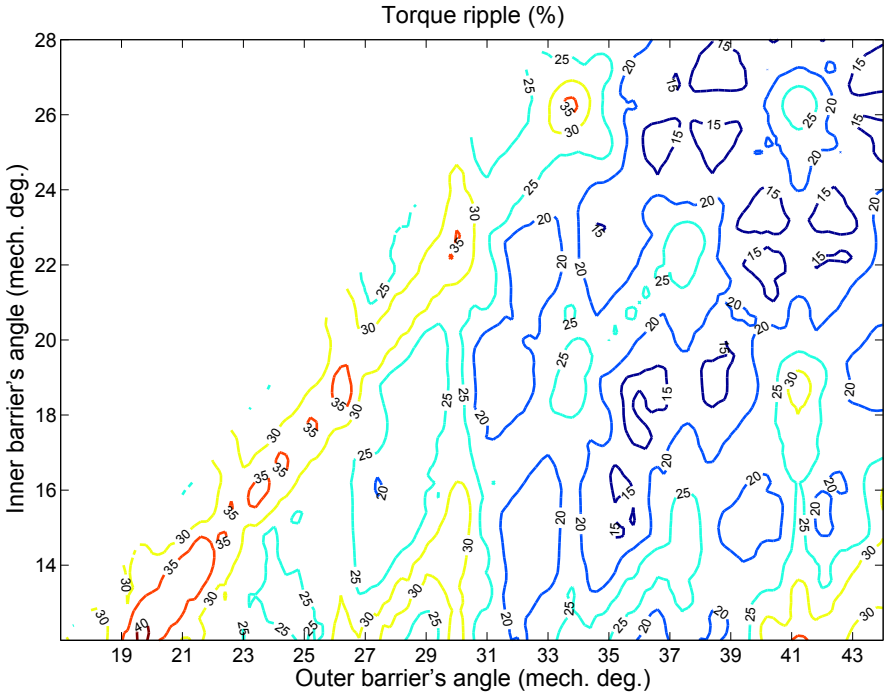

Figure 4.5: Map of the torque ripple

It could be noted that, in Fig. 4.4, the amplitude of the average torque increases

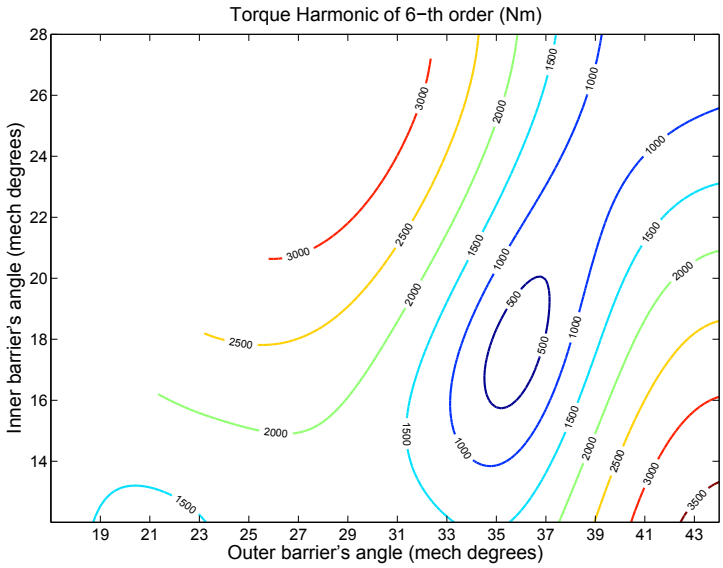

Figure 4.6: Map of torque harmonic of 6–th order

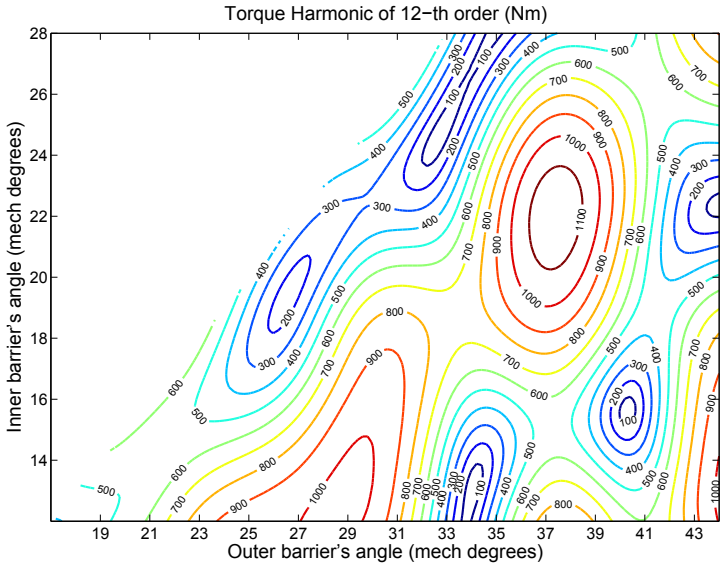

Figure 4.7: Map of torque harmonic of 12–th order

regularly, varying the angles ϑ_{b1} and ϑ_{b2}. However, the gradient is low: the flux–barrier angles have a limited influence on the average torque. The left side of the map is not taken into account, since values of $\vartheta_{b2} < \vartheta_{b1} + 5$ degrees have been not considered, to avoid that the two flux–barriers become too close one to the other.

Oppositely, a correct selection of the flux–barrier angles ϑ_{b1} and ϑ_{b2} is necessary in order to limit the torque ripple, as highlighted by Fig. 4.5. Fig. 4.6 to Fig. 4.10 highlight that each harmonic of the torque ripple shows a remarkable difference between the maximum and minimum values. Therefore, a limited variation of the flux–barrier

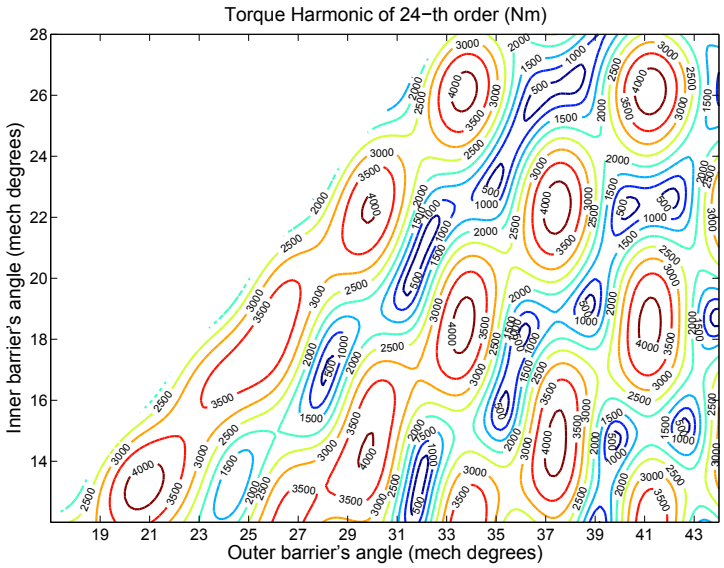

Figure 4.8: Design map of torque harmonic of 24–th order

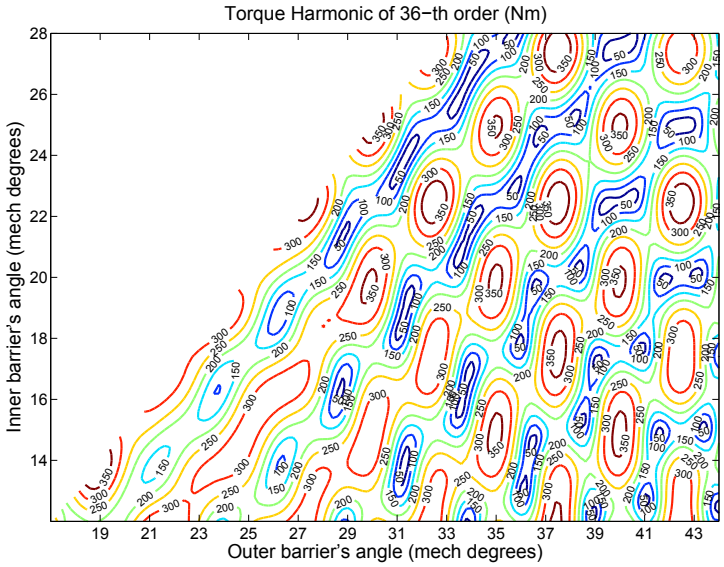

Figure 4.9: Design map of torque harmonic of 36–th order

angles causes a relevant variation of the high order harmonics amplitude.

The presented maps offer a valid help in the rotor design. It is possible to select directly those flux–barriers angle allowing the minima to be achieved in the corresponding Fig. 4.5. Or rather, as described above, the cancelation of one or more torque harmonics can be achieved adopting a "**machaon**" rotor structure (Fig. 4.11). This solution could be possible since, as one can observe from the design maps, there are several combinations of the two flux–barrier angles giving local or absolute minima.

Thus, in general it is possible to design the rotor with two different couples of

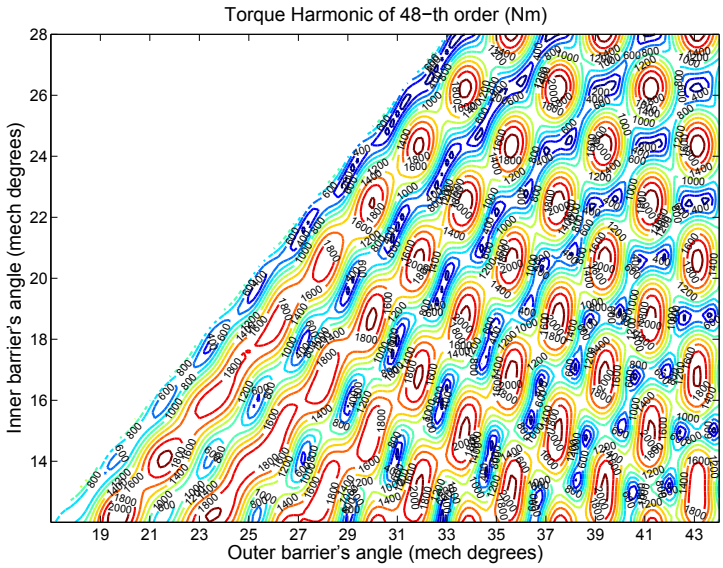

Figure 4.10: Design map of torque harmonic of 48–th order

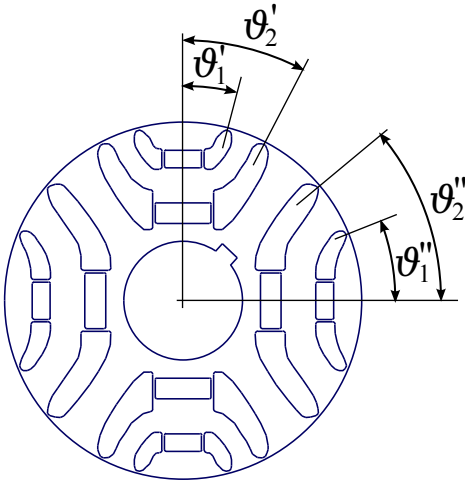

Figure 4.11: Example of rotor "Machaon" geometry with two flux–barrier per pole.

flux–barrier angle combinations. The two combinations are chosen in order to satisfy two constrains: (i) to cancel the torque harmonic of the same order, (i) to have same amplitude and opposite phase of another order of torque harmonic. Therefore, ideally both the selected order of torque harmonic are canceled. Even if the second constrain is not completely satisfied the corresponding torque harmonic order is minimized [33,34].

4.3. Comparison with a different technique of ripple minimization

In the field of torque ripple minimization for synchronous reluctance machines a relevant method has been presented by Vagati et al in the second part of 90s [36]. This method has been patented in Europe and US in the same year [38].

This method provides a very simple design criterion that correlates the rotor separation points number n_r with the number of stator slots per pole pair n_s. It has been obtained analyzing the interaction of both stator and rotor spatial harmonics that involves the torque ripple.

In fact, the torque ripple is due to two types of rotor reaction. The first type of rotor reaction, that is the one giving an $n_s\theta_{me}$ pulsation, can be strongly reduced if n_r is chosen so that the spatial harmonics $n_s \pm 1$ and $n_r \pm 1$ are of different order. It should be noted that both n_s and n_r must be even and positive numbers. The second type of reaction, characterized by a pulsation $2n_s\theta_{me}$, is due to stator and rotor tooth pitches are near to each other. Also this reaction has to be minimized, .

The general design criterion [38] is:

$$n_r = n_s \pm 4 \tag{4.1}$$

As explained in [36, 38] the solution +4 gives a better result.

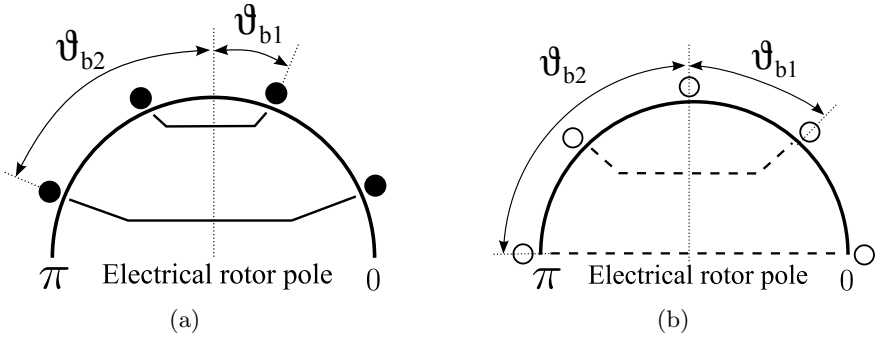

Figure 4.12: Synchronous reluctance rotor structure: (a) positive and (b) negative structure with $n_r = 8$.

The comparison between the patented model and the analytic model, presented in chapter 3 is limited to a synchronous motor provided with rotor with two flux–barriers per pole. Obliviously the rotor poles are equal one to each other, e.g. the "machaon" structure is not considered. A geometry with only two flux–barriers per pole has been selected since it allows a very rapid comparison of the patent results directly on the torque map obtained from the analytical model. A 24–slot 4–pole machine is selected, then the number of slots per pole results in $n_s = 12$. Both positive (Fig. 4.12(a)) and negative (Fig. 4.12(b)) rotor structure are considered. As sketched in Fig. 4.12(a) the rotor points individuates the flux–barrier angles. The rotor separation point number n_r refers to an electrical two poles machine, and thus it yields the angle span of each arc between two points. As an example in Fig. 4.12(a) with $n_r = 8$, the inner flux–barrier cover an angle equal to 45 electrical degrees and then the corresponding flux–barrier angle in the analytical model corresponds to 11.25 mechanical angles.

Table 4.2: Flux–barriers angles, for both positive and negative motor structure with $n_s = 12$, as a function of n_r.

n_r	Positive str.			Negative str.			Label
	θ_{b1} (mech. deg.)	θ_{b2} (mech. deg.)	ΔT (%)	θ_{b1} (mech. deg.)	θ_{b2} (mech. deg.)	ΔT (%)	
8	11.25	33.75	59	22.5	45	43	**A**
10	18	36	39	9	27	85	**B**
12	22.5	37.5	50	15	30	72	**C**
14	12.85	27.72	67	6.43	19.29	126	**D**
	12.85	38.57	44	6.43	32.14	67	**E**
	27.72	38.57	31	19.29	32.14	36	**F**
16	16.75	28.13	58	11.25	22.5	86	**G**
	16.75	39.38	33	11.25	33.75	59	**H**
	28.13	39.38	25	22.5	33.75	33	**I**
18	5	15	210	10	20	122	**J**
	5	25	154	10	30	84	**K**
	5	35	77	10	40	34	**L**
	15	25	65	20	30	63	**M**
	15	35	40	20	40	34	**N**
	25	35	35	30	40	34	**O**

The results reported in Table 4.2 refers to several values of the rotor separation number. The flux–barrier angles (ϑ_{b1},ϑ_{b2}) of both positive and negative structure are reported as well as the torque ripple ΔT computed using the analytical method. When the structure allows to have more than two flux–barriers, different combinations between them are considered in order to compare always the solutions with two flux–barriers per pole.

The torque ripple map (using per cent values) obtained with the analytical method is reported in Fig. 4.13(a) and Fig. 4.13(b) for positive and negative rotor structure respectively. On the torque ripple maps, the solutions of the patented method are highlighted by means of dots •.

As evaluated in [38] the best solution should have n_r equal to 16 ($n_r = n_s + 4$). This solution is verified in the analytic torque map since the combination labeled as **I** is located in one of the minimum regions for both positive and negative rotor structure. Therefore, it is confirmed that the two methods allow to achieve similar rotor geometry to solve the torque ripple issue. An interesting remark can be done observing the torque ripple map: similar results can be achieved with several combinations of flux–barrier angles since there are more than one minimum regions. This aspect could be very

useful in case of multi objective minimization, in particular in case of challenging goals (average torque, torque ripple, iron losses, etc).

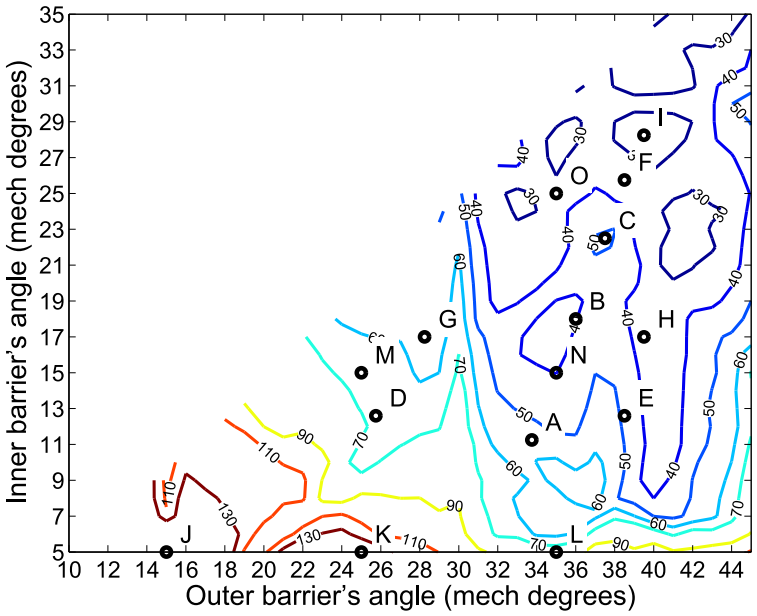

(a) Positive rotor structure

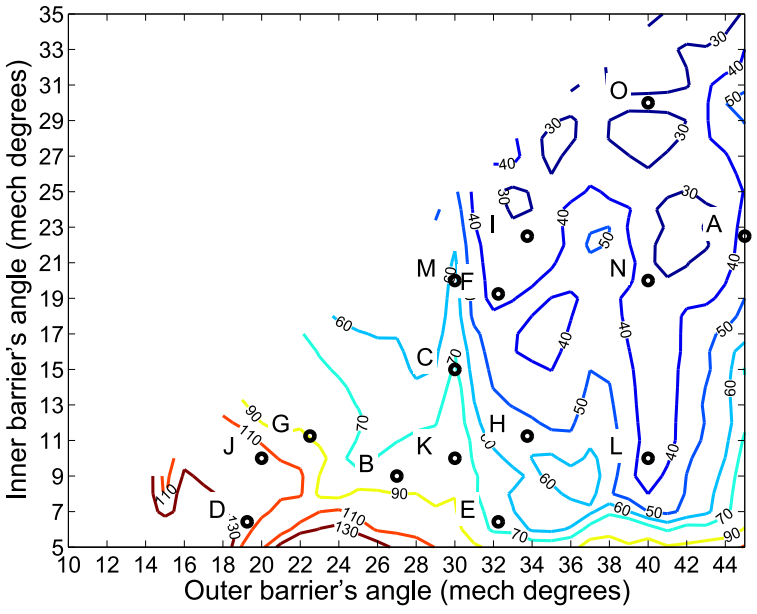

(b) Negative rotor structure

Figure 4.13: Maps of the torque ripple in per cent values: (a) positive and (b) negative rotor structure. The solutions of the patented method (Table 4.2) are highlighted by dots.

4.4. Implementation in an stochastic optimization

From the computations reported above, it has been noted that the most important rotor parameters are the flux–barrier angles [30]. However the best choice depends also on the number of poles, number of stator slots, winding arrangement, and PM volume, and thus it is not a trivial task to carry out manually through a trial–and–error method [39, 40].

Therefore, an optimizer is considered to solve the torque minimization problem. The optimizer is adopted as a flux–barrier angles generator, then if the selected combination of angles satisfy the mechanical constrains, the analytical model is solved. The results, as average torque and torque ripple, are store and the optimizer is run again considering the proper input of its algorithm.

The 24–slot 4–pole motor is adopted as a reference structure. Firstly the goal of the optimizer is the torque ripple minimization, evaluating both non–chorded and chorded winding. Then a multi–objective optimization has been carried out assuming as a additional goal the maximization of the average torque.

In the two flux–barrier per pole Machaon rotor arrangement , as of Fig. 4.11, the main degrees of freedom are the flux–barrier angles ϑ'_{b1}, ϑ'_{b2}, ϑ''_{b1} and ϑ''_{b2}. Thus the design problem can be cast as a scalar, four–parameter optimization problem.

The chosen optimizer is TRIBES [41], that is a variant of the Particle Swarm Optimization (PSO) meta–heuristic. PSO is a computational method that optimizes a problem by iteratively trying to improve a candidate solution with regard to a given measure of quality. Such methods are commonly known as meta–heuristics as they make few or no assumptions about the problem being optimized and can search very large spaces of candidate solutions. More specifically, PSO does not use the gradient of the problem being optimized. Therefore, PSO does not require for the optimization problem to be differentiable as is required by classic optimization methods such as gradient descent and quasi-Newton methods.

PSO optimizes a problem by having a population of candidate solutions, here dubbed particles, and moving these particles around in the search-space according to simple mathematical formulae. The movements of the particles are guided by the best found positions in the search-space which are updated as better positions are found by the particles.

Table 4.3: Main geometrical data of the 24–slot 4–pole motor adopted for the optimization with TRIBE.

D	=	70 mm	Stator inner diameter
L_{stk}	=	40 mm	Stack length
g	=	0.4 mm	Air gap thickness
p	=	2	Number of pole pairs
Q	=	24	Number of slots

While in classical PSO the topology and the type and quantity of social relation-

ships of the swarm are user–specified parameters, in TRIBES they evolve over time in response to performance feedback. With this modification PSO becomes a parameter–free algorithm greatly improving its robustness in solving arbitrary problems (at the cost of some efficiency to tackle a specific problem).

4.4.1. Comparison with finite element analysis

As a further comparison, Fig. 4.14 shows the FE results of different Machaon arrangement of flux barriers compared with the analytical ones. The results confirms a satisfactory agreement between analytical and FE analysis. The main difference is a slight reduction of the average torque with respect to the FE analysis, but the torque ripple remains the same, confirming the validity of the analytical formulation which can therefore be used within the optimization procedure.

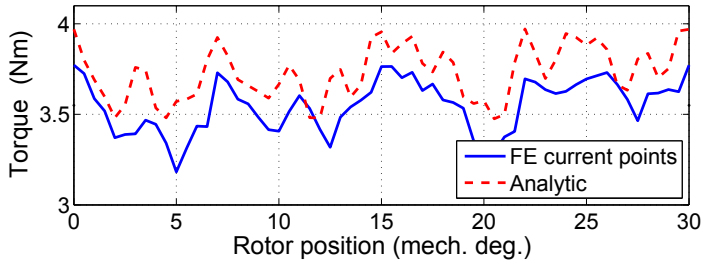

(a) ϑ'_{b1}=31.1°, ϑ'_{b2}=42.6° - ϑ''_{b1}=23.3°, ϑ''_{b2}=40.1°

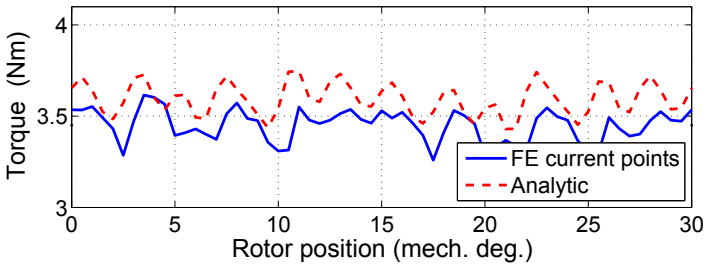

(b) ϑ'_{b1}=39.1°, ϑ'_{b2}=42.7° - ϑ''_{b1}=29.1°, ϑ''_{b2}=34.3°

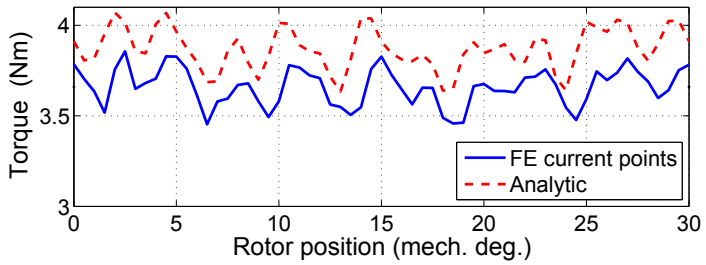

(c) ϑ'_{b1}=15.2°, ϑ'_{b2}=38.9° - ϑ''_{b1}=27.9°, ϑ''_{b2}=33.6°

Figure 4.14: Comparisons between analytical model and FE for different rotor flux–barrier angles combinations.

The highlighted torque overestimation of the analytical model can be explained as a consequence of the applied superimposition in the torque computation of the Machaon configuration. Since the analytical model considers only equal flux–barriers angle for

each rotor pole, the torque of the Machaon configuration is computed (for each rotor position θ_m) as the mean value of the two sets ϑ'_{b1}–ϑ'_{b2} and ϑ''_{b1}–ϑ''_{b2}. This procedure simplifies further the computation but neglects the potential difference among the pole flux. This is the fundamental cause of the average torque discrepancy.

4.4.2. The 24–slot 4–pole motor

All results refer to a motor whose data are reported in Table 4.3. The operating condition of the motor refers to a rms conductor current density of 6 A/mm^2 and a current phase α_i^e=45^o (i.e., d–axis current equal to q–axis current). Referring to a non–chorded winding [42]. The best solution found by the optimizer for the two sets of flux–barriers (M1 and M2) is:

M1 ϑ'_{b1}=28.0°, ϑ'_{b2}=34.1° **M2** ϑ''_{b1}=39.4°,ϑ''_{b2}=44.2°

with an average torque T_{avg} = 3.88 Nm and a torque ripple ΔT = 10.98%. Fig. 4.15 shows the torque behaviours vs. mechanical angle due to the first couple of barrier angles (ϑ'_{b1}, ϑ'_{b2}: Machaon 1), due to the second couple of barrier angles (ϑ''_{b1}, ϑ''_{b2}: Machaon 2), and the resulting total torque. The reduction of the torque ripple achieved by combining the effects of the two barriers is evident. The torque harmonic contents are shown in Fig. 4.16.

As noted above the final choice of the optimization process has the following interpretation: two sets of angles are chosen such that the torque harmonics of order 6 and 12 are quite low. In addition, they are chosen so that they are out of phase of 180°. Therefore, when the two torque components are considered together, the final solution exhibits almost zero torque harmonics of such orders.

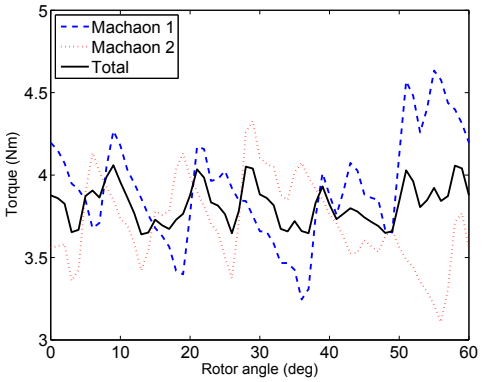

Figure 4.15: Torque vs. rotor angle (24–slot 4–pole motor, non–chorded).

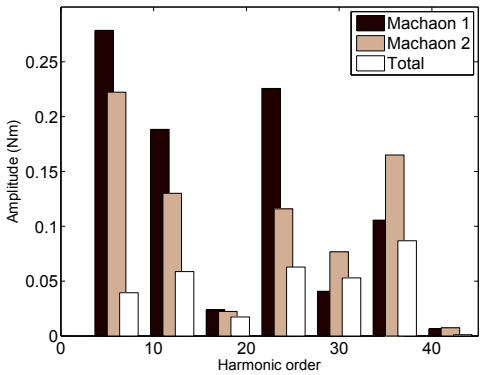

Figure 4.16: Torque harmonics (24–slot 4–pole motor, non–chorded).

An interesting comparison can be made with two flux barriers per pole having uniformly distributed tips obtained according to [38]. The angles are $\vartheta'_{b1} = \vartheta''_{b1}$=11.25° and $\vartheta'_{b2} = \vartheta''_{b2}$=33.75°. The average torque in this case is 3.74 Nm, which is similar to the one found by the optimizer. Conversely, the torque ripple is much higher at 41%. Another solution derived from [38] yields $\vartheta'_{b1} = \vartheta''_{b1}$=28.125° and $\vartheta'_{b2} = \vartheta''_{b2}$=39.375°. The average torque in this case is 3.99 Nm, once more similar to the one found by the optimizer, but the torque ripple is much higher at 31%.

Referring to a chorded winding with a pitch angle of 75 electrical degrees, the optimized solution is found with the following angles:

M1 ϑ'_{b1}=26.5°, ϑ'_{b2}=36.8° **M2** ϑ''_{b1}=39.8°, ϑ''_{b2}=44.0°

Fig. 4.17 shows the torque behaviours vs. rotor angle due to the first couple of barrier angles (ϑ'_{b1}, ϑ'_{b2}: Machaon 1), due to the second couple of barrier angles (ϑ''_{b1}, ϑ''_{b2}: Machaon 2), and the resulting total torque. The reduction of the torque ripple achieved by combining the effects of the two barriers is evident. The torque harmonic contents are shown in Fig. 4.18.

With chorded winding, the torque harmonics are lower than in the previous case, and thus the torque ripple of this Machaon IPM motor is extremely low. Also in this case the choice of the optimization algorithm can be interpreted. In fact, the fundamental harmonic and all the slot harmonics are only slightly reduced, while the other harmonics are much more. This is quantified by means of the pitch factor.

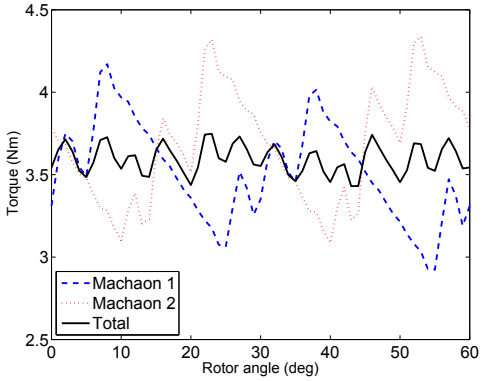

Figure 4.17: Torque vs. rotor angle (24–slot 4–pole motor, chorded).

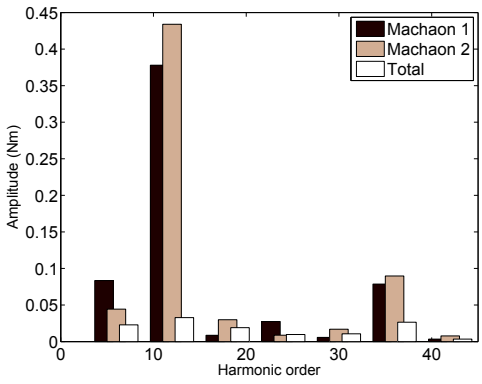

Figure 4.18: Torque harmonics (24–slot 4–pole motor, chorded).

The consequence of the reduction of the MMF harmonics yields a reduction of the corresponding torque harmonics. In the case of a 24–slot 4–pole motor, all torque harmonics which are multiples of six but not multiples of twelve (corresponding to the slot harmonics) are reduced by the chording. Taking advantage of the reduction of the former harmonics, the effort of the optimization process is mainly on selecting the flux barrier angles so as to reduce the harmonics multiple of twelve. This is evident in Fig. 4.18. The torque harmonics of sixth order are low for both the combinations with angles ϑ'_{b1}, ϑ'_{b2} and ϑ''_{b1}, ϑ''_{b2} (compare the amplitude of these harmonics with those of Fig. 4.16 referring to a non–chorded winding.) On the contrary, the torque harmonics of twelfth order are high for both angle combinations. However, these harmonics are out of phase of 180 degrees, so that their sum yields a drastic ripple reduction.

As a conclusion, the adoption of a chorded winding allows a reduction of all torque harmonics. In the example under study, chording allows to further reduce the torque ripple from 11% to 8.8%.

As introduced above, it has been evaluated that the thickness of the flux barriers has a very limited impact on both average torque and torque ripple. Variations of up to ±50% of the flux barrier thickness have been explored, finding that optimal angles differ slightly, but in all cases the average torque and the torque ripple remain equal

Table 4.4: Impact of the number of slots

	Q	β_r^e (degrees)	T_{avg} (Nm)	ΔT (%)
non-chorderd	24	0	3.82	10.98
	36	0	3.89	6.67
	48	0	3.74	4.50
chorded	24	30	3.59	8.83
	36	20	3.72	5.15
	48	15	3.74	3.27

to $T_{avg} = 3.9$ Nm and close to $\Delta T = 11\%$, respectively (with non–chorded winding). Once again the adoption of a chorded winding yields a reduction of the torque ripple to about 8.5%.

Variation of the number of slots and poles The number of stator slots has a major impact on the torque ripple. This is because the amplitudes of the MMF harmonics decrease as the number of slots per pole and per phase increase. In addition, the slot harmonics have a higher order. The impact of the number of slots, Q, is reported in Table 4.4 for to the 4–pole motor. Increasing the number of slots the torque ripple noticeably decreases. It results more than halved when Q is doubled. This has been found for both non–chorded and chorded windings. Table 4.4 reports the optimized torque values for different chording angles β_r^e (in electrical degrees). In addition, the effect of the number of pole pairs has been investigated, exploring also p=3. The main geometrical dimensions remain as in Table 4.3, while the number of slots has been increased to $Q = 36$.

With a non–chorded winding, the optimized solution ($\Delta T = 7.21\%$) is found with the following angles: **M1** ϑ'_{b1}=18.1°, ϑ'_{b2}=29.7° **M2** ϑ''_{b1}=21.1°, ϑ''_{b2}=24.4°

With a chorded winding, the optimized solution ($\Delta T = 5.61\%$) is found with the following angles: **M1** ϑ'_{b1}=21.9°, ϑ'_{b2}=25.5° **M2** ϑ''_{b1}=20.5°, ϑ''_{b2}=23.6°

4.4.3. Multi–objective solution

It should be noted that the assistance of PM insets within the flux barriers causes the saturation of the ribs at the ends of the flux barriers, with a consequent torque and power factor increase. However, since the rotor magnetic potential depends on the PMs contributions, the optimal flux–barrier angles are influenced by the PM quantity.

The Pareto optimality is a concept initially proposed by Vilfredo Pareto in economics. In general, given an initial allocation of goods among a set of individuals, a change to a different allocation that makes at least one individual better off without making any other individual worse off is called a Pareto improvement. An allocation is defined as Pareto optimal when no further Pareto improvements can be made. It

follows that the Pareto frontier, e.g. Pareto set, is the set of choices that are Pareto efficient.

Therefore, two goals are identified: minimization of torque ripple and maximization of the average torque. These two objective are computed for several combinations of flux–barrier angle adopting the TRIBE optimizer, as in the previous optimization. In this case the two objective allows to evaluate the Pareto front. In particular, Fig. 4.4.3 refers to a non chorded winding, while Fig. 4.4.3 refers to a one–slot chorded winding.

It is worth noticing that the Pareto front can be approximated by two straight lines, one almost orthogonal to the other, so that a tradeoff solution (Pareto optimal) can be found at the intersection between the two lines. The rotor geometry that refers to this intersection point exhibits low torque ripple and a high average torque.

It is worth noticing that, with non chorded winding, the 6–Nm torque can be achieved with several solutions characterized by a torque ripple from 8% to 60%, as highlighted in Fig. 4.4.3. In this case a further reduction of the torque ripple requires a reduction of the average torque.

Differently, with a one–slot chorded winding, it is possible to reduce the torque ripple up to 3% ($\simeq 0.2Nm$) without a noticeable reduction of the average torque (Fig. 4.4.3).

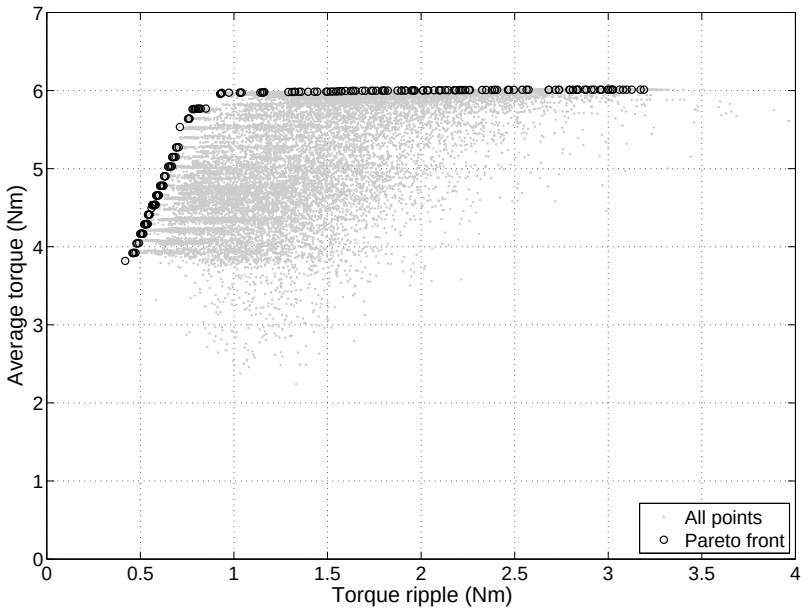

Figure 4.19: Pareto front of the torque–ripple and average torque optimization.

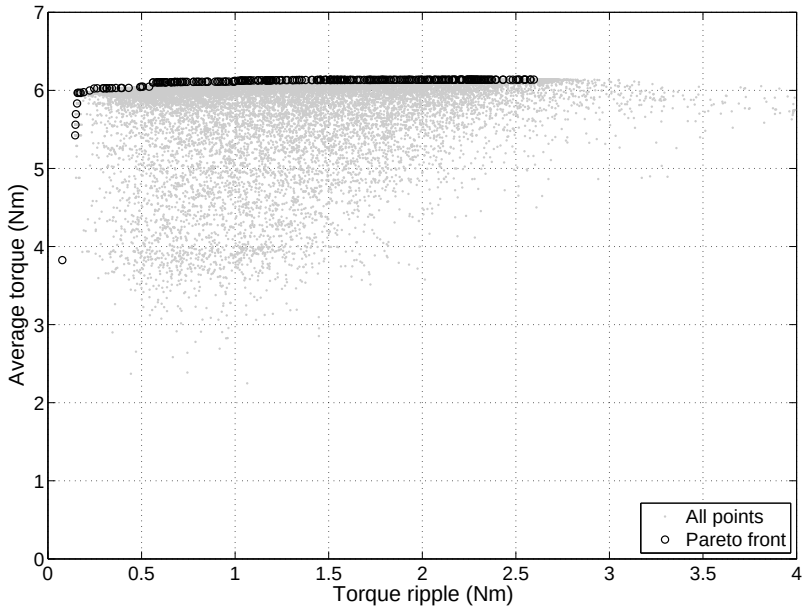

Figure 4.20: Pareto front of the torque–ripple and average torque optimization.

Chapter 5

Stator iron loss reduction

This chapter deals with the minimization of the eddy current iron loss. The geometries minimizing the stator iron losses are evaluated by means of an analytical model of the anisotropic rotor machine. The dependence of such losses on the rotor geometry, or rather the flux–barrier angles will be highlighted. The analysis is carried out considering a REL machine with one flux–barrier per pole rotor and an IPM machine with two flux–barriers per pole rotor. The results of the analytical model are compared with both finite elements and experimental tests.

5.1. The eddy current iron loss

IN anisotropic rotor motors, such as synchronous reluctance and interior permanent magnet motors, there are many harmonics in the air gap flux density distribution under all operating conditions. These harmonics mainly depend on the rotor geometry and are almost independent of the main flux per pole. During normal operations, they yield fluctuations of the flux density in the stator iron, mainly in the teeth, and then additional eddy current iron losses [43, 44].

This aspect is prominently evident during flux–weakening (FW) operations, when the motor runs above base speed and the main flux is weaken [44, 45]. In [46, 47], it is found that the iron losses increase even if the main flux decreases. The computation of iron losses in synchronous machines with anisotropic rotor is investigated in [46, 48, 49], although they do not present general design suggestions. A design optimization of a single flux–barrier rotor geometry is given in [50]. Some basic results based on simplified motor model are found in [47, 51].

In the following the analytical model presented in chapter 3 is adopted to evaluate the influence of the rotor geometry on the tooth eddy current iron losses. These losses are expected to be relevant during the flux–weakening operations since are proportional to the square of the frequency, e.g. the speed. Analogously to the torque ripple minimization issue presented in chapter 4, the iron losses results affected by the rotor geometry. The geometrical paramente that affects the machine behaviour is still the flux barrier angle. Obliviously, the references adopted hereafter are the same of the analytical model, reported in Fig. 5.1.

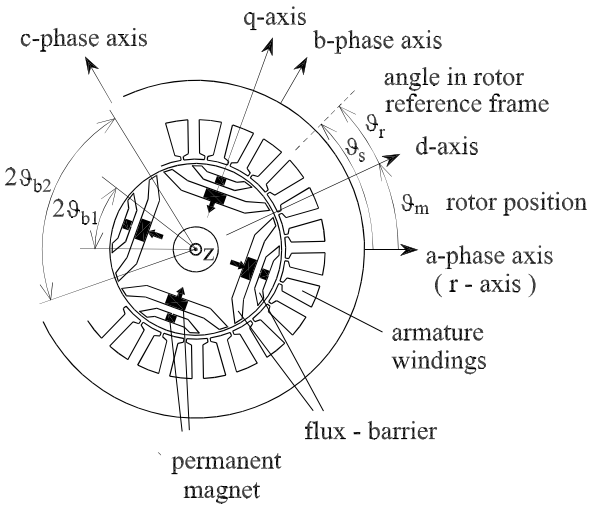

Figure 5.1: IPM synchronous motor with anisotropic rotor and reference axes adopted in the analytical model of the machine with anisotropic rotor.

5.2. Tooth flux density computation

The analytical model allows to compute the behaviour of the radial component of the air gap flux–density B_g (3.6), from the the difference between the stator and the rotor magnetic potential. As depicted in [47], the higher iron losses are in the stator teeth, so that the focus is on the tooth flux density, that is calculated from the analytical air gap flux density. Over one stator slot pitch the tooth flux density B_t is given as a scaled moving average of the air gap flux density:

$$B_t = \frac{p_s}{\alpha_s \, w_t} \int_{-\alpha_s/2}^{+\alpha_s/2} B_g(\vartheta_s) d\vartheta_s \tag{5.1}$$

where α_s is the slot angle, p_s is the slot pitch and w_t is the tooth width (Fig. 5.2).

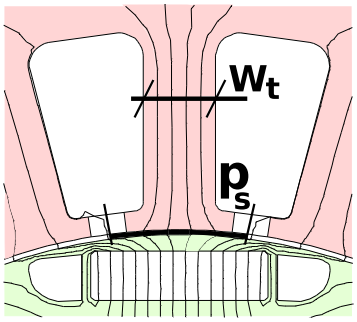

Figure 5.2: Tooth geometrical quantities.

The iron losses of a generic motor consist of the sum of the hysteresis loss, classical eddy current loss and excess loss. It is commonly expressed in the following form [52,53], considering a sinusoidally varying magnetic flux density $\hat{B}$ with frequency f:

$$p_{iron} = k_{hy} \, \hat{B}^{\beta} \, f + k_{ec} \, \hat{B}^2 \, f^2 + k_{ex} \, \hat{B}^{\frac{3}{2}} \, f^{\frac{3}{2}} \tag{5.2}$$

where k_{hy} and k_{ec} are the hysteresis and the classical eddy current constant, and β is the Steinmetz constant, often approximated as $\beta \simeq 2$. The k_{ex} is the eddy current excess losses constant. These losses are due to the dynamic losses of the Weiss domains when a variable magnetic field is applied to the magnetic material. The block walls discontinuous movements produce fast Barkhausen jumps and then eddy currents [54].

These constants should be obtained from material data sheet, but the Epstein frame test does not allow to differentiate between the eddy currents due to the classical losses and the eddy currents due to the excess losses, as verified in [52, 55].

From experimental tests reported in [52] the coefficient k_{ex} has been measured equal to zero for several ferromagnetic materials. The authors highlight the difficulty to separate the excess losses contribution from the classical eddy current losses. However, it is relevant to remember that the excess current loss component could be very significant in many lamination materials [54].

As a consequence, the effects of the excess losses are combined with the classical eddy current losses and a single eddy current losses coefficient is defined. Therefore an increased k_{ec} is used, neglecting the third addendum of (5.2).

The aim of the analysis is the eddy current loss computation, since such of losses are the main contribution of the whole iron loss at high speed, being proportional to the square frequency. The tooth eddy current losses are due to the fluctuations of the tooth flux density, in particular of the harmonic components superimposed to the fundamental. Then, the tooth eddy current iron loss density is proportional to the energy of the time differentiation of the tooth flux density:

$$p_{ec} = k'_{ec} \frac{1}{T_p} \int_0^T \left(\frac{\partial B_t}{\partial t} \right)^2 dt = k'_{ec} \frac{\omega_{me}^2}{2\,\pi} \int_0^{2\,\pi} \left(\frac{\partial B_t}{\partial \theta_{me}} \right)^2 d\theta_{me} \tag{5.3}$$

where $T_p = 2\pi/\omega$ is the period, while k'_{ec} is the generic eddy current constant, which is equal to $k_{ec}/2\pi^2$. The behavior of the tooth flux density, computed by (5.1), is expressed by means of the Fourier series expansion, as

$$B_t(\theta_{me}) = \sum_h \hat{B}_h \, \sin(h\theta_{me} + \alpha_h) \tag{5.4}$$

where h is the order of the spatial harmonic of the tooth flux density. Therefore

$$\frac{\partial B_t(\theta_{me})}{\partial \theta_{me}} = \sum_h \hat{B}_h \, h \, \cos(h\theta_{me} + \alpha_h) \tag{5.5}$$

The tooth eddy current iron loss density results in

$$p_{ec} = k'_{ec} \frac{\omega^2}{2\,\pi} \int_0^{2\,\pi} \sum_h \hat{B}_h^2 \, h^2 \, \cos^2(h\theta_{me} + \alpha_h) \, d\theta_{me} \tag{5.6}$$

and after some computations, it becomes

$$p_{ec} = k_{ec} \, f^2 \sum_h \hat{B}_h^2 \, h^2 \tag{5.7}$$

where f depends on the motor speed. This final formulation highlights that, thanks to the linearity hypothesis, the eddy current tooth iron loss is a function of three

parameters: the lamination loss factor k_{ec}, the frequency f and the tooth flux density waveform, that is, $\sum \hat{B}_h^2\, h^2$ which is a function of current vector angle α_i^e, electric loading K_s and rotor flux–barriers geometry (i.e. ϑ_{b1}, t_{b1}, l_{b1}, etc).

Let us note that varying these parameters it is possible to highlight the impact of the rotor geometry on the stator iron losses. The quantity $\sum \hat{B}_h^2\, h^2$ can be defined as the *iron loss factor*. It depends only of the given rotor geometry and the operating current vector [49].

5.3. Reluctance rotor with one flux–barrier per pole

Firstly a rotor geometry with only one flux–barrier without PM (REL motor) is considered in the analysis. The analytical behaviours of the air gap flux–density and the tooth flux–density are verified by means of simplified FE simulations. Then the behaviour of the iron loss during the flux–weakening operations is investigated, also considering a PM buried in the flux–barrier.

5.3.1. Finite element comparison

As described in Chapter 4, for the sake of a correct comparison the FE model adopted requires a slotless stator and a suitable set of current points in place of the slots, as in Fig. 4.1. A 24–slot 4–pole geometry is adopted for the comparison. Then the stator has been schematized by means of 24 current points, reproducing the 24 slot currents. The current of each current point is changed according to the rotor position ϑ_m, reproducing the actual current within the slots.

Fig. 5.3 shows the behaviour of the stator and rotor magnetic potential respectively: from the difference between them the flux density distribution in the air gap shown in Fig. 5.4 is computed. A satisfactory agreement between the analytical and FE models is evident.

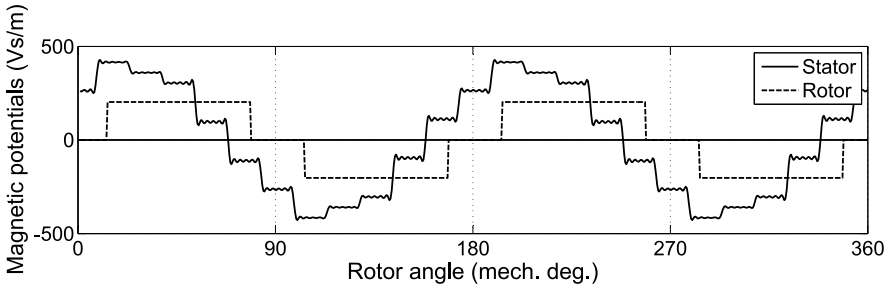

Figure 5.3: Analytical stator and rotor magnetic potential waveforms. The flux–barrier angle is $\vartheta_b = 32.7$ degrees.

It should be noted that the linear assumption applied both to the analytical model and the FE analysis is well suited to the FW operations. Usually in the FW region the machine is not saturated, especially in the stator, thanks to the relative low flux density values.

An example of the B_t waveform is shown in Fig. 5.5. Two teeth are considered since the motor has two slots per pole per phase. It is worth noticing that the waveforms are

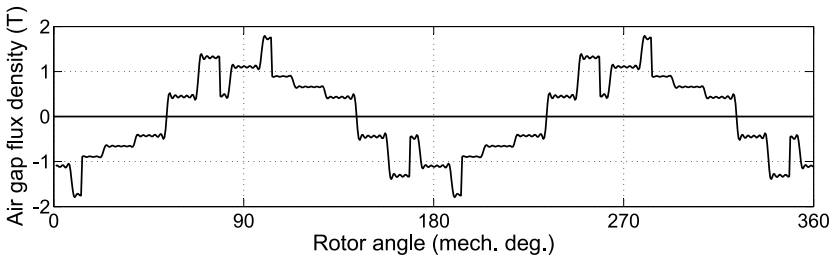

(a)

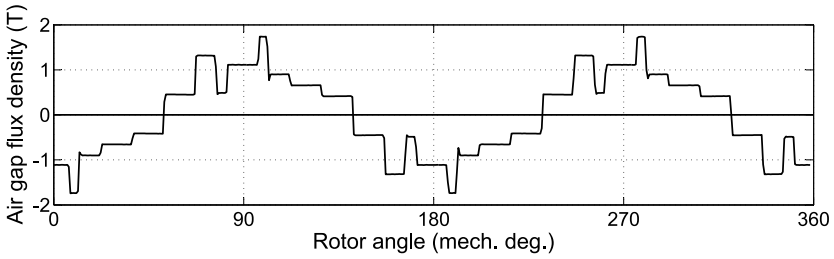

(b)

Figure 5.4: Flux density distribution in the air gap: (a) Analytical model and (b) FE model. The flux–barrier angle is $\vartheta_b = 32.7$ degrees.

quite different from sinusoidal waveforms. Fig. 5.5(a) refers to the analytical computation, and Fig. 5.5(b) refers to the FE simulation. There is a good agrement between the two waveforms. The same agreement is found at different current vector angles α_i^e. These results allow the analytical model to be adopted for the following considerations.

The tooth flux density B_t waveform result to be more distorted during flux–weakening operations, as shown in Fig. 5.6. This figure also shows that such a distortion remains also changing the geometry of the flux barrier (i.e. the angle ϑ_b). However, the peak amplitude of the waveform changes with ϑ_b. This means that the iron losses depend on the rotor flux–barrier geometry, as will be depicted later on.

5.3.2. Iron losses during flux–weakening operating conditions

At first, the flux–weakening speed of a synchronous reluctance motor is computed for different current vector angles. The trajectory of the current vector is reported in Fig. 5.7 in the (J_d, J_q) plane, where J_d and J_q are the densities of the d– and q–axis current components. As introduced above, the references are the same of the analytical model, shown in Fig. 5.1, that are different from the usual d–q axis references for the IPM machines, shown in Fig. 2.3.

From zero to nominal speed, the motor operates so as to achieve the maximum torque density, that corresponds to the point B in Fig. 5.7 for the REL machine ($J_d = J_q$, $\alpha_i^e = 45$ degrees). When the speed becomes higher than the nominal one, the voltage limit becomes prevailing. The current vector moves along the current limit circle (dotted line in Fig. 5.7) from point B to point P. In the operating point P the current vector reaches the trajectory of the maximum torque per voltage. In a reluctance motor, the condition $\Lambda_d = \Lambda_q$ is verified, where Λ_d and Λ_q are the d– and

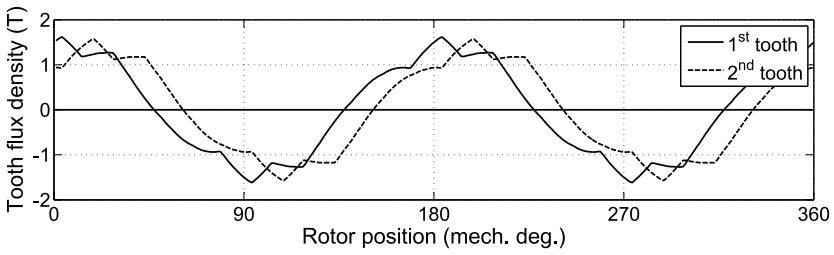

(a)

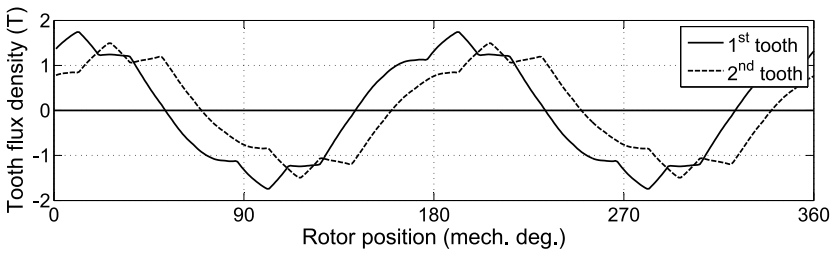

(b)

Figure 5.5: Tooth flux density: (a) analytical waveform and (b) FE waveform. Current density is $J_c = 6\ A/mm^2$ and the current vector angle is $\alpha_i^e = 45$ el. degrees.

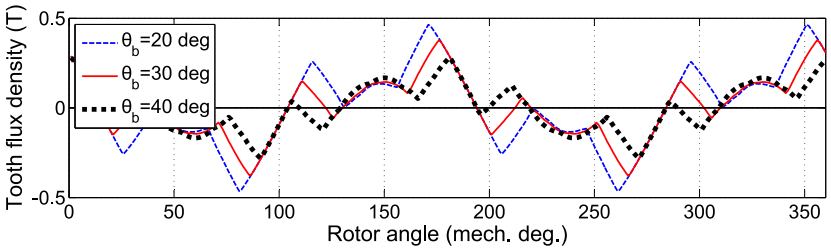

Figure 5.6: Flux density in the stator tooth versus time, corresponding to different flux–barrier angle ϑ_b ($\alpha_i^e = 80$ deg and $J_c = 2$ A/mm^2 are fixed).

q–axis flux linkages. In the example of Fig. 5.7, the current vector angle in point P is about $\alpha_i^e = 80$ degrees. Then, for higher speeds, the current vector moves along the trajectory of the maximum torque per voltage, that is, the angle α_i^e remains fixed and the current decreases towards zero. In Fig. 5.7 the current density decreases from 6 A/mm^2 (point P) to 2 A/mm^2 (point F).

The speed is computed as a function of the current vector, fixing the nominal speed to be 1000 r/min, at the operating point B, when $\alpha_i^e = 45$ deg and $J_c = 6$ A/mm^2. In such a point B, the nominal flux linkage is computed. Then, according to a new operating point, along the trajectory from B to P and then to F, the corresponding flux linkage is computed, and the speed ratio is inversely proportional to the flux linkage ratio.

Fig. 5.8(a) shows the increase of the speed corresponding to the increase of the current vector angle α_i^e from 45 to 80 deg, with fixed current density at maximum value $J_c = 6$ A/mm^2. It corresponds to the movement from point B to point P. Then,

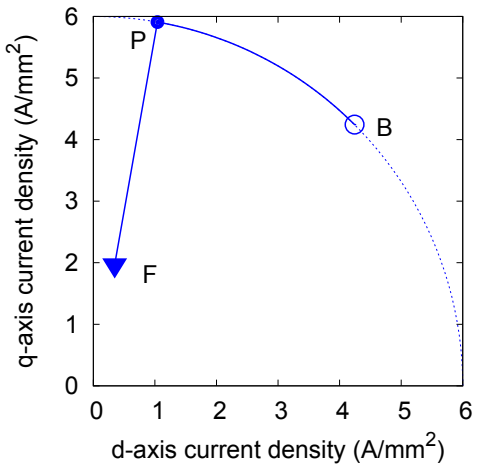

Figure 5.7: Trajectory of the current vector in the (J_d, J_q) plane for the synchronous reluctance motor during flux–weakening operations. The *d-q* axis refers to the references of Fig. 5.1.

Fig. 5.8(b) shows the increase of the speed corresponding to the decrease of the current density J_c from 6 to 2 A/mm^2, with fixed $\alpha_i^e = 80$ deg. It corresponds to the movement from point P to point F of Fig. 5.7.

For each combination of vector angle α_i^e and current density J_c, the speed is computed as described above. Then, the analytical model is used to derive the air gap flux density. The computation is repeated for various positions of the rotor. Finally, the tooth flux density waveform and the iron losses are predicted as described above.

Fig. 5.9(a) shows the iron loss density versus the current vector angle α_i^e. It is worth noticing that the loss density increases even though the flux is weakened. This means that the increase of the speed is higher than the reduction of the flux, so that the iron losses increase as the angle α_i^e increase (trajectory from B to P). On the contrary, when α_i^e is fixed and the current density decreases (trajectory from P to F), the increase of the speed is exactly balanced by the decrease of the flux, so that the iron losses remain constant, as shown in Fig. 5.9(b). A current density reduction involves a proportional reduction of the flux, and a consequent reduction of the flux density in the stator tooth. On the contrary, the speed increase is inversely proportional to the flux. Being the iron losses proportional to the square of both the speed and the flux density, they are constant along the trajectory from P to F without saturation. Although the analytical model adopts linear iron, there is no saturation with a current angle $\alpha_i^e = 80$ electrical degrees.

It is worth noticing that this is true when a synchronous reluctance motor is considered, in which the flux is directly proportional to the current. When a PM is inset in the rotor, the linearity between current and flux disappears, so that the losses tend to increase also along this trajectory.

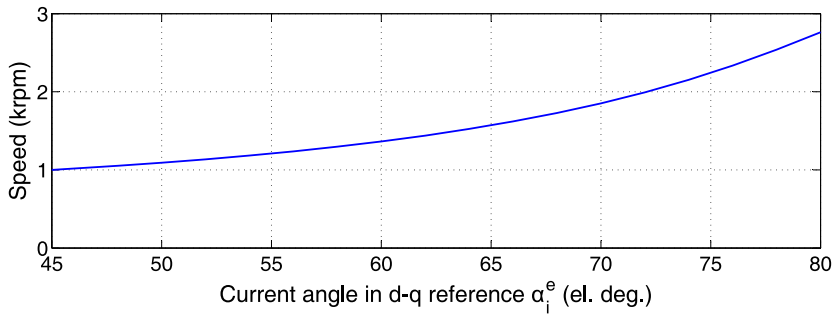

(a)

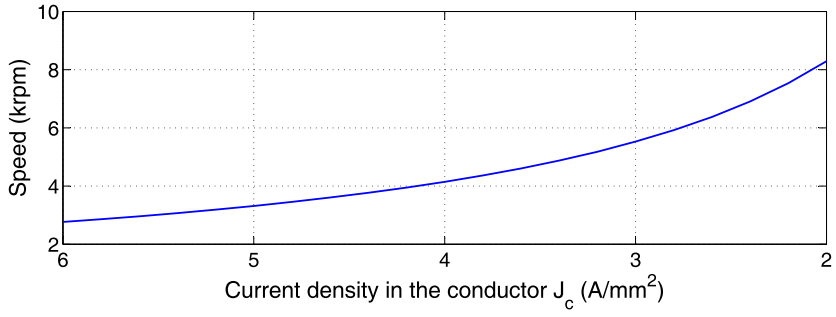

(b)

Figure 5.8: Motor speed as a function of: (a) the current vector angle α_i^e with fixed current density $J_c = 6\ A/mm^2$, (b) current density J_c with $\alpha_i^e = 80$ deg.

5.3.3. Optimization of the rotor geometry

The flux–barrier geometry can be optimized so as to reduce the stator iron losses, as also suggested in [49]. Considering a synchronous reluctance motor, Fig. 5.10 shows the iron losses versus the flux–barrier angle ϑ_b. The analysis is repeated for different flux–barrier angles ϑ_b in the range 20 to 42 degrees.

The current density is kept constant to $J_c = 6$ A/mm^2, and the angle α_i^e is changed from 50 to 80 degrees. It is worth noticing that there is an optimal flux–barrier angle at which there is a minimum of losses, regardless of the value of α_i^e. The minimum is achieved for $\vartheta_b \approx 37$ degrees, approaching the high torque density condition [56].

The PMAREL motor is obtained adding a PM within the flux–barrier. The PM has the same thickness of the flux–barrier, while its height is fixed to about one third of the flux–barrier length. The PM height is chosen in order to have a wide CPSR. Then the current vector moves from P to F in the (J_d, J_q) plane. It is found that the distortion of the tooth flux density increases with the presence of the PM flux.

As above, the analysis is repeated for different geometries of the flux–barrier, so as to achieve the optimal angle ϑ_b thet exhibits the iron loss minimum. Fig. 5.11 reports some waveforms of the tooth flux density according to three different flux–barrier angles of the PMAREL machine. Higher variations are observed with respect to those shown Fig. 5.6 for the REL machine.

Fig. 5.12 shows the iron loss density versus the flux–barrier angle ϑ_b, according to

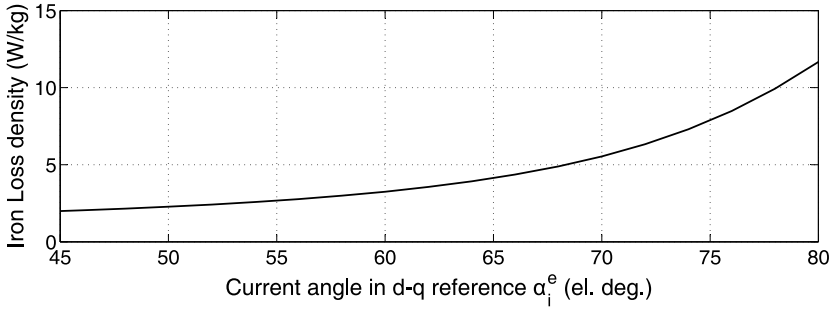

(a)

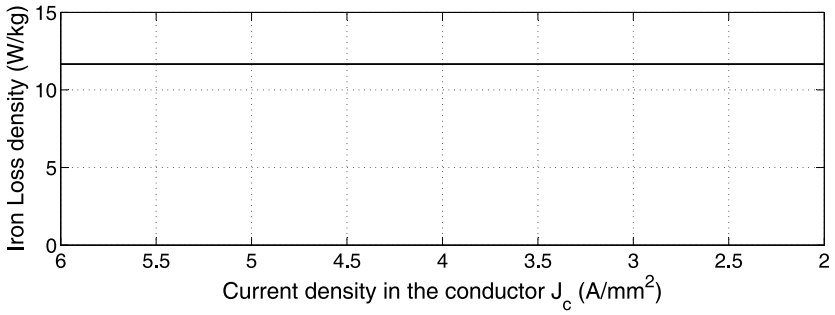

(b)

Figure 5.9: Iron losses in synchronous reluctance motor: (a) versus current angle α_i^e with $J_c = 6\ A/mm^2$ (trajectory B to P), (b) versus current density J_c with $\alpha_i^e = 80$ deg (trajectory P to F).

various current vector angle α_i^e. The iron losses exhibit a minimum when the flux–barrier angle is $\vartheta_b \approx 37$ degrees, as found for the synchronous reluctance motor.

It should be noted that the flux–barrier angle yielding the minimum value of the iron loss density is the same for the reluctance and the PMAREL motor. The PM involves an increase of the amplitude of the rotor island potential. This is a drawback during flux–weakening operations. Then, the orders of the spatial rotor harmonic remain the same, but the harmonic amplitudes increase yielding higher tooth stator iron eddy current losses.

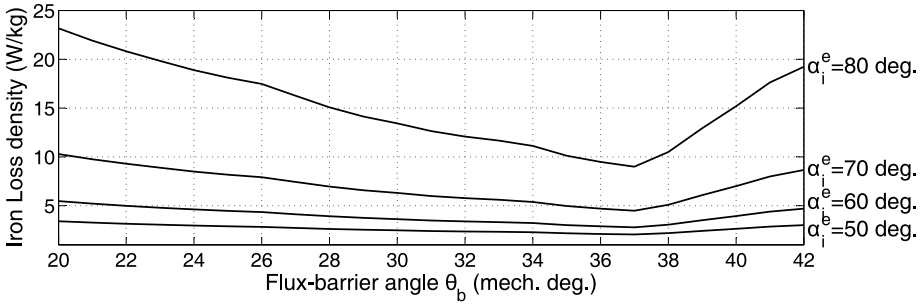

Figure 5.10: Iron loss density versus the flux–barrier angle ($J_c = 6$ A/mm^2) in synchronous reluctance motor ($\alpha_i^e = 45°$).

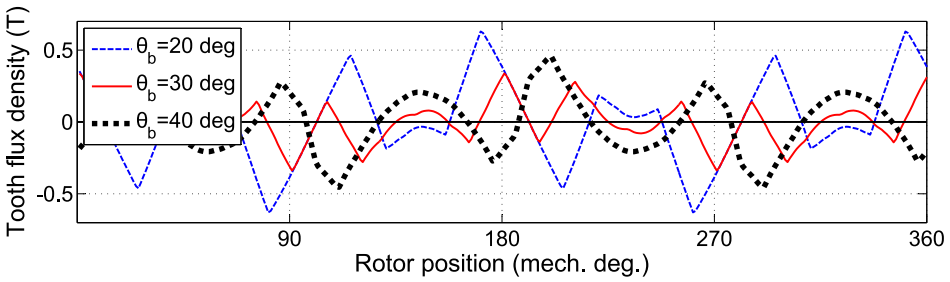

Figure 5.11: Flux density in the stator tooth versus time, corresponding to different flux–barrier angle ϑ_b^e (fixed $\alpha_i^e = 85$ deg and $J_c = 3$ A/mm^2), in PMAREL motor.

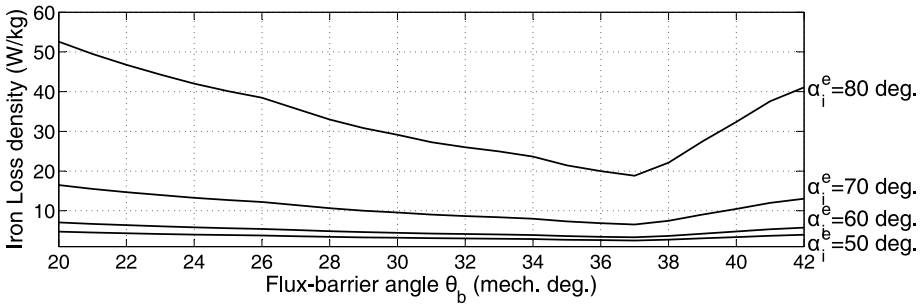

Figure 5.12: Iron loss density versus the flux–barrier angle ($J_c = 3$ A/mm^2) in PMAREL motor ($\alpha_i^e = 45°$).

5.4. Interior PM rotor with two flux–barriers per pole

The 24–slot 4–pole geometry of the available IPM motor prototype is considered for the iron loss analysis. The rotor is provided of two flux–barriers per pole with PMs. The rotor lamination is shown in Fig. 5.13(a). As for the analytical model, the subscript "1" will be used for the inner flux–barrier while the subscript "2" will be used for the outer flux–barrier.

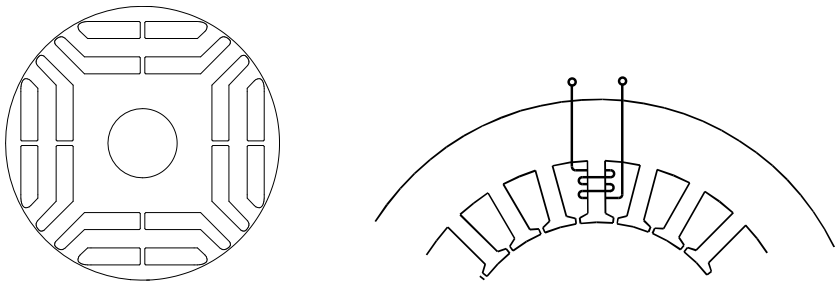

(a) rotor lamination (b) search coil

Figure 5.13: 24–slot 4–pole IPM prototype: (a) rotor lamination with two flux–barriers per pole, (b) search coil around the stator tooth.

A speed independent analysis has been carried out in order to highlight the influences of the flux–barrier angle and the operating conditions on the iron loss factor of

(5.7). Then, two rotor geometries are properly selected from the results of the analytical analysis in order to compute the iron losses during the flux–weakening operations.

5.4.1. Experimental validation of the analytical model

A sensible noise due to the stray losses, mechanical losses and rotor losses yields complicate the stator iron losses measurements. In addition the small size (less 1kW power) of the prototype increases the effect of this noise. Therefore, it has been preferred to compare measured flux–density waveforms with those predicted analytically and using the actual finite element model of the machine. The stator iron losses density is only computed from the flux–density waveforms, with the assumption described in sec. 5.2.

The stator of the prototype is provided of an additional coil wounded around a tooth, as shown in Fig. 5.13(b). From the measured EMF in the test coil, it is possible to compute the flux density waveform in the stator tooth. In Fig. 5.14(a) it is shown the IPM prototype during a voltage measurement in the high speed test bench. The winding terminal and the terminals of the search coils are shown in detail in Fig. 5.14(b).

The tests have been carried out dragging the rotor at the speed of 1500 rpm (corresponding to an electric frequency of 50 Hz), while the winding is connected to a three–phase load, as in Fig. 5.14(a). The IPM machine operates as a generator and the phase currents approximate sinusoidal waveforms. Such a test setup has been preferred because the measurement is not affected by PWM noise. Varying the three–phase load, it is possible to test various operating load points, with different negative d–axis current components.

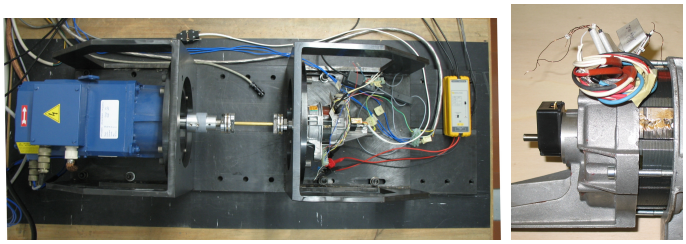

(a) (b)

Figure 5.14: 24–slot 4–pole IPM prototype: (a) high speed test bench during the coil voltage measurements, (b) winding phase conductors and search coils terminals.

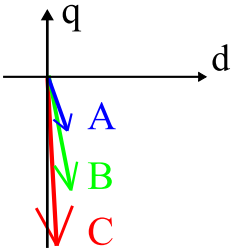

Figure 5.15: Current vectors during the EMF measurements.

The results of three measurements are reported to confirm the predictions. The tests refer to three operating conditions, labeled as **A**, **B**, and **C** in the following. The corresponding current vector position is sketched in Fig. 5.15. The measured conductor current density J_c and the corresponding current vector angle α_i^e are:

operating point A $J_c = 1.6$ A/mm^2 and $\alpha_i^e = -\pi/3$

operating point B $J_c = 3.4$ A/mm^2 and $\alpha_i^e = -7\pi/18$

operating point C $J_c = 5.3$ A/mm^2 and $\alpha_i^e = -4\pi/9$

The operation condition **C** is almost a three–phase short–circuit operating point, as highlighted in Fig. 5.15.

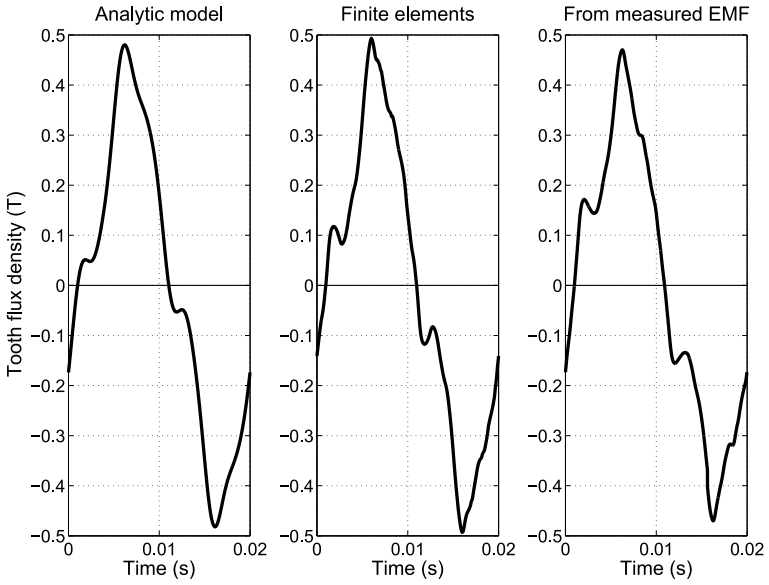

Figure 5.16: Tooth flux density waveforms obtained by means of the analytic model, the FE analysis and the EMF measured in the test coil, under the load point **A**.

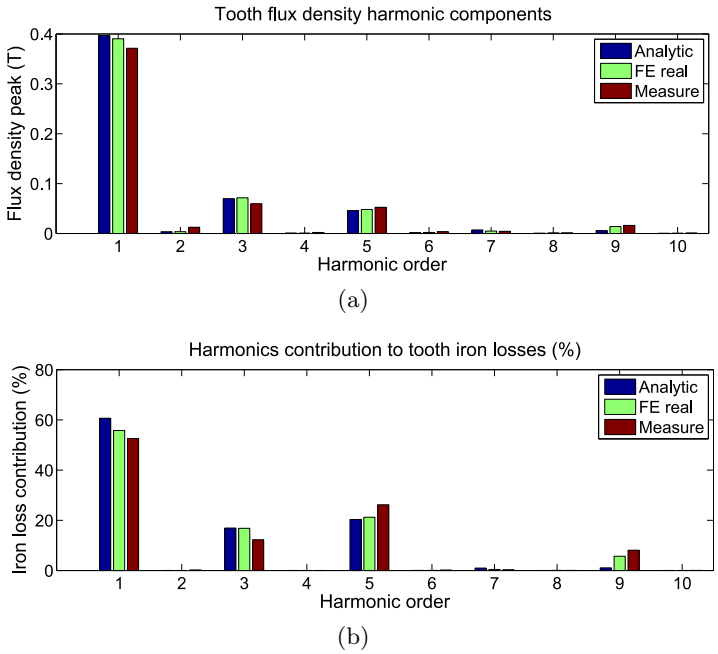

(a)

(b)

Figure 5.17: Tooth flux density waveforms harmonic content comparison under the point load **A**: (a) harmonic content, (b) estimated harmonic contribution to the eddy current iron losses.

Figs. 5.16, 5.18, and 5.20 report the comparison between the different tooth flux density waveforms obtained by means of (i) the analytic model, (ii) the FE analysis

(considering the actual motor geometry) and (iii) from the EMF measurement in the test coil. A satisfactory agreement among the three waveforms is achieved for all operating points.

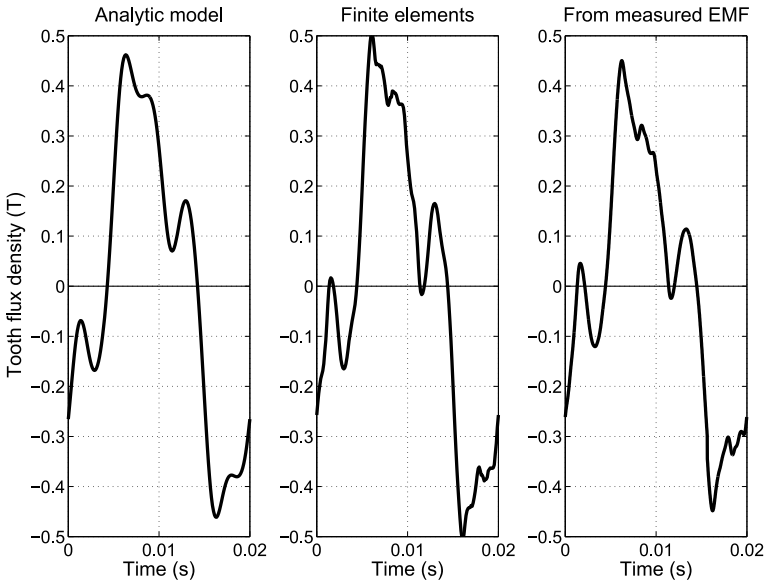

Figure 5.18: Tooth flux density waveforms obtained by means of the analytic model, the FE analysis and the EMF measured in the test coil, under the point load **B**.

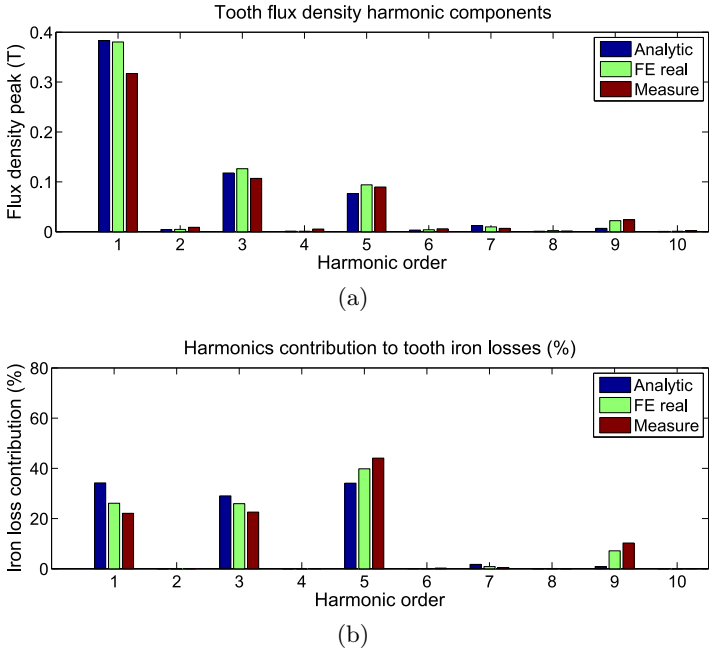

Figure 5.19: Tooth flux density waveforms harmonic content comparison under the point load **B**: (a) harmonic content, (b) estimated harmonic contribution to the eddy current iron losses.

Figs. 5.17(a), 5.19(a), and 5.21(a) compare the harmonic contents (obtained by means the Fourier series expansion) of the tooth flux density waveforms while Figs. 5.17(b), 5.19(b), and 5.21(b) show the contribution of the flux density harmonics to the tooth iron losses.

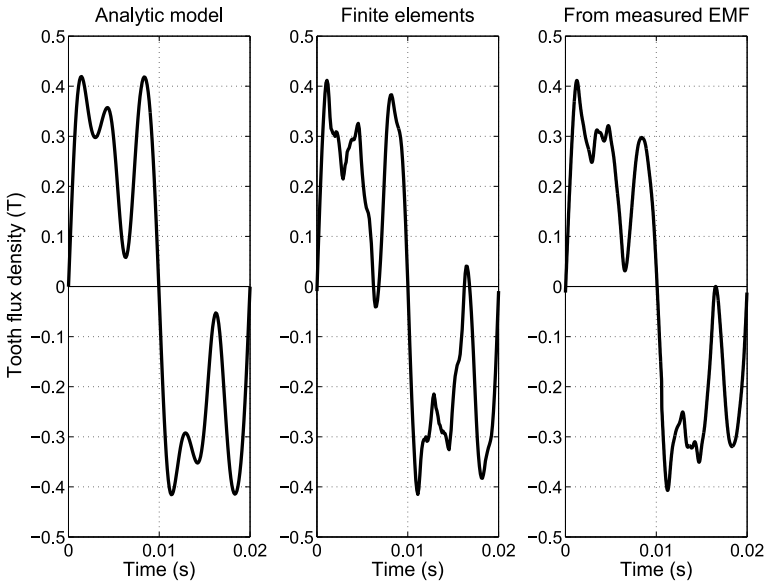

Figure 5.20: Tooth flux density waveforms obtained by means of the analytic model, the FE analysis and the EMF measured in the test coil, under the point load **C**.

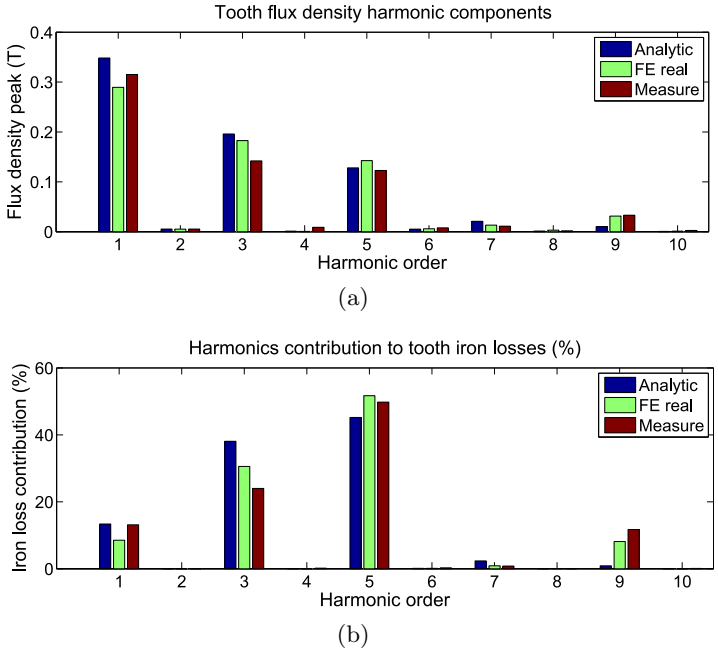

Figure 5.21: Tooth flux density waveforms harmonic content comparison under the point load **C**: (a) harmonic content, (b) estimated harmonic contribution to the eddy current iron losses.

It should be noted that the contribution of the fundamental harmonic of the flux density waveform to the iron losses decreases as the current vector angle α_i^e increases. It is 60% in the operating point **A**, Fig. 5.17(b), while it is reduced to 30% in the operating point **B**, Fig. 5.19(b) and further reduced up to 15% in the operating point **C**, Fig. 5.21(b). The high impact of flux distortion is evident.

To the purpose of make these comparisons independent of the motor speed, only the flux density peak and the per cent value of the estimated stator iron loss contribution are reported.

5.4.2. Rotor geometry impact on iron losses

Maps of iron loss factor

As highlighted in (5.7), a speed–independent parametric analysis can be carried out taking into account the rotor flux–barriers geometry, the current vector angle and the conductor current density. Varying these parameters, it is possible to highlight the impact of the rotor geometry on the stator iron losses.

The purpose of the study is to determine that rotor configuration that yields the minimum value of the sum $\sum \hat{B}_h^2\, h^2$, that is the *iron loss factor*. In the following, such an iron loss factor is mapped as a function of the flux–barrier angles ϑ_{b1} and ϑ_{b2}, for different values of the current vector angle α_i^e. The conductor current density J_c is fixed equal to 6 A/mm^2. The 24–slot 4–pole structure of the IPM prototype, with an integral–slot winding, is considered.

The iron loss maps are computed, firstly referring to a synchronous reluctance machine, then according to two different NdFeB magnets inset within the rotor flux–barriers. The PM heights are $h_m = h_{m1} = h_{m2} = 4.7$ mm and $h_m = h_{m1} = h_{m2} = 15.7$ mm, respectively. In both the flux–barriers, the ratio t_b/l_b is computed so as to be proportional to the flux–barrier angle ϑ_b.

A preliminary comparison between the different behaviour of the reluctance machine ($h_m = 0$ mm), the IPM with low PM contribution ($h_m = 4.7$ mm) and the IPM machine with high PM contribution ($h_m = 15.7$ mm) can be carried out analyzing the iron loss maps reported in Fig. 5.22. Firstly it is worth noticing that the maps have a similar shape independently of the PM size.

As expected from the analysis of the IPM motor with one–barrier per pole rotor described in section 5.3, it can be noted again that the quantity of PM inset in the rotor has a slight influence on the minimum region location. However, comparing Fig. 5.22(a) and Fig. 5.22(c), the PM reduces the minimum area and increases the minimum value.

Fig. 5.23 and Fig. 5.24 show the iron loss factor maps referring to the IPM machines only. Comparing the iron loss factor maps, it can be recognized that maximum and minimum values are found always in the same regions, independently of the current vector angle α_i^e. The maximum values are achieved with smaller flux–barrier angles ϑ_{b1} and ϑ_{b2} (on the bottom left of the maps). The minimum values are achieved on the right of the maps, with median values of ϑ_{b1} and high values of ϑ_{b2}.

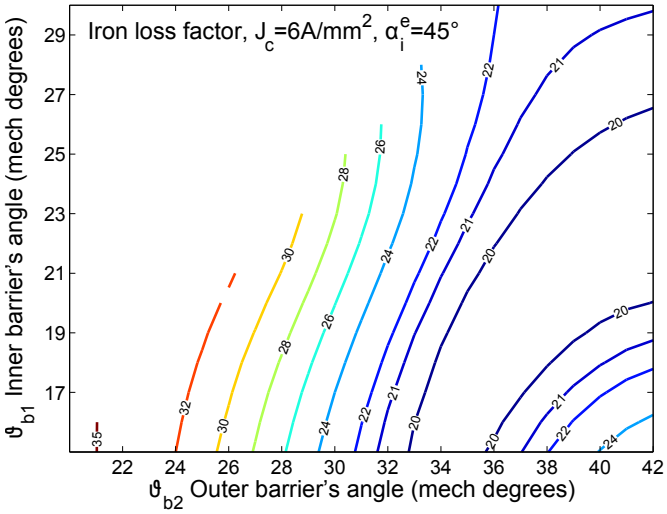

(a) REL machine, $h_m = 0$ mm

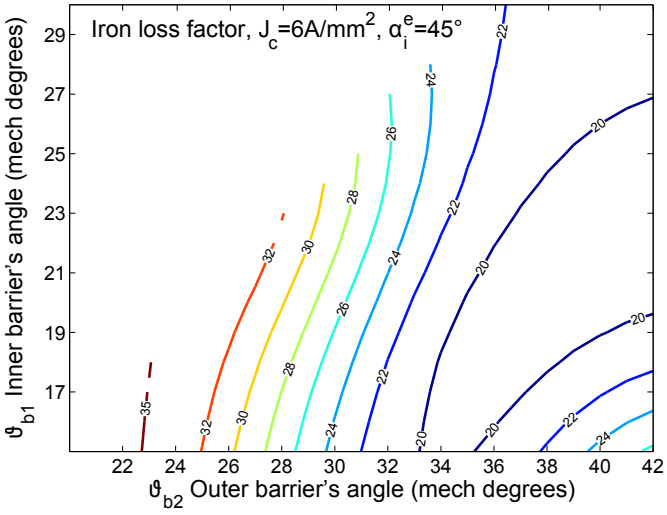

(b) IPM machine with low PM contribution, $h_m = 4.7$ mm

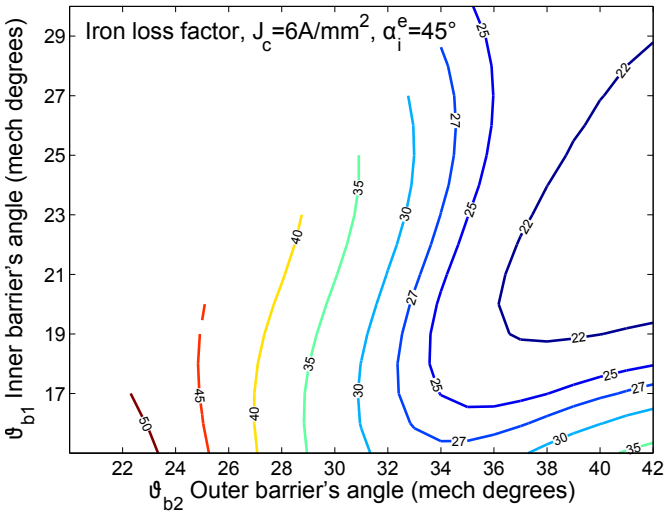

(c) IPM machine with high PM contribution, $h_m = 15.7$ mm

Figure 5.22: Iron loss factor maps for rotor with two flux–barriers per pole: (a) $h_m = 0$ mm, (b) $h_m = 4.7$ mm and (c) $h_m = 15.7$ mm at fixed $\alpha_i^e = 45°$.

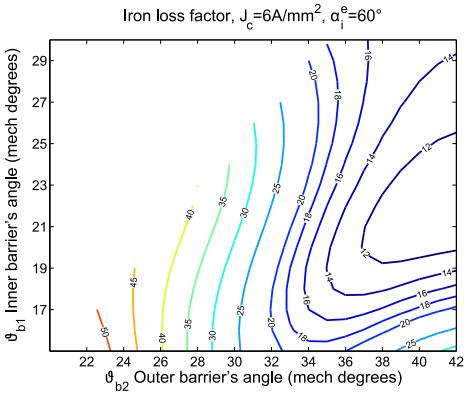

(a) $h_m = 15.7$ mm, $\alpha_i^e = 60°$

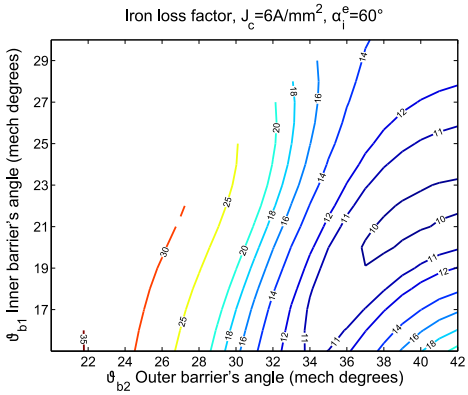

(a) $h_m = 4.7$ mm, $\alpha_i^e = 60°$

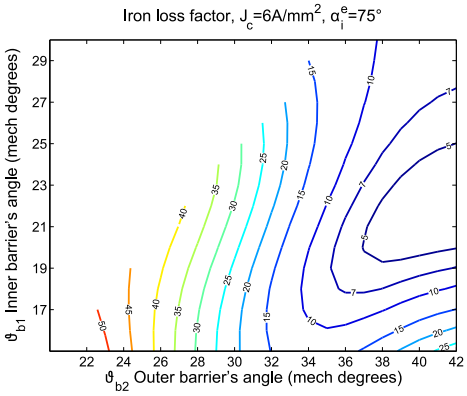

(b) $h_m = 15.7$ mm, $\alpha_i^e = 75°$

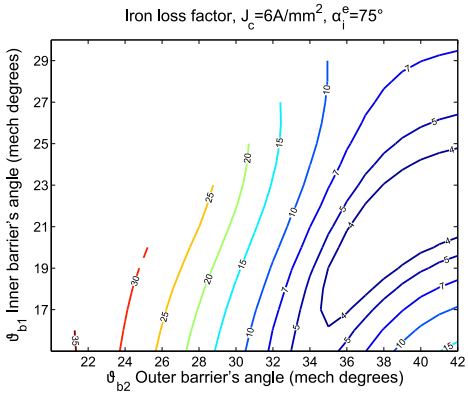

(b) $h_m = 4.7$ mm, $\alpha_i^e = 75°$

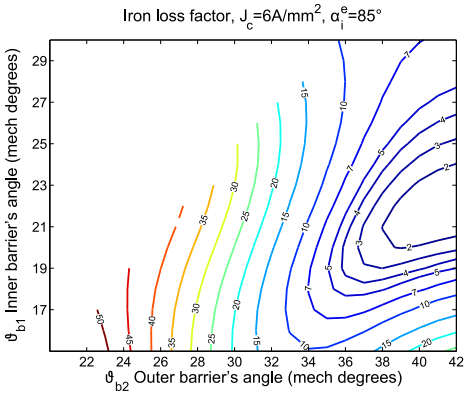

(c) $h_m = 15.7$ mm, $\alpha_i^e = 85°$

Figure 5.23: Iron loss factor maps for IPM rotor with two flux–barriers per pole and $h_m = h_{m1} = h_{m2} = 15.7$ mm.

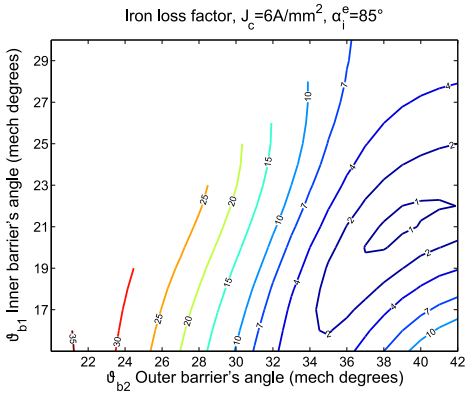

(c) $h_m = 4.7$ mm, $\alpha_i^e = 85°$

Figure 5.24: Iron loss factor maps for IPM rotor with two flux–barriers per pole and $h_m = h_{m1} = h_{m2} = 4.7$ mm.

The position of these two regions does not change, also under FW operations (e.g. at higher α_i^e). For instance, referring to Figs. 5.23(a), 5.23(b), and 5.23(c) of the motor with the higher PM size the region of minimum iron loss factor is located around

$\vartheta_{b1} = 22°$ and $\vartheta_{b2} = 40°$. It is also worth noticing that the iron loss factor increases considerably depending on the rotor geometry. A wrong choice of the flux–barrier angles implies an increase of the iron loss factor of about 4 times, for lower α_i^e, see Fig. 5.23(a) or Fig. 5.24(a), of about 10 times, for higher α_i^e, see Fig. 5.23(b) or Fig. 5.24(b) and up to 40 times for even higher α_i^e, see Fig. 5.23(c) or Fig. 5.24(c).

Comparing the various maps, one can also observe that increasing the current vector angle α_i^e, the minimum values reduce considerably, while the maximum values remain the same. This is due to the fact that, in the lower loss region, the flux distortion decreases together with the main flux. There is a sort of contemporary reduction of the fundamental harmonic and the high order harmonics of the air gap flux density. On the contrary, in the higher loss region, the amount of the flux density harmonics remains almost unchanged even if the fundamental flux decreases.

As anticipated above, further considerations can be carried out referring to the PM quantity. In particular, comparing the maps of Fig. 5.23 (higher h_m) and those of Fig. 5.24 (lower h_m), one can note that the iron loss factor increases with the PM height. It increases of about 20% in the minimum loss region and about 45% in the maximum loss region. This means that when the flux–barriers geometry is optimized the effect of the PM on the iron losses is limited. On the contrary, when a wrong flux–barriers geometry is designed, the effect of a higher PM flux on the iron losses is more evident.

Summarizing the results, the design of a proper rotor geometry is the key task to perform limited stator iron losses under various operating conditions. A rotor design characterized by flux–barrier angles ϑ_{b1} and ϑ_{b2} chosen in the minimum loss region results to be an optimal design choice regardless the operating conditions or the quantity of PM (i.e. regardless if a synchronous reluctance motor, a PM assisted motor or an IPM motor is considered).

5.4.3. An applicative example

The iron loss factor maps, computed for each current vector angle α_i^e, provide the loss index for each operating point. Therefore, the estimated stator iron losses have to be computed by considering the operating frequency f at the given angle α_i^e. For each combination of inner and outer flux–barrier angles, i.e. ϑ_{b1} and ϑ_{b2}, the torque versus speed curve is computed, so as to determine the motor speed (e.g. f) and the corresponding α_i^e angle. Then the iron losses are computed from (5.7).

The same 24–slot stator is considered for the four rotor configurations are considered. They are characterized by two couples of flux–barrier angles ϑ_{b1}–ϑ_{b2}: 20°–33° and 23°–39°. The first one is outside the minimum loss region, while the second one is inside such a region. For each rotor geometry, two PM heights are considered: $h_m = 4.7$ mm and $h_m = 15.7$ mm. Fig. 5.25 shows the two rotor geometries with the higher PM ($h_m = 15.7$ mm). For each configuration, the FW control starts at the motor speed equal to 200 rad/s. The value of k_{ec} is obtained considering a silicon iron lamination with specific iron losses equal to 1.5 W/kg at 1 T and 50 Hz. Letting $\beta = 2$ and $p_{ec}/p_{iron} = 0.3$ it results in $k_{ec} = 0.18 \cdot 10^{-3}$.

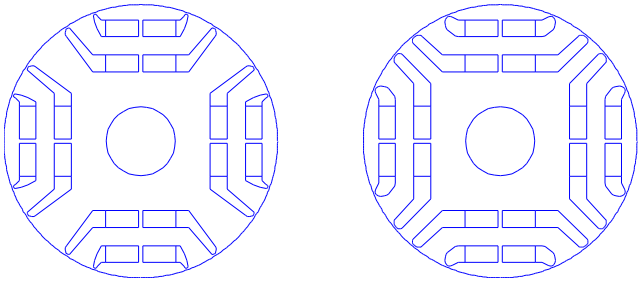

(a) (b)

Figure 5.25: Rotor configurations analyzed. The flux–barrier angles are: (a) $\vartheta_{b1} = 20°$ and $\vartheta_{b2} = 33°$, (b) $\vartheta_{b1} = 23°$ and $\vartheta_{b2} = 39°$.

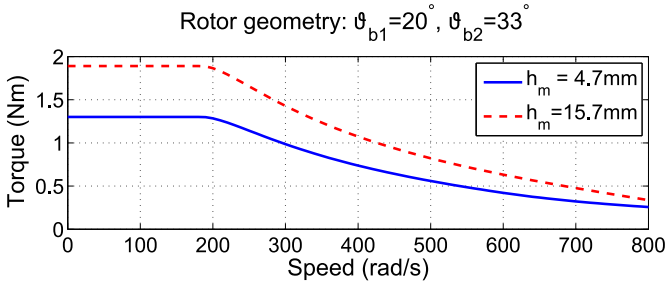

(a) Torque

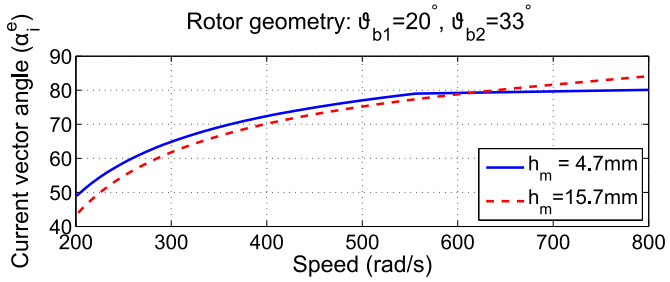

(b) Current vector angle

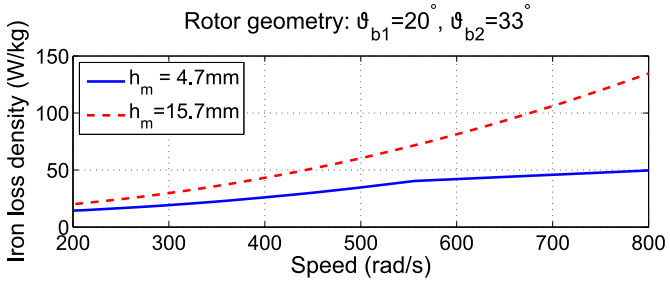

(c) Iron loss density

Figure 5.26: Rotor flux–barrier $\vartheta_{b1} = 20°$ and $\vartheta_{b2} = 33°$. Analytically computed behaviors: (a) torque to speed behavior, (b) current vector angle versus speed, (c) tooth iron loss density in the FW region.

Fig. 5.26(a) and Fig. 5.27(a) show the analytical torque versus speed curves of the four IPM motors. As expected, the increase of the PM yields an increase of the torque at low speed and a decrease of the maximum operating speed. In particular, with the rotor configuration 23°–39° with $h_m = 15.7$ mm, the IPM motor exhibits a constant power speed range lower than four. For given PM height, all motors exhibit a similar average torque at low speed, that is, the choice of different flux–barrier geometry affect slightly the motor torque, as already highlighted in chapter 4.

For each configuration, the current vector angle α_i^e is reported in Fig. 5.26(b) and Fig. 5.27(b) as a function of the speed. From the speed and the current vector angle α_i^e, the actual estimated stator iron loss density is computed. It is reported as a function of the rotor speed in Fig. 5.26(c) and Fig. 5.27(c).

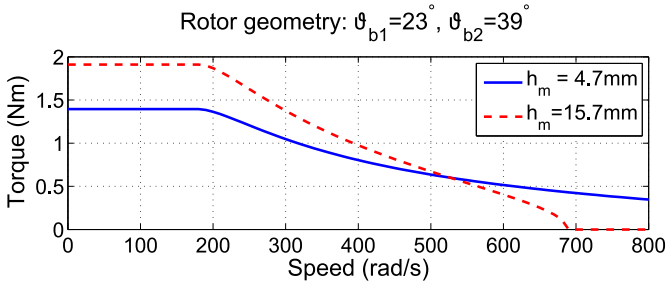

(a) Torque

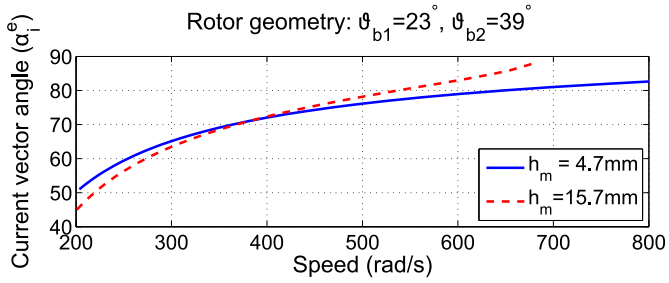

(b) Current vector angle

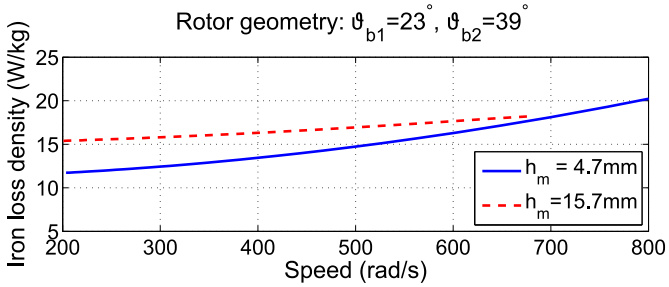

(c) Iron loss density

Figure 5.27: Rotor flux–barrier $\vartheta_{b1} = 23°$ and $\vartheta_{b2} = 39°$. Analytically computed behaviors: (a) torque to speed behavior, (b) current vector angle versus speed, (c) tooth iron loss density in the FW region.

As predicted from the iron loss factor maps shown in Fig. 5.23 and Fig. 5.24, the two

configurations 20°–33° (the flux–barrier angles are outside the minimum loss region) exhibit higher stator iron loss density at any operating speed. On the contrary, the two configurations 23°–39° (the flux–barrier angles are inside the minimum loss region) exhibit lower stator iron loss density.

When the rotor contains a high PM quantity, the iron loss density results always higher. Then, the increase of the PM flux yields a higher distortion of the air gap density especially during FW operating conditions. However, it is worth noticing that as predicted the increase of stator iron loss density is slight when the flux–barrier geometry is properly selected (inside the minimum loss region), as shown in Fig. 5.27(c). On the contrary, it is drastically high when the flux–barrier geometry is outside the minimum loss region, as in Fig. 5.26(c) with a PM height of $h_m = 15.7$ mm.

Finally Fig. 5.28 shows the distributions of the flux density in the air gap, B_g, and in the stator teeth, B_t, computed with finite elements. The two configurations refers to a PM height of $h_m = 15.7$ mm, and a current vector angle fixed to α_i^e=85°.

The first configuration shows a more irregular flux density distribution. In particular, the tooth flux density distribution of the rotor configuration 20°–33° exhibits a higher number of change of sign than the configuration 23°–39° (comparing Fig. 5.28(b) and Fig. 5.28(d)).

Therefore, the final remark from this analysis is that the rotor flux–barrier angle design is extremely relevant to limit the air gap flux density distortion and the consequent variations in the tooth flux density waveform (e.g. iron losses). It can be stated that, when the flux–barrier geometry is properly selected,

- the stator iron loss density is generally low,
- it increases slightly with the speed,
- the PM increase yields no dramatic increase of the stator iron losses.

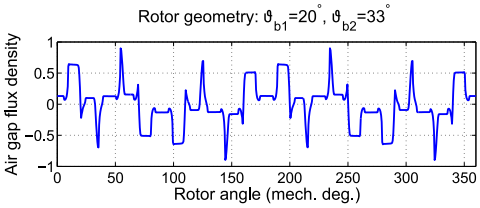

(a) Air gap flux density distribution

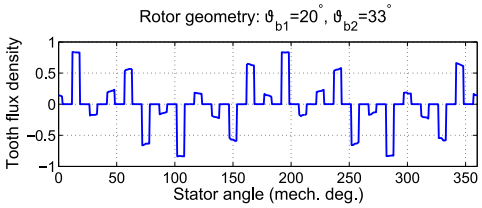

(b) Tooth flux density distribution

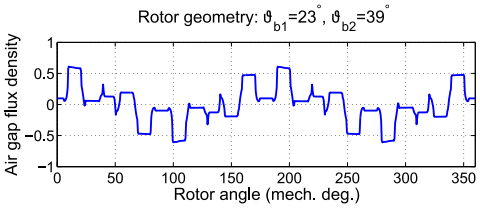

(c) Air gap flux density distribution

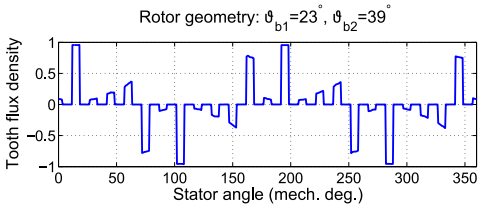

(d) Tooth flux density distribution

Figure 5.28: Flux density distributions in IPM motors with $h_m = 15.7$ mm, operating at $J_c = 6$ A/mm^2 and α_i^e=85°.

Chapter 6

Fractional–slot winding PM machines

This chapter deals with fractional–slot winding PM machines. The star of slots theory is introduced since it is easily adopted to design these windings. Referring to the IPM machine the relevance of the both PM and reluctance torque component is evaluated with both integral–slot and fractional–slot winding. Finally, two issues of the IPM machines with fractional–slot winding are described: (i) the issue of the reduction of finite elements simulations, (ii) the issue of the cross saturation. The latter aspect will be highlighted during the design of a fractional–slot IPM integrated starter alternator.

6.1. Advantages and drawbacks

THERE are several reasons pushing to choose a fractional–slot winding instead of a traditional integral–slot winding. Among the others, there are:

- Reduction of the cogging torque [57,58], due to the different combinations of number of slots and number of poles that allows to decrease the recurring interactions between the rotor PMs and the stator slots.
- Reduction of Joule losses for given torque [59]. For instance the non–overlapped coil windings have low end–winding lengths, yielding both copper weight and Joule losses to be reduced.
- Reduction of short–circuit current [60] due to the higher phase inductance as respect to the corresponding integral–slot machine.
- Increase of fault–tolerant capability [61–63] by means of configurations allowing the phases to be separated so as to avoid the propagation of the fault.
- Increase of flux–weakening capability [65, 66] due to the higher phase inductance as respect to the corresponding integral–slot machine.

However, the fractional–slot PM machines have not only advantages. In literature several drawbacks have been analyzed. For instance, it has been evaluated that

- some solutions exhibit low winding factor [59, 67],
- rotor losses can drastically increase [62],
- the armature MMF increases heavily [68, 69],
- MMF sub–harmonics can cause additional rotor losses and torque ripple [42, 63, 70].

In addition, referring to IPM machines, the adoption of fractional–slot winding usually involves a mutual interaction among the magnetics axes due to the iron saturation. This cross saturation phenomena yields further issues on both the machine design and the drive control.

As a consequence, it is imperative to correctly select the combination of the number of slots and pole in order to maximize the advantages and minimize the parasitic effects. In this field several authors have evaluated on solutions with a particular number of poles and slots and winding type, while effective rules for the design of the fractional–slot machines have been more deeply analyzed in [63, 64].

Hereafter a brief summary of the winding properties and the star of slots theory is reported [71]. It should be noted that the star of slots allow to design in a graphical and easy way conventional and non–conventional windings [71].

6.2. Background

According to the slot number Q, the pole pair number p and the phase number m, the ac winding is feasible when the following condition is satisfied:

$$\frac{Q}{mt} \quad \text{must be an integral number} \tag{6.1}$$

Letting q the number of slots per pole per phase

$$q = \frac{Q}{m2p} \tag{6.2}$$

It is possible to distinguish the windings as:

- integral–slot winding, when q is an integral number,
- fractional–slot winding, when q is a fractional number.

Among the fractional–slot windings the recent interest is focused on those that exhibits a value of $q \leq 1$ [72], in particular those characterized by non–overlapping coils. In addition, depending of the number of coil side within the slot the winding can be distinguish in double–layer (DL) and single–layer (SL) respectively. It is a DL winding when there are two coil sides, while it is a DL winding when there is only one coil side.

A relevant parameter of the winding that has to be firstly considered is the machine periodicity. It is computed as the greatest common divisor ($G.C.D.$) between Q and p. The value of t corresponds to the number of identical parts in which the machine could be split. Furthermore, t is the maximum possible number of parallel circuits, allowable with the specific combination of slots and poles.

6.2.1. AC winding factors

Three assumptions are considered: (i) the flux density along the air gap is sinusoidally distributed with wave length equal to the pole pitch, (ii) the coil pitch is fixed equal to the pole pitch, yielding the maximum flux linkage of one turn equal to the total flux per pole, (iii) each turn of the coil links the same flux at any instant. The peak value of the flux linked by the coils (N_t turns) is

$$\hat{\Lambda} = N_t \phi = N_t \hat{B} \frac{D L_{stk}}{p} \tag{6.3}$$

The peak value of the sinusoidal EMF induced in the coil when the rotor runs at constant speed results in:

$$\hat{E} = \omega_{me} \hat{\Lambda} = 2\pi f N_t \hat{B} \frac{D L_{stk}}{p} \tag{6.4}$$

Considering N_t turns close together in the same slot, it can be assumed that all turns links with the same flux at any instant of time. Conversely the EMFs induced in individual coils of a pole phase group are out of phase. They are displaced from each other by the electrical slot angle $\alpha_s^e = (2\pi p)/Q$. The resultant effective EMF of the coil group is equal to the geometric sum of q EMFs shifted from each other by α_s^e degrees.

$$k_d = \frac{\text{resultant EMF}}{\text{sum of EMFs of individual coils}} \tag{6.5}$$

is smaller than 1 and is called the distribution factor.

However it is common to adopt a coil pitch smaller than the pole pitch, letting chorded the winding, in order to reduce the turn length and the harmonic contents. Due to the chording, the maximum flux linkage with the coil is smaller than the pole flux. The ratio between the linked and the available flux is called pitch factor, and it is $k_p \leq 1$.

Then the product of k_d and k_p is defined as the winding factor $k_w = k_d k_p$. For an ac winding with N_w series turns per phase the EMF induced by a sinusoidally distributed flux results:

$$E = \frac{2\pi}{\sqrt{2}} f k_d k_p N_w \phi = \frac{2\pi}{\sqrt{2}} f k_w N_w \phi \tag{6.6}$$

The quantity $k_w N_w$ is referred to the number of effective turns per phase.

Let us note that when the flux density is not sinusoidally distributed in space, the flux density distribution can be expressed into a Fourier series expansion. Hence, the fundamental and the harmonic components are considered separately.

6.2.2. Winding design with the star of slots

The purpose in the design of a m–phase winding is to obtain: (i) the maximum amplitude of the main (synchronous) harmonic of EMF waveform, (ii) an equal EMF waveform in each phase, (iii) an angular displacement of $2\pi/m$ electrical radians among the phases.

A DL winding is considered, since the single layer winding is a particular case. The EMF is assumed to have sinusoidal waveform, thus symbolic phasors are adopted.

The star of slots is the complex representation of the EMFs induced in the coil within all slots of the machine. Therefore there are Q EMF phasors. The slots are numbered consecutively, as shown in Fig. 6.1. Then, the number of the phasor corresponds to the number of the slot in which the reference left–hand coil side is included.

It is possible to consider separately each coil sides since the complex representation of the coil side EMFs and the obtained results are the same as considering the EMFs induced in the coils. Therefore the star of slot results still formed by Q phasors numbered according to the number of the corresponding slot. According to the machine periodicity it is formed by Q/t spokes, each of them containing t phasors.

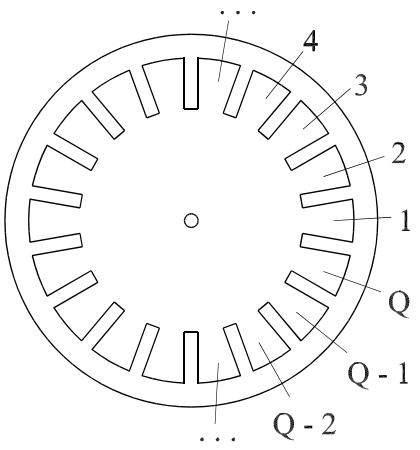

Figure 6.1: Slot numbers

The angle between the phasors of two adjacent slots is the electrical angle $\alpha_s^e = p\alpha_s$, where α_s is the slot angle in mechanical radians, i.e. $\alpha_s = 2\pi/Q$. The angle between two spokes results in

$$\alpha_{ph} = \frac{t}{p}\alpha_s^e \tag{6.7}$$

Let us note that electrical angles are considered, then the star of slots refers to the equivalent *two–pole machine*. Therefore, to the aim of the winding design, the star of slots is drawn according to the main harmonic, i.e., the synchronous harmonic characterized by $\nu = p$.

A graphical representation is adopted to identify the phasors of each phase. Two opposite sectors are drawn, each of them covering π/m radians. Hence, the phasors that are within the two sectors are assigned to the first phase, e.g. phase A. The coil sides within one sector are connected with positive polarity, while the coil sides within

the other sector are connected with negative polarity. According to $m = 3$, $q = 12$ and $2p = 10$ the sectors that refer to phase A are shown in Fig. 6.2, while the corresponding coils in Fig. 6.3.

For the phase B, it is sufficient to rotate the two sectors by an angle $2\pi/m$ radians, and to assign the phasors within these sectors to the phase B. Similarly for the phase C, rotating the two sectors by a further angle of $2\pi/m$ radians. In this way, the largest distribution factor of the main harmonic is obtained.

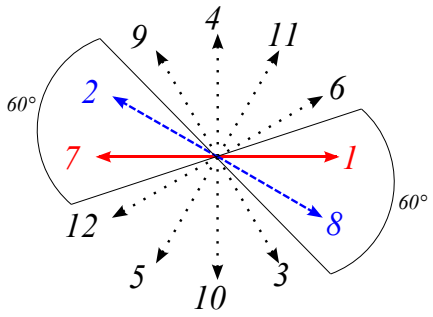

Figure 6.2: 12–slot 10–pole machine: star of slot and sectors of phase A.

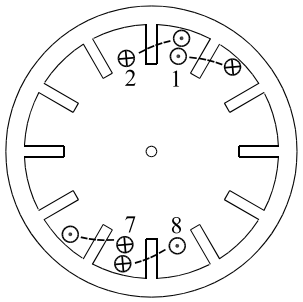

Figure 6.3: 12–slot 10–pole machine: coils of phase A.

It should be noted that adopting the star of slots theory it is possible to design also non–conventional windings. For instance it will be used in chapter 7 to design machines with an increased fault tolerant capability. Some properties of the star of slots are summarized in [63, 64].

6.3. Torque components

As highlighted in chapter 2 there is a growing interest towards the IPM machine, due to its advantages over other ac machine drives. The torque of the IPM machine is characterized by two components: the PM torque (due to the PM flux) and the reluctance torque (due to the rotor anisotropy). Thus, the presence of the reluctance torque yields a higher torque density and the capability to operate in flux–weakening conditions and to be sensorless controlled even at zero speed [35, 73, 74].

However, the rotor anisotropy makes the magnetic model of the IPM machine more complex than the corresponding SPM machine. At first, there is a higher saturation effect [75, 76]. Then, iron saturation does not only reduce the flux linkages at high current, but it also causes a mutual interaction between the d– and q–axis. Such of (phenomenon is known as cross–coupling saturation [77].

It is commonly though that the non–integral ratio of the number of slots per pole yields a reduction of the rotor anisotropy seen for the stator. For the sake of investigating this aspect, different IPM machine configurations are considered. The aim is to highlight (i) how the stator winding configuration impacts on the torque mechanism of PM machine, (ii) if one torque component is predominant to the other, and (iii) which of them is more affected by saturation.

6.3.1. Torque computation

In synchronous machines it is convenient to fix the rotor position ϑ_m, and d– and q–axis currents i_d and i_q as state variables. The choice of these stator currents as state variables is particularly convenient since they are the commands in the current–controlled synchronous machines, as well as they are the sources in the FE analysis. Therefore, in the synchronous $d-q$ reference frame, the motor electromagnetic torque is computed as in (2.18), that is:

$$T = \frac{3}{2}p\left(\lambda_d i_q - \lambda_q i_d\right) + \frac{\partial W'_m}{\partial \vartheta_m} \tag{6.8}$$

where W'_m is the magnetic coenergy, which must be expressed as a state function of the state variables, as in (2.17) [29]. Adopting the finite element model of the machine, the torque T can be computed by integrating the Maxwell stress tensor along the rotor periphery (i.e. T_{Mxw}):

$$T_{Mxw} = \frac{D^2 L_{stk}}{4}\int_0^{2\pi} \frac{B_g B_{g,\theta}}{\mu_0} d\theta_m \tag{6.9}$$

The torque is computed rotating the rotor of an angle corresponding to a sixth of the electrical period.

The first term of the second member of (6.8) is labeled as T_{dq}, that is,

$$T_{dq} = \frac{3}{2}p(\lambda_d i_q - \lambda_q i_d) \tag{6.10}$$

This terms could be used to simplify the average torque computation under some assumptions, as demonstrated [78] and reported in 6.4.

As shown in chapter 2, the d–axis corresponds to the PM axis, while the q–axis corresponds to the leading quadrature axis. As far as the saturation is concerned, a positive and negative q–axis current yields the same effect, due to the symmetry of the magnetic circuit with respect to the q–axis itself. Of course, the q–axis flux linkage will have reversed sign, correspondingly to the sign of the q–axis current.

On the contrary, the d–axis current produces a flux that is in the same direction with the PM flux (when the d–axis current is positive) or in the opposite direction (when it is negative). Therefore, the analysis has to be consider both positive and negative d–axis current.

As a consequence, the torque reverses its sign when the q–axis current changes from positive to negative. On the contrary, this does not happen when the d–axis current changes its sign. In this case, only the reluctance torque component is reversed, while the PM torque component is modified almost proportionally with the variation of the flux along the d–axis itself.

For a given couple of currents (i_d, i_q) it is possible to split the torque in its two components [75]: a permanent magnet T_{pm} and a reluctance T_{rel} torque component, given by:

$$T_{pm} = \frac{1}{2}\Big[T(i_d, i_q) + T(-i_d, i_q)\Big] \tag{6.11}$$

$$T_{rel} = \frac{1}{2}\Big[T(i_d, i_q) - T(-i_d, i_q)\Big] \tag{6.12}$$

6.3.2. Machine configurations

Different machine configurations are considered, fixing rotor poles or stator slots respectively. Each configuration is analyzed investigating its torque components in different operating conditions. The configurations are:

4–poles Fig. 6.4 reports the geometries of the two 4–pole **IPM–A** machines analyzed: the first with a 24–slot stator and the second with a 6–slot stator. The corresponding values of the slot per pole per phase q are 2 and 1/2, respectively.

24–slots Fig. 6.5 reports the geometries of the four **IPM–B** rotors considered with a fixed 24–slot stator geometry. The number of poles evaluated are 4, 16, 20, 22. The corresponding values of the slot per pole per phase q are 2, 1/2, 2/5, 4/11.

The different geometries analyzed have been distinguished in two families (A and B) since they refers to different geometries. The IPM–A machines refers to an external diameter equal to 55 mm and a stack length of 30 mm. The IPM–A machines refers to an external diameter equal to 150 mm and a stack length of 100 mm. The different machine volume is related to its application. However this difference is non significant in the proposed analysis, since it is devoted to evaluate the contribution of the two torque components.

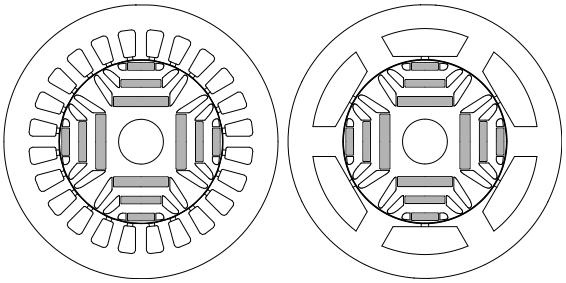

(a) 24–slot machine (b) 6–slot machine

Figure 6.4: Cross–sections of the 4–pole **IPM–A** machines.

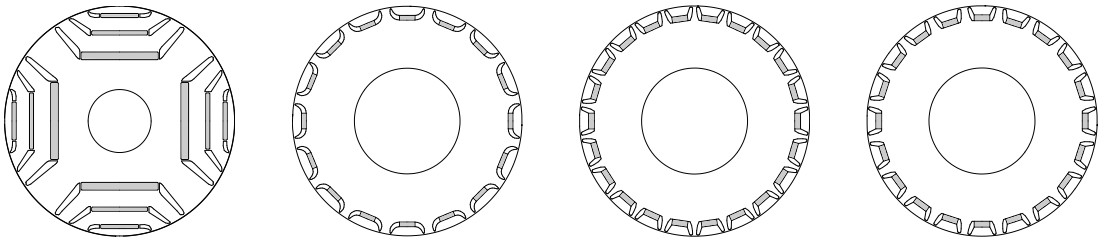

(a) 4–pole rotor (b) 16–pole rotor (c) 22–pole rotor (d) 20–pole rotor

Figure 6.5: Cross–sections of the 24–slot **IPM–B** machines.

Table 6.1: Torque components for the 24–slot 4–pole IPM–A machine.

I/I_N	$T_{Mxw,avg}$	ΔT_{Mxw}	$T_{dq,avg}$	$T_{pm,avg}$		$T_{rel,avg}$	
(–)	(Nm)	(%)	(Nm)	(Nm)	(%)	(Nm)	(%)
1	0.344	50.9	0.342	0.168	49.0	0.17	51.0
2	1.044	39.9	1.040	0.329	31.7	0.71	68.3
4	2.726	36.6	2.729	0.658	24.1	2.07	75.9

Table 6.2: Torque components for the 6–slot 4–pole IPM–A machine.

I/I_N	$T_{Mxw,avg}$	ΔT_{Mxw}	$T_{dq,avg}$	$T_{pm,avg}$		$T_{rel,avg}$	
(–)	(Nm)	(%)	(Nm)	(Nm)	(%)	(Nm)	(%)
1	0.310	55.7	0.313	0.149	47.5	0.164	52.5
2	0.874	66.4	0.883	0.306	34.6	0.577	65.4
4	1.943	92.8	1.969	0.544	27.7	1.424	72.3

6.3.3. Finite element results

In the following, T_{Mxw}, T_{pm}, T_{rel} are reported, referring to the nominal current, I_N, and to two higher currents. All the simulated operating conditions refer to the corresponding operating point along the maximum torque per Ampere characteristic (MTPA).

Referring to the 4–pole IPM–A configurations, the computed torque components versus the rotor position for the 24–slot machine are shown in Fig. 6.6(a) while for the 6–slot machine in Fig. 6.6(b). The results of the computations are reported in Table 6.1 and Table 6.2. From the comparison, it follows that:

- The total average torque of the 6–slot machine is lower than the corresponding torque of the 24–slot machine. This is mainly evident at higher currents, when higher saturation occurs, which limits the torque.
- The decrease of the total average torque of the fractional–slot machine is almost equally divided between the two torque components. Both PM and reluctance torque components decrease in the same way. Thus, the iron saturation affects both the PM and reluctance torque components in an balanced way. This is not expected, since the q–axis path is mainly affected by the saturation than the d–axis path.
- As far as the dependance of the torque components on the current is concerned, the results confirm the expectations: the PM torque increases linearly with the current, while the reluctance torque increases with the current squared (at least until the magnetic circuit remains linear).

- The torque ripple of the 6–slot machine is always higher. This is more evident at higher currents, that is, during overload operating conditions. This means that the iron saturation is more influent in the fractional–slot machine. In particular, the tooth tips are more saturated.
- There is not a significant decrease of the reluctance torque components in the 6–slot machine. This is not as expected since, as reported above, it is commonly though that the rotor anisotropy seen for the stator is reduced adopting a fractional–slot winding. Nevertheless the reluctance torque remains a feature of the rotor and it is slightly modified by the stator configuration.

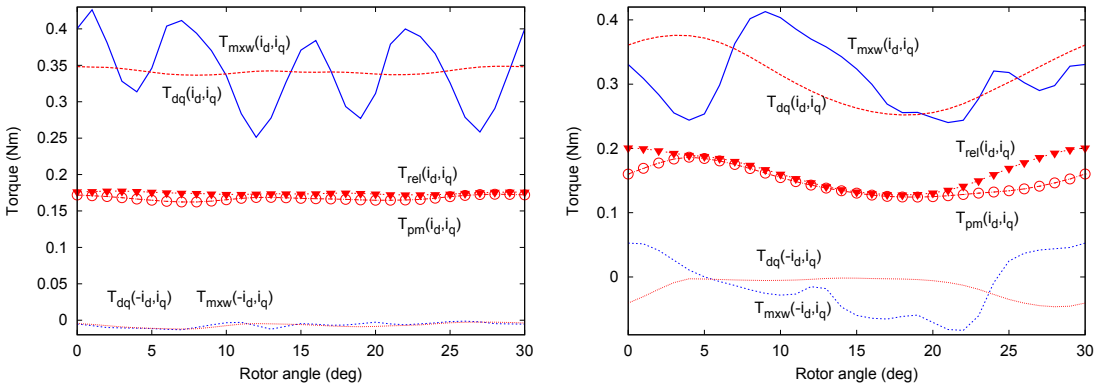

(a) 24–slot 4–pole IPM–A (b) 6–slot 4–pole IPM–A

Figure 6.6: Torque components of IPM–A machines versus rotor position (operation at nominal current).

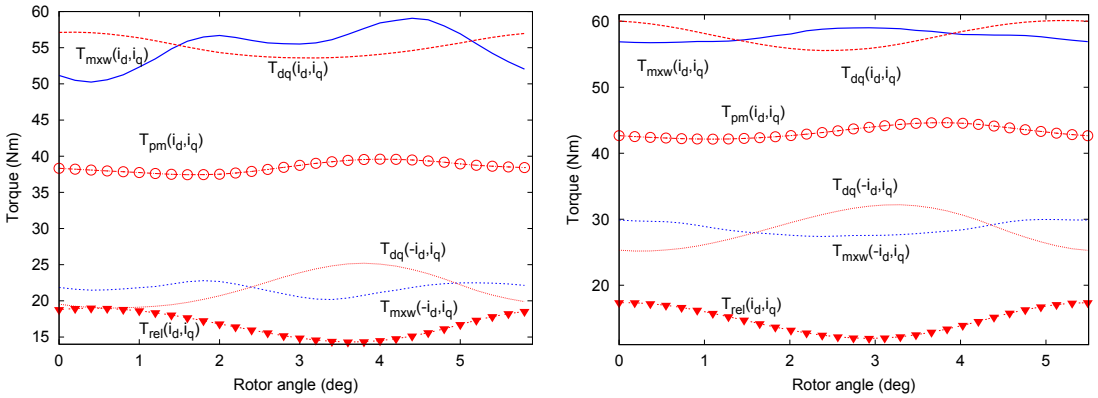

(a) 24–slot 20–pole IPM–B (b) 24–slot 22–pole IPM–B

Figure 6.7: Torque components of IPM–B machines versus rotor position (operation at nominal current).

Similar results are achieved with the 24–slot IPM–B configurations. The computed torque components versus the rotor position for the 20–pole machine are shown in Fig. 6.7(a) while for the 22–pole machine in Fig. 6.7(b). The results are reported in Table 6.3, 6.4, 6.5, and 6.6. Let us note that in these tables the additional results, as ΔT_{dq} and $T_{dq}(\theta_m = 0)$, are reported even they will be discussed in the following section.

Table 6.3: Torque components for the 24–slot 4–pole IPM–B machine.

I/I_N	$T_{mxw,avg}$	ΔT_{Mxw}	$T_{dq,avg}$	ΔT_{dq}	$T_{dq}(\theta_m = 0)$	$T_{pm,avg}$		$T_{rel,avg}$	
(–)	(Nm)	(%)	(Nm)	(%)	(Nm)	(Nm)	(%)	(Nm)	(%)
0.5	70.8	41.9	70.1	3.8	70.1	37.2	53.0	32.9	47.0
1	139.0	36.8	138.1	4.0	138.6	69.3	50.2	68.8	49.8
2	249.4	34.8	247.4	9.4	245.0	119.0	48.1	128.4	51.9
3	332.4	42.4	329.8	17.4	331.2	150.5	45.6	179.3	54.4

Table 6.4: Torque components for the 24–slot 16–pole IPM–B machine.

I/I_N	$T_{mxw,avg}$	ΔT_{Mxw}	$T_{dq,avg}$	ΔT_{dq}	$T_{dq}(\theta_m = 0)$	$T_{pm,avg}$		$T_{rel,avg}$	
(–)	(Nm)	(%)	(Nm)	(%)	(Nm)	(Nm)	(%)	(Nm)	(%)
0.5	42.6	65.0	43.1	29.9	49.5	22.3	51.8	20.8	48.2
1	105.5	60.0	106.9	34.0	124.1	52.8	49.4	54.1	50.6
2	172.4	83.1	174.9	16.6	190.2	84.2	48.2	90.6	51.8
3	183.4	115.0	184.5	63.0	139.4	87.7	47.5	96.9	52.5

In particular it could be noted that, increasing the pole number from 4 to 16, the weight of the two torque components is maintained, even if the number of flux–barriers per pole has been reduced from three to one. Oppositely the IPM–B geometries with 20 and 22 poles respectively shows a remarkable reduction of the reluctance torque component. In this case the high number of poles yields complicate to design a rotor pole geometry with more than one flux–barrier, limiting the possibilities to obtain a sufficient value of saliency, e.g. reluctance torque.

Contrarily to the common expectations, fractional–slot machines maintain a high reluctance torque component. Under overload operating conditions, both PM and reluctance torque components decrease at the same time. This means that fractional–slot machines are able to maintain the same features due to the rotor saliency.

The behaviour of fractional–slot machines is worst under overload with respect the corresponding integral–slot machines. In particular, the average torque decreases and the torque ripple increases. This is mainly due to the higher saturation. It occurs mainly along q–axis path affecting both T_{rel} and T_{pm}.

Table 6.5: Torque components for the 24–slot 20–pole IPM–B machine.

I/I_N	$T_{mxw,avg}$	ΔT_{Mxw}	$T_{dq,avg}$	ΔT_{dq}	$T_{dq}(\theta_m = 0)$	$T_{pm,avg}$		$T_{rel,avg}$	
(–)	(Nm)	(%)	(Nm)	(%)	(Nm)	(Nm)	(%)	(Nm)	(%)
0.5	55.13	16.0	55.2	6.4	57.1	38.5	69.7	16.7	30.3
1	121.2	16.6	121.3	17.8	131.4	78.3	64.5	43.0	35.5
2	214.1	15.5	214.0	34.5	246.1	130.3	60.9	83.7	39.1
3	253.2	9.05	253.9	48.8	318.0	150.0	59.1	103.9	40.9

Table 6.6: Torque components for the 24–slot 22–pole IPM–B machine.

I/I_N	$T_{mxw,avg}$	ΔT_{Mxw}	$T_{dq,avg}$	ΔT_{dq}	$T_{dq}(\theta_m = 0)$	$T_{pm,avg}$		$T_{rel,avg}$	
(–)	(Nm)	(%)	(Nm)	(%)	(Nm)	(Nm)	(%)	(Nm)	(%)
0.5	57.8	3.92	57.9	7.9	60.0	43.2	74.6	14.7	25.4
1	126.9	9.06	127.7	22.9	140.5	90.6	71.0	37.1	29.0
2	225.9	13.7	228.1	51.4	267.8	154.4	67.7	73.6	32.3
3	268.2	16.5	272.0	82.5	355.3	179.0	65.8	93.0	34.2

6.4. Torque computation issues

The finite element analysis of current controlled synchronous permanent magnet machines is commonly based on the classical d–q axis theory [79]. Taking advantages of d–q axis theory, some procedures have been developed recently to reduce the number of FE solutions necessary to compute the average torque and the torque ripple. The average torque of a synchronous PM motor can be estimated by means of a single FE analysis, if only fundamental harmonic is considered [78]. The model can be generalized considering MMF harmonics, highlighting the difference of the computation using the Maxwell stress tensor and the $d-q$ axis flux linkages, in [80]. Another approach, mainly based on the phase quantities, is described in [81] where techniques to estimate the motor losses are also introduced.

The reduction of number of FE simulations to estimate the average torque is imperative to limit the time of the analysis. Therefore it results extremely relevant in case of optimizations in which FE simulation are required instead of analytic methods.

In the aforementioned works, it has been shown that few finite elements solutions are enough to estimate the average torque and the torque ripple. This yields an immediate advantage on the computation time of a given machine geometry.

6.4.1. Torque behaviours

As reported in (6.8), the electromagnetic torque results equal to the sum of two terms: the $d-q$ flux component T_{dq} and the coenergy variation $\partial W'/\partial\vartheta_m$. For instance, Fig. 6.8 shows the motor torque T computed using the Maxwell's stress tensor T_{Mxw} using a solid line [82–84]. Then, the dashed line refers to the torque component T_{dq}. Obliviously the sum of torque component T_{dq} and the coenergy variation $\partial W'/\partial\vartheta_m$ yields the actual torque, (6.8), as shown by circles in Fig. 6.9. It corresponds perfectly to the torque computed using Maxwell's stress tensor.

With sinewave currents, d– and q–axis currents are constant with the rotor position. The partial derivative of magnetic coenergy with the rotor position, expressed in (2.17), is

$$\frac{\partial W'_m}{\partial\vartheta_m} = \frac{3}{2}p\left(i_d\frac{\partial\lambda_d}{\partial\vartheta_m} + i_q\frac{\partial\lambda_q}{\partial\vartheta_m}\right) - \frac{\partial W_m}{\partial\vartheta_m} \tag{6.13}$$

Therefore, since the coenergy variation is linked to the rate of change of flux linkage harmonics, it could be expected that the torque ripple is mainly included in the second torque term expressed by (6.8). It is possible to hypothesize that the variation of the flux linkages λ_d and λ_q is lower than the variation of their rates of change that appear in (6.13). In fact, the rate of change of a flux linkage harmonic of ν–th order is proportional to the flux linkage harmonic amplitude times the order ν. Consequently, the torque component T_{dq} (6.10) should be only slightly affected by the harmonics of the flux linkages.

This remark has been verified if an integral–slot winding is considered [78, 80]. Conversely, with a fractional–slot winding the torque component T_{dq} exhibits a relevant ripple that could be comparable or higher than the actual motor torque. As example is reported in Fig. 6.8(b). This behavior, caused by the iron saturation, affects mainly the IPM synchronous machine topology.

In the following the IPM–B geometries reported in Fig. 6.5 are considered in the torque analysis.

6.4.2. Motor capability computation

In order to compute the MTPA trajectory it is necessary to compute both flux linkage at various current vector angle α_i^e, with fixed current amplitude. By fixing the voltage limit, the flux linkage is used to compute the maximum motor speed for each operating condition. Then the torque versus speed can be pointed out [79].

To the aim of reducing the number of FE simulations the rotor position is fixed at a given value ϑ_m, and only a single simulation is carried out for each current vector angle α_i^e [80]. Both T_{Mxw} and T_{dq} are computed. The behavior of the torque versus the current vector angle α_i^e, with constant rotor position and current amplitude, exhibits obviously a maximum for a specific value of α_i^e. This angle, evaluated along the T_{dq} behaviour, usually individuates for integral–slot winding the point of the maximum torque per Ampere (MTPA) trajectory with a suitable approximation (at a given current amplitude).

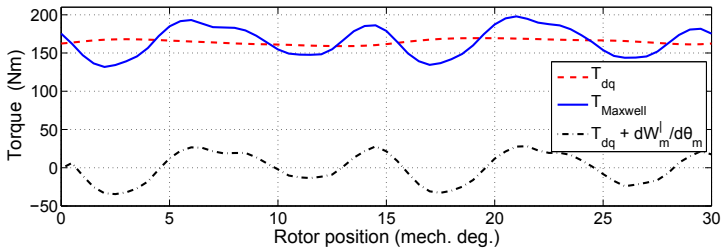

(a) IPM 24/04 - integral–slot winding

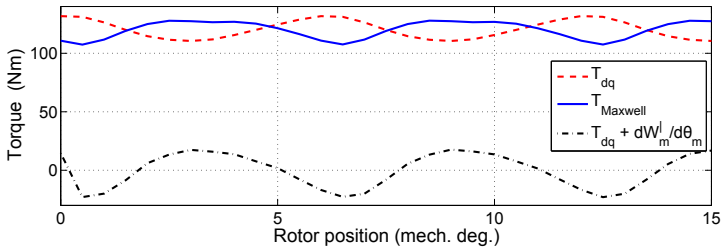

(b) IPM 24/20 - fractional–slot winding

Figure 6.8: Torque behavior: solid line refers to Maxwell's stress tensor torque computation, dashed line refers to the torque computation of (6.10), and the dot-dashed line refers to the coenergy variation $\partial W'/\partial\vartheta_m$.

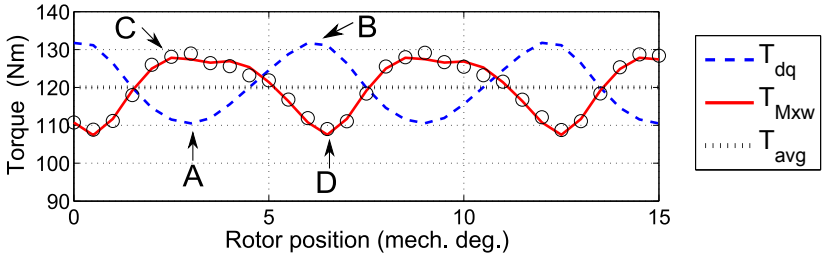

Figure 6.9: 24/20 IPM–B Torque behavior: solid line refers to the computation using Maxwell's stress tensor, whose average value is reported as dotted line, dashed line refers to (6.10), circles refer to (6.8).

However, the torque ripple highlighted in Fig. 6.9 (for both T_{Mxw} and T_{dq}) involves a dependance of the torque on the rotor mechanical position ϑ_m. The rotor position considered in the FE simulations are: $\theta_{m,A}$, $\theta_{m,B}$, $\theta_{m,C}$ and $\theta_{m,D}$. These rotor angles refer to the maximum and minimum oscillation points of torque behaviors, T_{Mxw} (solid lines) and T_{dq} (dashed lines), respectively. The reference points selected are highlighted in Fig. 6.9 for the24/20 IPM–B configuration. The discrepancy between two torque behaviours computed at different rotor mechanical position ϑ_m, is highlighted in Fig. 6.10 for the configuration 24/04 and 24/20 IPM–B.

It could be noted that, when the torque versus current vector angle curves are close one to the other there is a minimum influence of the rotor position ϑ_m on the torque computation. Conversely the influence of ϑ_m results to be relevant when the curves are significantly different.

As expected, the integral–slot winding shows shows a torque component T_{dq} that

results to be appropriate for the average torque computation, since the maximum discrepancy is about 4%. Conversely the motor torque T_{Mxw} results highly affected by the rotor mechanical position ϑ_m, with an oscillation of 70 Nm.

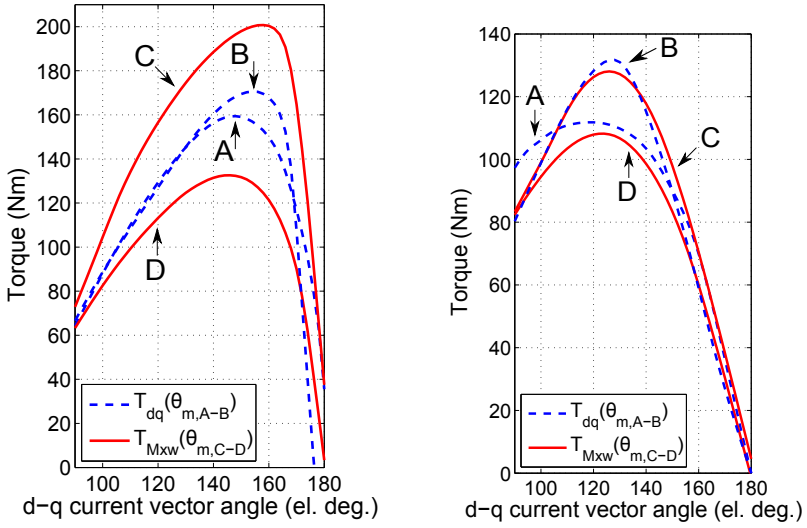

(a) 24/04 IPM (b) 24/20 IPM

Figure 6.10: IPM–B motors: torque versus current vector angle α_i^e with nominal current I_N at different rotor position θ_m.

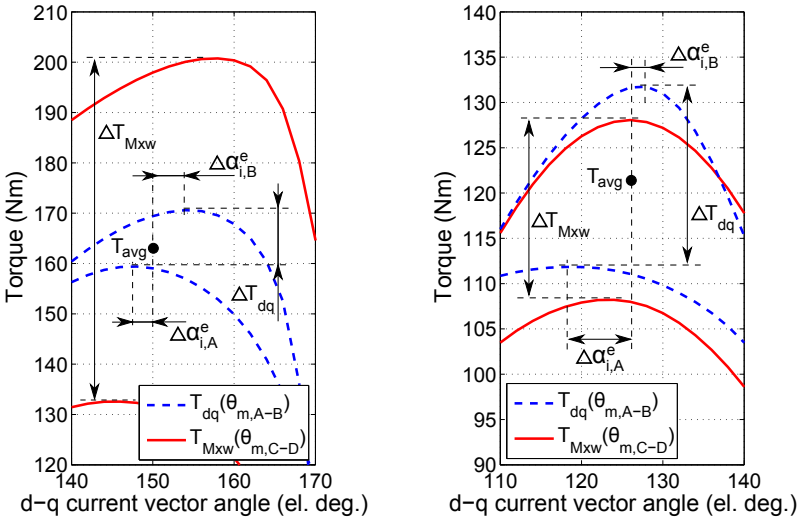

(a) 24/04 IPM (b) 24/20 IPM

Figure 6.11: IPM–B motors: detail of the torque versus current vector angle α_i^e with nominal current I_N at different rotor position θ_m.

On the other hand, the fractional–slot configurations exhibit a relevant dependence of both T_{dq} and T_{Mxw} on the rotor position. The difference of the torque behaviors T_{dq}, computed at rotor angle $\vartheta_{m,A}$ and $\vartheta_{m,B}$ results to be comparable or higher than

Table 6.7: Average torque and torque ripple for the 24–slot 20–pole SPM machines with both double–layer (DL) and single–layer (SL) winding.

I/I_N	SPM DL				SPM SL			
	$T_{Mxw,avg}$	T_{dq} $[\theta_m = 0]$	ΔT_{Mxw}	ΔT_{dq}	$T_{Mxw,avg}$	T_{dq} $[\theta_m = 0]$	ΔT_{Mxw}	ΔT_{dq}
(–)	(Nm)	(Nm)	(%)	(%)	(Nm)	(Nm)	(%)	(%)
0.5	94.9	95.0	3.2	0.9	97.8	97.3	12.0	1.1
1	187.5	188.1	1.6	0.9	189.8	190.8	10.1	2.6
2	358.3	360.3	2.7	2.5	349.4	359.7	6.5	7.4
3.75	577.5	584.4	2.6	5.5	533.4	559.5	4.7	10.1

the corresponding variation obtained using T_{Mxw}. The influence of the rotor angle ϑ_m involves also a wrong estimation of the MTPA angle that can reach an error of 20%.

This error $\Delta\alpha_i^e$ is highlighted in Fig. 6.11 for both the 24/20 and the 24/22 configuration respectively. The figures report the position of the MTPA point T_{avg} obtained with different rotor mechanical position ϑ_m. The actual MTPA point that refers to the average torque is labeled as T_{avg}. It could be noted that, as expected, for the 24/20 configuration the error in the current angle estimation in point A ($\Delta\alpha_{i,A}^e$) is more than double the variation obtained for the 24/04 configuration ($\Delta\alpha_{i,A}^e$ and $\Delta\alpha_{i,B}^e$). In Fig. 6.11 is also highlighted the amplitude of the torque ripple, computed using Maxwell's stress tensor ΔT_{Mxw} and the $d-q$ axes theory ΔT_{dq}.

6.4.3. Finite elements analysis

Some results of the FE simulations have been already reported in Tables 6.3, 6.4, 6.5, and 6.6. In addition to the IPM–B configurations of Fig. 6.5, two SPM 24–slot 20—pole synchronous machines are considered in order to evaluate the impact of the anisotropic rotor geometry. The SPM machines have different fractional–slot winding: double–layer winding and single–layer winding respectively.

Torque. The average torque and the torque ripple values have been computed using both the Maxwell's stress tensor T_{Mxw} and the $d-q$ fluxes T_{dq}. In addition the first value of the T_{dq} behaviour, computed for $\vartheta_m = 0$ degree, is reported under the label $T_{dq}(\theta_m = 0)$. Adopting the assumptions of [78] described above, the value of $T_{dq,\theta_m=0}$ should represent a suitable approximation of the average torque $T_{Mxw,avg}$.

Fixing the nominal peak slot current $\hat{I}_{slot} = 1700$ A, the simulations are carried out at different values of the electrical load; corresponding to 0.5, 1, 2 and about 3 times the nominal one.

Referring only to IPM machines the integral–slot winding configuration (24/4) shows the lowest value of ΔT_{dq}, even if actual torque ripple is remarkable. Conversely

the fractional–slot machines highlight a high torque ripple of the T_{dq} component (ΔT_{dq}), that result to be even higher that the actual one (ΔT).

Conversely, the SPM machines seems to be less affected by the winding topology. In fact, even if provided of a fractional–slot winding both the SPM machines (with double–layer and single–layer winding) allow an excellent approximation of the average torque with only one value of the T_{dq} torque, i.e. $T_{dq}(0)$. Finally it has been evaluated that with the nominal slot current, the effect of a different current vector angle α_i^e (e.g. different demagnetizing current component) is negligible on the torque ripple.

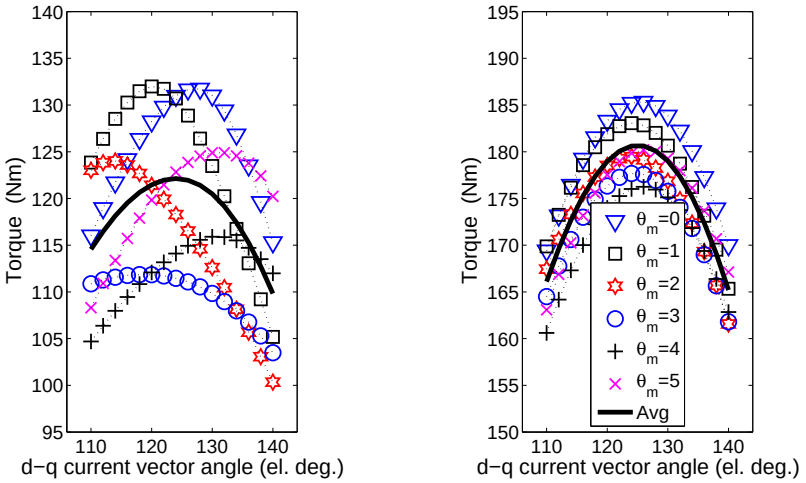

(a) Saturated 24/20 IPM

(b) Linear 24/20 IPM

(c) Saturated 24/22 IPM

(d) Linear 24/22 IPM

Figure 6.12: Torque behaviours vs current vector angle for different rotor position both with saturated iron and linear iron (I_N).

Saturation influence. Comparing the FE results it is visible the relevance of the iron saturation results as a cause of the torque ripple for both T_{Mxw} and T_{dq}. Let us note that, with a peak slot current equal to three times the nominal one, all the configurations exhibit a ΔT_{dq} comparable or higher than the corresponding actual ΔT.

In order to underline the effect of saturation, some FE simulations with linear (non saturated) iron have been carried out. Thus the iron saturation greatly affects the oscillation of the torque component T_{dq}.

Fig. 6.12 shows the behaviour of the torque component T_{dq} versus the current vector angle α_i^e, referring to both saturated iron and linear iron (constant $\mu_r = 7000$). Each behaviour refers to a different position of the rotor ϑ_m (from 0 to 5 mech. degrees). In addition the actual behaviour is reported with solid line (labeled as Avg). The discrepancy between the different behaviours with saturated iron is considerable. Oppositely with linear iron the discrepancy of the torque behaviours results negligible, confirming the rule of the iron saturation.

It should be noted that, for the linear iron simulations, the rotor geometry is modified removing the iron ribs. Air ribs are considered both between the flux–barriers and PMs and between the flux–barriers and the air gap. This increase of the main flux yields, of course, an increase of the average torque of the motor.

MMF sub–harmonics influence. The configurations 24/20 and 24/22 are characterized by the presence of spatial sub–harmonics in the MMF harmonic content. In addition the 24/20 configuration, if realized with a single–layer winding, shows an higher harmonics amplitude (especially the first sub–harmonic) than the corresponding double–layer one [85].

Comparing the results of Table 6.7 for the SPM motors, it can be noticed a significant increase of the torque ripple ΔT_{dq}. The torque ripple increase is directly linked to the higher sub–harmonic amplitude.

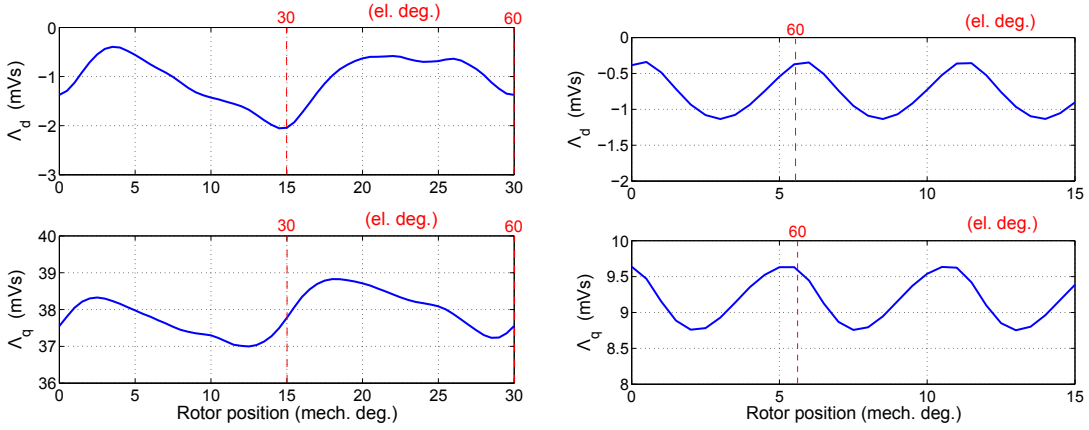

(a) 24/04 IPM ($\alpha_i^e = 150$ deg)

(b) 24/22 IPM ($\alpha_i^e = 124$ deg)

Figure 6.13: IPM motor $d-$ and q–axis flux linkages versus rotor position under load (nominal current I_N).

Flux linkages. From the FE simulations, it has been verified that the flux ripples increase due to the saturation but not as much as the torque ripple of the T_{dq} component.

Analyzing the harmonic content of the flux linkages behavior, it is possible to note that both integral–slot IPM machines and fractional–slot unsaturated SPM machines show $d-$ and $q-$axis fluxes characterized by harmonics of sixth and twelfth order. The amplitude of the two components results to be comparable.

Conversely the fractional–slot IPM machines and the fractional–slot saturated SPM machines exhibit flux linkages characterized by only a relevant harmonic of sixth order. This difference is evident comparing the flux linkages of the 24/4 configuration and the 24/22 configuration in Fig. 6.13(a) and Fig. 6.13(b) respectively. The preponderance of one harmonic is due to the relevance of the sub–harmonics, which induced frequency results to be a harmonic of sixth order [85].

6.4.4. Summary of the results

From the results reported above it is evident that a special care has to be dedicated to the computation of both average torque and torque ripple in case of IPM machines with fractional–slot winding. A significant discrepancy between the estimated average torque (simulating only one rotor position) and the actual value is highlighted. It is possible to summarize the results as:

- The iron saturation is the fundamental cause of the torque ripple for the component T_{dq}.
- During high overload the torque T_{dq} is highly oscillating, regardless of the machine topology. In this case, higher the demagnetizing current component (i.e. negative I_d) higher the torque ripple ΔT_{dq}.
- With nominal electric load (i.e. rms current density of 6 A/mm^2) only the IPM machines exhibits a significant oscillation of the torque component T_{dq}. It has been highlighted that the presence of MMF sub–harmonics yields an increase of the torque ripple ΔT_{dq} while the value of the current vector angle α_i^e result to have negligible effects.

From these remarks, it results that a proper estimation of average torque and ripple of the motor under overload (high saturation) requires a set of field computations within a sixth of the electric period avoiding a single computation. This is remarkable with fractional–slot machines.

6.5. Application: design of a fractional–slot ISA machine

6.5.1. Introduction

The size of the electric generator in the modern car is more and more increasing in the last years, as a consequence of the highest demand of electric power described in chapter 1. There is a worldwide effort in using more and more electrical driven auxiliaries in road vehicles and in replacing the hydraulic and mechanical actuators by the electromechanical counterpart.

As an example both ICE starting and successive power generation features can be performed by a single electrical machine. Such an electrical machine is called Integrated Starter–Alternator (ISA) [86]. The interest in ISA is growing up in order to remove the starter motor from the vehicle, reducing the system cost. In addition, the ISA system is crucial to achieve stop/restart at urban traffic jam and traffic lights, driving/launching assistance to ICE during vehicle acceleration, braking regeneration during vehicle deceleration, vibration damping etc. These functions are far beyond what the name of ISA self explains.

An IPM machine geometry has been chosen as a candidate for a ISA application.

6.5.2. Application requirements

Typically an ISA drive has to deliver a starting torque of some tens of Nm (or more for big trucks), from standstill up to $200-400$ rpm, which is the minimum starting speed of an ICE. The duration of the starting phase is normally shorter than 1 second. At higher speed, ISA has to operate in generating mode from the minimum ICE operating speed (generally about 1000 rpm) up to the maximum ICE speed, with a wide constant–power speed range and a proper efficiency.

The main specifications of the developed ISA prototype [1] were (i) 1 kW at 3000 rpm output power capability, (ii) 30 Nm standstill torque capability, (iii) 250 V dc input supply. Three main operating regions have to be considered [2]:

- a constant starting torque of 30 Nm from standstill to 300 rpm;
- above 300 rpm up to a speed in the range of 1500 to 2500 rpm, an accelerating torque decreasing inversely with the speed, for a constant power of 1 kW;
- then, the ISA drive should change smoothly from motoring to generating mode, exhibiting a constant torque of -3 Nm, up to the maximum speed of 3000 rpm.

[1] The designed ISA prototype has been developed for the IEEE International Future Energy Challenge (IFEC) 2007.

[2] During the competition a further limit for European researcher are the US NEMA56 size constraints that has to be satisfied.

6.5.3. The ISA machine design

A 12–slot 8–pole structure is selected, thus the machine is provided of a fractional–slot winding with non–overlapped coils. Fig. 6.14 shows the final stator and rotor geometry adopted in the manufactured prototype.

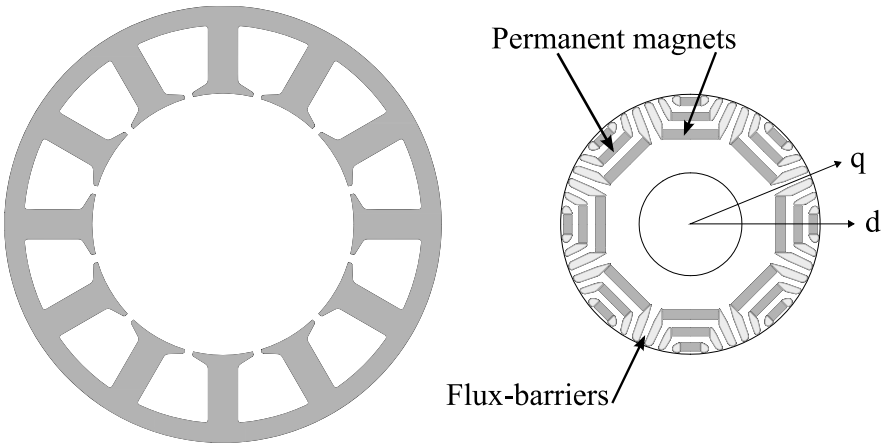

Figure 6.14: Structure of the ISA prototype: 12–slot 8–pole IPM machine.

The main data of the final prototype are reported in Table 6.8. The rotor has three flux barriers per pole. The cross section dimensions of the PMs are equal to 2.5×5.8 mm, 2.5×11.6 mm and 3×17.4 mm respectively.

Some geometric characteristics of Table 6.8 (i.e. external diameter, air–gap, fill factor) were fixed a priori due to the size limitations of both the requirements and the partner company. Then, the inner diameter has been maximized in order to limit iron saturation.

Preliminary design steps. At first some preliminary evaluations of the machine parameters and performance have been carried out in order to estimate the possibility to fulfill the requirements.

In order to maximize the the saliency a pole structure with three flux–barriers is adopted, Fig. 6.14. Each flux–barrier is provided of NdFeB PM placed on the pole axis. The thickness of the barrier is designed according to the PM thickness, which is selected so as to avoid PM demagnetization with the higher currents.

From a preliminary parameter estimation [11] the PM flux linkage has been roughly evaluated equal to $\Lambda_m = 0.18\, Vs$. Then the analytical model based on a lumped–parameter network, presented in chapter 3, has been adopted to select the suitable set of flux–barrier angles that satisfy the requirements of average torque.

From the results of the model, the values of the current density, tooth and back iron flux densities are estimated. The copper losses are computed from the copper volume and the current density. The iron losses are roughly computed adopting the peak value of the flux density in the teeth, B_t, and in the back iron, B_{bi}. A sinusoidal

Table 6.8: Geometric characteristics of definitive geometry

Characteristic		Dimensions
External diameter	D_e	140 mm
Inner diameter	D	84 mm
Phases number	m	3
Pole number	$2p$	8
Slot number	Q	12
Slot area	S_{slot}	377.1 mm^2
Slot height	h_s	21.83 mm
Back iron height	h_{bi}	6.17 mm
Air–gap	g	0.4 mm
Stack length	L_{stk}	75 mm
Shaft diameter	D_{sh}	33 mm
Fill factor	k_{fill}	0.3
PM remanent flux density	B_{rm}	1.05 T

flux density waveform is assumed. From the specific loss of the lamination, the losses in the operating points are computed according to the electrical speed.

Therefore, the efficiency of the entire system is estimated to be $\eta_t = 82.7\%$ at 67 Hz and $\eta_t = 78\%$ at 200 Hz, assuming an efficiency of the inverter to be 95%.

Finite element computation. Finite element analysis has been adopted to refine the design of the machine. At first, the result obtained from the analytical study has been compared with the finite element computation.

As an example, the no–load flux density computed with the analytical method and the no–load flux density obtained with FE simulation are compared in Fig. 6.15. The flux density distribution computed analytically results to be a three step square shape. A satisfactory agreement between them is evident.

The adopted three–phase star–connected fractional–slot double–layer winding with non–overlapped coils is provided of 76 turns per coils (conductor diameter: 2×0.71 mm).

Finite element analysis is used to compute the d– and q–axis flux linkages of the machine. A correct prediction of such flux linkages, including saturation and cross–saturation effects, is necessary for the design of the control algorithms performed later. Fig. 6.16 shows the d– and q–axis flux linkages Λ_d and Λ_q versus d– and q–axis currents I_d and I_q.

The d–axis flux linkage values have been performed for negative d–axis current setting to zero the q–axis current and then setting the q–axis current to 12 A. They are reported on the left half plane, as $\Lambda_d(I_d, 0)$ versus I_d using solid line, $\Lambda_d(I_d, 12)$ versus I_d using dashed line. At the same manner, the q–axis flux linkage has been derived as

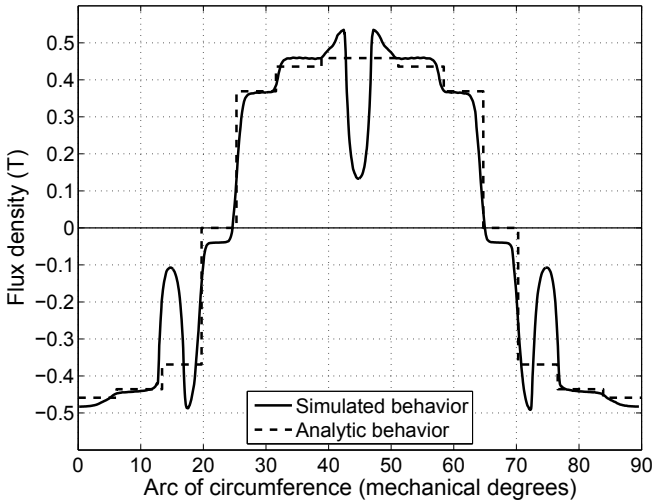

Figure 6.15: Air–gap flux density distribution at no–load

a function of q–axis current and setting the d–axis current to zero and then to -12 A, respectively. They are reported on the right half plane, as $\Lambda_q(0, I_q)$ versus I_q using solid line, $\Lambda_d(-12, I_q)$ versus I_q using dashed line.

Fig. 6.16 highlights the relevance of the iron saturation that occurs along both the axes and mutually between them. Due to the cross–saturation phenomena there is a relevant variation of the d–axis flux linkages due to the q–axis current. The analysis of the cross–coupling effect is strongly affected by the material properties. In fact, some characteristics are not often available with a suitable detail. For instance the B–H iron curve, the mechanical tolerance and the physical effect due to the manufacture process. In addition a suitable procedure has to be adopted during the measurements in order to avoid significant errors.

The discrepancy between prediction and the initial measurements in Fig. 6.16 is due to these uncertainties. This aspect will be deeply analyzed in a dedicated section of this chapter.

Fig. 6.17 and Fig. 6.18 show the simulated torque behavior versus rotor angle, corresponding to two torque levels: the base torque of 9.6 Nm and the overload starting torque of 30 Nm. The nominal torque, equal to 9.6 Nm, is obtained at base speed (1000 rpm) with the nominal current density equal to 6 A/mm^2. This corresponds to a stator current $\hat{I}_{FE} = 6.7$ A. The predicted torque behaviour is reported in Fig. 6.17, and compared with measurements that are described hereafter.

The estimated torque ripple is about 25%, which has been assumed acceptable for this application. The remarkable torque ripple is due to the rotor structure, that has been designed in order to maximize the starting torque. In fact, a relevant volume of PM has been used, causing local iron saturation and then additional torque ripple.

With current density amplitude about four times the nominal one (i.e. 22 A/mm^2), an average starting torque equal to 30 Nm is achieved. In such operating point, the torque ripple is equal to 25.8% as shown in Fig. 6.18.

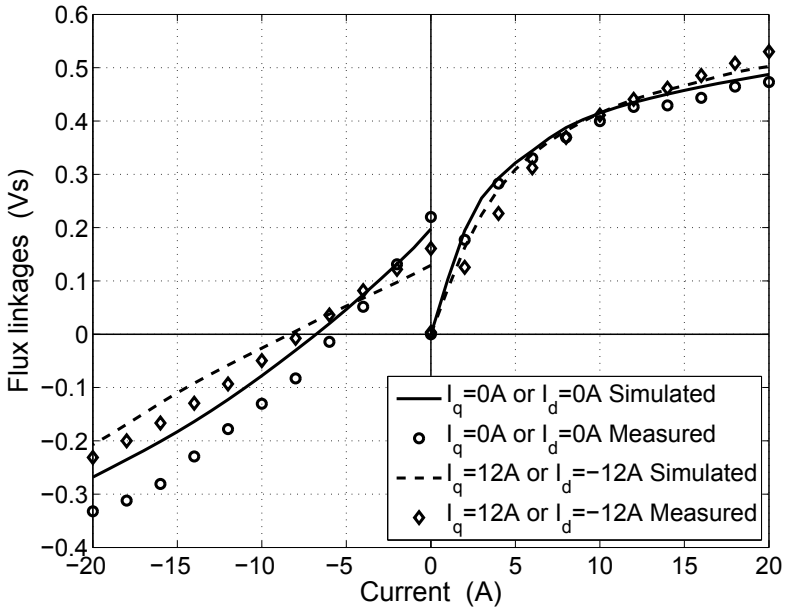

Figure 6.16: Simulated and measured current–flux characteristics: $\Lambda_d(I_d, I_q)$ in the left half plane, $\Lambda_q(I_d, I_q)$ in the right half plane

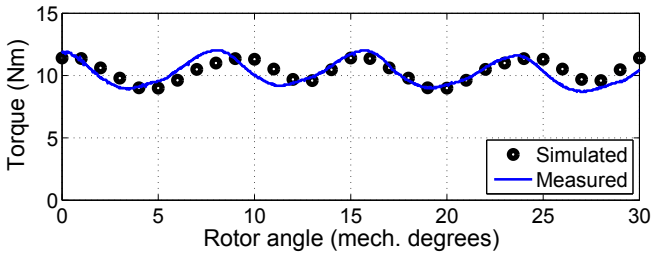

Figure 6.17: Simulated and measured torque behavior vs. rotor angle at nominal current ($\hat{I}_{FE} = 6.3$ A, $\hat{I}_{ME} = 6.7$ A)

6.5.4. Control algorithms of the ISA drive

A vector current control in synchronous $d - q$ reference frame is implemented in the prototype inverter, as shown in Fig. 6.19. The two current loops are closed using two PI controllers. Current references are derived from the torque demand τ^*, the limits of which are managed according to ISA specifications. The drive is a torque controlled drive; however it includes a speed loop in order to manage the transition from motoring to generating operations in automatic way.

Current reference signals are derived from the desired torque. The adopted solution consists in implementing an operating line placed on the MTPA locus to satisfy the starting specifications (lower speed). The line then moves toward the MTPV locus in the low torque range (that is at high speed when the drive operation is limited by the voltage capabilities of the inverter). The implemented torque–to–current control law is

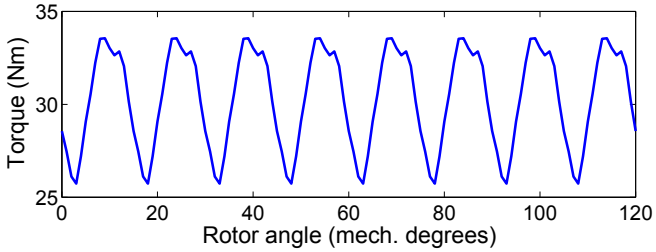

Figure 6.18: Torque behavior vs. rotor angle at current higher than the nominal current ($\hat{I}_{FE} = 23.2$ A)

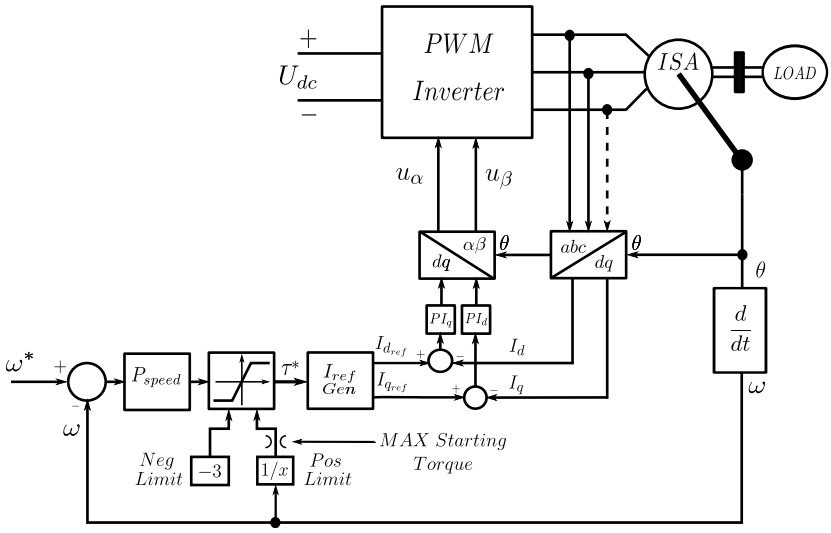

Figure 6.19: Control scheme of the ISA drive

shown in Fig. 6.20, and is given by

$$i_q = 0.5 \cdot \tau^* \tag{6.14}$$

$$i_d = -6.5 - 0.5 \cdot |i_q| \tag{6.15}$$

It is worth noticing that the no–load d–axis current is equal to -6.5 A. It corresponds to the short–circuit current of the ISA, i.e. the machine characteristic current that makes the d–axis flux linkage to be zero.

The value is directly recognizable in Fig. 6.16, while the measured value results slightly lower. Thus the no–load currents $i_d = -6.5$ A and $i_q = 0$ A are the coordinates of the short circuit operating point in the $d - q$ current plane, that is the center of the voltage limits. Lower (in absolute value) no–load d–axis current can be adopted to reduce the Joule losses in the low–medium speed range. Considering the uncontrolled generator operations (UGO), it has been verified that the current is limited by the machine self–inductance avoiding to exceed the nominal current. Therefore, inverter diodes will not be exposed to dangerous overcurrents.

Motoring to generating transition is managed by an outer speed loop incorporating a simple P (proportional) controller. The output of the controller is the non–limited

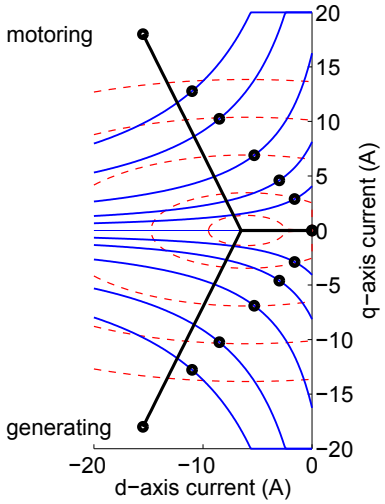

Figure 6.20: Constant torque loci (solid line) and constant voltage loci (dashed line), torque–to–current control law (bold line), and MPTA locus (dots)

torque demand, which is the input of the torque limit strategy described above. The speed reference ω_{ref} is the speed of the transition from motoring to generating operation. The gain of the P controller is high enough to cause the action of torque limiter at any speed (producing a torque control mode operation as required), apart from a narrow range of speed around the speed reference where the transition occurs.

6.5.5. Experimental tests

The ISA prototype is shown in Fig. 6.21. The ISA drive uses a prototype three–phase IGBT inverter controlled by a Digital Signal Processor programmable via serial communication line. The inverter used for the experimental tests, applies a vector PWM control with a switching frequency of 10 kHz. The currents are measured by means of 2 Hall sensors.

Several tests have been carried out on the IPM machine with a 250 V dc bus voltage. A picture of the test benches used for the motor characterization is shown in Fig. 6.22. With the high speed bench, a vector–controlled induction motor is used to load the ISA drive during motoring mode, and to impose the speed during generating mode. The torque measurements are carried out by means of the low speed test bench. A 100–Nm torque transducer has been used for all measurements.

The first test is the measurement of the back EMF, which has been performed at 606 rpm as shown in Fig. 6.23. From this test, the PM flux linkage is achieved to be $\Lambda_m = 0.248$ Vs. Such a PM flux linkage results slightly higher than predicted ($\Lambda_m = 0.195$ Vs), probably due to the different temperature of the PM and the different saturation of the iron bridges.

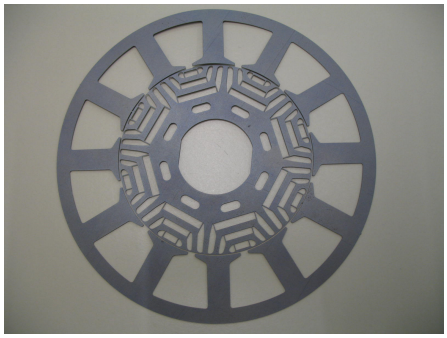

(a)

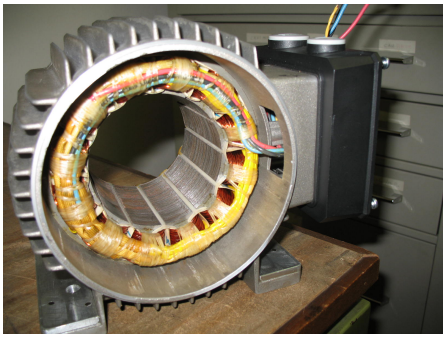

(b)

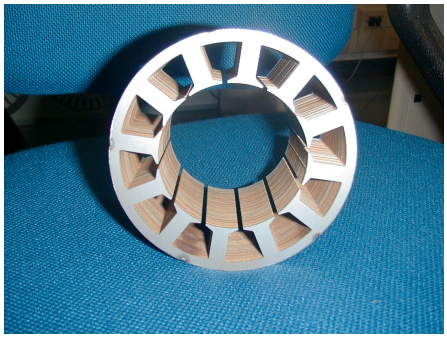

(c)

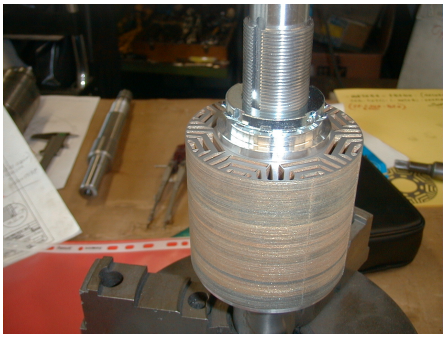

(d)

(e)

(f)

(g)

Figure 6.21: ISA prototype: (a) machine, (b) motor, (c) stator, (d) rotor, (e) commercial inverter, (f) end winding connections side, (g) end winding.

Torque measurements

In order to verify the predicted value of torque, some measures at base speed have been carried out with different d– and q–axis currents. The obtained contour map of torque is shown in Fig. 6.24. It was found an appreciable agreement between tests and predictions.

An example of torque time–behavior is reported in Fig. 6.17, under nominal current, in which it is possible to compare such torque behavior with that simulated. At nominal

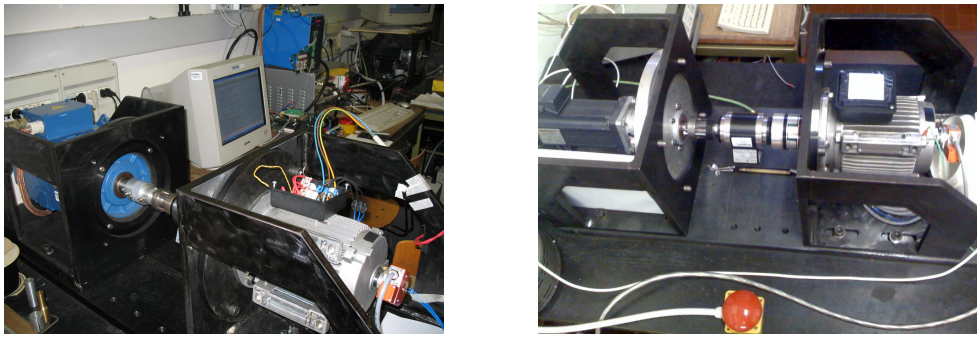

(a) (b)

Figure 6.22: Test benches for ISA machine: (a) high speed, (b) low speed.

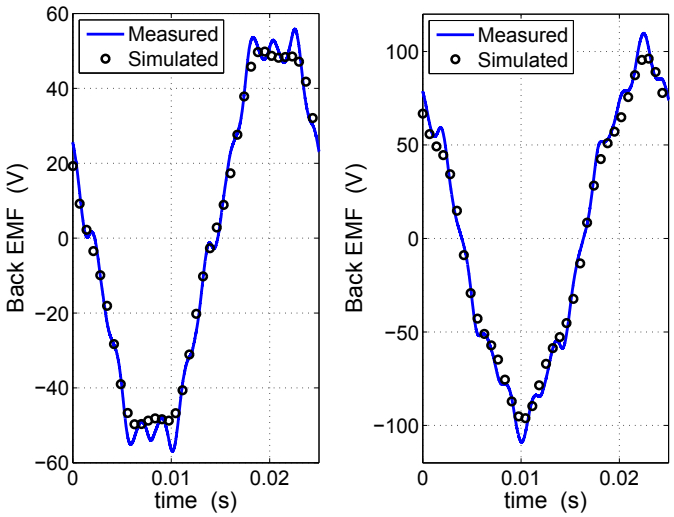

(a) (b)

Figure 6.23: Measured and simulated back EMF vs. time: (a) phase–to–neutral voltage, (b) phase–to–phase voltage.

current, the average measured torque results slightly higher than 10 Nm, satisfying the requirements. The ripple of torque is equal to about 29% of the average value.

The current vector angle yielding the MTPA is detected by means of locked–rotor tests for each phase current amplitude. The rotor is locked and the stator is supplied so as that the magnetic field rotates at very low speed (i.e. the supply frequency is fixed to $f \simeq 0.5$ Hz). The torque behavior versus the current vector angle is shown in Fig. 6.25, for different current amplitudes. The comparison between the measured peak torque and the predicted values is shown in Fig. 6.26, showing a good agreement. Each torque curve can be expressed by means of the Fourier series expansion, so as to achieve the first and the second harmonic due to the PM and the rotor saliency torque contributions, respectively.

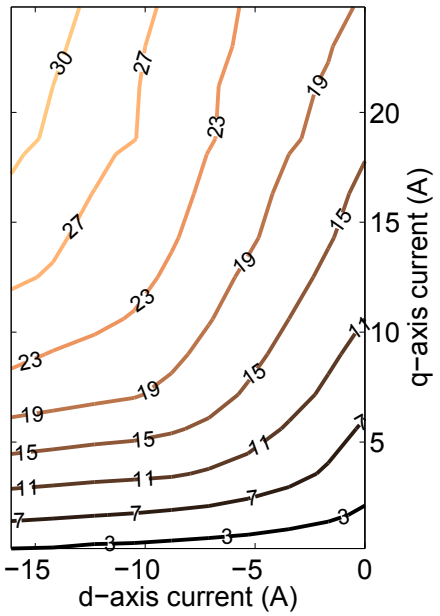

Figure 6.24: Map of measured constant–torque loci in the I_d–I_q plane

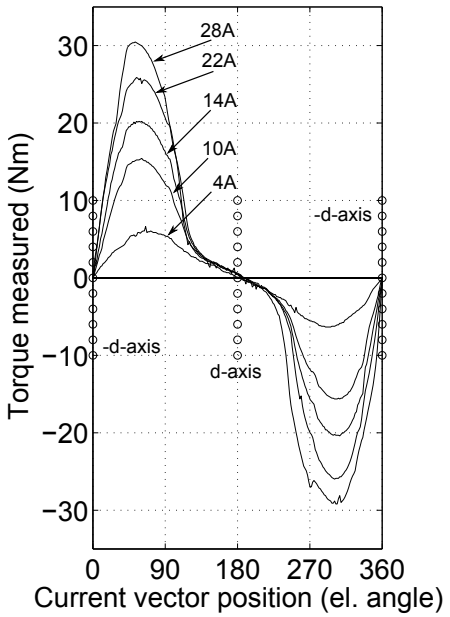

Figure 6.25: Measured torque behavior with locked–rotor and different phase current ($\hat{I} = 4, 10, 14, 20, 28$ A).

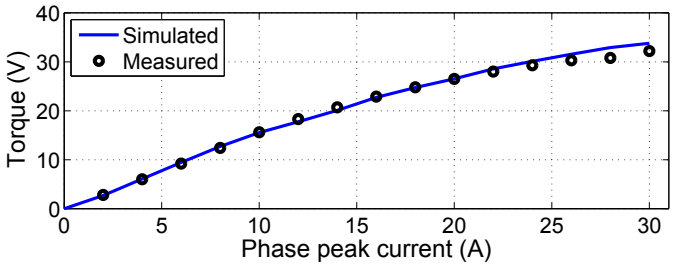

Figure 6.26: Simulated and measured, with locked rotor tests, torque at different phase peak current.

Table 6.9: Measured peak phase current, peak torque and current vector angle α_i^e with locked–rotor test.

$\hat{I}$ (A)	$\hat{T}$ (Nm)	α_i^e	$\hat{I}$ (A)	$\hat{T}$ (Nm)	α_i^e	$\hat{I}$ (A)	$\hat{T}$ (Nm)	α_i^e
2	2.8	91	12	18.3	123	22	28	121
4	6	115	14	20.7	124	24	29.3	126
6	9.2	123	16	22.9	124	26	30.3	125
8	12.4	123	18	24.8	115	28	30.8	128
10	15.6	121	20	26.5	118	30	32.2	130

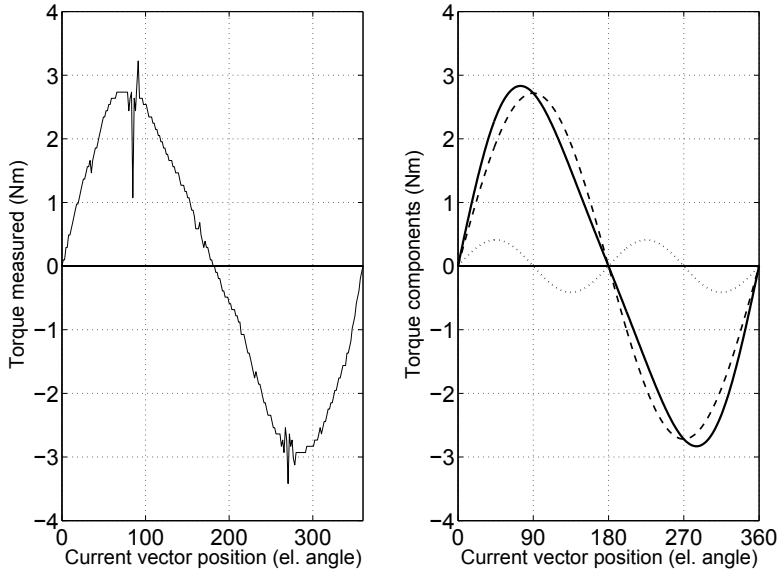

(a) $\hat{I} = 2$ A

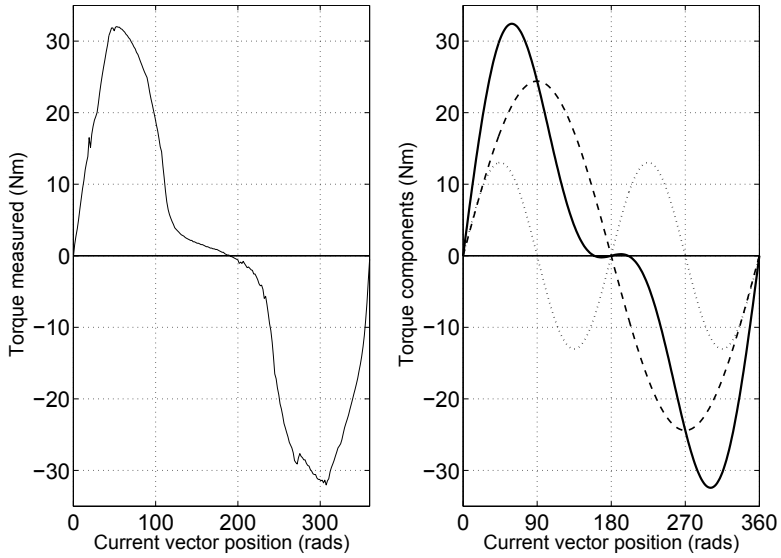

(b) $\hat{I} = 30$ A

Figure 6.27: Measured torque with locked–rotor test and its components: (a) current amplitude $\hat{I} = 2$A, (b) current amplitude $\hat{I} = 30$A. The measured torque curve (solid line) is split in its two component: PM torque component (dashed line) and reluctance torque component (dotted line).

Two examples are reported in Fig. 6.27: the torque behaviour measured is repeated filtered (solid line) on the right as a sum of the PM torque component (dashed line) and the reluctance component (dotted line). With a current amplitude of $\hat{I} = 2$ A the reluctance component is piratically equal to zero, while with $\hat{I} = 30$ A the two components are almost comparable. Comparing Fig. 6.27(a) and Fig. 6.27(b) the shift of the peak torque is evident. This shift corresponds to variation of the increase of the current vector angle yielding the MPTA from low saturation condition to the high

saturation condition (overload). It is worth noticing that, Fig. 6.27 shows the capability of the machine to provide the the starting torque is achieved with a current lower than the inverter limit (30 A).

The torque behaviours of Fig. 6.25 has value equal to zero when q–axis current is zero and only d–axis current is supplied. Therefore the transition of the current vector across d–axis can be easily recognized in Fig. 6.25 or in Fig. 6.27(b). The maximum torque occurs when the current vector meets the MTPA trajectory.

The distance between two corresponding zero crossings corresponds to half period of the torque waveform. By measuring the x–axis distance between torque peak occurrence and zero crossing point, the current vector angle of the MPTA trajectory is found. Therefore the corresponding values of α_i^e for given currents are reported in Table 6.9.

Dynamic tests

In order to verify the correct behavior of the control some dynamic tests have been carried out. During the tests a cut–off speed equal to 1500 rpm is considered, while the starting-torque is limited to the value of 20 Nm, avoiding an excessive inverter stress. Fig. 6.28 and Fig. 6.29 show the behavior of motor torque, speed and d–q axis current versus time during the starting of the ISA. It should be noted in Fig. 6.29 that d-q axis currents follow the corresponding current references in a satisfactory way.

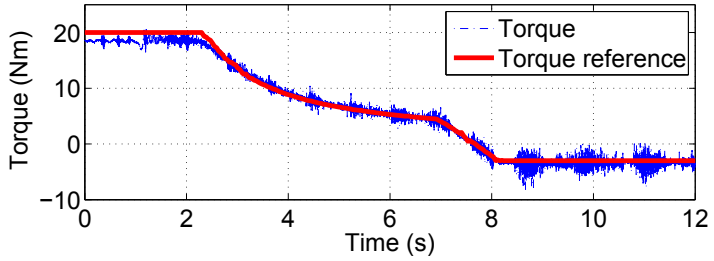

(a) Torque

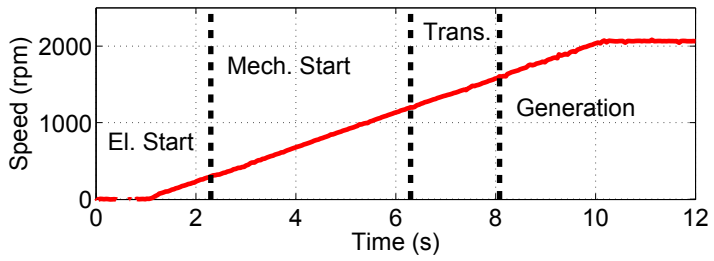

(b) Speed and operating regions

Figure 6.28: Test with starting-torque $T_{st} = 20$ Nm and cut–off speed $n_{cut} = 1500$ rpm: (a) torque, (b) speed. Operating conditions: ISA starts ICE (El. Start), ICE is started (Mech. Start), transition between motoring and generating (Trans.), ISA charges the battery (Generation).

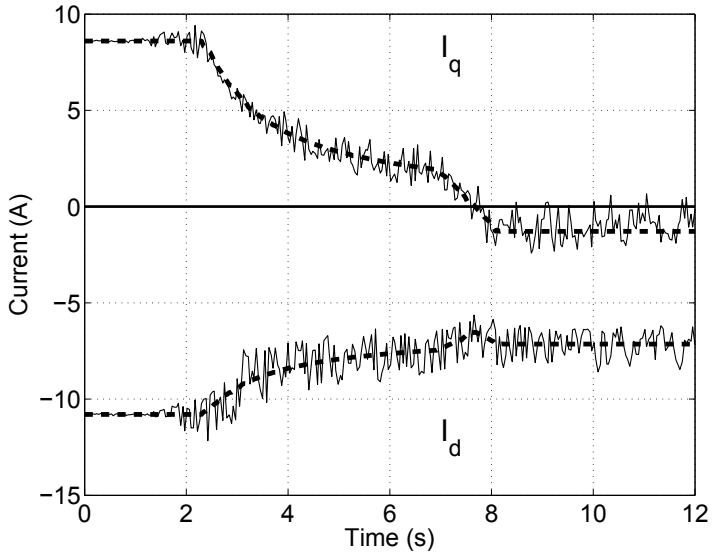

Figure 6.29: Measured I_d behavior and I_q behavior during test with starting-torque $T_{st} = 20$ Nm and cut–off speed $n_{cut} = 1500$ rpm (solid lines are measured currents and dashed lines are references currents)

Further tests with higher cut-off speed had been done [3]. The satisfaction of the requirements has been verified, confirming the machine design.

6.6. Measurement of cross saturated flux linkages

For the sake of a correct evaluation of the cross saturation phenomena a more detailed series of measurements have been carried out so as to determine the flux linkages versus current characteristics. The tests has been carried out with steady state operations, e.g. with constant speed ($\omega_{me} = \Omega_{me}$). Therefore in the synchronous reference frame the flux–linkages, voltages and currents have constant amplitude.

The measurement of $\Lambda_d(I_d, I_q)$ and $\Lambda_q(I_d, I_q)$ behaviours for different couples of d-q currents is imperative if a high performance control is designed to drive an IPM machine [87].

The flux linkage is derived from the steady–state voltages while the motor is rotating at constant speed. Therefore, as in chapter 1 the electric and mechanical quantities becomes constat. In steady–state, the d- and q–axis voltages are given by

$$\mathrm{V}_d = R \cdot I_d - \Lambda_q(I_d, I_q)\Omega_{me} \tag{6.16}$$

$$\mathrm{V}_q = R \cdot I_q + \Lambda_d(I_d, I_q)\Omega_{me} \tag{6.17}$$

where U_d and U_q are obtained from the outputs of the d- and q–axis current controllers, compensating the deadtime (as in Fig. 6.19), while R is the phase resistance.

[3] During the final event of the competition at MPC Products in Skokie (IL, USA) a starting torque equal to $\simeq$ 35 Nm was achieved. Additionally, the ISA was tested in generating mode at 3000 rpm with 1 kW output power.

From (6.16) and (6.17), using the measured d- and q–axis voltage, the flux linkages can be directly computed as

$$\Lambda_d(I_d, I_q) = \frac{\mathrm{V}_q - RI_q}{\Omega_{me}} \tag{6.18}$$

$$\Lambda_q(I_d, I_q) = -\frac{\mathrm{V}_d - RI_d}{\Omega_{me}} \tag{6.19}$$

A first method to measure the d–q flux linkages is to apply the relationships (6.18) and (6.19). Initially, a current vector with only d- or q–axis components respectively is applied, while the other component is set null. Secondly, one of the current component is kept constant (different from zero) while the other is changed. Resistance voltage drop is taken into account by computing it on the basis of previously measured value.

It is clear from (6.18) and (6.19) that the resistance have a relevant influence on the flux measurement. In order to avoid this dependance it is necessary to measure the resistance during all the tests, compensating the variations due to the temperature. This measurement could be quite difficult, increasing the sources of uncertainties.

Therefore a second method, requiring only voltage and current measurements, have to be adopted instead of it. It is possible to carry out two measurements applying the couples of currents: (I_d, I_q) and $(I_d, -I_q)$.

For the sake of considering the same phase resistance the two test has to be consecutive. Therefore, supplying I_d and I_q the voltages V' are:

$$\mathrm{V}'_d = RI_d - \Lambda_q(I_d, I_q)\Omega_{me} \tag{6.20}$$

$$\mathrm{V}'_q = RI_q + \Lambda_d(I_d, I_q)\Omega_{me} \tag{6.21}$$

while supplying I_d and $-I_q$, the voltages V'' becomes

$$\mathrm{V}''_d = RI_d - \Lambda_q(I_d, -I_q)\Omega_{me} \tag{6.22}$$

$$\mathrm{V}''_q = RI_q + \Lambda_d(I_d, -I_q)\Omega_{me} \tag{6.23}$$

Combining the voltage expressions during the two tests, and assuming a constant resistance, it follows that:

$$\mathrm{V}'_d - \mathrm{V}''_d = \Lambda_q(I_d, -I_q)\Omega_{me} - \Lambda_q(I_d, I_q)\Omega_{me} \tag{6.24}$$

$$\mathrm{V}'_q - \mathrm{V}''_q = \Lambda_d(I_d, -I_q)\Omega_{me} + \Lambda_d(I_d, I_q)\Omega_{me} \tag{6.25}$$

Applying the flux symmetries $\Lambda_d(I_d, I_q) = \Lambda_d(I_d, -I_q)$ and $\Lambda_d(I_d, I_q) = -\Lambda_q(I_d, -I_q)$ it is possible to obtain the relationships:

$$\mathrm{V}'_d - \mathrm{V}''_d = -2\Lambda_q(I_d, I_q)\Omega_{me} \tag{6.26}$$

$$\mathrm{V}'_q - \mathrm{V}''_q = 2\Lambda_d(I_d, I_q)\Omega_{me} \tag{6.27}$$

Finally the d–q flux linkages results expressed as:

$$\Lambda_d(I_d, I_q) = \frac{\mathrm{V}'_q + \mathrm{V}''_q}{2\Omega_{me}} \tag{6.28}$$

$$\Lambda_q(I_d, I_q) = -\frac{\mathrm{V}'_d - \mathrm{V}''_d}{-2\Omega_{me}} \tag{6.29}$$

It is worth noticing that a further advantage of this second method is the intrinsic elimination of potential offsets. Then the measured flux linkages are verified comparing the torque measurements with the torque computed from the measured flux linkages, given by:

$$T = \frac{3}{2} p \Big[\Lambda_d(I_d, I_q) I_q - \Lambda_q(I_d, I_q) I_d \Big] \tag{6.30}$$

Hereafter this second method is applied to evaluate the impact of the cross saturation in two IPM machines: the first with a fractional–slot winding and the second with an integral–slot winding.

6.6.1. Fractional–slot machine

The 12–slot 8–pole ISA, described in section 6.5, is considered as example of the fractional–slot machine. Its nominal current is 6.7 A.

It should be noted that the results presented in Fig. 6.16 have been measured adopting the first method. In addition, the value of the resistance has been only initially evaluated at room temperature, resulting equal to about 1.4 Ω. These are the causes of the discrepancy highlighted between predictions and measurements, shown in Fig. 6.16.

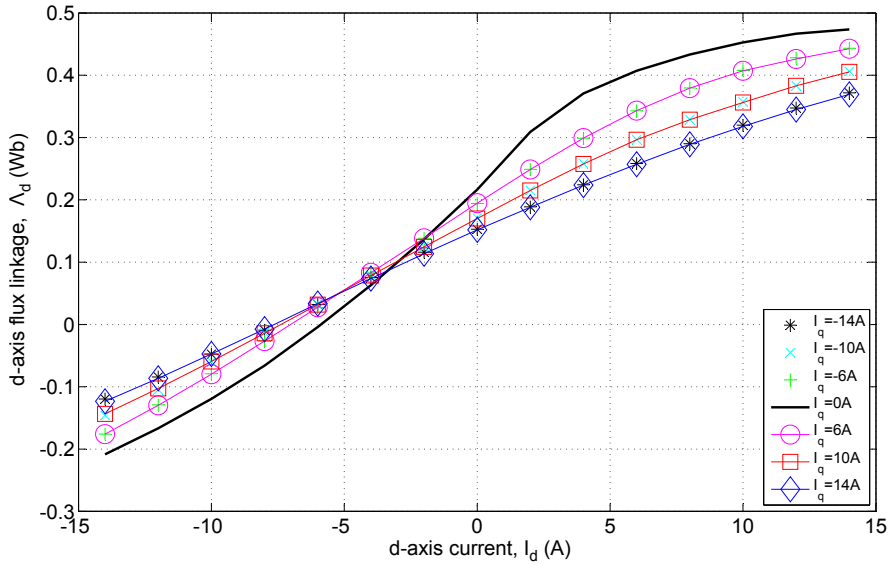

Figure 6.30: Fractional–slot 12/08 IPM: Measured d–axis current–flux linkages characteristic $\Lambda_d(I_d, I_q)$

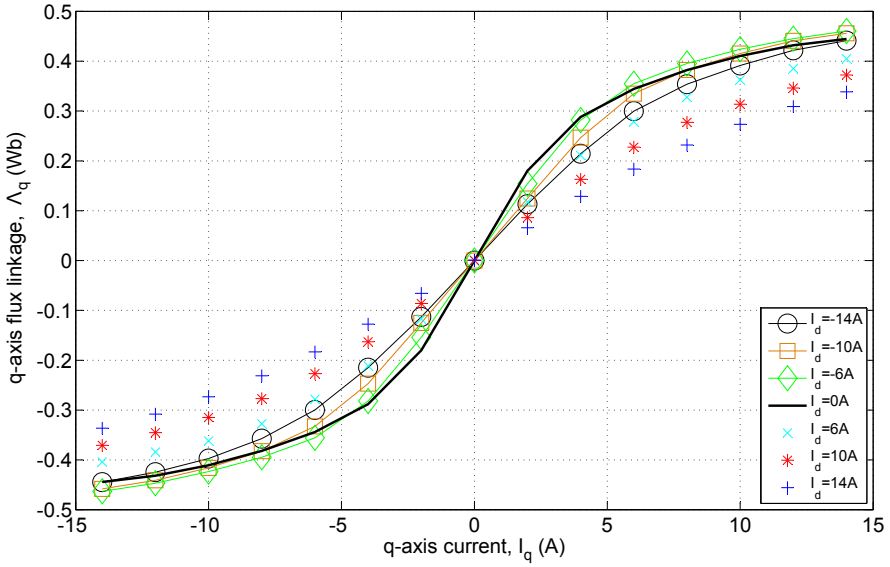

Figure 6.31: Fractional–slot 12/08 IPM: Measured q–axis current–flux linkages characteristic $\Lambda_q(I_d, I_q)$

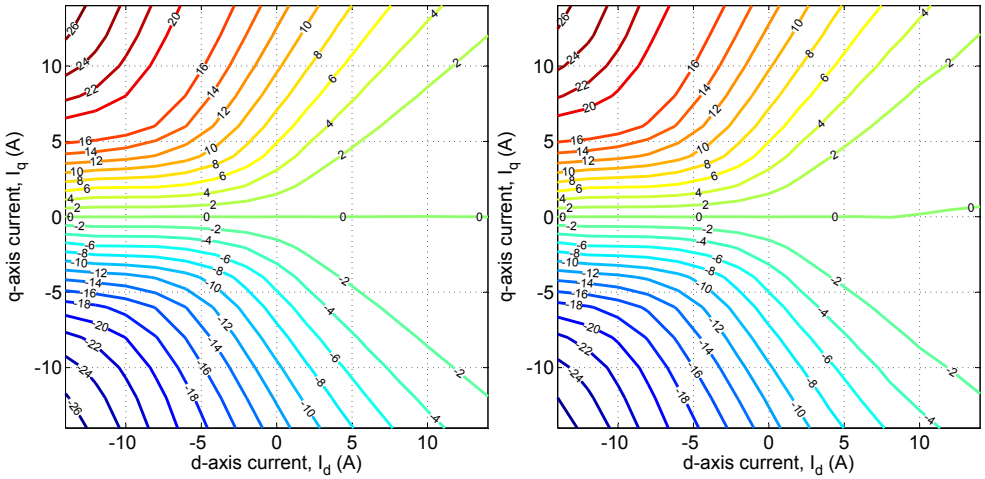

(a) Measured map (b) Reconstructed map

Figure 6.32: Fractional–slot 12/08 IPM: (a) measured torque map, (b) torque map computed from the measured flux linkages.

Fig. 6.30 and Fig. 6.31 shows the measured d– and q–axis flux linkages respectively, adopting the second method with the two consecutive tests. Both the flux linkage characteristics are parameterized as a function of the supplied current in the other axis (d or q). Positive and negative current are considered. The comparison between the measured torque map and those obtained from the measured flux linkages is presented in Fig. 6.32, showing a very good agreement that confirms the procedure.

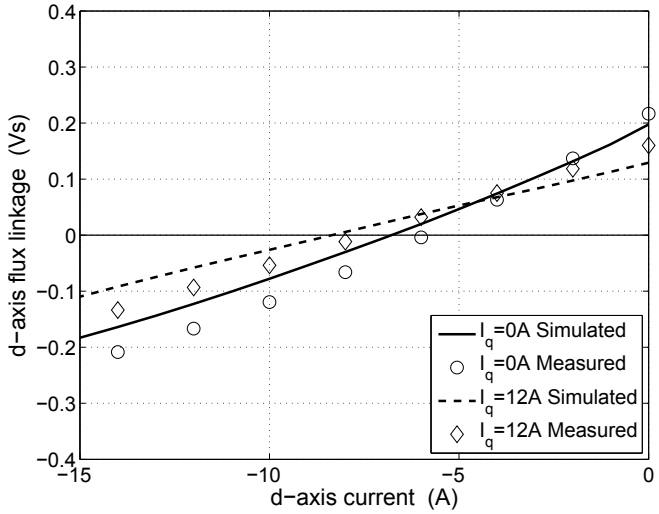

(a)

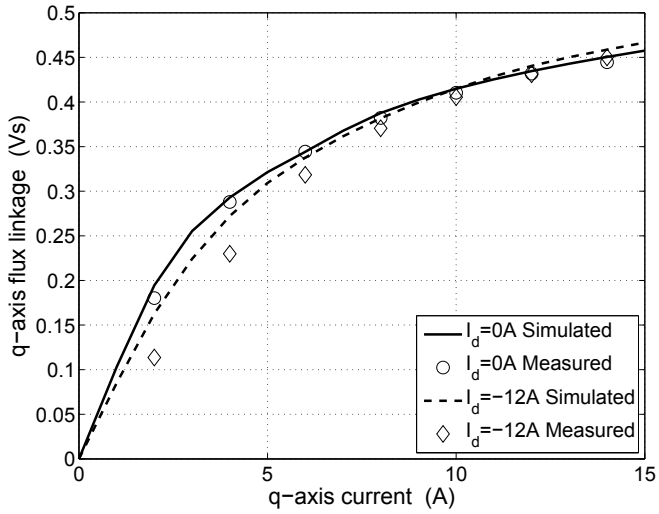

(b)

Figure 6.33: Fractional–slot 12/08 IPM: comparison between measured and predicted flux linkages along (a) d–axis, (b) q–axis.

The results highlight the relevance of the cross saturation phenomena in a IPM machine provided of a fractional—slot winding with non–overlapped coils. Fig. 6.33 shows the same *d*–*q* flux behaviours reported in Fig. 6.30. The initial discrepancy between predictions and measurements has been at least halved adopting the second method described above.

6.6.2. Integral–slot machine

A 24–slot 4–pole IPM prototype has been adopted as example of a integral–slot machine. The rotor is characterized by three flux–barriers per pole, each of them provided with Ferrite PMs. The rotor lamination is shown in Fig. 6.34(a), while the prototype in Fig. 6.34(b). The motor is also characterized by a skewed rotor for the minimization of the torque ripple. Its nominal current is 3.5 A.

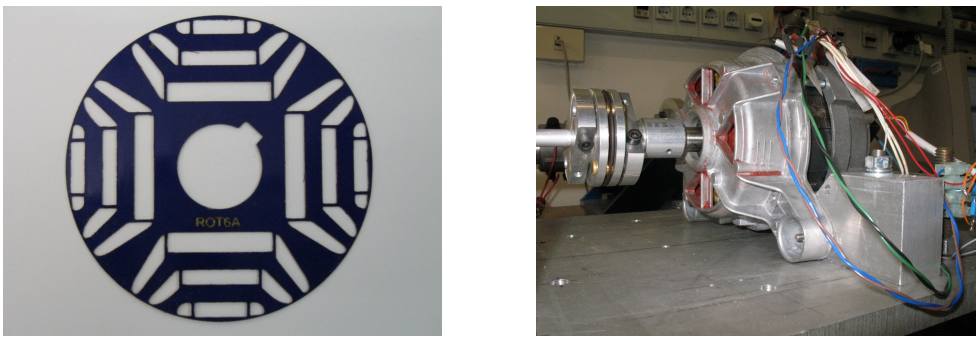

(a) (b)

Figure 6.34: 24–slot 4–pole IPM prototype: (a) rotor lamination with three flux–barriers per pole, (b) complete prototype.

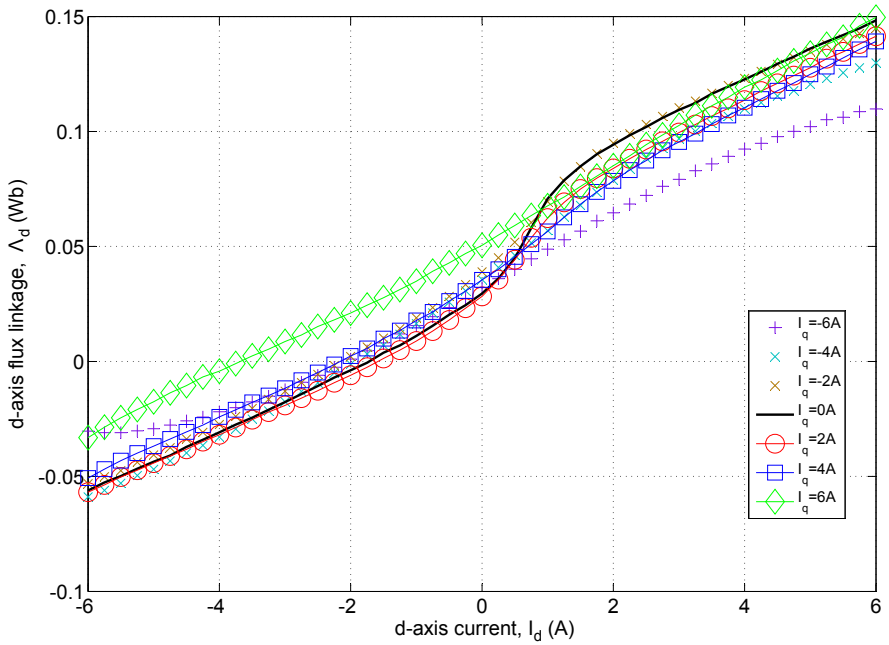

Figure 6.35: Integral–slot 24/04 IPM: Measured d–axis current–flux linkages characteristic $\Lambda_d(I_d, I_q)$

Fig. 6.35 and Fig. 6.36 shows the measured d– and q–axis flux linkages respectively, adopting the second method with the two consecutive tests. Both the flux linkages

curves are parameterized as a function of the current in the other axis (d or q). The results highlight that the cross saturation phenomena in this case is greatly reduced as respect to the 12–slot 8–pole fractional–slot machine. Also in this case, Fig. 6.37 shows a very good agreement between the torque measurements and the torque obtained from the measured fluxes.

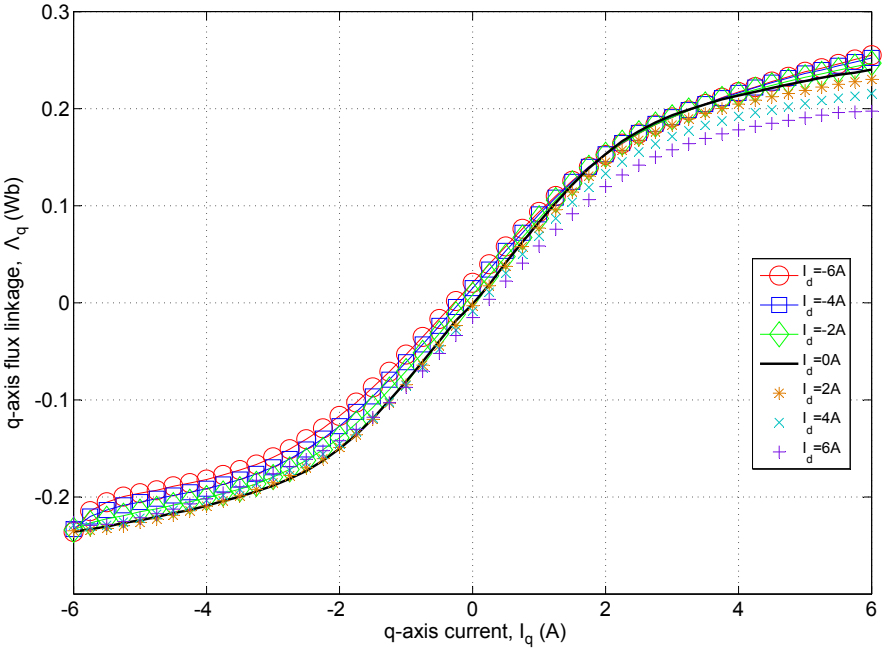

Figure 6.36: Integral–slot 24/04 IPM: Measured q–axis current–flux linkages characteristic $\Lambda_q(I_d, I_q)$

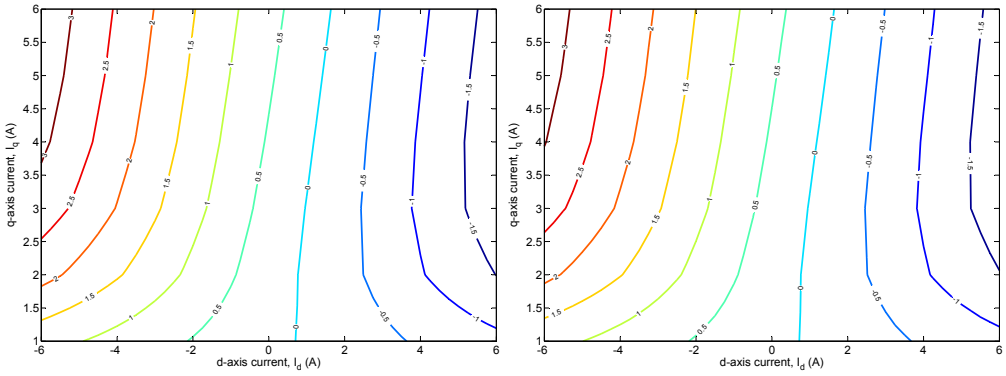

(a) Measured map (b) Reconstructed map

Figure 6.37: Integral–slot 24/04 IPM: (a) measured torque map, (b) torque map computed from the measured flux linkages.

Chapter 7

Dual three–phase machine

This chapter introduces the concept of fault tolerance in the electrical machine drive. Then, it analyzes the capability of a permanent magnet machine with a dual three–phase winding under faulty operating conditions. Such a machine balances the requirements of fault tolerance and the adoption of standard components since it has two separate three–phase windings, each of them supplied by a separate standard converter. Several aspects are evaluated under faulty conditions, among the others: average torque, torque ripple, radial forces, short circuit current, mutual coupling, overload capability. The conditions to operate the machine as a multi–phase machine are presented. Simple design rules are proposed to select those slot and pole combinations allowing a six–phase machine to be obtained.

7.1. Fault–tolerant motors

THE the fault-tolerance is the property of the system to continue to operate at a reduced power in the event of the failure of one or more of its components. The fault–tolerance is not only a property of individual machines. It may also characterizes the rules by which they interact. In fact fault-tolerance can be achieved with a proper design of the individual system or using a simple duplication of the initial system (redundancy).

Among the several potential faults, which can occur in a electrical machine the more relevant for the electrical machine are:

- winding open circuit,
- winding short circuit (phase to ground or within a phase),
- winding short circuit at the terminals (three–phase).

The fault–tolerant capability of electrical drives is an essential feature in applications such as aerospace and aeronautic but it is becoming more and more important also in applications like more–electric aircrafts, electric vehicles, rail traction and ship propulsion [60, 88, 89]. In several applications of the mentioned fields the continuous

operation is mandatory, even in the presence of a fault. Due to the increase of electrical applications in the industrial sectors, this feature is becoming attractive also for industrial motor drives.

The first solution to increase the fault–tolerance of a system is to adopt a complete redundant system, that is, to adopt two motors and two inverters. This is a expensive solution and it requires to double the volume and the weight. A better approach consist in the design of multi–phase machines that have been proven to exhibit a high fault-tolerant capability [88, 90–93].

Multi–phase variable speed drives (with phase number greater than 3) have been proven to have also further advantages as respect to standard three–phase machines [94]: higher efficiency, higher torque–to–weight ratio, higher torque–to–volume ratio. In addition, considering the same voltage and power, the increase of the number of phases yields a reduction in the current per phase. Then, it is possible to downsize the components of the inverter. However the main drawback is that both the machine and the converter usually involves custom and expensive design.

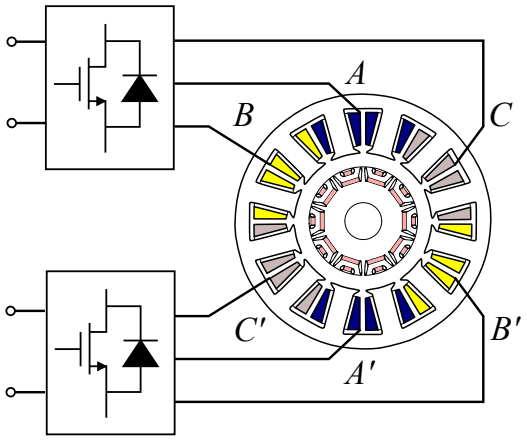

Figure 7.1: Scheme of the dual three–phase machine drive.

The multi–phase machine theory has been widely covered in literature, mainly regarding to induction machines [95–101]. Then, the interest has been devoted in analyzing pure PM multi–phase machines, i.e. the five–phase motor drive [102–104].

This chapter investigates the capability of a permanent magnet (PM) machine with a dual three–phase winding that could be elected as viable alternative to the multi–phase machine. Such a machine balances the requirements of fault tolerance and the adoption of standard components. The motor has two separate three–phase windings, each of them supplied by a separate standard converter, whose Volt–Amps rating corresponds to half motor power. This aspect could be extremely relevant in high power applications, due to the converter cost. It should be noted that, the PM dual three–phase machine is marginally dealt with in literature, especially if designed with a fractional–slot winding as in this study.

As described in chapter 6, such a fractional–slot winding allows a high fault–tolerant capability to be achieved, yielding a physical and thermal separation between phases [88]. Of course, when fractional–slot winding are employed, only PM machines can

be adopted, since the increase of MMF harmonics in the air gap makes the induction machine an impracticable solution.

A sketch of the dual three–phase machine drive is shown in Fig. 7.1. Although it is only a schematic picture, the phases of the two windings are labeled as A, B, and C for the first winding, and A', B', and C' for the second one. In the event of a fault in one part of the machine, the faulty winding is disconnected and the machine is operated by means of the healthy winding only. Such a system can be considered a modular solution [105].

The machine exhibits different performance under faulty conditions, in term of torque and overload capability, according to the various arrangements of the coils of the two windings. Different winding configurations will be considered and analyzed in order to evaluate the advantages and drawbacks of each solution.

7.2. The interior PM machine prototype

For the sake of investigate the dual three–phase machine topology a suitable IPM machine provided of a fractional–slot winding with non–overlapped coils has been designed. A 12–slot and 10–pole machine has been manufactured. Its stator and rotor are shown in Fig. 7.2. The main data are reported in Table 7.1.

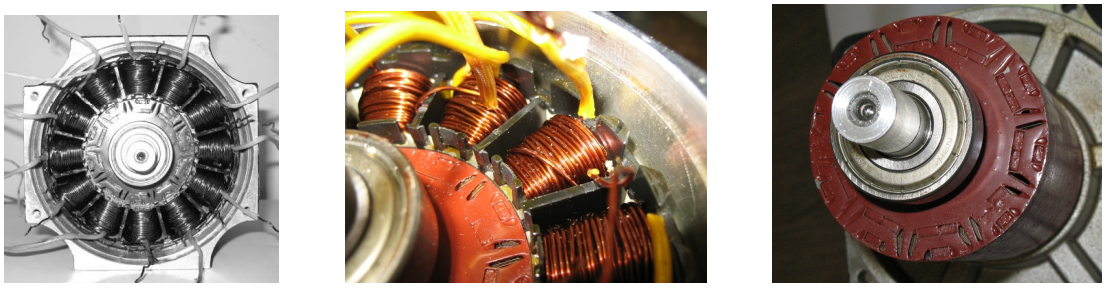

(a) Prototype (b) Coils (c) Rotor

Figure 7.2: The 12–slot 10–pole IPM machine prototype.

Table 7.1: Main geometric data of the IPM prototype

Characteristic		Dimensions
Stator outer diameter	D_e	134 mm
Stator inner diameter	D	71.5 mm
Slot tooth height	h_s	21.83 mm
Air–gap	g	0.4 mm
Stack length	L_{stk}	90 mm
Number of turns per coil	N_t	59
Wire diameter	d_c	1.12 mm

Such a 12–slot and 10–pole machine has been proven to be well suited for fault–tolerant applications [106, 107]. Even though a double–layer winding is adopted, a physical separation among the phases is achieved by means of coil separators within the slots, as shown in Fig. 7.2(b). This IPM machine is characterized by a high self inductance and a theoretical zero mutual inductance, allowing to limit the current in the event of short–circuit and to avoid magnetic coupling between faulty and healthy phases.

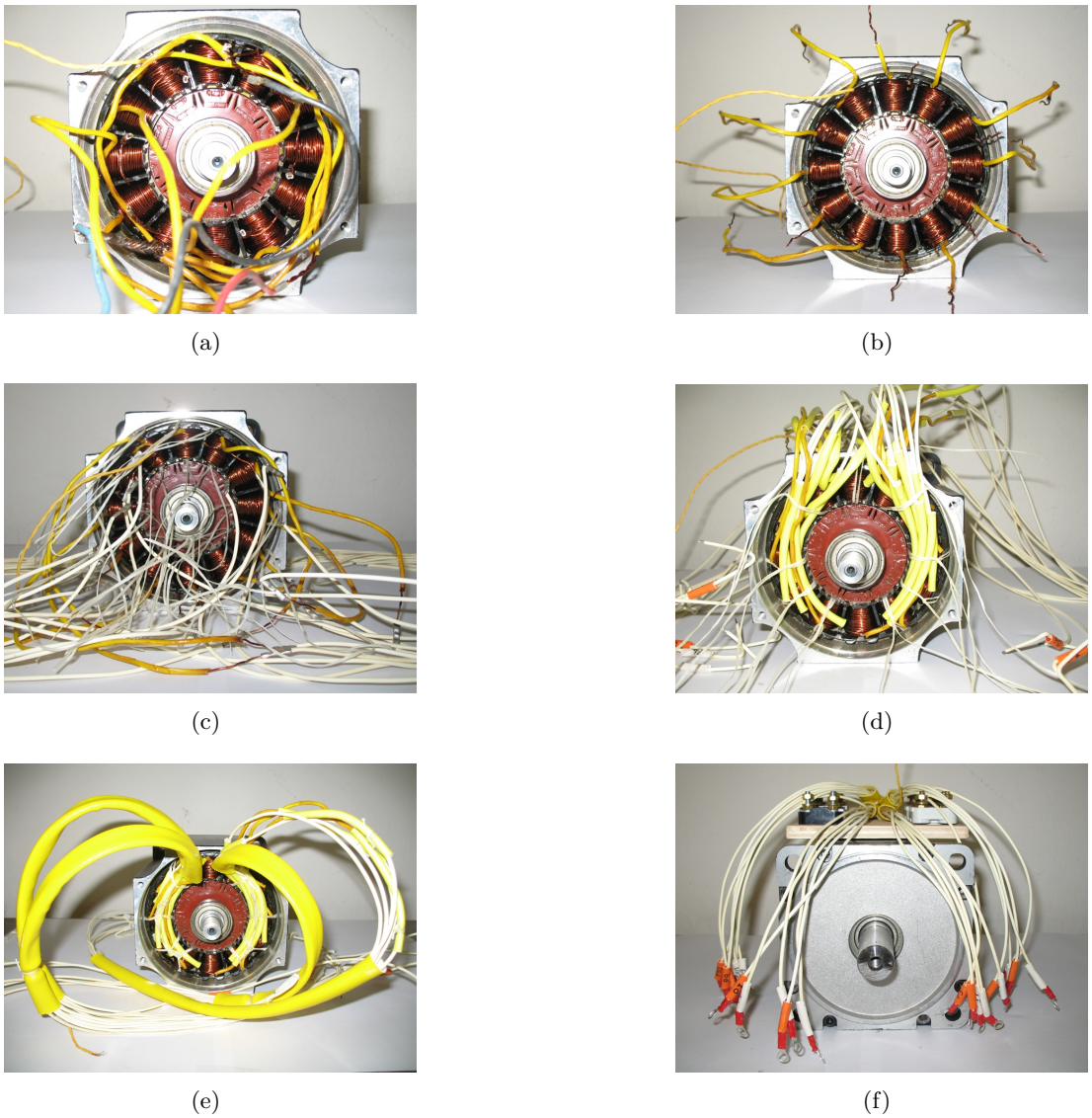

(a) (b) (c) (d) (e) (f)

Figure 7.3: The 12–slot 10–pole IPM machine prototype: from a three–phase motor to a test machine with all the coils terminal available.

The initial three–phase motor has been completely reconnected in order to have such a modular solution, as shown in the photo sequence of Fig. 7.3. Therefore each coil terminal is available allowing to test the machine capabilities to different types of winding fault and configurations. Thus the behaviour of both double–layer and single–

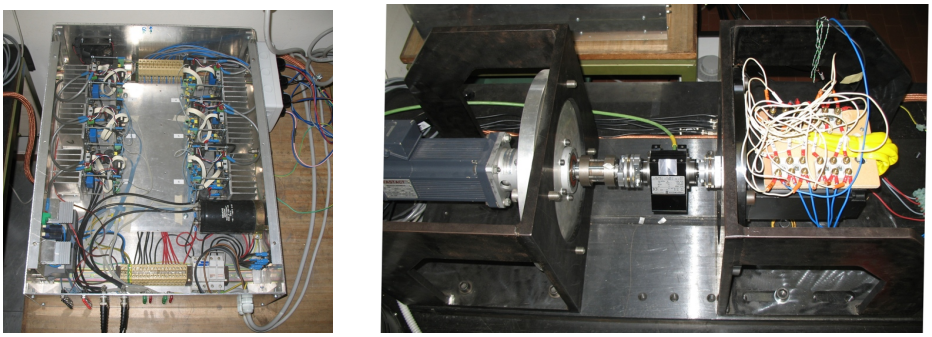

(a) Multi–phase inverter (b) Test bench

Figure 7.4: Test assembly: (a) six–phase power converter and (b) low speed test bench used for the 12–slot 10–pole IPM prototype measurements.

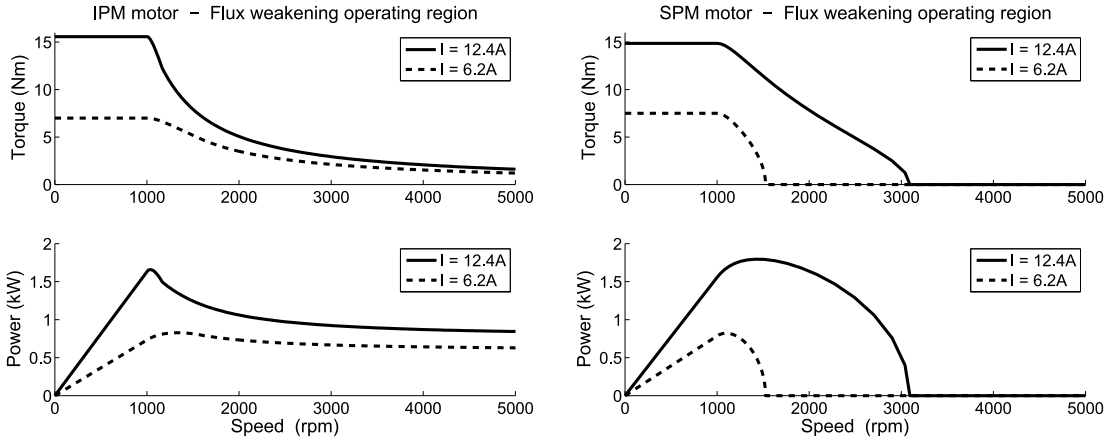

(a) (b)

Figure 7.5: 12–slot 10–pole torque and power versus speed behaviours: (a) IPM prototype, (b) SPM machine.

layer winding can be evaluated. However, since the single–layer winding is achieved by disconnecting every second coil, the SL winding results to have half a number of turns N_t of the allowable rated number.

In order to make a comparison between predictions and measurements the phase current amplitude is limited to 6.2 A (peak value), that is the rating of the available multi–phase converter, shown in Fig. 7.4(a). This power converter with six separated full–bridges has been employed for all AC tests. The prototype mounted on the speed test bench is shown in Fig. 7.4(b).

Even if the IPM machine has been adopted as a reference in the study, a comparison with a further SPM machine is considered. The SPM rotor has the same bore diameter of the IPM rotor. The main purpose is to highlight the differences due to the rotor anisotropy. Adopting the same high energy PM the nominal torque is achieved reducing the stack length to the 50% of the IPM design. Even if the base speed is the same the flux–weakening capability is completely different, as shown in Fig. 7.5. The SPM

machine is also characterized by a higher short–circuit current due to the lower self–inductance. However, it should be noted that despite of the different motor length, the two designs have the same PM volume.

7.3. Arrangement of the two three–phase windings

As introduced above, in the following the phases of the two windings are labeled as A, B, and C for the first winding, and A', B', and C' for the second one.

7.3.1. Remark about the mechanical arrangement

As far as the mechanical arrangement of the windings is concerned, there are two possibilities:

1. the stator is split in two separate parts, each of them containing one of the two three–phase windings,
2. the coils of the two windings are alternated along all the stator circumference.

Although the same performance is achieved, when the machine operates in healthy conditions (i.e. when both three–phase windings are supplied), the choice of the phase coils arrangement has some bounces on the motor performance under faulty operating conditions. In particular

- an unbalanced force on the rotor (and on the bearings) can arise,
- a thermal coupling can be present, especially when a double–layer winding is adopted.

Referring to double–layer windings, Fig. 7.6, Fig. 7.7, and Fig. 7.8 show the arrangement of the coils of the two three–phase windings. The solid contour lines refer to the phases A, B, and C, while the dotted contour lines refer to the phases A', B', and C'. After the fault, the coils of the phases A', B', and C' are considered to be open circuited.

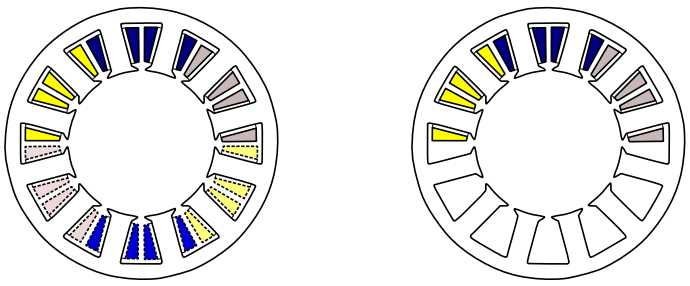

(a) healthy (b) one winding only

Figure 7.6: Configuration with double–layer winding DL-1.

(a) healthy (b) one winding only

Figure 7.7: Configuration with double–layer winding DL-2.

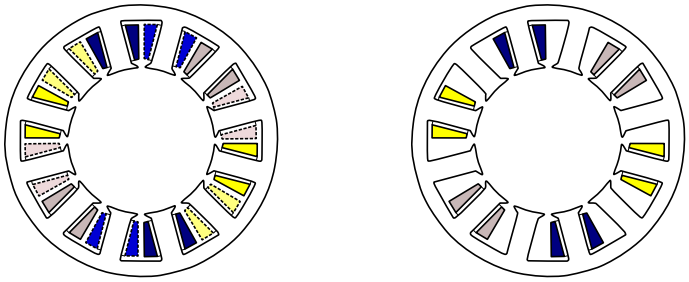

(a) healthy (b) one winding only

Figure 7.8: Configuration with double–layer winding DL-3.

Configuration DL-1 has two windings disposed in two different parts of the stator. Configuration DL-2 has an intermediate arrangement of the windings: groups of coils are alternated along the stator circumference. Configuration DL-3 has the coils of the two windings alternated every other tooth.

Similarly, referring to single–layer windings, Figs. 7.9 and 7.10 show the arrangement of the coils of the two three–phase windings. Note that in the single–layer winding the coils are wound each other tooth, and each coil is formed by a double number of turns. Configuration SL-1 has the two windings concentrated in a part of the stator. Configuration SL-2 has the two windings with alternated coils.

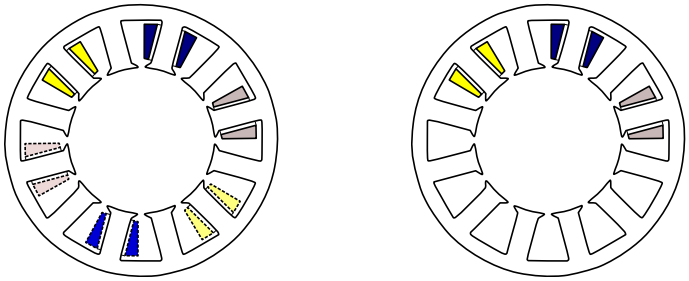

(a) healthy (b) one winding only

Figure 7.9: Configuration with single–layer winding SL-1.

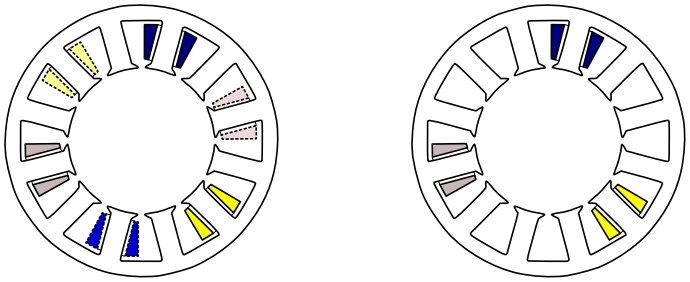

(a) healthy (b) one winding only

Figure 7.10: Configuration with single–layer winding SL-2.

7.3.2. Remark about the electrical arrangement

According to the electrical arrangement of the windings, there are two different supply conditions:

- The two windings are supplied with currents "in phase". This means that the same current feeds phase A and phase A', and similarly for phases B and B', and for phases C and C'.
- Taking advantage of the presence of the two separate three–phase windings, the two windings are supplied with currents out of phase of 30 electrical degrees. In this case, there are six different angles for the the six phases and the motor results to be exactly a six–phase motor [96, 108].

However, not all the winding arrangements allow such a second supply strategy. A mechanical shift is necessary between the phases A, B, and C and the phases A', B', and C', corresponding to 30 electrical degrees.

Therefore, as far as the 12–slot 10–pole motor is concerned, a six–phase motor can be achieved only when the DL-3 configuration is adopted (Fig. 7.8). Neither the single–layer windings nor the double–layer windings with DL-1 and DL-2 configurations can be adopted, since there is no displacement between the axis of the coils of the corresponding phases.

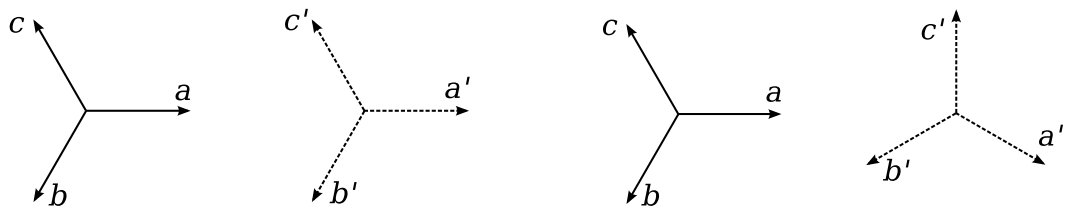

(a) in phase (b) out of phase

Figure 7.11: Phase current vectors in the two three–phase windings.

7.4. Torque behavior

This section reports some finite element results and experiments about the torque behavior of the PM motors, operating with different winding arrangements. The motor operates under both healthy conditions (feeding both windings) and faulty conditions (feeding one winding only).

Table 7.2 according to the IPM motor, and Table 7.3 according to the SPM motor, show the comparison of the simulated average torque, the peak–to–peak torque ripple and the peak of the radial force on the rotor, including various winding configurations. The phase currents are sinewaves with the following peak values:

- $\hat{I}$=3.1 A (2.2 A/mm^2, 18.23 kA/m).
- $\hat{I}$=6.2 A (4.4 A/mm^2, 36.47 kA/m).
- $\hat{I}$=12.4 A (8.8 A/mm^2, 72.93 kA/m).

The values reported in the brackets refers respectively to the current density in the conductor (Arms/mm^2) and the linear current density, or electric peak loading (kA/m).

7.4.1. Healthy operating conditions

At first, let us compare the performance of the motor under healthy operating conditions. It should be noted that the assumption of synchronization between the two drives is always considered in simulated healthy operating conditions.

With the six–phase supply (the two windings are supplied with currents out of phase, as in Fig. 7.11(b)), there is a slightly higher average torque, and a lower torque ripple, with respect to the standard DL supply. The six–phase supply involves a higher winding factor (unity distribution factor), and a lower MMF harmonic contents. It could be noted that the torque increase is lower for the SPM motor, thanks to the higher air gap that limits the effect of the stator MMF.

With the DL–healthy configuration (double–layer winding and phase vectors in phase, Fig. 7.11(a)), the torque ripple, remains almost the same regardless of the current amplitude for the IPM motor. On the contrary, it decreases with the increase of the electric loading for the SPM motor (the peak–to–peak difference remains almost constant). The torque ripple of the SPM machine corresponds to cogging torque (about the same at low current Table 7.3), while the IPM motor is characterized by a torque ripple due to the harmonics interaction.

With healthy single–layer winding, the average torque results to be slightly higher than those exhibited by adopting the double layer winding, and comparable with the six–phase supply only for the IPM motor. In addition, the torque–to–current ratio of the IPM motor decreases according to the increase of the current due to the saturation (e.g., comparing DL–healthy and SL–healthy values of Table 7.2).

However in motors with single–layer winding, the resulting torque ripple is always higher than those exhibited by other configurations. The unbalanced radial force under healthy operating conditions is negligible for all configurations.

Table 7.2: Simulated performance with various winding arrangements IPM motor.

Motor config.	$\hat{I}$=3.1 A peak			$\hat{I}$=6.2 A peak			$\hat{I}$=12.4 A peak		
	Average torque (Nm)	Torque ripple (%)	Unbalanced radial force (N)	Average torque (Nm)	Torque ripple (%)	Unbalanced radial force (N)	Average torque (Nm)	Torque ripple (%)	Unbalanced radial force (N)
six–phase	2.80	9.03 %	0.4	7.01	4.39 %	1.78	14.78	5.09 %	2.55
DL healthy	2.67	13.3 %	0.3	6.66	11.0 %	1.3	14.07	13.6 %	1.84
SL healthy	2.89	14.0 %	0.6	6.72	16.2 %	3.0	12.78	18.32 %	2.32
DL–1	1.32	13.8 %	360	3.28	14.8 %	1009	6.92	22.1 %	1654
DL–2	1.24	15.4 %	244	3.00	23.0 %	723	6.39	30.0 %	1150
DL–3	1.20	12.2 %	0.1	2.89	14.0 %	0.6	6.72	16.2 %	3.02
SL–1	1.42	11.4 %	332	3.38	16.1 %	813	6.38	22.7 %	1443
SL–2	1.45	14.1 %	358	3.37	20.1 %	605	5.96	28.0 %	791

Table 7.3: Simulated performance with various winding arrangements SPM motor, 50% stack length.

Motor config.	$\hat{I}$=3.1 A peak			$\hat{I}$=6.2 A peak			$\hat{I}$=12.4 A peak		
	Average torque (Nm)	Torque ripple (%)	Unbalanced radial force (N)	Average torque (Nm)	Torque ripple (%)	Unbalanced radial force (N)	Average torque (Nm)	Torque ripple (%)	Unbalanced radial force (N)
six–phase	3.91	8.91 %	0.67	7.80	4.21 %	0.68	15.35	2.37 %	0.65
DL healthy	3.87	10.83 %	0.81	7.71	5.71 %	0.72	15.15	3.90 %	0.64
SL healthy	4.00	11.37 %	0.63	7.91	5.68%	0.58	15.27	6.75 %	0.70
DL–1	1.94	20.7 %	75.5	3.86	10.6 %	146	7.59	6.21 %	274
DL–2	1.94	20.7 %	21.2	3.86	10.7 %	44.9	7.60	6.59 %	91.0
DL–3	2.01	21.4 %	0.60	4.00	11.37 %	0.63	7.91	5.68 %	0.58
SL–1	2.00	21.1 %	51.0	3.96	10.6 %	109	7.63	7.65 %	234
SL–2	2.01	21.4 %	36.4	3.97	11.3 %	66.2	7.67	7.81 %	119

7.4.2. Simulated torque with one open–circuited winding

The motors operate with one of the two three–phase windings open circuited. As regards the average torque, regardless of the winding configuration and the motor topology, all motors exhibit obliviously almost half a torque, for given current.

In the IPM motor, the torque ripple remains almost the same with low current density, while it increases with the increase of the current density (Table 7.2). Among the others the DL–3 configuration exhibits always a torque ripple almost equal to the healthy configuration.

On the other hand, the SPM motor shows always a torque ripple almost twice than the DL–healthy value (Table 7.3). As under the healthy operating conditions, the torque ripple decreases with the increase of the phase current.

7.4.3. Measured torque under faulty operating conditions

Some experimental behaviors of the measured torque versus rotor position are shown in Fig. 7.12 to Fig. 7.15. For each configuration, under both healthy and faulty operating conditions, the average torque results in good agreement with predictions. On the contrary, the measured torque ripple is generally higher than predicted, especially under the healthy operating conditions. In particular, a surprisingly high torque ripple is found when six–phase currents are supplied (in DL–3 configuration). This is probably due to an unbalance of the six currents, caused by using the six separate full–bridge converters. A similar effect can be expected also in case of lack of synchronization the two three–phase winding drives.

Referring to the tests of the single–layer winding motors, the effective number of turns per coil of the prototype is half the proper number, that is, $N_t/2$ instead of N_t. It follows that the measured torque is half the torque predicted in Table 7.2, thus simulated value is halved in Fig. 7.15.

Summarizing, with one winding supplied the average torque is almost halved, independently of the winding arrangement and rotor topology. Conversely, there is a general increase of the the torque ripple in faulty conditions, as confirmed by measurements.

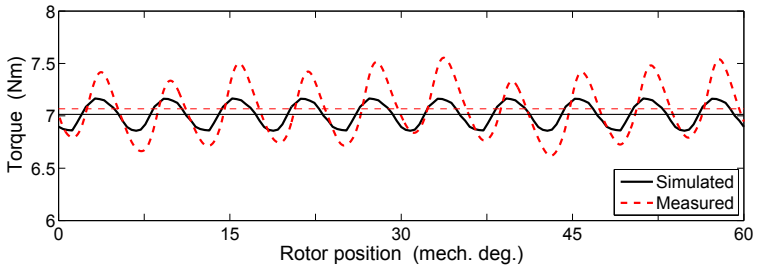

Figure 7.12: IPM machine: simulated and measured torque versus rotor position with six–phase current supply ($\hat{I}$=6.2 A).

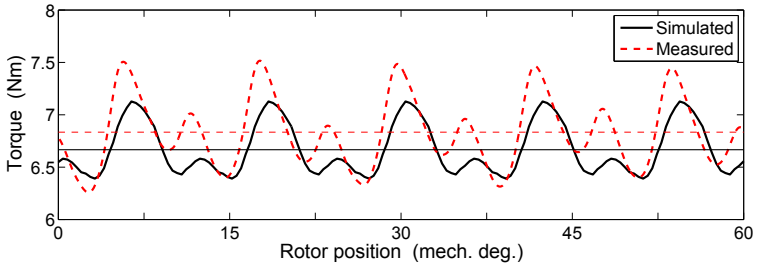

Figure 7.13: IPM machine: simulated and measured torque versus rotor position with double–layer winding arrangements (healthy condition, $\hat{I}$=6.2 A).

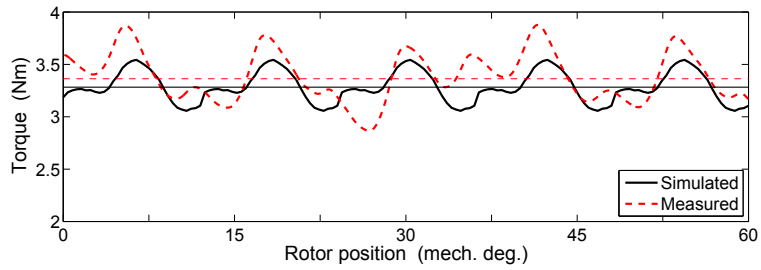

(a) DL–1 ($\hat{I}$=6.2 A)

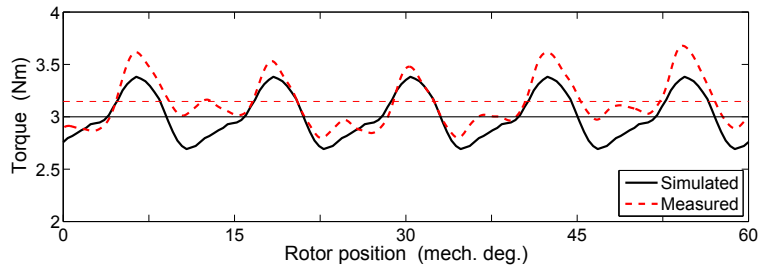

(b) DL–2 ($\hat{I}$=6.2 A)

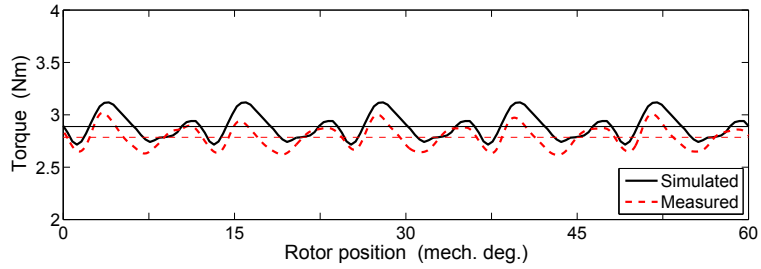

(c) DL–3 ($\hat{I}$=6.2 A)

Figure 7.14: IPM machine: simulated and measured torque versus rotor position with various double–layer winding arrangements.

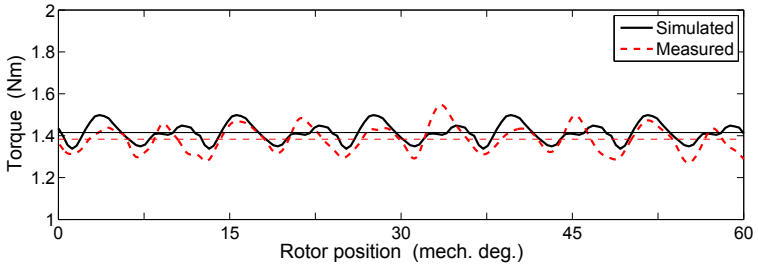

(a) SL–1 ($\hat{I}$=6.2 A, $N_t/2$)

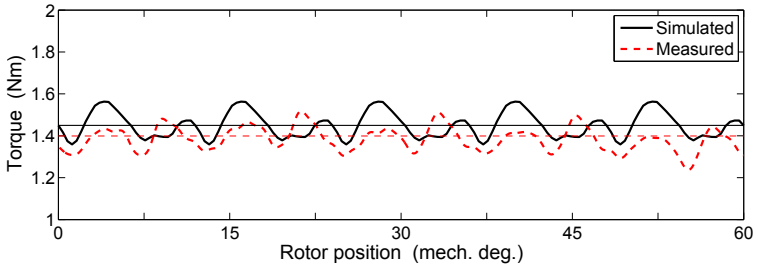

(b) SL–2 ($\hat{I}$=6.2 A, $N_t/2$)

Figure 7.15: IPM machine: simulated and measured torque versus rotor position with various single–layer winding arrangements.

7.4.4. Discussion on the unbalance radial force

It is worth considering the peak of the unbalanced radial force on the rotor. The worst case is achieved with the configuration DL–1 since the winding is asymmetric, covering only a part of the stator, Fig. 7.6. Notwithstanding the symmetric winding arrangement, the configuration DL–2 also exhibits a non negligible unbalanced radial force. The lowest force is achieved when the configuration DL–3 is adopted, since pull forces are always balanced being the coils of the same phase placed on opposite parts of the stator.

The unbalance radial force on the rotor seriously stresses the bearings and could involves radial vibration modes and undesired magnetic noise [77]. In addition, the mechanical vibrations in the air gap yield slight rotor displacements and then instant eccentricities that are one of the more frequent failures in the electrical machines. This topic is covered in literature, i.e. in [109] it is applied to a dual–stator winding induction machine.

Although the standard machine, provided of a sole winding, also suffers of unbalanced radial forces [77], the high peak radial forces reported in Table 7.2 clearly indicate a significant drawback of some configurations. In the prototype under test these forces can be sustained by commercial bearings while in larger machines the higher unbalanced forces can be a reason to reject the configurations DL–1 and DL–2.

It follows that, according to the 12–slot 10–pole machine, only the DL–3 arrangement allows to minimize the unbalanced radial force during a fault. The key feature of such an arrangement is the geometrical symmetry of the coils.

However, this partial conclusion is greatly affected by the selected combination of

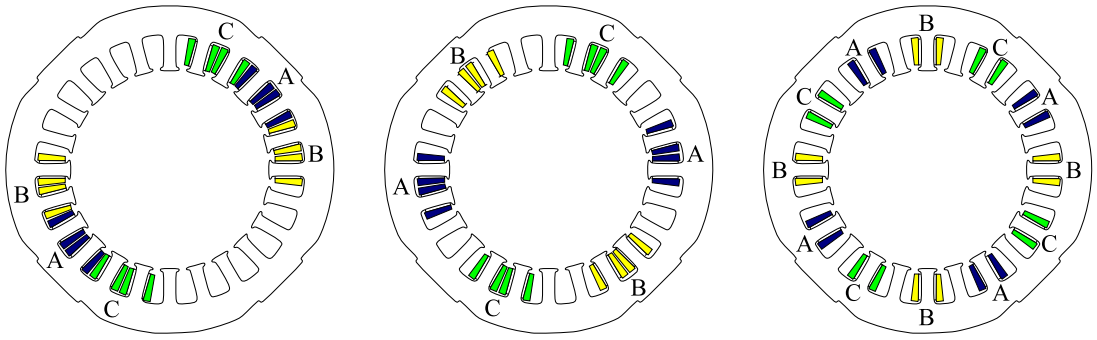

(a) DL–1 (b) DL–2 (c) DL–3

Figure 7.16: Symmetric 24–slot 20–pole configurations.

stator slots and poles. In fact, increasing the periodicity of the machine, the unbalanced radial force can be reduced for each winding configuration. For instance, the 24–slot 20–pole machine has periodicity equal to two. In this case, during the faulty conditions, the machine symmetry is achieved with any configuration, as reported in Fig. 7.16. Thus, in the following sections, all the configurations are still considered in order to deeply evaluate advantages and drawbacks.

7.5. Mutual inductance

This section deals with the analysis of the mutual inductances among the two three–phase windings.

7.5.1. Simulation of the flux linkages

Referring to the IPM machine, Fig. 7.17, Fig. 7.18 and Fig. 7.19 show the flux linkages versus rotor position, according to the winding arrangements DL-1, DL3, and SL-2, respectively. The simulations are carried out imposing constant currents in the phases of one winding (e.g. phases A, B, and C), and considering the other winding disconnected. In particular, $I_A = \hat{I} = 1A$ and $I_B = I_C = -\hat{I}/2 = -0.5A$. The PM is removed from the rotor, so as to have a zero PM flux, and the rotor iron ribs (normally saturated by the PM flux) are removed as well.

According to the configuration DL-1, Fig. 7.17(a) shows the behaviour of the flux linkages of the supplied phases. With constant current, such a behaviour corresponds to the behaviour of the rotor permeance, and it follows the approximation given in [27]. The saliency ratio that can be extracted from the simulation is about two.

Similarly, Fig. 7.17(b) shows the behaviour of the flux linkages of the phases of the disconnected winding. It is worth noticing that the flux linkages approach zero. This means that there is a minimum interaction between the two three–phase windings, adopting the configuration DL-1. This is reasonable, since the two windings are placed in two separate parts of the stator, see Fig. 7.6. Similar behaviours are achieved using the configuration DL-2.

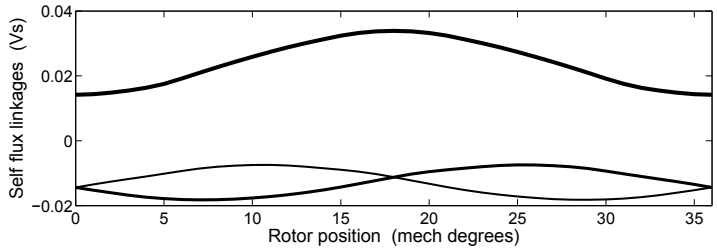

(a) DL–1 (flux linkages of the supplied phases)

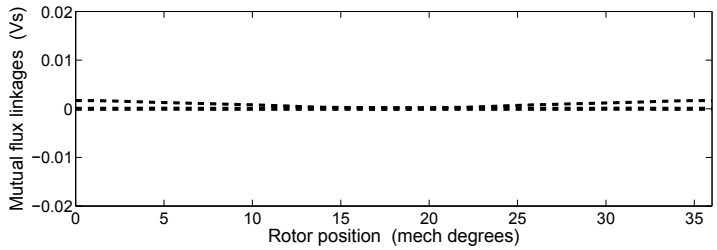

(b) DL–1 (flux linkages of the disconnected phases)

Figure 7.17: IPM machine: flux linkages versus rotor position with DL–1 double–layer winding arrangement.

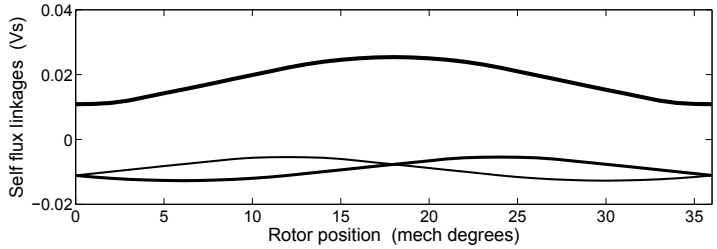

(a) DL–3 (flux linkages of the supplied phases)

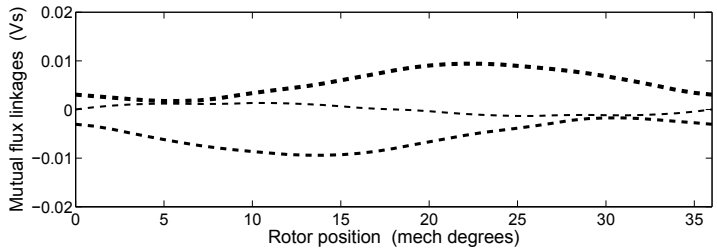

(b) DL–3 (flux linkages of the disconnected phases)

Figure 7.18: IPM machine: flux linkages versus rotor position with DL–3 double–layer winding arrangement.

However, such a decoupling does not occur with all winding configurations. Fig. 7.18 shows the behaviour of the flux linkages of the supplied and the disconnected winding, referring to the configuration DL-3. With this winding arrangement, the higher mutual coupling between the two windings is found. In fact, the flux induced in the

disconnected phases is comparable with the flux linkage of the supplied phases. This is a direct consequence of the arrangement of the coils of the two windings.

According to the single–layer winding, both configurations yield a very low mutual coupling between the windings. As an example, Fig. 7.19 shows the behaviour of the flux linkages of the SL-1 configuration. The flux linkages of the disconnected phases are negligible. Table 7.4 reports the FE results of the d–q inductances, and the mutual coupling ratio (L_M/L) for both the IPM machine and SPM machine. Regardless of the rotor structure the results shows the same trend. As example the DL–3 configuration yields the higher mutual coupling.

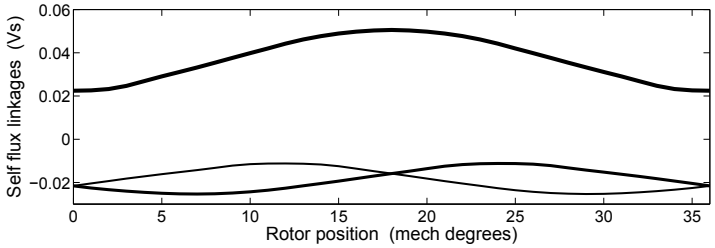

(a) SL–2 (flux linkages of the supplied phases)

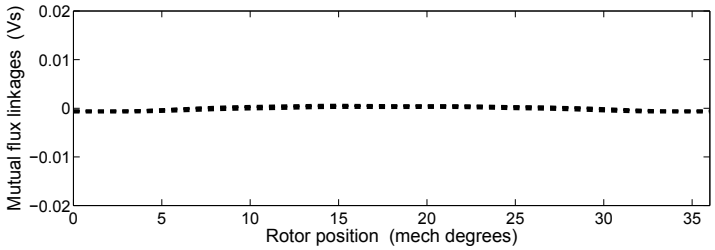

(b) SL–2 (flux linkages of the disconnected phases)

Figure 7.19: IPM machine: flux linkages versus rotor position with SL–2 single–layer winding arrangement.

Table 7.4: Comparison of simulated self inductances and mutual interaction according to various winding configurations.

Winding config.	IPM			SPM	
	L_d (mH)	L_q (mH)	L_M/L max (%)	L (mH)	L_M/L max (%)
DL–1	14.2	33.9	0	0.42	0
DL–2	13.1	31.6	8.4	0.38	9.2
DL–3	10.9	25.4	45.0	0.31	34.4
SL–1	19.2	46.3	13.6	0.56	9.8
SL–2	22.4	50.6	0.5	0.62	0.2

7.5.2. Tests of induced voltages

Some tests have been carried out on the motor prototype. The three phases of one winding (e.g., A, B, C) are supplied by means of alternate voltages at 50 Hz, while the phases of the other winding (e.g., A', B', C') are open–circuited (Fig. 7.20). Both supplied currents and voltages induced in the disconnected phases are measured. The rotor is rotated at very low speed, about few rounds per minute, so that the back emf due to the PM can be neglected.

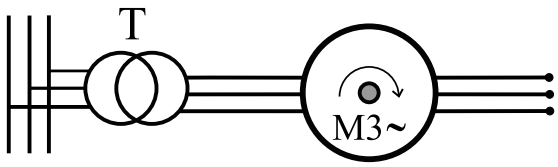

Figure 7.20: Test setup for the induced voltages measurement.

Table 7.5: IPM machine: comparison of measured self inductances and mutual interaction according to various winding configurations.

Winding config.	min synch. inductance (mH)	max synch. inductance (mH)	max V_M (%)
DL–1	15.8	33.7	13.3
DL–2	15.1	30.8	13.6
DL–3	12.2	24.7	52.2
SL–1	25.3	47.4	14.6
SL–2	26.8	51.7	5.0

From the supply voltage and the current measured, it is possible to compute the synchronous inductance of the machine. Since the rotor is anisotropic, this varies from a maximum value (i.e. L_q) to a minimum value (i.e. L_d).

Also the voltages induced in the open–circuited phases vary according to the rotor position. The maximum of the induced voltage has been considered as the reference voltage, regardless the phase where this peak voltage is measured.

Table 7.5 summarizes the results of the experimental tests. For the various winding configurations, the minimum and maximum inductances are reported. It is observed that the saliency ratio, that is, the ratio between the maximum and minimum inductance, approaches to two as in the simulations described above.

Then, the ratio between the maximum induced voltage and the supply voltage (V_M) is reported. It is worth noticing that with configurations DL-1, DL-2 and SL-1, this ratio does not exceed 15%. With the configuration SL-2, the mutual coupling is negligible, as also observed from simulations, see Fig. 7.19. Conversely, the configuration DL-3

exhibits the higher mutual coupling between the two windings, that is, higher than 50%, confirming the simulation results of Fig. 7.18.

7.6. Short circuit fault tests

In this section, the impact of a short–circuit fault applied to different mechanical arrangements is evaluated. Only simulation and measurements on the IPM prototype are reported. Fig. 7.21 shows a sketch of the test layout for simulating the short–circuit faults.

7.6.1. All–phase short–circuit fault

At first, the impact of the short–circuit fault in the IPM prototype is quantified dragging the rotor by a master drive with all the stator coils short–circuited. The intrinsic fault capability of the adopted fractional–slot winding is highlighted by the low measured values of braking torque T_{brk} and steady state short–circuit currents I_{shc}, shown in Fig. 7.22. Such quantities can also be evaluated by means of analytic equations [21]:

$$T_{brk} = -\frac{3}{2} p R \Lambda_m^2 \, \omega_{me} \, \frac{R^2 + \omega_{me}^2 L_q^2}{(R^2 + \omega_{me}^2 L_d L_q)^2} \tag{7.1}$$

$$I_{shc} = \frac{\sqrt{(\omega_{me}^2 L_q \Lambda_m)^2 + (\omega_{me} R \Lambda_m)^2}}{R^2 + \omega_{me}^2 L_d L_q} \tag{7.2}$$

even though the analytical model considers sinewave currents, which are not exactly verified experimentally. Both the steady–state braking torque and the short–circuit current amplitude result to be a function of the electrical speed ω_{me}. Then, the short–circuit current always increases with the speed, approaching Λ_m / L_d.

Fig. 7.22 shows a good agreement between measurements and predictions. The small discrepancy is due to the estimation error of the parameters, which are assumed to be constant in the analysis (resistance R, PM flux Λ_m and d–q inductances).

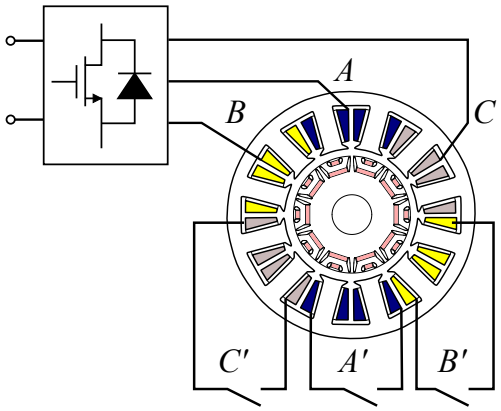

Figure 7.21: Test layout for testing the machine capability with a single phase or a complete three–phase winding short–circuited.

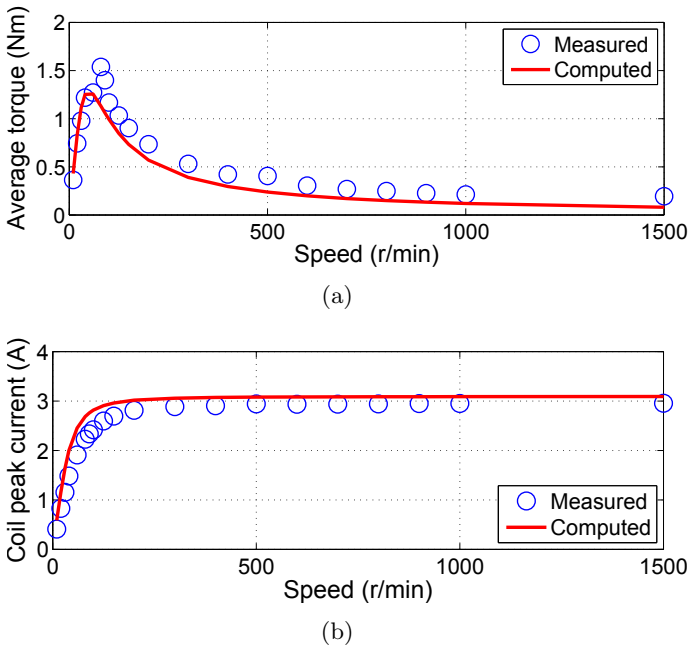

Figure 7.22: Measured braking torque (a) and short–circuit rms current (b), versus speed with dragged rotor and all coils short–circuited.

7.6.2. Operations with a short–circuited winding

Further tests have been carried out with one winding supplied by the converter, and the other winding short–circuited. Two cases have been tested: (i) with only one phase short–circuited, (ii) with all three phases short–circuited. Table 7.6 reports the measured values of the average torque T_{avg}, the peak–to–peak torque ripple ΔT and the short–circuit current amplitude (peak value) $\hat{I}_{shc}$. In addition, the average torque reduction T_{Fa} between the short–circuit fault and the open–circuit fault is reported. It is obtained comparing the measured values of Table 7.2 and Table 7.6.

However, the amplitude of the short–circuit current remains limited and close to the estimated value in the complete short–circuit, regardless of the configuration adopted. The DL–3 configuration, that exhibits the higher mutual coupling between the windings, exhibits the higher induced short–circuit current. It also exhibits the higher reduction of average torque with a three–phase short–circuit fault, as respect of the open–circuit fault. It results about 33%, while for DL–1 and DL–2 configurations it is around 20%.

As far as the torque ripple is concerned, it increases more with only one phase short–circuited rather than with the three phases short–circuited. This is due to the pulsating torque that occurs with one faulty phase. Comparing Table 7.2 and Table 7.6 further considerations can be carried out about the torque ripple depending on the fault type in the second winding: open–circuit fault or three–phase short–circuit fault. The DL–2 and DL–3 configurations exhibit almost the same torque ripple while for the DL–1 configuration the torque ripple is doubled. This is due to the lower symmetry of such a configuration.

Table 7.6: Measured average torque, torque ripple and short–circuit (ShC) current, while one winding continues to be properly supplied ($\hat{I}$=6.2 A peak).

Wind. conf.	1–ph Short–Circuit				3–ph Short–Circuit			
	T_{avg} (Nm)	ΔT (%)	$\hat{I}_{shc}$ (A)	T_{Fa} (%)	T_{avg} (Nm)	ΔT (%)	$\hat{I}_{shc}$ (A)	T_{Fa} (%)
DL–1	3.05	38.6%	2.23	9.4%	2.73	38.9%	2.26	18.7%
DL–2	2.87	36.8%	2.68	8.6%	2.44	29.2%	2.56	22.2%
DL–3	2.61	41.3%	3.52	6.5%	1.86	16.0%	3.54	33.4%

7.7. Overload Capability

The IPM machine performance has been further tested in order to investigate the overload capability. For the sake of overcoming the inverter current limit, a DC current has been imposed in the coils of two phases, while the rotor is rotating at a very low speed and while the torque behaviour is measured by means of a torquemeter. The scheme of the test setup is shown in Fig. 7.23. For instance, Fig. 7.24 shows the torque behaviour along a complete rotor round (6.28 mech. radians) with a supplied DC current equal to 15A and healthy winding configuration. The torque behaviour shows ten peaks that correspond to the rotor poles. The measured peak torque for each DC current supplied are reported in Fig. 7.25(a) for the DL configurations, and in Fig. 7.25(b) for the SL configurations.

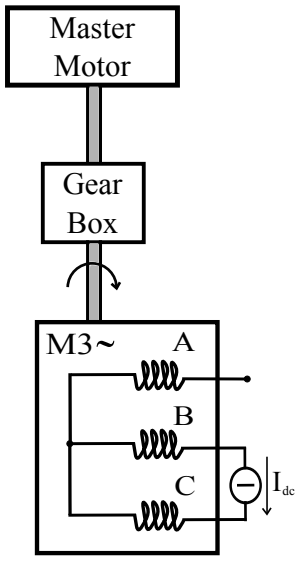

Figure 7.23: Test setup with DC current supply and dragged rotor.

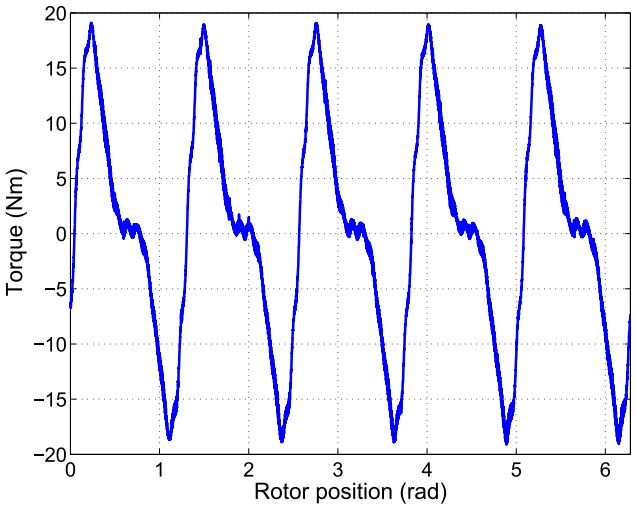

Figure 7.24: Measured torque versus rotor position with healthy winding (15A DC current supplied and dragged rotor).

Let us note that there is almost a linear proportion between torque and current up

to a DC current equal to 16 A. The equivalent peak current of a three–phase system is estimated as $\hat{I} = 2I_{DC}/\sqrt{3} = 18.4$ A(peak), corresponding to a current density of 13.1 A/mm^2.

In the case of open–phase winding fault, this linear behaviour allows to compensate the average torque reduction with a slight overload.

The DL–3 configuration exhibits an average torque lower than DL–1 and DL–2 configurations at low current, as reported in Table 7.2. Conversely, Fig. 7.25(a) shows that the DL–3 configuration exhibits the highest average torque at higher currents. This is due to the lower iron saturation at higher currents, thanks to the better distribution of the coils in such a configuration.

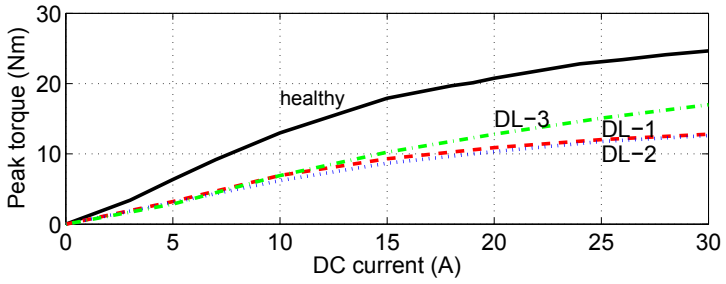

(a) Double–layer

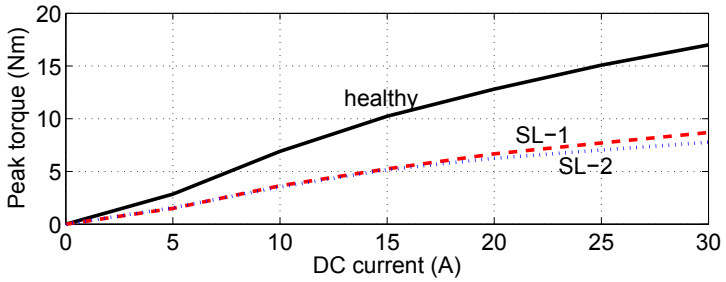

(b) Single–layer $N_t/2$

Figure 7.25: Measured torque versus current with (a) single–layer winding configurations and (b) single–layer winding configurations (DC current supply and dragged rotor).

It is worth noticing that this overload current can be applied only for a short period Δt. The latter can be estimated assuming an adiabatic heating. Assuming the thermal energy generated for Joule effect equal to the energy stored in the copper, it follows

$$\Delta t = \frac{c_{cu}\gamma_{cu}}{\rho_{cu}} \frac{\Delta\theta}{J_c^2} \tag{7.3}$$

where ρ_{cu} is the copper resistivity, γ_{cu} the copper density and c_{cu} the specific heat. The insulation used in the prototype allows a maximum temperature rise $\Delta\theta$, with a room–temperature of 25 °C, equal to 130 K. Thus for instance the insulation is able tolerate the maximum current of 30 A (DC) only for about 30 s.

However, during the DC current test a suitable pause between the tests at different current has not been completely satisfied yielding two phases to be burnt as shown in

Fig. 7.26(a). It could be noted in Fig. 7.26(b) that the non supplied phase (4 coils) has not been affected by the fault. This is due to the plastic separator and the winding structure with non overlapped coils. After the fault, the burnt phases have been rewind as highlighted in Fig. 7.26(d). The tests with DC current have been repeated confirming values of the measurements early the fault.

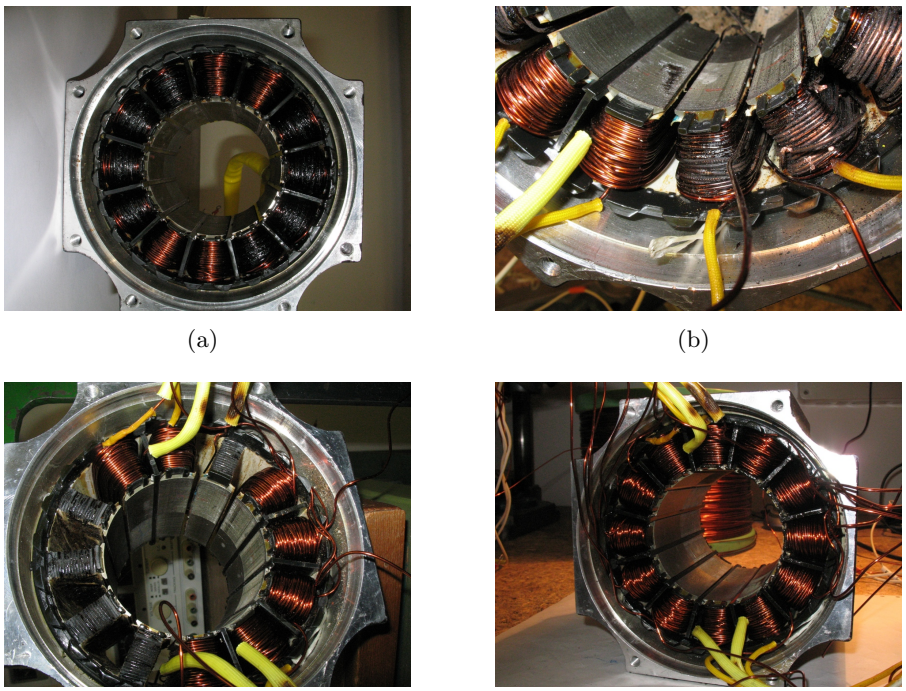

(a) (b)

(c) (d)

Figure 7.26: The 12–slot 10–pole IPM machine prototype: two phase burnt after high current test and new hand made winding.

7.8. Thermal tests

In the event of a fault and before the incoming repair, it could be very interesting to maintain the nominal torque. In this case the healthy winding has to be supplied with a current higher than the nominal value. A minimum overload conditions can be defined if it allows to satisfy the thermal limits of the healthy operating conditions. Therefore, it is required to maintain the thermal flow due to the copper losses lower or equal than the nominal value.

In order to evaluate the thermal behavior of the different configurations, some thermal tests have been carried out. Since the interest is mainly on the available standstill torque, the machine is supplied with a fixed DC current equal to $I_{DC} = 5\,A$. The phases of the winding are connected in series. During the tests only the natural cooling of the air is present. The prototype is provided of a complete set of thermal sensors (fourteen), placed in the slots and directly in contact with different stator coils as shown in Fig. 7.27 and Fig. 7.28. The signal of each sensor have been acquired by

means of a proper data acquisition system managed via serial port. The test setup is shown in Fig. 7.29.

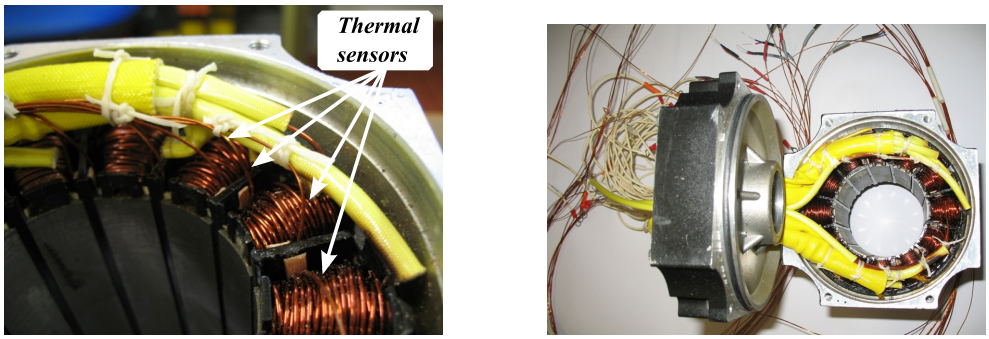

(a) (b)

Figure 7.27: Thermal sensors on IPM prototype: (a) displacement in the stator slots, (b) view of the motor and sensors cables.

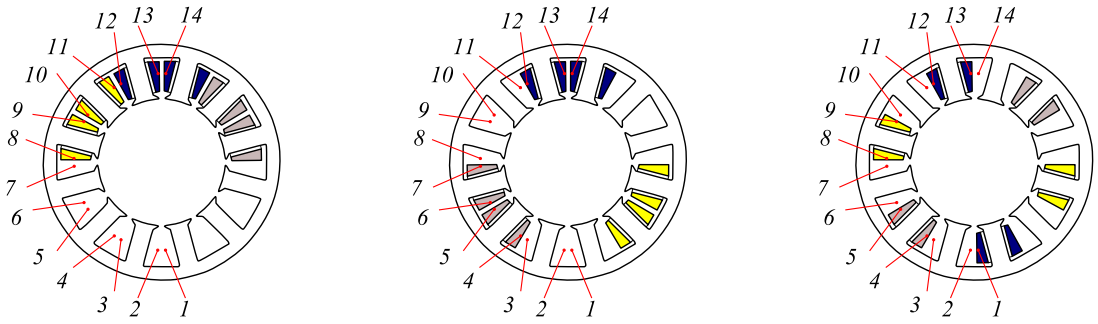

(a) DL–1 (b) DL–2 (c) DL–3

Figure 7.28: Relative position of the mechanical arrangements as respect to the thermal sensors.

(a) (b)

Figure 7.29: Thermal test: (a) acquisition system and DC current supply, (b) motor under test and oil box for ambient temperature.

Depending on the number of coil sides supplied in the slot, three different cases are

identified:

1. the slot that contains two active supplied coils ("full slot"),
2. the slot that contains one supplied coil ("half slot"),
3. the slot that does not contain any supplied coil ("empty slot").

As shown in Fig. 7.28, the distribution of the thermal sensors allows to evaluate the copper temperature with any winding configuration. Finally, two thermal sensors are placed on the machine frame, while an additional one is dedicated to the ambient temperature measurement.

Table 7.7: Measured steady–state temperature rises of different slot case study and frame.

Winding	Full slot (K deg.)	Half slot (K deg.)	Empty slot (K deg.)	Frame
Healthy	88.0	-	-	67.7
DL–1	57.0	42.3	33.8	36.1
DL–2	54.4	46.0	38.2	35.7
DL–3	-	45.2	-	35.3

Initially, a test has been carried out connecting in series all the coils of the machine in order to simulate the healthy operating conditions. The temperature behavior of the copper, as respect to the frame and the ambient, is shown in Fig 7.30(a).

Then, supplying the same DC current, only one winding is connected. Figs. 7.30(b) and 7.30(c) reports the measured behaviour of the absolute temperatures for the DL–1 and DL–3 configuration, respectively. Each figure also reports the copper temperature of the healthy test using solid line, so as to highlight the difference with the faulty conditions. The average copper temperature rise in faulty operations results in about half of corresponding value in healthy conditions. The temperature behaviour of the DL–2 configuration is not reported being very similar to the DL–1 behaviour.

The measured temperature rises of the three cases of the slot are reported in Table 7.7. The DL–3 configuration results to have the lower temperature rise. Obliviously, the "full slot" reaches the highest temperature rises for both DL-1 and DL-2 configurations. Conversely, the "half slot" temperature rise reaches similar values for each configuration. In particular it correspond to the average value between the "full slot" and the "empty slot" temperature rise.

Since the DL-3 configuration exhibits the "half slot" temperature rise in any slot, it results as the more suitable configuration for overload operations. Let us note that, in healthy conditions the copper temperature rise is almost two times the same value obtained with the DL–3 configuration. This ratio corresponds to the available difference on the joule losses in the winding.

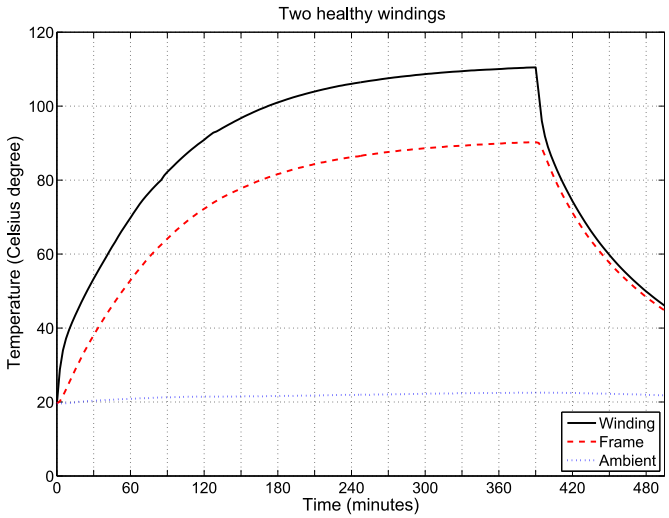

(a)

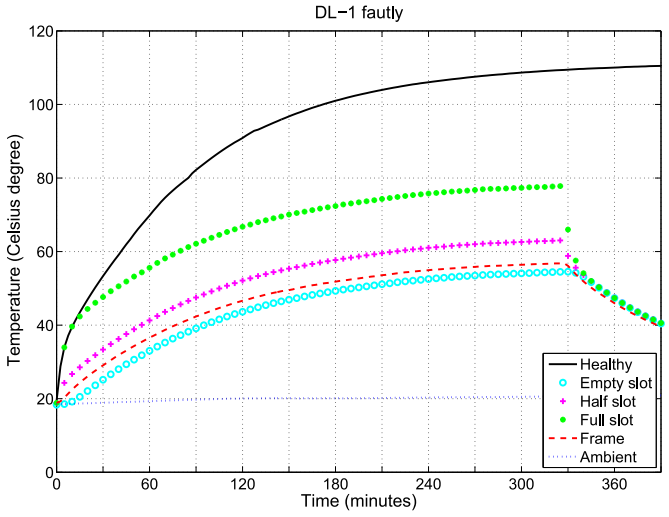

(b)

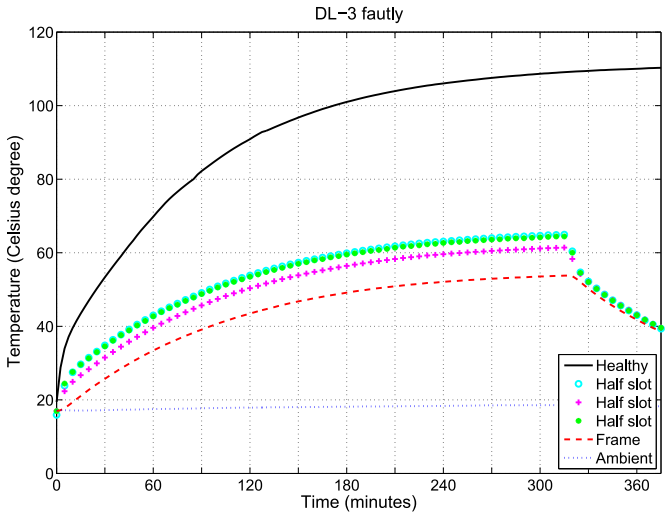

(c)

Figure 7.30: Thermal test: (a) healthy supply, (b) DL–1 open phase faulty supply, (c) DL–3 open phase faulty supply.

It follows that, it is possible to increase the phase current of about 40%, reaching the healthy thermal load. The overload current results in $I_{DC,over} = 7\ A$. A proper test has been carried out: firstly the machine is supplied considering the DL–3 healthy configuration. At the thermal steady state one winding is opened simulating the open circuit fault. Then the healthy winding is supplied with the estimated overload current. As shown in Fig. 7.31 the overload is reached again confirming the overload capability. The temperature rise of both the winding is reported, i.e. W1Q1 refers to the slot number 1 of the first winding.

According to Fig. 7.25(a), the peak torque during the open–phase fault overload increase from the 45% to the 71% of the healthy torque. This aspect could be very attractive, if integrated with a diagnostic system, allowing to minimize the performance reduction before the incoming repair. Furthermore, the effective current overload required to achieve the heathy torque results about 2 times, as previously evaluated from Table 7.2 and Fig. 7.25(a).

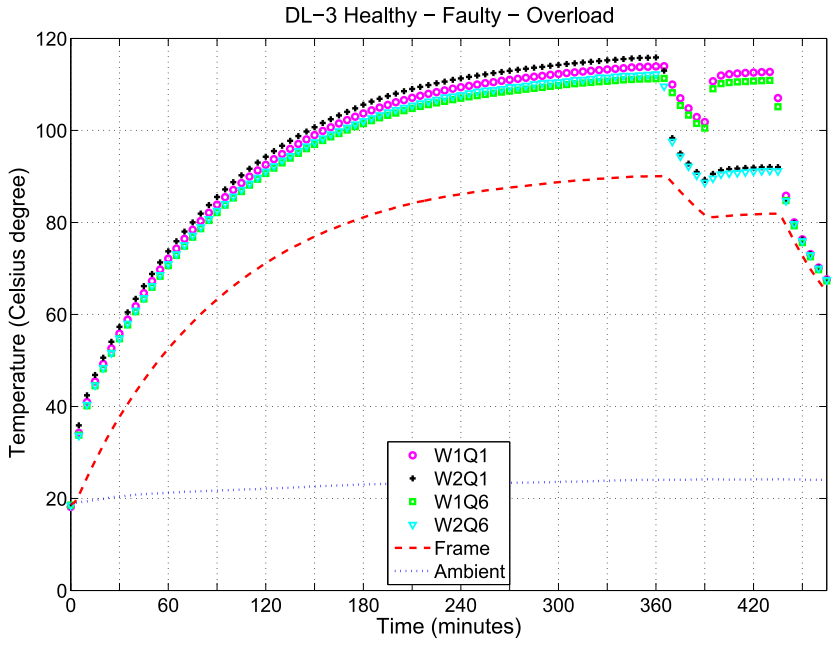

Figure 7.31: Thermal test with simulated fault and overload.

7.9. Experimental comparison with a five–phase PM machine

In this section an available five–phase PM prototype is presented. The measurements under healthy and faulty conditions are briefly reported in order to give the the basis data for the final discussion of advantages and drawbacks. Such of final comments propose to compare the five–phase machine and the dual three–phase machine.

7.9.1. The machine

The five–phase motor is characterized by a number of slots multiple of 5. It requires both custom laminations and custom inverter to supply the five–phase motor, as sketched in Fig. 7.32. Two kinds of converter can be used: a half–bridge and a full–bridge converter. The second solution has two main advantages: (i) the phase currents are independent, i.e. they are not constrained to satisfy the condition $\sum i = 0$, as in the half–bridge converter; (ii) there is not electrical interaction among phases, so that one can be disconnected independently from the others [90]. As reported in [102], the Volt–Amps rating (given by the product of rated current by *dc* voltage and by the switch numbers) of the full–bridge converter is about 105 % the Volt–Amps rating of the half–bridge one. On the contrary the use of full-bridge converter requires both terminals of the motor winding to be available. A comparison of the performance of the motor drive under faulty operating condition using half–bridge and full–bridge converter is reported in [103, 104].

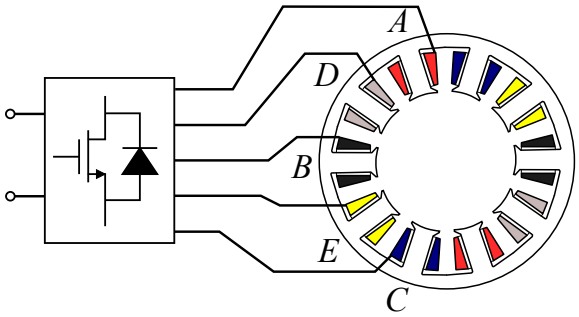

Figure 7.32: Scheme of the five–phase motor drive.

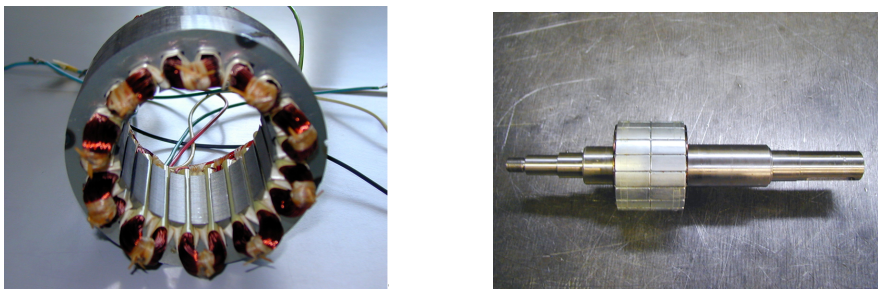

(a) (b)

Figure 7.33: Five–phase PM prototype: photo of the (a) stator and (b) rotor.

In the event of a fault, the current control strategy is modified so as to enable a smooth running also under faulty operations [102,103]. The current control strategy is modified with respect to normal conditions and current harmonics of third–order can be injected to the aim of increasing the average torque and reducing the torque ripple.

The experimental results described in this section refer to a 5–phase 20–slot 18–pole SPM motor prototype, shown in Fig. 7.33. The prototype is provided of a SL winding, as evident in Fig. 7.33(a). Each phase of the motor is fed separately by means of the six–phase power converter shown in Fig. 7.4(a).

7.9.2. Measurements

The results of torque measurements under heathy and faulty conditions are reported in Table 7.8 according to different current control strategies that are reported in [103]. Hereafter the results that yield the lowest torque ripple are summarized.

Table 7.8: Five–phase PM motor: measured performance with various open circuit faulty mode operations.

	Half–bridge		**Full–bridge**	
Motor config.	Average torque	Torque ripple	Average torque	Torque ripple
healthy	100 % (5.5Nm)	5 %	100 % (5.5Nm)	5 %
1 phase open circuit	74 % (4.07Nm)	8 %	78 % (4.29Nm)	7 %
2 non adj. phases open circuit	59 % (3.25Nm)	13 %	57 % (3.14Nm)	16 %
2 adj. phases open circuit	20 % (1.1Nm)	100 %	56 % (3.08Nm)	15 %

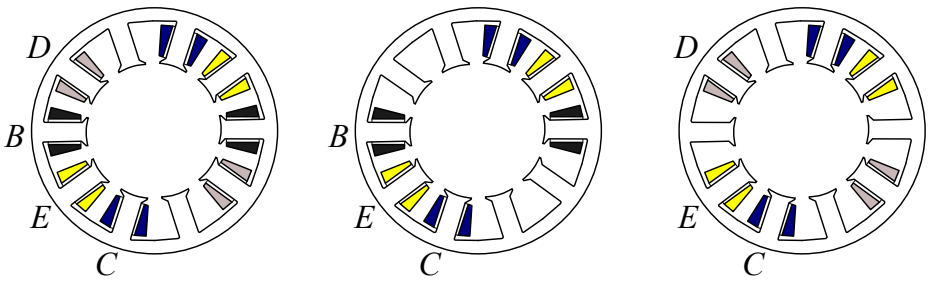

(a) (b) (c)

Figure 7.34: Five–phase PM motor: examples of the loss of one or two phases. (a): one phase open circuit; (b): two adjacent phases open circuit; (c): two non adjacent phases open circuit.

The average torque is equal to 5.5 Nm, in a good agreement with the torque computed analytically [103], while the torque ripple (mainly due to the cogging torque) is slightly higher than predicted [103], even if remains low.

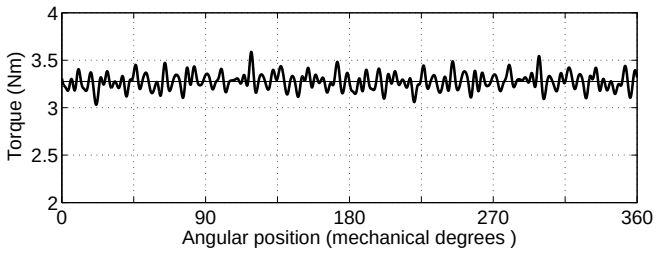

(a)

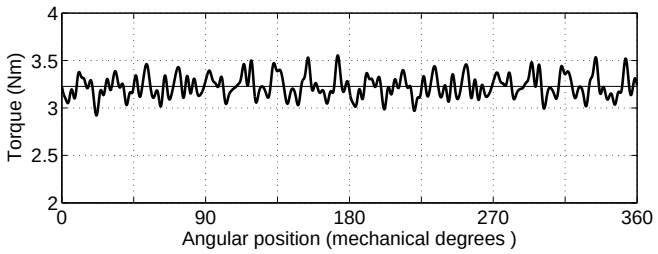

(b)

Figure 7.35: Five–phase PM motor: open circuit of two non–adjacent phases. Measured torque behaviours. (a) half–bridge converter; (b) full–bridge converter.

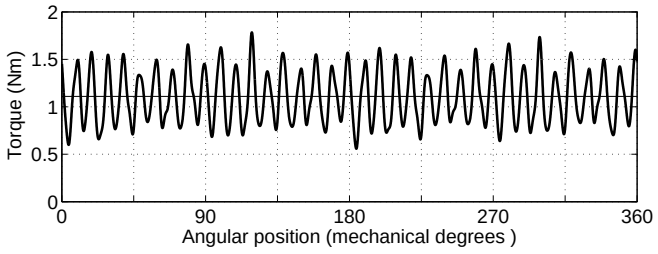

(a)

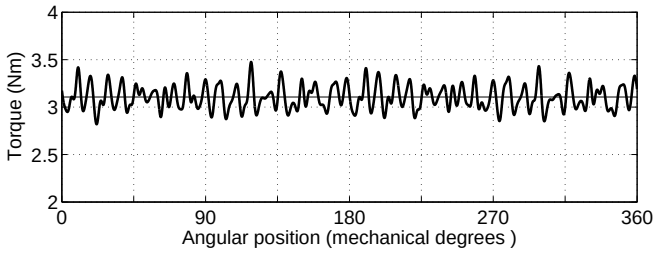

(b)

Figure 7.36: Five–phase PM motor: open circuit of two adjacent phases. Measured torque behaviours. (a) half–bridge converter; (b) full–bridge converter.

Referring to operating conditions with one open circuited phase with adjustment of the currents in the other healthy phases, it is worth to notice that using both the converters, a smooth torque is achieved with a satisfactory average torque (about 78 % of in healthy conditions). Figs. 7.35(a) and 7.35(b) show the measured torque behaviour using half–bridge and full–bridge converter corresponding to two open circuited non–adjacent phases. The resulting torque is quite smooth with average value slightly lower than 60%.

In case of fault of two adjacent phases the advantages of using the full–bridge converter are highlighted. In particular Fig. 7.36(a) refers to the half–bridge converter, while Fig. 7.36(b) refers to the full–bridge converter considering two open circuited adjacent phases after the application of the proper current control strategy. The use of the full–bridge converter gives a substantial improvement of the motor performance: properly high average torque and reduced torque ripple are achieved.

7.9.3. Discussion

Concerning the five-phase motor drive, advantages and drawbacks are summarized as follow:

- Custom laminations have to be designed and stamped, for the five–phase motor stator.
- A non standard five–phase converter is needed to control the motor.
- The main advantages of using a five–phase motor drive are found in its reliability to operate properly also in faulty conditions. It can operate with one or two open circuited phases (adjacent or not) giving the drive a high tolerance to faults.
- In all faulty cases, a proper current control strategy can be found so as to limit the torque ripple, and this could be a mandatory requirement in several applications.
- When the drive operate in faulty conditions, the average torque results to be proportional to the number of the healthy operating phases, for phase currents amplitude fixed to nominal value.
- When two adjacent phases are open circuited the best result is achieved adopting a full–bridge inverter. It allows a properly high average torque and a low torque ripple to be obtained.

As far as the dual three–phase winding motor drive is concerned, the following considerations are made:

- The major advantage is the possibility to use standard components available on the market, as three–phase inverters and three–phase laminations,
- In the event of fault of one winding or one converter, the motor is operated by means of the remaining healthy winding only at halved power. Independently of the winding arrangement, the average torque for given current is approximately halved, while the torque ripple generally increases.

- A high unbalanced radial force on the rotor arises when supplying a single winding, even if the coils of this winding are distributed along the stator circumference. In order to limit this radial force, it is necessary to arrange the phase coils on symmetrical parts of the stator, as the configuration DL-3 of the 12–slot 10–pole machine.

- Finally, all winding arrangements yield a low mutual coupling between the two windings, but the configuration DL-3. This is not surprising, since such a configuration is characterized by alternate coils of the two windings.

7.10. Six–phase feasibility

From the results presented in this chapter it is evident that the adoption of six–phase configuration during healthy operating conditions is preferable. It yields advantages of getting both a multi–phase machine (on performance side) and a dual three–phase machine (on cost side).

Hereafter the feasibility of the six–phase configuration is investigated analyzing different pole and slot number combinations. Both double–layer (DL) and single–layer (SL) fractional–slot windings with non–overlapped coils are considered ($y_q = 1$). The analysis is carried out using the properties of the star of slots.

The classical theory of the star of slots, presented in chapter 6, is extended to the design of unconventional fractional–slot windings [64]. It allows to evaluate the phasors relationships that identify the slot and pole combinations allowing a six–phase supply strategy to be applied.

With six phases, e.g. $m = 6$, each phase sector of the star of slot covers 30°. Fig. 7.37 shows the star of slot of the 24–slot 22–pole configuration. An an example, the two sectors of phase A and phase A' can be highlighted allowing a quick verification of the six–phase feasibility.

Let us note that, the transformation from a DL to a SL winding can be done directly starting from the analysis of the star of slots. For instance, referring to the star of slots of Fig. 7.37(a), the even phasors are removed, obtaining the SL winding, Fig. 7.37(b).

Winding requirements

In order to obtain a structure suitable for the six–phase supply strategy a shift between the two windings is necessary [96, 108]. The shift angle between the phases, e.g. phase A and phase A', has to be equal to 30 electrical degrees. Referring to an induction machine, this six–phase solution is discussed in literature with different names: six–phase, split–phase, dual–three phase, dual–stator or asymmetrical six–phase machine.

From the analysis of the properties of the star of slots, of those configurations allowing a six–phase machine to be obtained using a dual three–phase configuration,

two specific condition are required to be satisfied. The winding properties are:

$$\begin{aligned} &\frac{Q}{2t} && \text{is even, with DL winding} \\ &\frac{Q}{4t} && \text{is even, with SL winding} \end{aligned} \tag{7.4}$$

Therefore each phase of the two windings is formed by $Q/6t$ spokes of the star of slots. From (7.4) it follows that the ratio between slot number Q and machine periodicity t has to be even, although it is not enough to get a suitable structure for a six–phase machine. In addition the condition Q/t even, that implies both of (7.4), involves some properties [110]. They are:

- Adjacent phasors are even and odd alternatively,
- Opposite phasors always exist, that is, phasors out of phase of 180° electrical. If $Q/2t$ is even the two opposite phasors are both even or odd, while if $Q/2t$ is odd one phasor is odd and the other is even,
- If periodicity is higher than unity ($t > 1$), the phasors superimposed refer all to even slots or all to odd slots,
- There are all harmonics multiple of the periodicity t.

Results of the analysis

The results of the analysis of the star of slots of some windings are summarized in Table 7.9 and Table 7.10. For each combination of pole number ($2p$) and slot number (Q) the following data is reported:

- the winding factor k_w of main harmonic,
- the machine periodicity t,
- the ratio between slot number and periodicity Q/t,
- the feasibility to get a standard three–phase single–layer (SL) winding,
- the absolute difference between the slot number and the pole number $|Q - 2p|$. Since it is common to consider winding satisfying $|Q - 2p|$ equal to 1 or 2, only these cases are highlighted,
- The number of slot per pole per phase q.

Finally according to (7.4), Table 7.9 and Table 7.10 highlight when the ratios $Q/2t$ and $Q/4t$ are even, with the marker ★ and ■ respectively. They are the conditions to achieve the six–phase machine with DL and SL winding respectively.

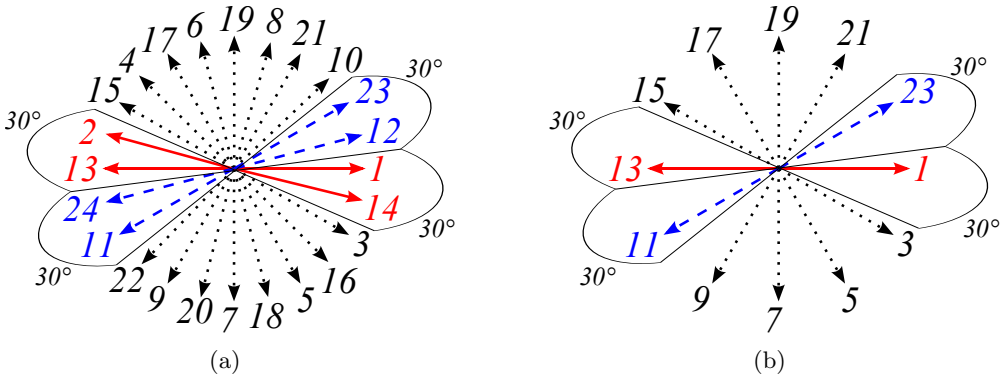

Figure 7.37: Star of slots with Q=24, $2p$=22, $y_q = 1$, six–phase sectors of phase A with (a) DL winding and (b) SL winding.

Table 7.9: Poles and slot number combinations from 2 to 14 poles. Notes: ★ means $Q/2t$ even, ■ means $Q/4t$ even.

$2p$	Q	k_w	t	Q/t	SL	$\|Q-2p\|$	q	Notes
2	3	0.866	1	3	-	+1	1/2	
4	3	0.866	1	3	-	+1	1/4	
	6	0.866	1	3	yes	+2	1/2	
6	9	0.866	3	3	-	-	1/2	
8	6	0.866	2	3	yes	+2	1/4	
	9	0.945	1	9	-	+1	3/8	
	12	0.866	4	3	yes	-	1/2	
	15	0.711	1	15	-	-	5/8	
10	9	0.945	1	9	-	+1	3/10	
	12	0.933	1	12	yes	+2	2/5	★
	15	0.866	5	3	-	-	1/2	
	18	0.735	1	18	yes	-	3/5	
12	9	0.866	3	3	-	-	1/4	
	18	0.866	6	3	yes	-	1/2	
14	**12**	0.933	1	12	yes	+2	2/7	★
	15	0.951	1	15	-	+1	5/14	
	18	0.902	1	18	yes	-	3/7	
	21	0.866	7	3	-	-	1/2	

Table 7.10: Poles and slot number combinations from 16 to 30 poles. Notes: ★ means $Q/2t$ even, ■ means $Q/4t$ even.

$2p$	Q	k_w	t	Q/t	SL	$\lvert Q-2p\rvert$	q	Notes
16	15	0.951	1	15	-	+1	5/16	
	18	0.945	2	9	yes	+2	3/8	
	21	0.890	1	21	-	-	7/16	
	24	0.866	8	3	-	-	1/2	
18	27	0.866	9	3	-	-	1/2	
20	18	0.945	2	9	yes	+2	3/10	
	21	0.953	1	21	-	+1	7/20	
	24	0.933	2	12	yes	-	2/5	★
	27	0.877	1	27	-	-	9/20	
	30	0.866	10	3	yes	-	1/2	
22	21	0.953	1	21	-	+1	7/22	
	24	0.949	1	24	yes	+2	4/11	★ ■
	27	0.915	1	27	-	-	9/22	
	30	0.874	1	30	yes	-	10/22	
	33	0.866	11	3	-	-	1/2	
24	18	0.866	6	3	yes	-	1/4	
	27	0.945	3	9	-	-	3/8	
	36	0.866	12	3	yes	-	1/5	
26	**24**	0.949	1	24	yes	+2	4/13	★ ■
	27	0.954	1	27	-	+1	9/26	
	30	0.936	1	30	yes	-	5/13	
	33	0.903	1	33	-	-	11/26	
	36	0.867	1	36	yes	-	6/13	★
	39	0.866	13	3	-	-	1/2	
28	**24**	0.933	2	12	yes	+2	2/7	★
	27	0.954	1	27	-	+1	9/28	
	30	0.951	2	15	yes	+2	5/14	
	33	0.928	1	33	-	-	11/28	
	36	0.902	2	18	yes	-	3/7	
	39	0.863	1	39	-	-	13/28	
30	27	0.945	3	9	-	-	3/10	
	36	0.933	3	12	yes	-	3/5	★
	45	0.866	15	3	-	-	1/2	

Summarizing the results of the analysis, the slot/pole combinations allowing a six–phase supply strategy are:

- **12 slots**: 10, 14 poles,
- **24 slots**: 20, 22, 26, 28 poles,
- **36 slots**: 26, 30 poles.

All of them have a slot number multiple of twelve, although this condition is not enough to have $Q/2t$ even. The star of slots of the combinations satisfying the six–phase feasibility condition are shown in Fig. 6.2 and in Fig. 7.38. The phasors composing the phase A are drawn with solid line while the vectors of phase A' are dashed (remainder vectors are dotted).

7.10.1. Discussion

The 12–slot combinations

The 12–slot 10–pole configuration, provided with an IPM rotor, has been analyzed and experimentally tested both with a six–phase supply and with a three–phase supply in this chapter. The torque performance of the DL–3 configuration are reported in Table 7.2.

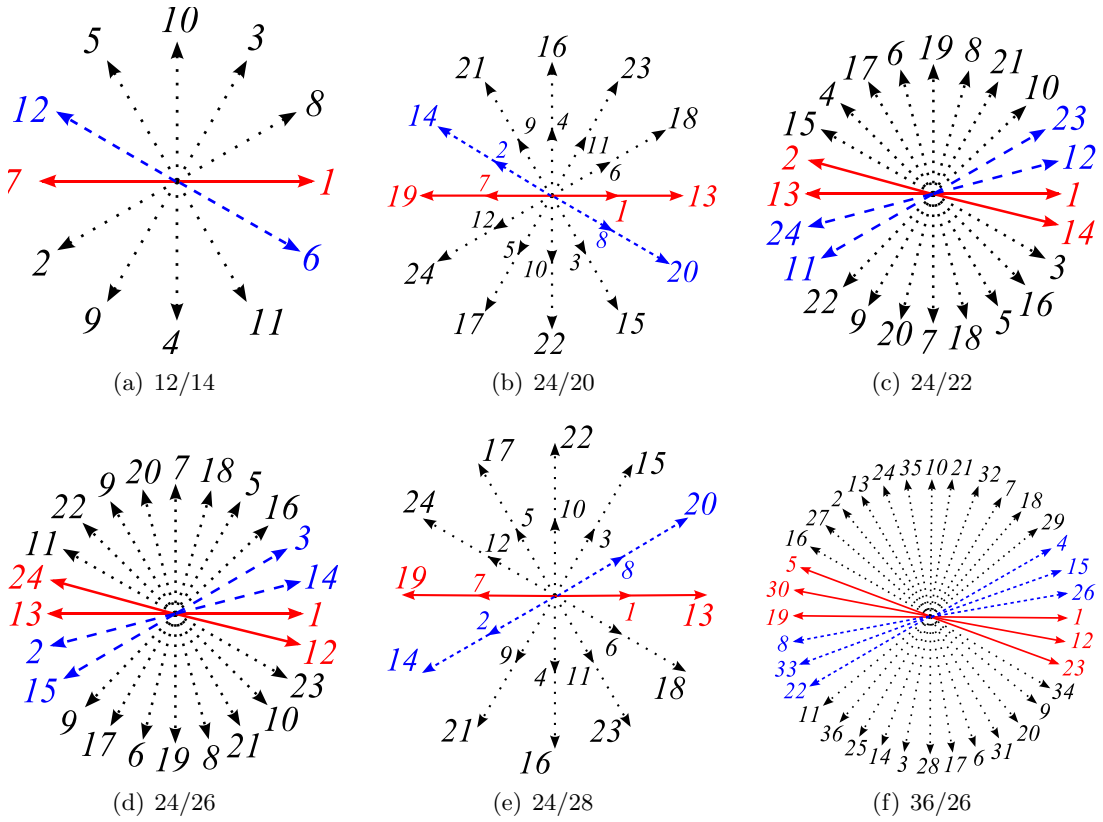

(a) 12/14 (b) 24/20 (c) 24/22

(d) 24/26 (e) 24/28 (f) 36/26

Figure 7.38: Star of slot of some slots/poles combination allowing six–phase supply.

A comparison between measured torque behaviors under healthy and faulty conditions is shown in Fig. 7.39. It is confirmed experimentally that, with a six–phase supply strategy, the average torque is higher than with standard three–phase supply. In addition, the six–phase supply allows the torque ripple to be reduced since the sixth order torque harmonic is zero, as highlighted in Fig. 7.39.

In general, since the condition $Q < 2p$ involves a higher harmonic contents, those slot and pole combinations exhibit worse performance than those that satisfy the common condition $Q > 2p$. Therefore, the 12/10 configuration has better performance as respect to the 12/14. Finally, SL configurations of both 12/10 and 12/14 are not suitable for the six–phase supply strategy, since the second condition of (7.4) is not satisfied.

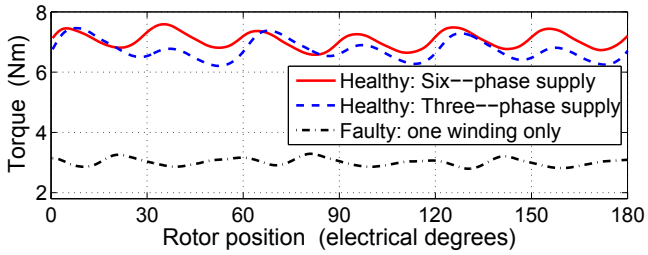

Figure 7.39: IPM 12–slot 10–pole measured torque behaviors under healthy and open circuit faulty conditions.

The 24–slot combinations

The 24/20 configuration results to be similar to the 12/10 configuration, with a periodicity equal to 2. Also in this case the six–phase supply strategy is not feasible with SL winding. Conversely, the 24/22 configuration allows the SL winding to be a proper alternative removing all even phasors. Fig. 7.37 shows the corresponding star of slots.

Both configurations have been already highlighted as interesting solutions in [72, 111]. The number of slot per poe per phase q for both configurations is between 1/2 and 1/3, giving the best performance without tooth tips asymmetrical design [72]. As highlighted above, the condition $Q < 2p$ yields for the combinations 24/26 and 24/28 a higher harmonic contents as respect to the 24/22 and 24/20 configuration, respectively.

The 36–slot combinations

Referring to the 36–slot combinations, the one with 26 poles has the lowest winding factor ($k_w = 0.867$) while the one with 30 poles is equal to the 12/10 configuration but with periodicity equal to 3.

7.10.2. Alternative structures

Six–phase solutions with a four–layers winding

An alternative solution of using the DL winding is to adopt a four–layer winding. Such a winding has been studied in [69] and recently investigated further [112]. In addition, a recent patent [113] presents a solution based on doubling the two–layer winding in the 12–slot 10–pole configuration and an additional shift of the two halves of winding by one slot. In this way the fundamental winding factor is reduced by 3.4% but some space harmonics are reduced.

Starting from a DL winding, the number of coils is doubled, achieving two levels for the coils within the slots. Then, the coils of one level are shifted with respect the coils of the other level. The transformation from two– to four–layer winding is illustrated in Fig. 7.40 together with the corresponding stars of slots. It follows that those combinations that satisfy (7.4) are suitable to obtain the six–phase machine even with the four–layer winding.

The drawback of such a four–phase winding is that it requires a double number of coils in the stator, with respect the traditional DL winding. On the contrary, the

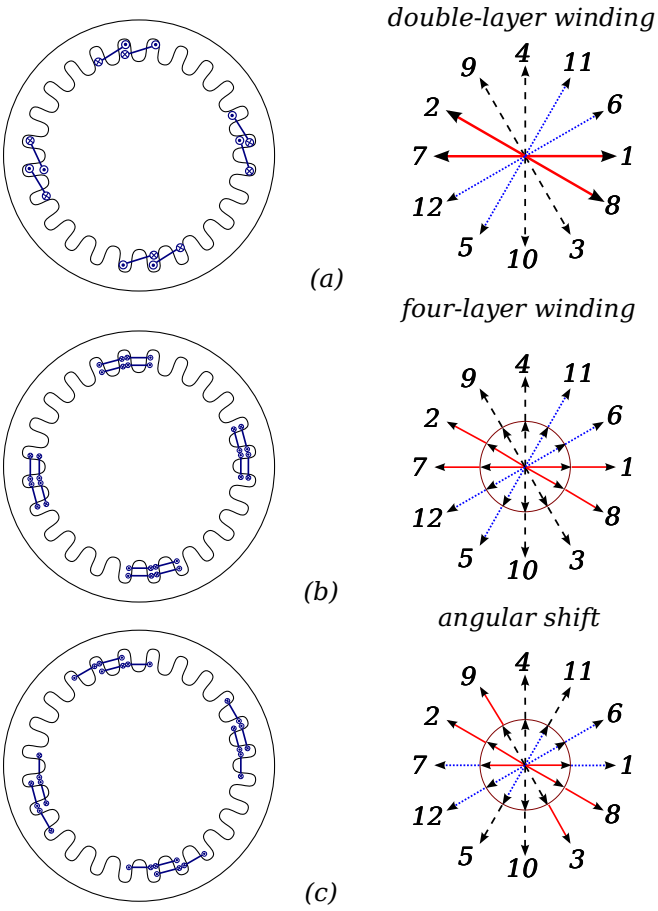

Figure 7.40: Four–layer winding concept.

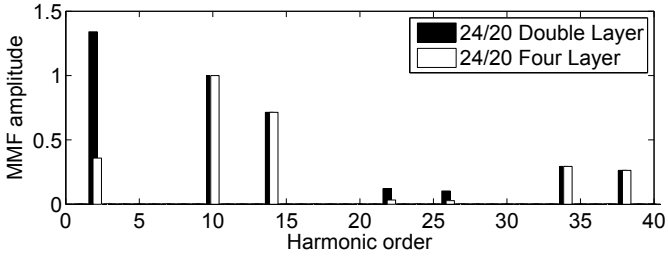

Figure 7.41: MMF harmonic content for the 24/20 configuration: double and four layer.

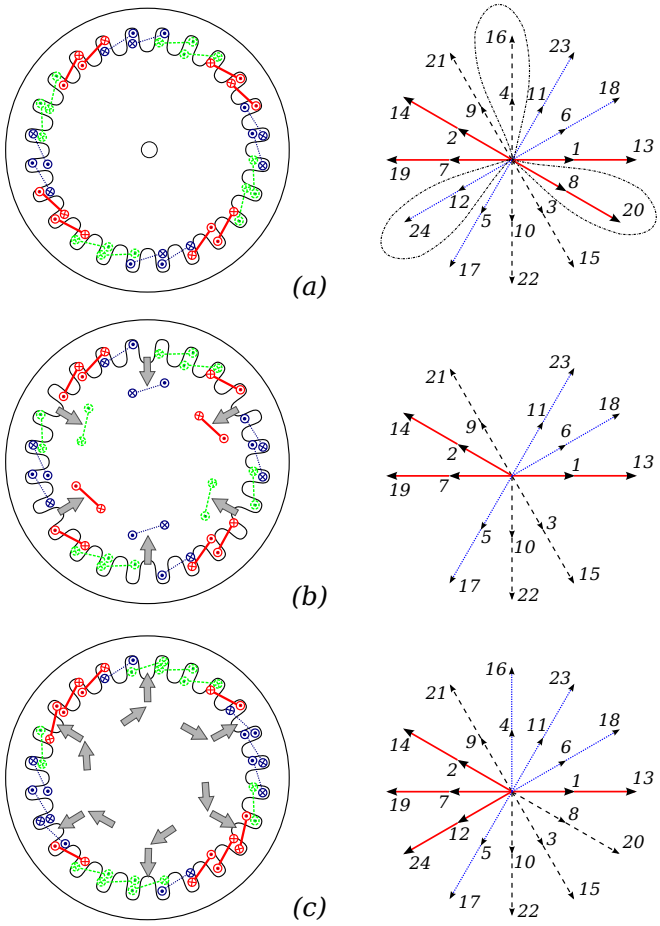

Figure 7.42: Sketch of the double–shifted winding. A 24–slot 20–pole winding is considered.

advantage is a further reduction of the MMF harmonic contents. Adopting a four–layer winding, a strong reduction of the winding factor is achieved for all the harmonics but the main harmonic and the slot–harmonics. For instance Fig. 7.41 shows a large reduction of the sub–harmonics of order $\nu = 2$ for the 24/20 combination.

The order of slot–harmonics in fractional–slot machine is computed as $\nu = kQ \pm p$, where Q and p are the number of slots and poles, respectively, while k is a positive integer.

Double–shifted winding

A six–phase winding can be also achieved adopting a double–shifted winding [114], that is obtained by means of a cyclic shift of coils inside the same repeatable group of the proper angle.

The double–shifted winding is allowable for all configurations with periodicity t even, or with periodicity t odd but Q/t even. Fig. 7.42 explains the concept of double–shift referring to the configuration 24/20. The double–shifted winding is achieved by removing some coils of each phase which are out of phase of 120 electrical degrees. Then they are shifted and rearranged in the vacant positions.

The corresponding star of slots is shown on the right part of Fig. 7.42. The phasors 8, 20, 12, 24, 4, and 16 are shifted of 120 electrical degrees. In this way, the phase A is achieved by phasors 1, 2, 13, and 14, while the phase A' is achieved by phasors 7, 12, 19, and 24.

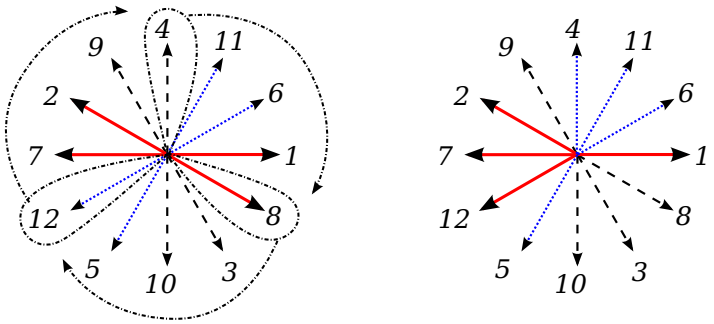

Figure 7.43: Star of slot of a double–shifted 12–slot 10–pole winding.

Similarly, this double–shift is also possible adopting the configuration 12/10. In this case the machine periodicity t is odd ($t = 1$) but the number of spokes Q/t is even ($Q/t = 12$). The corresponding star of slots is shown in Fig. 7.43.

Although this solution is feasible, there are some drawbacks. The worst one is that the machine becomes asymmetric in the event of faulty operating conditions. There is an unbalanced force that is not compensated among the poles.

7.10.3. A preliminary comparison of promising configurations

From Table 7.9 and Table 7.10 together with the related result analysis reported in Section 7.10, it follows that the more interesting configurations are the 24–slot 20–pole (24/20) and the 24–slot 22–pole (24/22). This section reports a preliminary comparison of these two configurations.

At first standard three–phase machines are considered to compare some winding properties and FE results, that are summarized in Table 7.11.

Winding properties

As reported in Tables 7.9, 7.10 and 7.11, the fundamental winding factor for the three–phase 24/22 with DL winding is $k_w = 0.949$, while it is $k_w = 0.933$ for 24/20, with a reduction of 1.6% in torque production.

On the other hand, the 24/20 is more symmetric since the winding periodicity is $t = 2$, twice with respect to the 24/22. This means that the winding allows a higher number of parallel paths in the machine. In the 24/22 configuration, due to $t = 1$, there is also more radial unbalance and then more risk for vibrations and noise, especially in faulty conditions. In addition, it should be noted that the 24/22 configuration exhibits higher MMF harmonic contents, in particular more sub–harmonics, as shown in Fig. 7.44. This aspect results more relevant adopting the SL winding.

Table 7.11: IPM geometry: comparison between 24/20 and 24/22 standard three–phase configurations.

Winding property					FE results	
$Q/2p$	t	Q/t	N_p	k_w (3–ph.)	ξ	L_M/L max (%)
24/20	2	12	5	0.933	3.0	54.7
24/22	1	24	11	0.949	3.2	26.8

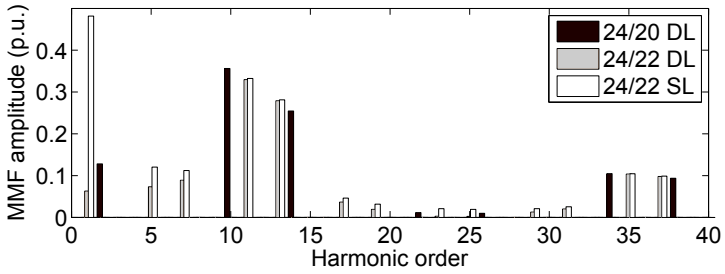

Figure 7.44: MMF harmonic content for the 24/20 and 24/22 configuration.

Cogging torque

The cogging torque is caused by the interaction between the PMs mounted on the rotor and the stator slotting. The number of periods N_p of the cogging torque waveform during a rotation of a slot pitch is computed as:

$$N_p = \frac{2p}{GCD(Q, 2p)} \tag{7.5}$$

It follows that higher the number of periods, lower the amplitude of the cogging torque. The 24/22 configuration has $N_p = 11$ while the 24/20 configuration has $N_p = 5$.

The 24/22 has an inherited less tangential cogging torque (since the higher the cogging frequency, the lower the magnitude).

Average torque and ripple

A fixed 24–slot stator geometry has been used to compare both the 24/20 and 24/22 configurations using a proper IPM rotor geometry. The torque behaviour are shown in Fig.fig:IPMtorque247.45 while Table 7.12 reports both average torque (T_{avg}) and torque ripple (ΔT).

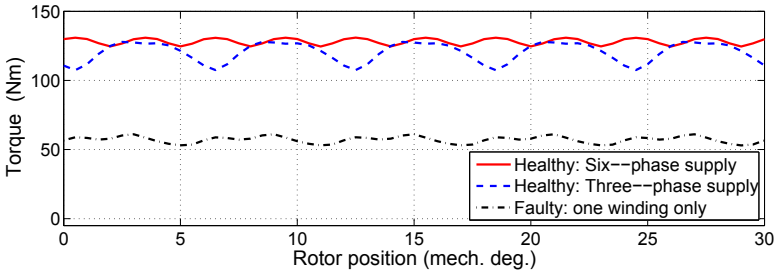

(a) 24/20 configuration

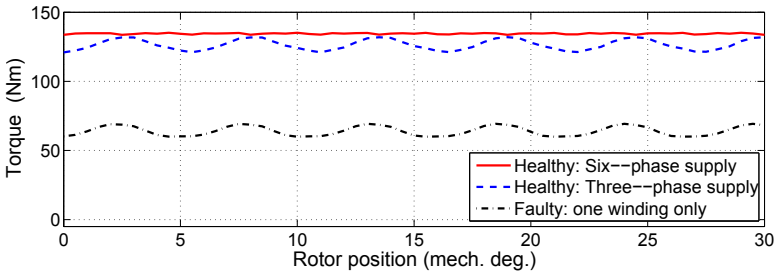

(b) 24/22 DL configuration

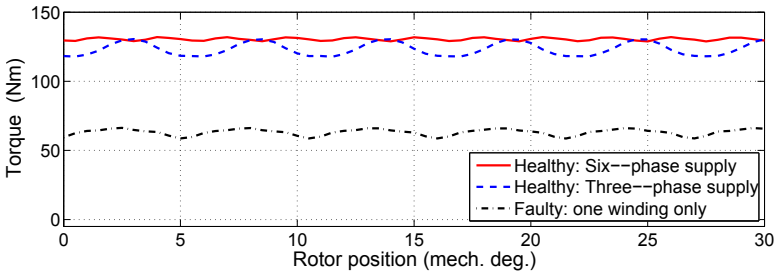

(c) 24/22 SL configuration

Figure 7.45: Torque behaviors for the (a) 24/20 and both the (b) 24/22 DL and (c) SL IPM configurations

As in Table 7.2, different supply strategies and operating conditions are considered: standard three–phase supply, six–phase supply, healthy and faulty operating conditions. As expected, the 24/20 configuration shows slightly lower average torque than the 24/22 one. The difference is slightly higher than the analytical difference between the winding factors, since the PM geometry of each rotor pole is always the same, but the number of poles is increased (i.e. the PM volume).

Table 7.12: FE results with various winding arrangements for the 24/20 and 24/22 machine ($J_{rms} = 6\ A/mm^2$).

Operating condition	24/20		24/22 DL		24/22 SL	
	T_{avg} (Nm)	ΔT (%)	T_{avg} (Nm)	ΔT (%)	T_{avg} (Nm)	ΔT (%)
Healthy 3–ph.	120.3	17%	126.5	9%	123.3	10%
Healthy 6–ph.	128.2	5%	134.5	1%	130.5	2%
Faulty	57.1	14%	64.1	15%	63.2	12%

Regardless of the different PM volume of the rotor, for each configuration the adoption of the six–phase machine yields a slight increase of the average torque (as expected from the winding factor increase) and a significant reduction of the torque ripple. As for the 12/10 configuration (Table 7.2 and Fig. 7.39), during a open winding fault the dual three–phase machine continues to provide almost half of the torque.

The 24/22 SL configuration has performance very similar to the corresponding DL configuration, but the fault–tolerance capability is higher since there is no possibility of contact between the phases in the slot.

The high number of poles, for an IPM machine, yields a relatively low saliency ratio ξ, as reported in Table 7.11.

Mutual coupling

With an IPM rotor the mutual coupling between phase A and A' is affected by the arrangements of the coils. Fig. 7.46 shows the phase displacement (for instance A and A') for the two configurations. A priori, the coils of phase A' link almost half of the flux of phase A with the 24/20 configuration while the same coils link no flux in the 24/22 configuration.

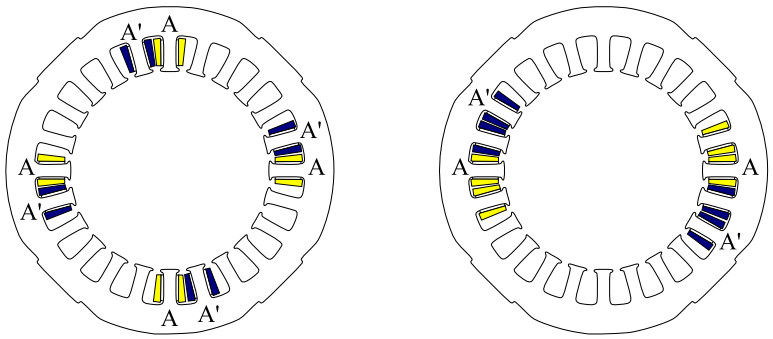

(a) 24/20 (b) 24/22

Figure 7.46: Mechanical displacement of the phases A and A' for the (a) 24/20 and (b) 24/22 configurations.

As expected, FE analysis confirms the significant mutual coupling between phase A and phase A' in the 24/20 configuration, being the ratio of the mutual inductance on the self inductance equal to about 55%. In the 24/22 configuration this ratio is lower, even though not negligible (about 27%). It is due to the anisotropy of the rotor. The flux linkages computed for the phase A and A' are shown in Fig. 7.47.

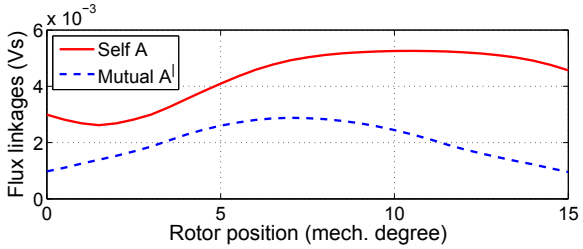

(a) 24/20 configuration

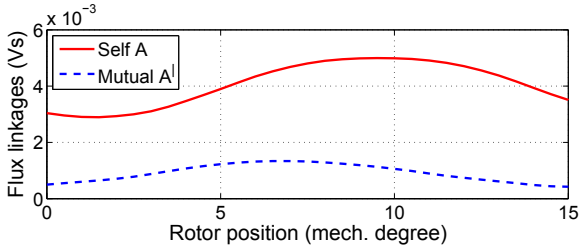

(b) 24/22 configuration

Figure 7.47: IPM configuration: flux linkage amplitude of phase A and of the open phase A', when only one winding set is supplied.

Summary

The arrangement of the winding coils of both 24/20 and 24/22 allows a symmetric structure to be got not only during healthy operating conditions but also during faulty ones, avoiding unbalanced radial forces. Under faulty operating conditions both of them exhibit satisfactory results. The average torque results about 50% of the rated value. The torque ripple is limited, lower than 15%. Configuration 24/22 allows a single–layer winding to be adopted. The performance achieved with such a winding are comparable to the others, in spite of the worst MMF harmonic content.

Therefore it can be summarized that, when parallel paths are not necessary, the 24/22 configuration results to be the more promising candidate exhibiting higher average torque, lower torque ripple, lower mutual coupling and the single–layer configuration possibility.

Conclusions

In this work some design aspects of the anisotropic PM synchronous machines for HEV are dealt with. Different methods have been adopted, including an analytical approach and finite element simulations. The results have been verified experimentally by means of prototypes, confirming the goodness of the models.

At first, a brief panorama on the hybrid electric vehicles is presented. This overview indicates the new trend of adopting permanent magnet synchronous machines onboard for propulsion and generation. The electrical propulsion will become more and more relevant in future vehicles.

The analytical model for the anisotropic synchronous PM machine has been proven to be a valid design tool. It can be used to select the optimal flux–barrier angles that minimize the torque ripple and the stator tooth eddy current iron losses

The adoption of fractional–slot windings is introduced since it allows advantages, especially regarding the efficiency, compactness, flux–weakening capability and fault–tolerant solutions. However, such a winding yields also further drawbacks and parasitic effects. Some computational issues are dealt with, in particular the effect of iron saturation is investigated.

Among the fractional–slot winding machines, the dual three–phase machine with an IPM rotor has been deeply investigated under both healthy and faulty conditions.

The following conclusions can be stated from this doctoral study:

On the machine design using the analytical approach

- The analytic model is an useful tool for the optimization of REL and IPM motors. It is able to consider the variation of different geometrical parameters, such as slot and pole combinations, PM characteristic, flux–barrier number, Machaon design.
- The torque ripple analysis highlights that it is possible to obtain always a limited oscillation maintaining a satisfactory average value.
- The tooth flux–density oscillation greatly affects the stator iron losses, which reach unacceptable values if a proper design is not adopted. When the flux–barrier geometry is properly selected the loss density increases slightly with the speed, even if the PM is buried in the rotor.

On the adoption of fractional–slot windings

- The adoption of a fractional–slot winding does not affect appreciably the machine saliency, even if the average torque results slightly reduced as respect to a machine with an integral–slot winding. A tradeoff has to be evaluated between advantages (loss increase and volume reduction) and drawbacks (current and torque ripple increase).
- The iron saturation makes the magnetic model more complex, e.g. how described in the ISA design. Thus a special care has to be adopted in both machine design and control.

On the dual three–phase machine

- The dual three–phase machine provided of a fractional–slot winding with non–overlapped coils and IPM rotor is an interesting candidate for those application in which a cost increase is acceptable in order to achieve a fault–tolerance capability. The measurements on the 12–slot 10–pole prototype have highlighted both positive peculiarities and parasitic phenomena.
- A machine with higher periodicity (e.g. 24–slot 20–pole) allows to limit the drawbacks exhibited by the measurements on the prototype.
- The six–phase configuration has been proven to be advantageous as far as the average torque and torque ripple are concerned. The design rules to achieve such of machine are found.

Bibliography

[1] S. Bolognani. *Introduction to IPM machines*, in *Design, Analysis, and Control of Interior PM Synchronous Machines (N. Bianchi, T.M. Jahns editors)*, IEEE IAS Tutorial Course notes, IAS Annual Meeting, CLEUP, Seattle, October 3, 2005, chapter 1, pages 1.1–1.35. (info@cleup.it).

[2] International Energy Agency (IEA), *World Energy Outlook, 2008*, OECD/IEA, Ed. 2008, www.iea.org.

[3] C. C. Chan and Y. S. Wong, "The state of the art of electric vehicles technology," in *The 4th International* Conference on Power Electronics and Motion Control, 2004. IPEMC, vol. 1, Xi'an, Aug. 14–16, 2004, pp. 46–57.

[4] U.S. Department of Energy (DOE) Energy Efficinecy and Renewable Energy (EERE) Office, www.eere.energy.gov.

[5] M. Ehsani, Y. Gao, S. Gay, and A. Emadi, *Modern Electric, Hybrid Electric, and Fuel Cell Vehilces*, C. P. (www.crcpress.com), Ed. 2005.

[6] I. Boldea, L. Tutelea, and C. I. Pitic, "PM-assisted reluctance synchronous motor/generator (PM-RSM) for mild hybrid vehicles: electromagnetic design," *IEEE Transactions on Industry Applications*, vol. 40, no. 2, pp. 492–498, Mar./Apr. 2004.

[7] N. Bianchi and J. F. Gieras, "Electric motors for light traction," in *EPE Journal*, vol. 12, no. 1, February 2004, pp. 12–23.

[8] L. Parsa and H. A. Toliyat, "Fault-tolerant Interior-permanent-magnet Machines for Hybrid Electric Vehicle Applications," *IEEE Transactions on Vehicular Technology*, vol. 56, pp. 1546–1552, July 2007.

[9] R. Dutta and M. F. Rahman, "Design and Analysis of an Interior Permanent Magnet (IPM) Machine with Very Wide Constant Power Operation Range," in *IEEE 32nd Annual Conference on Industrial Electronics, IECON 2006*, Paris, France, Nov. 2006, pp. 1375–1380.

[10] N. Bianchi, S. Bolognani, and B. J. Chalmers, "Salient-rotor PM synchronous motors for an extended flux-weakening operation range," *IEEE Transactions on Industry Applications*, vol. 36, no. 4, pp. 1118–1125, July/Aug. 2000.

[11] N. Bianchi and S. Bolognani, "Parameters and volt-ampere ratings of a synchronous motor drive for flux-weakening applications," *IEEE Transaction on Power Electronics*, vol. 12, no. 5, pp. 895–903, Sept. 1997.

[12] Z. Q. Zhu and D. Howe, "Electrical Machines and Drives for Electric, Hybrid, and Fuel Cell Vehicles," *Proceedings of the IEEE*, vol. 95, no. 4, pp. 746–765, Apr. 2007.

[13] M. Ehsani, Y. Gao, and S. Gay, "Characterization of electric motor drives for traction applications," in *The 29th Annual Conference of the IEEE Industrial Electronics Society, IECON '03.*, vol. 1, Nov. 2–6, 2003, pp. 891–896.

[14] C. C. Chan, "Global Sustainable Mobility and EV/HEV/FCEV development in China & Japan," in *Vehicle Power and Propulsion Conference, 2006. VPPC '06 Keynote Presentation. IEEE*, Windsor, Sept. 6–8, 2006.

[15] K. Asano, Y. Inaguma, H. Ohtani, E. Sato, M. Okamura, and S. Sasaki, "High Performance Motor Drive Technologies for Hybrid Vehicles," in *Power Conversion Conference - Nagoya, 2007. PCC '07*, Nagoya, Apr. 2–5, 2007, pp. 1584–1589.

[16] S. Matsumoto, "Advancement of hybrid vehicle technology," in *European Conference on Power Electronics and Applications, 2005*, Sept. 11–14, 2005.

[17] T. Yaegashi, *Challenge of Achieving Sustainable Mobility through Hybridization*, Research and Development of Hybrid Vehicles in Japan and Sweden Seminarim, Göteborg, Sweden, November 29, 2006.

[18] M. Elliot, *SAAB BioPowerHybrid Concept*, Research and Development of Hybrid Vehicles in Japan and Sweden Seminarim, Göteborg, Sweden, November 29, 2006.

[19] M. A. Rahman, "IPM motor drives for hybrid electric vehicles," in *Int. Aegean Conference on Electrical Machines and Power Electronics, ACEMP '07*, Bodrum, Turkey, Sept. 10–12, 2007, pp. 109–115.

[20] K. M. Rahman, N. R. Patel, T. G. Ward, J. M. Nagashima, F. Caricchi, and F. Crescimbini, "Application of Direct-drive Wheel Motor for Fuel Cell Electric and Hybrid Electric Vehicle Propulsion System," *IEEE Transactions on Industry Applications*, vol. 42, no. 5, pp. 1185–1192, Sept./Oct. 2006.

[21] N. Bianchi, M. Dai Prè, and S. Bolognani, "Design of a Fault–Tolerant IPM Motor for Electric Power Steering," *IEEE Transaction on Veicular Thecnology*, vol. 55, no. 4, pp. 1102–1111, July 2006.

[22] J.F. Gieras and M. Wing, *Permanent magnet motors technology – design and application*, 2nd edition, Marcel Dekker, New York, 2002.

[23] E. Levi, *Polyphase Motors – A Direct Approach to Their Design*, John Wiley & Sons, New York, 1984.

[24] V. B. Honsinger, "The fields and parameters of interior type AC permanent magnet machines," *IEEE Transaction on Power Apparatus and Systems*, vol. 101, pp. 867–876, January 1982.

[25] B. E. Donald, D. W. Novotny, and T. A. Lipo, "Field weakening in buried permanent magnet ac motor drives," *IEEE Transactions on Industry Applications*, vol. 21, no. 2, pp. 398–407, Mar–Apr 1987.

[26] W. Soong and T. Miller, "Field–weakening performance of brushless synchronous ac motor drives," *IEE Proc.– Electr. Power Appl.*, vol. 141, no. 6, pp. 331–339, 1994.

[27] A. Fitzgerald, C. Kingsley Jr., and A. Kusko, *Electric Machinery*, 3rd ed. McGraw-Hill Book Company, 1987.

[28] N. Bianchi. *Analysis of the IPM motor – Part I, Analytical approach*, in *Design, Analysis, and Control of Interior PM Synchronous Machines (N. Bianchi, T.M. Jahns editors)*, IEEE IAS Tutorial Course notes, IAS Annual Meeting, CLEUP, Seattle, October 3, 2005, chapter 3, pages 3.1–3.33. (info@cleup.it).

[29] D.C. White and H.H. Woodson, *Electromechanical Energy Conversion*, 1st edition, ohn Wiley and sons, New York, 1959.

[30] A. Fratta, GP. Troglia, A. Vagati, and F. Villata. "Evaluation of torque ripple in high performance synchronous reluctance machines." *Records of IEEE Industry Application Society Annual Meeting*, I:163–170, October Toronto, Canada, 1993.

[31] T.M. Jahns and W. L. Soong. "Pulsating torque minimization techniques for permanent magnet ac motor drives – a review." *IEEE Transaction on Industrial Electronics*, IE–43(2):321–330, April 1996.

[32] A. Fratta, A. Vagati, and F. Villata, "Permanent magnet assisted synchronous reluctance drive for constant-power application: Drive power limit," in *Proc. of Intelligent Motion European Conference, PCIM*, April Nurnberg, Germany, 1992, pp. 196–203.

[33] N. Bianchi, S. Bolognani, D. Bon, and M. Dai Pre,"Rotor Flux-Barrier Design for Torque Ripple Reduction in Synchronous Reluctance and PM-Assisted Synchronous Reluctance Motors," in *IEEE Transaction on Industry Applications*, vol. 45, no. 3, pp. 921–928, May.–Jun. 2009.

[34] N. Bianchi, S. Bolognani, D. Bon, and M. Dai Pre,"Torque Harmonic Compensation in a Synchronous Reluctance Motor," in *IEEE Transaction on Energy Conversion*, vol. 23, no. 2, pp. 466–473, June 2008.

[35] A. Fratta, A.Vagati, and F. Villata, "Design criteria of an IPM machine suitable for field–weakened operation," *Proc. of International Conference on Electric Machines, ICEM*, pp. 1059–1064, Sept. 1990.

[36] A. Vagati, M. Pastorelli, G. Franceschini, and S.C. Petrache. "Design of low-torque-ripple synchronous reluctance motors." *IEEE Transaction on Industry Application*, IA-34(4):758–765, July–Aug. 1998.

[37] T.J.E. Miller, *Brushless Permanent Magnet and Reluctance Motor Drives*, cap. 4, Oxford University Press, Oxford, 1989.

[38] A. Vagati. *Synchronous Reluctance Electrical Motor Having a Low Torque–Ripple Design.* U.S. Patent, 5,818,140, Oct. 6, 1998.

[39] Bianchi, N. and Bolognani, S., "Design optimisation of electric motors by genetic algorithms," *IEE Proceedings - Electric Power Applications*, vol. 145, no. 5, pp. 475–483, Sep. 1998.

[40] T. Matsuo, and T.A. Lipo, "Rotor design optimization of synchronous reluctance machine," *IEEE Transactions on Energy Conversion*, vol. 9, no. 2, pp. 359–367, Jun. 1994.

[41] L. Coelho and P. Alotto, "Tribes optimization algorithm applied to the loney's solenoid," *IEEE Transactions on Magnetics*, vol. 45, no. 3, pp. 1526–1529, June 2009.

[42] M. Liwschitz-Garik, and C.C. Whipple, "Electric Machinery", vol.II, A-C Machines. New York: D. Van Nostrand Company Inc., 1960.

[43] V. Zivotic-Kukolj, W. L. Soong, and N. Ertugrul, "Iron loss reduction in an interior pm automotive alternator," *IEEE Transaction on Industry Applications*, vol. 42, no. 6, pp. 1478–1486, Nov./Dec. 2006.

[44] R. Schiferl and T. Lipo, "Core loss in buried magnet permanent magnet synchronous motors," *IEEE Transaction on Energy Conversion*, vol. 4, pp. 279–284, June 1989.

[45] Z. Q. Zhu, Y. S. Chen, and D. Howe, "Iron loss in permanent-magnet brushless AC machines under maximum torque per ampere and flux weakening control," *IEEE Transactions on Magnetics*, vol. 38, pp. 3285–3287, September 2002.

[46] F. Magnussen, Y. Chin, J. Soulard, A. Broddefalk, S. Eriksson, and C. Sadarangani, "Iron losses in salient permanent magnet machines at field-weakening operation," in *Conf. Rec. of the IEEE 39th Industry Applications Society Annual Meeting, IAS'04*, Seattle, Washington, 3–7 October 2004, pp. 40–45.

[47] S. H. Han, W. L. Soong, and T. M. Jahns, "An analytical design approach for reducing stator iron losses in interior pm synchronous machines during flux-weakening operation," in *Conf. Rec. of the IEEE 42th Industry Applications Society Annual Meeting, IAS'07*, New Orleans, Louisiana, 23–27 September 2007, pp. 103–110.

[48] W. Roshen, "Iron loss model for permanent-magnet synchronous motors," *IEEE Transaction on Magnetics*, vol. 43, no. 8, pp. 3428–3434, August 2007.

[49] K. Yamazaki and Y. Seto, "Iron loss analysis of interior permanent-magnet synchronous motors-variation of main loss factors," *IEEE Transaction on Industry Applications*, vol. 42, no. 4, pp. 1045–1052, July/Aug. 2006.

[50] K. Yamazaki, S. Ohki, A. Nezu and T. Ikemi, "Development of Interior Permanent Magnet Motors Reduction of Harmonic Iron Losses by Optimizing Rotor Structures", *in Proc. of IEEE International Electric Machines & Drives Conference, 2007. IEMDC'07,* Antalya, May 3–5, vol. 1, pp. 489–494.

[51] S. H. Han, T. M. Jahns, and Z. Q. Zhu, "Design Tradeoffs between Stator Core Loss and Torque Ripple in IPM Machines," in *Conf. Rec. of the IEEE 43th Industry Applications Society Annual Meeting, 2008, IAS'08*, Edmonton, Alberta, October 5–9, pp. 1–8.

[52] A. Boglietti, A. Cavagnino, M. Lazzari, and M. Pastorelli, "Predicting Iron Losses in Soft Magnetic Materials With Arbitrary Voltage Supply: An Engineering Approach," *IEEE Transactions on Magnetics*, vol. 39, no. 2, pp. 981–989, March 2003.

[53] C. Mi, G. R. Slemon, and R. Bonert, "Modeling of iron losses of permanent-magnet synchronous motors," *IEEE Transactions on Industry Applications*, vol. 39, no. 3, pp. 734–742, May/Jun. 2003.

[54] G. Bertotti, *Hysteresys an Magnetism: For Physicists, Material Scientists, and Engineers*, Academic Press, 1998.

[55] Z. Gmyrek, A. Boglietti, and A. Cavagnino, "Iron Loss Prediction With PWM Supply Using Low- and High-Frequency Measurements: Analysis and Result Comparison," *IEEE Transactions on Industrial Electronics*, vol. 55, no. 4, pp. 1722–1728, April 2008.

[56] V. B. Honsinger, "The Inductances Ld and Lq of Reluctance Machines," *IEEE Transaction on Power Apparatus and Systems*, vol. 90, no. 1, pp. 298–304, January 1971.

[57] Z.Q.Zhu and D.Howe, "Influence of design parameters on cogging torque in permanent magnet machines," *IEEE Trans. on Energy Conversion*, vol. 15, no. 4, pp. 407–412, December 2000.

[58] N. Bianchi and S. Bolognani, "Design techniques for reducing the cogging torque in surface–mounted PM motors," *IEEE Trans. on Industry Applications*, vol. 38, no. 5, pp. 1259–1265, 2002.

[59] N. Bianchi, S. Bolognani, and P. Frare, "Design Criteria of High Efficiency SPM Synchronous Motors," *IEEE Trans. on Energy Conversion*, vol. EC–21, no. 2, pp. 396–404, 2006.

[60] B. Mecrow, A. Jack, D. Atkinson, G. Atkinson, A. King, and B. Green, "Design and testing of a four–phase fault–tolerant permanent–magnet machine for an engine fuel pump," *IEEE Trans. on Enegy Conversion*, vol. 19, no. 4, pp. 671–678, December 2004.

[61] B. Mecrow, A. Jack, and J. Haylock, "Fault–tolerant permanent–magnet machine drives," *IEE Proc., Electr. Power Applications*, vol. 143, no. 6, pp. 437–442, Dec. 1996.

[62] A. Jack, B. Mecrow, and J. Haylock, "A comparative study of permanent magnet and switched reluctance motors for high–performance fault–tolerant applications," *IEEE Trans. on Industry Applications*, vol. IA–32, no. 4, pp. 889–895, July/Aug 1996.

[63] N. Bianchi, M. Dai Prè, G. Grezzani, and S.Bolognani, "Design Considerations on Fractional–Slot Fault–Tolerant Synchronous Motors," *IEEE Trans. on Industry Applications*, vol. 42, no. 4, pp. 997–1006, 2006.

[64] N. Bianchi, M. Dai Prè, "Use of the star of slots in designing fractional–slot single–layer synchronous motors," *IEE Proc. – Electr. Power Appl.*, vol. 153, no. 3, pp. 459–466, May 2006.

[65] J. Cros, J. Figoeroa, and P. Viarouge, "BLDC Motors with Surface Mounted PM Rotor for Wide Constant Power Operation," in *Conf. Rec. of IEEE Industry Applications Annual Meeting, IAS'03*, no. 3, Salt Lake City, 12–16 October 2003, pp. 1933–1940.

[66] A. El-Refaie and T. Jahns, "Comparison of Synhronous PM Machine Types for Wide Constant–Power Speed Range Operation," *Conf. Rec. of the 40th IEEE Ind. App. Annu. Meeting*, vol. 2, IAS05, Kowloon, Hong Kong, pp. 1015–1022, 2–6 October 2005.

[67] F. Magnussen and C. Sadarangani, "Winding Factors and Joule Losses of Permanent Magnet Machines with Concentrated Windings," in *in Proc. of IEEE International Electric Machines and Drives Conference (IEMDC'03)*, vol. 1, 2–4 June 2003, Madison, WI, pp. 333–339.

[68] J. Wang, Z. Xia, and D. Howe, "Analysis of three–phase surface–mounted modular permanent magnet machines," in *Proc. of IEE International Conference on Power Electronics, Machines and Drives (PEMD'04)*, Edinburgh, UK, March 31 – April 2, 2004, pp. CD–Rom.

[69] A. D. Gerlando, R. Perini, and M. Ubaldini, "High pole number, PM synchronous motor with concentrated coil armature windings," in *Proc. of International Conference on Electrical Machines, ICEM'04*, Cracow, Poland, 5–8 Sept. 2004, pp. 1–6, CD–Rom, paper no.58.

[70] N. Bianchi and E. Fornasiero, "Impact of MMF Space Harmonic on Rotor Losses in Fractional–Slot Permanent–Magnet Machines," *IEEE Trans. on Energy Conversion*, vol. 24, no. 2, pp. 323–328, June 2009.

[71] N. Bianchi, M. D. Pré, L. Alberti, and E. Fornasiero, *Theory and Design of Fractional–Slot PM Machines*, ser. IEEE IAS Tutorial Course notes, IAS'07 Annual Meeting. printed by CLEUP, Padova (Italy), New Orleans, LA, September 23, 2007, (info@cleup.it).

[72] J. Cros, and P. Viarouge, "Synthesis of high performance PM motors with concentrated windings," *IEEE Trans. on Energy Conversion,*, vol. 17, no. 2, pp. 248–253, June 2002.

[73] T. Jahns, G. Kliman, and T. Neumann, "Interior PM synchronous motors for adjustable speed drives," *IEEE Trans. on Industry Applications*, vol. IA–22, no. 4, pp. 738–747, July/Aug 1986.

[74] T. Jahns, "Flux–weakening regime operation of an interior permanent magnet synchronous motor drive," *IEEE Trans on Industry Applications*, vol. IA–23, no. 3, pp. 681–689, May 1987.

[75] E. Armando, P. Guglielmi, G. Pellegrino, M. Pastorelli, and A. Vagati, ''Accurate Modeling and Performance Analysis of IPM-PMASR Motors," *IEEE Transactions on Industry Applications*, vol. 45, no. 1, pp. 123–130, Jan. 2009.

[76] S. Morimoto, M. Sanada, and Y. Takeda, "Effects and compensation of magnetic saturation in flux–weakening controlled permanent magnet synchronous motor drives," *IEEE Transactions on Industry Applications*, vol. 30, no. 6, pp. 1632–1637, Nov–Dec 1994.

[77] F. Magnussen and H. Lendenmann, "Parasitic effects in PM machines with concentrated windings," in *IEEE Transaction on Industry Applications*, vol. 43, no. 5, pp. 1223–1232, Sept.–Oct. 2007.

[78] T.J.E. Miller, M. Popescu, C. Cossar, M.I. McGilp, M. Olaru, A. Davies, J. Sturgess, and A. Sitzia, "Embedded Finite-Element Solver for Computation of Brushless Permanent-Magnet Motors," *IEEE Transaction on Industry Applications*, vol. 44, no. 4, pp. 1124–1133, Jul./Aug. 2008.

[79] N. Bianchi. *Electrical Machine Analysis using Finite Elements*. Power Electronics and Applications Series. CRC Press, Taylor & Francis Group, Boca Raton, FL, USA, 2005.

[80] N. Bianchi, and L. Alberti, "Harmonics Effect on the Embedded FE Analytical Computation of PM Motors," *IEEE Transactions on Industry Applications*, vol. 46, no. 2, pp. 812–820, Mar./Apr. 2010.

[81] D. Ionel and M. Popescu, "Finite Element Surrogate Model for Electric Machines with Revolving Field – Application to IPM Motors," *Records of IEEE Energy Conversion and Conference and Exposition, ECCE*, San José, CA, 20–24 Sept. 2009.

[82] N. Ida and J. Bastos, *Electromagnetics and Calculation of Fields*. New York, USA: Springer-Verlag Inc., 1992.

[83] J. Jin, *The Finite Element Method in Electromagnetics*. New York, USA: John Wiley & Sons, 1992.

[84] S. Salon, *Finite Element Analysis of Electrical Machine*. USA: Kluwer Academic Publishers, 1995.

[85] N. Bianchi and E. Fornasiero, "Index of rotor losses in three-phase fractional-slot permanent magnet machines," *Electric Power Applications, IET*, vol. 3, no. 5, pp. 381–388, 2009.

[86] C. P. Mudannayake and M. F. Rahman. "An integrated starter alternator for the 42V powernet". In *Power Electronics and Drive Systems, 2003. PEDS 2003. The Fifth International Conference on*, volume 1, pp. 648–653, November 17–20, 2003.

[87] S. Bolognani, R. Petrella, A. Prearo and L. Sgarbossa, "Automatic tracking of MTPA trajectory in IPM motor drives based on AC current injection," *Records of IEEE Energy Conversion and Conference and Exposition, ECCE*, San José, CA, 20–24 Sept. 2009.

[88] J. Haylock, B. Mecrow, A. Jack, and D. Atkinson, "Operation of fault tolerant PM drive for an aerospace fuel pump application," *IEE Proc. – Electr. Power Appl.*, vol. 145, no. 5, pp. 441–448, Sept. 1998.

[89] D. Diallo, M. Benbouzid, and A. Makouf, "A fault tolerant control architecture for induction motor drives in automotive applications," *IEEE Transactions on Vehicular Technology*, vol. 53, no. 6, pp. 1847–1855, Nov. 2004.

[90] T.M. Jahns, "Improved Reliability in Solid-state AC Drives by Means of Multiple Independent Phase Drive Units," *IEEE Transaction on Industry Applications*, vol. 16, no. 3, pp. 321–331, May 1980.

[91] G. Singh and V. Pant, "Analysis of a multiphase induction machine under fault condition in a phase–redundant ac drive system," *Electric Machines and Power Systems*, vol. 28, no. 6, pp. 577–590, Dec. 2000.

[92] E. Levi, "Multiphase electric machines for variable-speed applications," *IEEE Transactions on Industrial Electronics*, vol. 55, no. 5, pp. 1893–1909, May 2008.

[93] G.K. Singh, "Multi-phase induction machine drive research – A survey," *Electr. Power Syst. Res.*, vol. 61, no. 2, pp. 139–147, Mar 2002.

[94] J.M. Apsley, S. Williamson, A.C. Smith, and M. Barnes, "Induction motor performance as a function of phase number," *IEE Proc. of Electric Power Applications,*, vol. 153, no. 6, pp. 898–904, Nov. 2006.

[95] J.M. Apsley, S. Williamson, A.C. Smith, and M. Barnes, "Induction motor performance as a function of phase number," *IEE Proceedings - Electric Power Applications*, vol. 153, no. 6, pp. 86–93, Nov. 2006.

[96] E.A. Klingshirn, "High phase order induction motors–Part I–Description and theoretical considerations," *IEEE Trans. on Power Apparatus*, vol. PAS-102, pp. 47–53, Jan. 1983.

[97] A. Boglietti, R. Bojoi, A. Cavagnino, and A. Tenconi, "Efficiency Analysis of PWM Inverter Fed Three-Phase and Dual Three-Phase High Frequency Induction Machines for Low/Medium Power Applications," *IEEE Transactions on Industrial Electronics,*, vol. 55, no. 5, pp. 2015–2023, May 2008.

[98] S. Williamson, and S. Smith, "Pulsating torque and losses in multiphase induction machines," *IEEE Transaction on Industry Applications*, vol. 39, no. 4, pp. 986–993, Jul./Aug. 2003.

[99] A.R. Munoz, T.A. Lipo, "Dual Stator Winding Induction Machine Drive," *IEEE Trans. on Inductry Applications*, vol. 36, no. 5, pp. n1369–1379, Sep./Oct. 2000.

[100] R. Bojoi, E. Levi, F. Farina, A. Tenconi, and F. Profumo, "Dual three-phase induction motor drive with digital current control in the stationary reference frame," *IEE Proc. of Electric Power Applications,*, vol. 153, no. 1, pp. 129–139, 2006.

[101] R. Bojoi, M. Lazzari, F. Profumo, and A. Tenconi, "Digital field-oriented control for dual three-phase induction motor drives," *IEEE Transactions on Industry Applications,*, vol. 39, no. 3, pp. 752–760, May-June 2003.

[102] N. Bianchi, S. Bolognani, and M. D. Pré, "Design and tests of a fault–tolerant five–phase permanent magnet motor," in *Proc. of IEEE Power Electronics Specialist Conference, PESC'06*, Jeju, Korea, 18–22 June 2006, pp. 2540–2547.

[103] N. Bianchi, S. Bolognani S, M. Dai Pre, E. Fornasiero "Post-fault operations of five-phase motor using a full-bridge inverter" *Power Electronics Specialists Conference, 2008. PESC 2008. IEEE* Rhodes, Greece, 15-19 June 2008 Page(s): 2528-2534

[104] N. Bianchi, S. Bolognani, and M. D. Pré, "Strategies for the fault-tolerant current control of a five-phase permanent-magnet motor," *IEEE Transaction on Industry Applications*, vol. 43, no. 4, pp. 960–970, July/Aug. 2007.

[105] Y. Fujimoto and T. Sekiguchi, "Fault–tolerant configuration of distributed discrete controllers," *IEEE Transactions on Industrial Electronics*, vol. 50, no. 1, pp. 86–93, February 2003.

[106] A.M. El-Refaie, "Fractional-Slot Concentrated-Windings Synchronous Permanent Magnet Machines: Opportunities and Challenges," *IEEE Trans. on Industrial Electronics*, vol. 57, no. 1, pp. 107–121, Jan. 2010.

[107] B.A. Welchko, T.M. Jahns, W.L. Soong, and J.M. Nagashima. "IPM synchronous machine drive response to symmetrical and asymmetrical short circuit faults." *IEEE Transactions on Energy Conversion*, EC–18, Jun. 2003.

[108] R.H. Nelson, and P.C. Krause, "Induction Machine Analysis for Arbitrary Displacement Between Multiple Winding Sets," *IEEE Trans. on Power Apparatus and Systems*, vol. PAS-93, no. 3, pp. 841–848, 1974.

[109] R.N. Andriamalala, H. Razik, L. Baghli and F.M. Sargos, "Eccentricity Fault Diagnosis of a Dual-Stator Winding Induction Machine Drive Considering the Slotting Effects," *IEEE Transaction on Industrial Electronics*, vol. 55, no. 12, pp. 4238–4251, Dec. 2008.

[110] R. Richter, "Lehrbuch der Wicklungen Elektrischer Machinen," W. Bucherei, Ed. Karlsruhe: G. Braun, Germany, 1952.

[111] M.R. Shah, and A.M. EL-Refaie, "Eddy-Current Loss Minimization in Conducting Sleeves of Surface PM Machine Rotors With Fractional-Slot Concentrated Armature Windings by Optimal Axial Segmentation and Copper Cladding," *IEEE Trans. on Industry Applications,*, vol. 45, no. 2, pp. 720–728, March-April 2009.

[112] M. V. Cistelecan, F. F. Ferreira, and M. Popescu, "Three phase tooth-concentrated multiple-layer fractional windings with low space harmonic content," in *Proc. of IEEE Energy Conversion Energy and Expo, ECCE 2010, Atlanta, Georgia (USA),*, September 12-16, 2010.

[113] K. Ito, K. Naka, M. Nakano, and M. Kobayashi, *Electric machine*, US Patent 7, 605, Ed. Mitsubishi Electric Corporation, issued 20 Oct 2009.

[114] M. Liwschitz, "Doubly chorded or doubly shifted fractional–slot lap wave windings," *Trans. of the American Institute of Electrical Engineers*, vol. 67, pp. 684–686, 1948.

List of Symbols

The symbols are divided among Roman symbols, Greek symbols and acronyms. The more common subscripts adopted are reported at first. The dimensionless coefficients defined in chapter 3 are not reported, since they may cause misunderstanding with other symbols. However, it should be noted that these coefficients are not further adopted in the others chapters.

Common subscripts

1, 2, 3, 4	flux–barrier order from inner to outer position
a, b, c	machine phases
avg	average value
d, q	axes of the rotating reference frame
dq	computed as cross vector product of d-q flux–linkages and current
FE	results of finite elements simulations
ME	results of measurements
Mxw	computed integrating the Maxwell's stress tensor
pm	permanent magnet component
rel	reluctance component

Roman symbols

$\hat{B}$	stator tooth flux density, peak value
B_g	radial air gap flux density
$B_{g,\theta}$	tangential air gap flux density
B_t	stator tooth flux density
B_{rm}	remanent permanent magnet flux density
c_{cu}	copper specific heat
d_c	winding wire diameter
D	stator inner diameter
D_e	stator external diameter
D_{fr}	stator frame external diameter diameter
e	time back electromotive force
f	electrical frequency
g	air gap thickness
i	time dependant current
I	current, steady state value
I_{DC}	phase dc current
I_{nom}	nominal rms current
I_C	current component of the voltage limit center
I_{slot}	slot current, peak value
I_N	amplitude of spatial vector of nominal current
$\hat{I}$	phase current, peak value
I_{shc}	short circuit steady state current
h	harmonic order
h_{bi}	stator back iron height
h_m	permanent magnet length
h_s	stator slot height
H_c	permanent magnet coercitive force
J_c	slot rms conductor current density
J	slot conductor current density component
k_d	distribution factor
k_{ec}	eddy current iron loss constant computed from data sheet
k'_{ec}	generic eddy current iron loss constant
k_{ex}	excess iron loss constant
k_{hy}	hysteresis iron loss constant
k_p	pitch factor
k_{pm}	PM contribution to the rotor flux–barrier potential
k_w	winding factor
k_τ	torque constant

K_s	electric loading, peak value
$\hat{K}_\nu$	electric loading harmonic of ν^{th} order, peak value
l_b	flux–barrier length
L	inductance
L_{fr}	machine frame maximum length stack
L_{Mss}	phase mutual–inductance
L_{ss}	phase self–inductance
L_M/L	mutual coupling ratio between faulty and healthy phases
L_{stk}	machine stack length
m	number of phases
N_p	number of periods of the cogging torque
N_t	number of coil turns
N_w	number of turns of the winding
n_r	rotor separation points
n_s	stator slots per pole pair
p_s	stator slot pitch
p_{ec}	specific eddy current iron loss
p_{iron}	specific iron loss
q	number of slots per pole per phase
Q	slot number
R	phase resistance
R_b	flux–barrier reluctance
S_{slot}	stator slot area
p	number of pole pairs
t_b	flux–barrier thickness
t	time instant
t	machine periodicity
T	electromagnetic torque
T_{brk}	braking torque under short circuit fault
T_{dq}	torque computed as cross vector product between flux linkages and currents
T_{Fa}	average torque reduction from open circuit to short circuit fault
T_{Mxw}	torque computed integrating the Maxwell's stress tensor
T_p	electrical period
v	time dependant voltage
V	voltage, steady state value
V_{nom}	nominal rms voltage
V_M	mutual voltage between faulty phase and healthy phase
V_N	amplitude of spatial vector of nominal voltage

U_r	rotor magnetic potential
U_s	stator magnetic potential
w_t	stator tooth width
W'_m	magnetic energy
W'_m	magnetic coenergy

Greek symbols

α_h	electrical initial angle of h harmonic order
α_{ph}	electrical angle between two spokes of the star of slots
α_s	stator slot angle
α_s^e	stator electrical slot angle
α_i^e	electrical phase angle of the current in d-q reference
β	Steinmetz constant
β_r^e	electrical chording angle
γ_{cu}	copper density
$\Delta\theta$	maximum overload temperature rise with adiabatic heating
Δt	maximum overload time with adiabatic heating
ΔT	torque ripple
η_t	efficiency of the entire ISA drive
θ_b	mechanical flux–barrier angle
θ_b^e	electrical flux–barrier angle
θ_b'	mechanical flux–barrier angle of first machaon's set
θ_b''	mechanical flux–barrier angle of first machaon's set
ϑ_r	coordinate mechanical angle in the rotor reference frame
ϑ_s	coordinate mechanical angle in the stator reference frame
ϑ_m	rotor mechanical angle
ϑ_{me}	rotor electrical angle
λ	time dependant flux–linkage
$\hat{\Lambda}$	coil flux–linkage, peak value
Λ_m	maximum value of the flux–linkage due to the PM
μ_0	vacuum magnetic permeance
μ_r	relative magnetic permeance
ν	harmonic order
ρ_{cu}	copper resistivity
ϕ	sinusoidal air gap flux over a rotor pole, peak value
ϕ_{rem}	permanent magnet remanent flux

τ_m	analytical electromotive torque
τ^*	torque reference demand in the control law of ISA
ω_m	mechanical speed
ω_{me}	electrical speed
Ω_B	base electrical speed, steady state value
Ω_{me}	electrical speed, steady state value
Ω_P	electrical speed at which the MTPV controls starts, steady state value
$\Omega_{max,e}$	maximum electrical speed, steady state value

Acronyms

AC	alternate current
DC	direct current
DL	double layer
EMF	electromotive force
FE	finite element
FW	flux–weakening
GCD	greatest common divisor
HEV	hybrid electric vehicle
ICE	internal combustion engine
$IGBT$	insulated gate bipolar transistor
IPM	synchronous interior permanent magnet
ISA	integrated–started alternator
MMF	magnetomotive force
$MTPA$	maximum torque per ampere
$MTPV$	maximum torque per volt
PM	permanent magnet
$PMASR$	permanent magnet assisted synchronous reluctance
PSO	particle swarm optimization
PWM	pulse width modulation
RMS	root mean square
SL	single layer
SPM	surface permanent magnet
REL	reluctance
UGO	uncontrolled generator operation